3465

FERROMAGNETISM, METALLICITY, CHARGE ORDERING

AND RELATED ASPECTS OF RARE EARTH

MANGANATES AND COBALTATES

A Thesis

Submitted for the Degree of
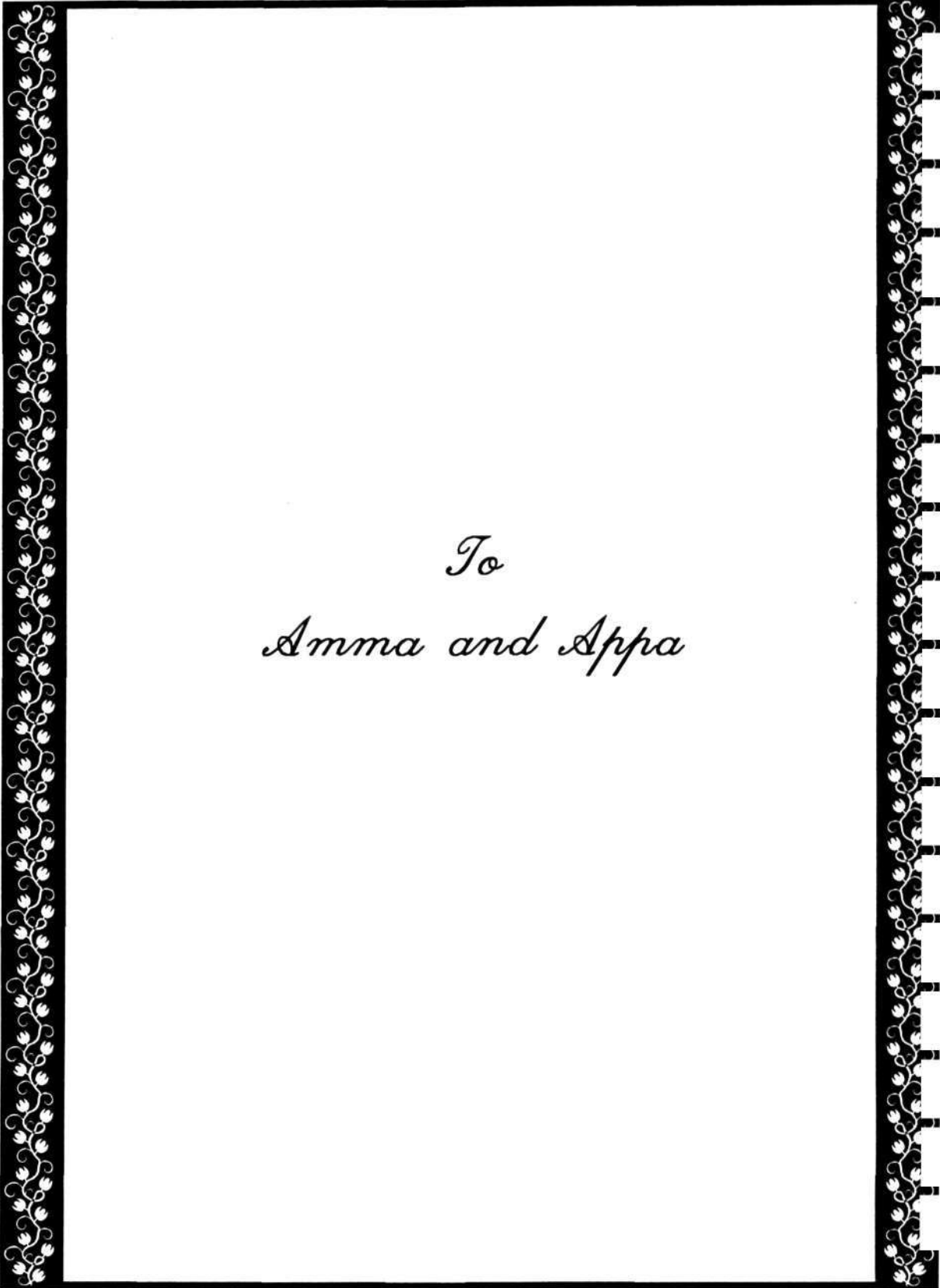
Doctor of Philosophy

By

P. VINMATHI VANITHA

Chemistry and Physics of Materials Unit

Jawaharlal Nehru Centre for Advanced Scientific Research

(A Deemed University)

Bangalore – 560 064, INDIA

2002

To
Amma and Appa

"गुरू गोविन्द दोउ खड़े, काके लागो पाय ।
बलिहारी गुरू आपने, गोविन्द दियो बताय ॥"

Statement

I hereby declare that the contents of this thesis titled "**Ferromagnetism, metallicity, charge-ordering and related aspects of rare earth manganates and cobaltates**" is a result of bonafide investigations carried out by me in the Chemistry and Physics of Materials Unit, Jawaharlal Nehru Center for Advanced Scientific Research, Bangalore, India, under the supervision of Prof. C. N. R. Rao.

In keeping with the general practice of reporting scientific observations, due acknowledgement is made wherever the work described is based on findings of other investigators. Any omission that might have occurred by oversight or error of judgement is regretted.

P. Vinmathi Vanitha

Certificate

Certified that the work described in this thesis titled "**Ferromagnetism, metallicity, charge-ordering and related aspects of rare earth manganates and cobaltates**" is the result of investigations carried out by Ms. P. Vinmathi Vanitha in the Chemistry and Physics of Materials Unit, Jawaharlal Nehru Centre for Advanced Scientific Research, Jakkur, Bangalore under my supervision.

Prof. C. N. R. Rao

ACKNOWLEDGEMENTS

PREFACE

This thesis presents the results of investigations of rare earth manganates and cobaltates. The thesis is organized into four chapters. Chapter 1 gives a brief overview of colossal magnetoresistance, charge ordering and related properties of rare earth manganates of the formula $Ln_{1-x}A_xMnO_3$ (Ln = rare earth, A = alkaline earth). The scope of the investigations carried out is described in Chapter 2. Preparation and characterization of the materials form Chapter 3.

The results of the investigations of the manganates and cobaltates are discussed at length under six subsections in Chapter 4. Charge ordering and related properties of the rare earth manganates form the major part of these investigations. Electrical and magnetic measurements have been employed to study the phenomena after suitably characterizing the materials by X-ray diffraction. The various aspects studied involve effects of cation disorder, B-site (Mn-site) doping by other cations and the effect of magnetic fields. Mössbauer spectroscopy has also been used to examine charge ordering and phase separation in the rare earth manganates. The re-entrant ferromagnetic transition in rare earth manganates with relatively small size A-site cations wherein ferromagnetism occurs on cooling the charge-ordered state has been investigated in detail. Charge ordering and related aspects have been investigated in electron-doped compositions of the rare earth manganates as well. The effects of cation size and disorder on the properties of rare earth cobaltates of the formula $Ln_{0.5}A_{0.5}CoO_3$ (Ln = rare earth, A = Sr, Ba) have been examined.

CONTENTS

SUMMARY OF RESULTS*

The important results obtained from the various investigations of rare earth manganates and cobaltates of the type $Ln_{0.5}A_{0.5}Mn(Co)O_3$ (Ln = rare earth, A = alkaline earth) presented in this thesis are briefly summarized below.

The effect of cation size disorder on charge ordering in the rare earth manganates of the type $Ln_{0.5}A_{0.5}MnO_3$ (Ln = rare earth, A = alkaline earth) has been investigated for two series of compositions with fixed average A-site radii, $\langle r_A \rangle$ of 1.24 Å and 1.17 Å and variable A-site size-variance, σ^2. The size variance, σ^2 is defined as $\sigma^2 = \sum x_i r_i^2 - \langle r_A \rangle^2$, where x_i is the fractional occupancy of A site ions and r_i is the corresponding ionic radii. The compositions with $\langle r_A \rangle = 1.24$ Å are akin to $Nd_{0.5}Sr_{0.5}MnO_3$ exhibiting distinct ferromagnetic and charge-ordering transitions both in the magnetization and resistivity data whereas the compositions with $\langle r_A \rangle = 1.17$ Å, akin to $Nd_{0.5}Ca_{0.5}MnO_3$, undergo a charge ordering transition around 240 K (T_{CO}) and remain insulating down to low temperatures. The temperature variation of electrical transport and magnetization yields the ferromagnetic transition temperature, T_C and the charge ordering temperature, T_{CO}, in these compounds. The charge-ordering transition in the rare-earth manganates, $Ln_{0.5}A_{0.5}MnO_3$, is not very sensitive to the mismatch between the sizes of the A-site cations or to the orthorhombic lattice distortion arising from the small cation size. The decrease in the charge-ordering transition temperature

---

1

at high $\langle r_A \rangle$ is consistent with the observed quadratic dependence upon $(r^0_A - \langle r_A \rangle)$, where $r^0_A \approx 1.13$ Å.

The effect of substitution of the Mn-site of rare earth manganates of the type $Ln_{0.5}A_{0.5}MnO_3$ with various non-transition (Al, Ga and Ge) and transition metal (Ti, Cr, Fe, Co, Ni, Zr and Ru) ions in small concentrations (less than 10%) has been investigated in detail. The Mn-site doping was carried out for half-doped manganates with different average A-site radii, $\langle r_A \rangle$, namely $Y_{0.5}Ca_{0.5}MnO_3$ ($\langle r_A \rangle = 1.127$ Å), $Nd_{0.5}Ca_{0.5}MnO_3$ ($\langle r_A \rangle = 1.17$ Å) and $Nd_{0.5}Sr_{0.5}MnO_3$ ($\langle r_A \rangle = 1.24$ Å). The aim of the study was to explore the possibility of chemical melting of the charge-ordered states in materials with different $\langle r_A \rangle$ values and the different behaviour of the charge ordered states with respect to chemical melting. The charge-ordered state in the manganate $Y_{0.5}Ca_{0.5}MnO_3$ with a very small $\langle r_A \rangle$ is very robust and there is no effect of impurity doping at the B-site on the magnetic and electrical transport properties. Substitution of Al, Ga, Ge or Fe does not significantly affect the properties of $Nd_{0.5}Ca_{0.5}MnO_3$. Substitution of Cr, Co, Ni and Ru at the B-site induces ferromagnetism in $Nd_{0.5}Ca_{0.5}MnO_3$, the best effects being observed with Ru substitution. However, low concentrations of these metal ions do not destroy the charge ordering completely. The ferromagnetic transition in these substituted compositions appears to be re-entrant in nature. The ferromagnetic transition temperature, T_C, increases with the increase in Ru substitution unlike in the case of Cr, Co or Ni. The properties of $Nd_{0.5}Sr_{0.5}MnO_3$ are affected to a greater extent by substitution at the B-site by the different ions. Substitution of Cr, Co, Ni and Ru makes $Nd_{0.5}Sr_{0.5}MnO_3$ ferromagnetic and metallic. Ru substitution gives the best results increasing the ferromagnetic T_C to room

temperature. It appears that the marked effect of Ru doping is due to its unique electronic configuration that facilitates electron hopping. The presence of empty e_g orbitals in the substitutent transition metal ion may be necessary for destroying the charge ordered state in these rare earth manganates.

The rare earth manganates with $\langle r_A \rangle$ in the range of 1.17-1.20 Å show interesting magnetic and electrical properties arising from the competition between ferromagnetism and charge ordering. Thus, $Nd_{0.25}La_{0.25}Ca_{0.5}MnO_3$ with a $\langle r_A \rangle$ of 1.185 Å shows an incipient charge-ordered state below ~ 200 K and undergoes a transition to a charge delocalized ferromagnetic state on cooling. The latter transition has been considered to be a re-entrant transition since the charge ordered insulating state reverts back to a ferromagnetic state which is opposite to what is normally observed in half-doped manganates with higher $\langle r_A \rangle$. We have grown single crystals of the type $Nd_{0.5-x}La_xCa_{0.5}MnO_3$ by the floating zone technique to verify if the re-entrant ferromagnetic state is exhibited in the single crystals of manganates. To understand the role of $\langle r_A \rangle$ on the ferromagnetism and charge-ordering properties of the manganates in this $\langle r_A \rangle$ regime, compositions of the type $Nd_{0.5-x}La_xCa_{0.5}MnO_3$ and $Pr_{0.5-x}La_xCa_{0.5}MnO_3$, with $\langle r_A \rangle$ values in the range 1.172-1.198Å were prepared and characterized using magnetization and resistivity measurements. A series of manganates with a fixed $\langle r_A \rangle$ value of 1.185Å corresponding to $Nd_{0.25}La_{0.25}Ca_{0.5}MnO_3$ was investigated to understand the effect of size disorder, σ^2. The ferromagnetic Curie temperature, T_C, of the re-entrant transition increases markedly with x or $\langle r_A \rangle$ in the two series of manganates in the $\langle r_A \rangle$ regime of 1.17-1.20 Å. The plots of T_{CO} and T_C against $\langle r_A \rangle$ intersect at a value of 1.195 Å, indicating a change in the relative stabilities of the ground states. Below a

3

$\langle r_A \rangle$ of 1.195 Å, $T_{CO} > T_C$ and it is likely that the charge ordered and ferromagnetic metallic states coexist in the temperature range between T_{CO} and T_C, with the width of the coexistence regime (T_{CO}-T_C) decreasing with increase in $\langle r_A \rangle$. Site disorder arising from size mismatch has a profound effect on the T_C corresponding to the re-entrant transition in this $\langle r_A \rangle$ regime of the manganates although the T_{CO} is affected to a much smaller extent. Unlike with $\langle r_A \rangle$, the coexistence regime (T_{CO}-T_C) increases with increase in σ^2.

^{57}Fe Mössbauer spectroscopy has been used as a microscopic probe to investigate the charge ordering phenomena and phase separation in rare earth manganates. To carry out Mössbauer spectroscopic studies of rare earth manganates, two typical charge ordered systems, $Nd_{0.5}Sr_{0.5}MnO_3$ and $Nd_{0.5}Ca_{0.5}MnO_3$ were doped with 2 % ^{57}Fe. After ensuring that the small doping does not change the structure or the nature of the transitions, ^{57}Fe Mössbauer spectroscopic studies were carried out at different temperatures in the 300 to 4.2 K range. The isomer shift values is characteristic of Fe in the 3+ state in both the manganates. The evolution of the Mössbauer spectra as a function of temperature shows that long-range magnetic order does not emerge in a clean manner in both the manganates studied. The well resolved magnetic hyperfine Mössbauer spectra at 4.2 K of both $Nd_{0.5}Ca_{0.5}Mn_{0.98}{}^{57}Fe_{0.02}O_3$ and $Nd_{0.5}Sr_{0.5}Mn_{0.98}{}^{57}Fe_{0.02}O_3$ indicate the presence of more than one magnetic phase. A weak paramagnetic component is also evident in the spectra at 4.2 K of $Nd_{0.5}Ca_{0.5}Mn_{0.98}{}^{57}Fe_{0.02}O_3$ and $Nd_{0.5}Sr_{0.5}Mn_{0.98}{}^{57}Fe_{0.02}O_3$. Mössbauer spectroscopy of these two manganates confirms that these materials undergo phase separation at low temperatures.

4

The effect of $\langle r_A \rangle$, A-site cation size mismatch, σ^2 as well as of Mn-site doping on charge-ordering in the electron-doped systems, $Ca_{1-x}Ln_xMnO_3$ (Ln = rare earth) were investigated to examine the similarities, if any, with the hole-doped manganates. For this purpose, compositions of the type, $Ca_{1-x}Ln_xMnO_3$ (Ln = La, Pr, Nd, Gd or Y), in particular the compositions corresponding to x = 0.36 where charge-ordering should be favored were investigated. The effect of substitution of Cr, Ga and Ge at the Mn site in few of these electron-doped manganates was also studied. To study the effect of size disorder, measurements on two series of electron-doped manganates, $Ca_{0.64}Ln_{0.36}MnO_3$, with fixed $\langle r_A \rangle$ values of 1.174 and 1.18 Å were carried out. The investigations demonstrate that charge ordering in electron doped manganate is distinctly different from that in the analogous hole-doped manganates. In a given family of manganates, the charge-ordering transition temperature, T_{CO}, increases with the electron concentration and the magnitude of the ferromagnetic interaction, rather than with decrease in $\langle r_A \rangle$. The T_{CO} decreases with decrease in $\langle r_A \rangle$, unlike in the case for the $Ln_{0.5}A_{0.5}MnO_3$ manganates, where it increases. Also, the T^0_{CO} value is higher for the electron-doped manganates, $Ca_{1-x}Ln_xMnO_3$ with x = 0.36 when compared to the half-doped manganates. Substitution of the B-site in electron-doped manganates (x = 0.36) by a transition metal ion such as Cr does not affect the charge-ordering and the charge-ordered state in these manganates is more robust than those of the half-doped manganates.

The rare earth cobaltates, $Ln_{0.5}A_{0.5}CoO_3$ (Ln = rare earth, A = Sr, Ba) have been investigated to understand the evolution of electrical and magnetic properties as a function of $\langle r_A \rangle$ as well as A-site cation disorder. To study the structure-property

relations in these cobaltates, the structures of several members with A = Sr and Ba, were investigated based on Rietveld analysis of powder X-ray diffraction patterns. Two series of rhombohedral cobaltates of the general formula $Ln_{0.5-x}Ln'_xA_{0.5-y}A'_yCoO_3$ with constant $\langle r_A \rangle$ values of ~ 1.357Å and 1.369Å were prepared in order to study the effect of the A-site cation size mismatch on the properties. The structure of $Ln_{0.5}Sr_{0.5}CoO_3$ is rhombohedral ($R\overline{3}c$) when Ln = La, Pr or Nd, but orthorhombic (Pnma) when Ln = Gd. The $Ln_{0.5}Ba_{0.5}CoO_3$ compounds are all orthorhombic (Pmmm). The ferromagnetic Curie temperature, T_C, of $Ln_{0.5}A_{0.5}CoO_3$ increases with the average size of the A-site cation upto a $\langle r_A \rangle$ of 1.40Å, and decreases thereafter due to size mismatch. It is found that T_C decreases linearly with σ^2, according to the relation, $T_C = T^0_C - p\sigma^2$. When σ^2 is large (> 0.012Å^2), the material becomes insulating, providing evidence for a metal-insulator transition caused by cation size-disorder. Thus, $Gd_{0.5}Ba_{0.5}CoO_3$ with a large σ^2 is a charge-ordered insulator below 340 K. The study demonstrates that the average A-cation radius, as well as the cation size-disorder affect the magnetic and transport properties of the rare earth cobaltates significantly.

1. COLOSSAL MAGNETORESISTANCE, CHARGE ORDERING AND RELATED PROPERTIES OF RARE EARTH MANGANATES: A BRIEF OVERVIEW

1.1 Introduction

Ever since the discovery of superconductivity in copper-based oxides some fifteen years ago, transition metal oxides have become a subject of intense research for the physics, chemistry and materials communities. Transition metal oxides show diverse properties such as ferroelectricity (as in $BaTiO_3$), ferromagnetism (as in $SrRuO_3$), superconductivity (as in cuprates), metallicity (as in $LaNiO_3$) and antiferromagnetism (as in $LaCrO_3$). Most of the above mentioned oxides possess the perovskite structure [1]. In 1993, the phenomenon of colossal magnetoresistance (CMR) was discovered in a class of manganese oxides with the general formula $Ln_{1-x}A_xMnO_3$ where Ln is a rare earth ion and A is an alkaline earth ion. Magnetoresistance (MR) is the change in electrical resistance of a material in response to an applied magnetic field. The magnitude of magnetoresistance is given by

$$MR = [R(H)-R(0)]/ R(0)$$

where R(H) and R(0) represent the values of the resistance or resistivity in the presence and absence of a magnetic field respectively. In the rare-earth manganates MR was found to be extremely large and hence termed as colossal magnetoresistance by *Jin et al.* [2]. CMR revived interest in the manganese oxides which had previously been studied widely in the 1950's [3-5], since it opens up the possibility of producing sensitive devices for a

7

range of sensor and storage applications. Apart from CMR, the rare earth manganates exhibit rich phase diagrams spanning over a wide range of magnetic properties and phenomena like charge-ordering, phase segregation and phase separation [6]. It is possible to tune the properties of these perovskite manganese oxides either by external factors or chemical means. Hence they are preferred materials for tailoring devices to fulfil a wide range of applications apart from being a subject for basic research. The magnetic, electronic and crystal lattice properties of these manganates are intimately related. Hence, it is appropriate to have a brief overview of the structure, properties and mechanisms in these manganese oxides.

1.2 Crystal structure

The rare earth manganates, $Ln_{1-x}A_xMnO_3$, crystallize in the perovskite structure. The perovskite is a simple cubic structure with space group Pm3m (Fig. 1.1a). The perovskite of the general formula ABX_3 are regarded as derived from the ReO_3 structure (Fig. 1.1b) with large A cation occupying the body centered 12-coordinate position. The perovskite structure is most stable when the tolerance factor, t, is unity. The tolerance factor, t as defined by *Goldschmidt* is,

$$t = (r_A + r_X)/\sqrt{2}(r_B + r_X)$$

where r_A, r_B and r_X denote the empirical radii of ions A, B and X respectively.

The perovskite structure occurs only with in the range $0.75 \leq t \leq 1.00$. Also, the necessity for the A and B cations to be stable in their respective twelve- and six-fold coordinations
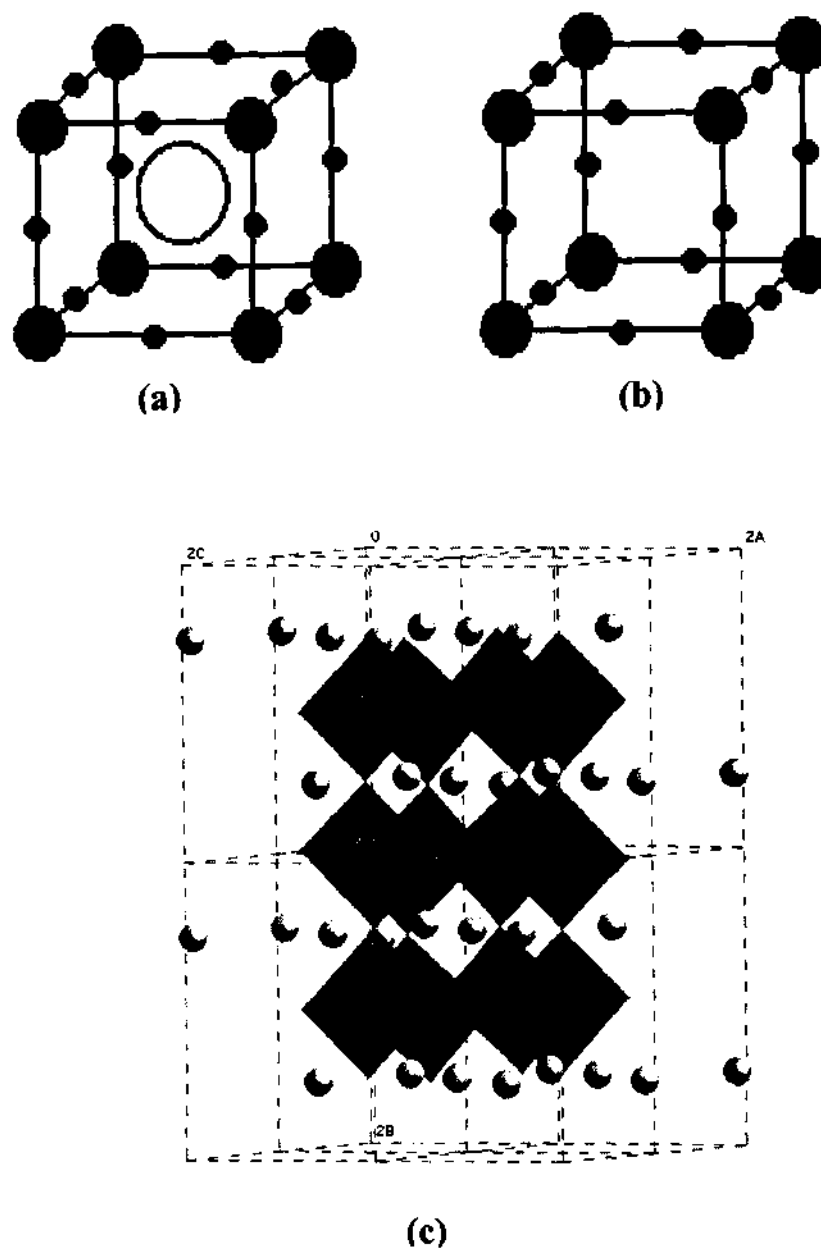
Fig. 1.1 (a) Cubic perovskite structure (b) ReO_3 structure (c) $GdFeO_3$ structure

sets the lower limits for their radii; these being $r_A > 0.90$ Å and $r_B > 0.51$ Å. When $t < 1$, there is a compression of the Mn-O bonds and this in turn induces tension on the Ln-O bonds. A cooperative rotation of the MnO_6 octahedra and a distortion of the cubic structure counteract these stresses. When $0.75 < t < 0.9$, the MnO_6 octahedra are tilted cooperatively to give an enlarged orthorhombic Pbnm structure of $GdFeO_3$ (Fig. 1.1c). For $0.9 < t < 1.00$, buckling of octahedra is not found and small distortions leading to a lower symmetry structure. Hence, rotation about a [111] axis giving the rhombohedral $R\bar{3}c$ structure of $LaAlO_3$ or a rotation about a [001] axis giving the tetragonal structure of low temperature $SrTiO_3$ may occur. These rotations bend the Mn-O-Mn bond angle from 180° to (180°-ϕ) and ϕ increases as t decreases from unity.

Another type of distortion that can arise in the perovskites is due to the Jahn-Teller (J-T) effect leads to the distortion of the MnO_6 octahedron in the manganates giving rise to long and short Mn-O bonds. The octahedral ligand environment around Mn ion splits the Mn d levels into a t_{2g} triplet and an e_g doublet state. The intra-atomic exchange energy responsible for Hund's highest multiplicity rule, $\Delta_{ex} > \Delta_c$, where Δ_{ex} and Δ_c are the intra-atomic exchange energy and crystal field splitting energy respectively for the Mn^{3+}, stabilizes an orbitally two fold degenerate t^3e^1, ^5E_g localized-electron configuration in cubic symmetry. This orbital degeneracy leads to a Jahn-Teller splitting or instability. The degeneracy is removed by the vibrational modes of E_g symmetry or the optical breathing mode axial displacements of the oxygen atoms on either side of Mn^{3+}. These displacements lead to the distortion of the MnO_6 octahedron and hence the lowering of the site symmetry from cubic to tetragonal or orthorhombic. The splitting of the e_g level opens

a gap at the Fermi level. In $LaMnO_3$, the cooperative J-T distortions are static and long-range below an orthorhombic-rhombohedral transition temperature T_t. Oxidation of the MnO_3 array leading to the reduction in the Mn^{3+} ions leads to a lowering of T_t till the structure remains rhombohedral to the lowest temperature. The rhombohedral symmetry does not allow a static, long-range-cooperative deformation of the local octahedral sites, but strong electron coupling to the short-range-cooperative breathing-mode displacements of oxygen atoms on either side of a Mn atom can be expected to persist so long as the Mn-e electrons remain localized. These structural distortions play a major role in the electron transport properties of these rare-earth manganates.

1.3 Electronic and Magnetic Interactions

The rare-earth manganates of the type $Ln_{1-x}A_xMnO_3$ have rich phase diagrams. The doping of a divalent ion at the A-site introduces Mn^{4+} in the otherwise pure Mn^{3-} stoichiometric parent manganate. The relative concentration of Mn^{3+} and Mn^{4+} play an important role in determining the electrical and magnetic properties of these manganates. The magnetic moments of the Mn ions are coupled by indirect exchange mechanisms in these perovskite manganates. This coupling in turn depends on the extent of orbital overlap and hence the position of the Mn ions relative to each other in the crystal structure. Thereby, the crystal symmetry, electrical transport properties and magnetic properties of these compounds are interrelated. The indirect exchange interactions between the Mn ions have been explained based on the superexchange, semicovalent exchange and double exchange mechanisms.

Superexchange interaction

Superexchange interaction based on the nonionic character of the lattice [7-9] accounts for the coupling between the electrons of the d-orbitals in transition metal oxides. According to the superexchange model, electron is excited from the anion to the d-orbital of the neighboring transition metal cation. The *Goodenough-Kanamori* rules for predicting the magnetic nature of the metal oxide involving the superexchange mechanism is summarized in Table 1.1 [10,11]. Several contributions to the superexchange interactions of the electron configurations in Table 1.1 have been identified. Among these the major ones are the delocalization, correlation and polarization superexchange. In superexchange model, it is assumed that the exchange energy is smaller than the energy difference between the lattice-orbital and the d-orbital energy levels. Hence there is no way for atoms to couple ferromagnetically in one direction and antiferromagnetically in another due to absence of anisotropy. Also it is not adequate to explain lattice distortions seen in perovskite oxides.

Semicovalent exchange and Magnetic ordering

Goodenough proposed a theory to show the role of covalence in the perovskite manganates [5]. His qualitative proposals, called the semicovalent exchange theory explain the magnetic interaction in the perovskite manganates. According to this model, Mn^{3+} ion hybridizes stable dsp^2 lattice orbitals which are square planar whereas Mn^{4+}

Table 1.1

Rules for 180° superexchange interactions (from Ref. 5)
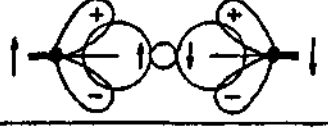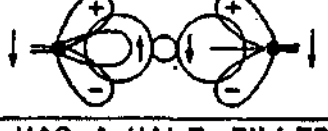
CASE NO.	*CATIONS 1	*CATIONS 2	OUTER ELECTRON CONFIGURATIONS	MAGNETIC COUPLING (Relative strength given anion sublattice)
1	A	A		STRONG ANTIFERRO- MAGNETIC
2	B	B		WEAK ANTIFERRO- MAGNETIC
3	A	B		MODERATE FERRO- MAGNETIC

*AN "A" CATION HAS A HALF-FILLED, A "B" CATION AN EMPTY, e_g ORBITAL DIRECTED TOWARDS THE ANION.

 IS AN ANION WITH ITS FILLED $p\sigma$ ORBITALS SPIN POLARIZED, AS INDICATED, BY INTER-ACTIONS WITH NEIGHBORING CATION e_g ORBITALS. THE t_{2g} ORBITALS ARE SEEN TO BE ORTHOGONAL TO THE $p\sigma$ ORBITALS.

 IS AN "A" CATION WITH OCCUPIED t_{2g} (+ AND -) AND HALF-FILLED e_g ORBITALS.

 IS A "B" CATION WITH OCCUPIED t_{2g} (+ AND -) AND EMPTY e_g ORBITALS.

Table 1.2

Semicovalent model for the magnetic coupling of manganese ions in the perovskite-type anganites [La,M (II)]MnO₃. N is the number of semicovalent bonds which can be formed by a manganese ion with its six neighboring ions. T_0 and T_C are the transition temperatures for ond ordering and magnetic ordering, respectively. In the column for schematic electron-spin onfigurations the cations, marked 4+ and 3+ have an empty orbital pointing towards the O^{2-} p orbitals if they are joined by a dash (from ref. 5)

Low-energy, empty lattice orbitals			
Ion	Outer elec. config.	Empty low-energy orbitals	*N*
Mn⁴⁺	d^3	Octahedral (d^2sp^3)	6
Mn³⁺	d^4	Square (dsp^2)	4

SCHEMATIC ELECTRON-SPIN CONFIGURATIONS	Mn-Mn SEPARATION	TRANSITION TEMPS.	RESISTIVITY	CASE
ORDERED LATTICES				
ANTIFERROMAGNETIC (4+ OR 3+ ... 4+ OR 3+)	SMALLEST	$T_0 > T_c$	HIGH	1
FERROMAGNETIC (3+ OR 4+ ... 3+)	LARGE	$T_0 > T_c$	HIGH	2
PARAMAGNETIC (3+ ... 3+)	LARGEST	$T_c \approx 0$	HIGH	3
DISORDERED LATTICES				
FERROMAGNETIC (4+ ... 3+ / + / 3+ ... 4+)	SMALL	$T_0 \cdot T_c$	LOW	4

14

hybridizes stable d^2sp^3 orbitals which are octahedral and point toward the neighboring six O^{2-} ions. This concept of semicovalent exchange in combination with the concepts of covalence and superexchange offers a consistent model for explaining the complicated variations with chemical composition of crystal structure and magnetic interactions. Also, it explains the orbital ordering evident in these materials. There could be three possible Mn-O bonds in perovskites:

1) A covalent or semicovalent bond if an empty Mn orbital points toward the O^{2-} ion which is most stable and shortest.

2) An ionic bond if the empty Mn^{3+} orbitals point away from the O^{2-} ion and it is the least stable and the longest.

3) A metallic-like bond if the O^{2-} ion is between a Mn^{3+} and a Mn^{4+} ion in a lattice of disordered Mn^{3+}, Mn^{4+} ions.

At some transition temperature these bond types are admixed. A transition from covalent or ionic bonding to admixed bonding is not necessarily associated with a magnetic transition but a transition from semicovalent to covalent or from a metallic- like to admixed bonding is accompanied by a magnetic transition. Hence if two or more bond types occur in the same crystal, the long-range magnetic transition all occur at about the same temperature because of the cooperative character of magnetic ordering. According to this model, there are four possible Mn-O-Mn bonding arrangements, each having a different Mn-Mn separation and a different indirect coupling of the Mn magnetic moments in the rare-earth manganates, $Ln_{1-x}A_xMnO_3$. This has been summarized in Table 1.2 [5]. *These rules for indirect coupling between the Mn ions by semicovalent exchange predict*

and corroborate the different kinds of magnetic order evident in these rare-earth manganates.

Wollan and Koehler [4] studied the magnetic and crystallographic lattices in the series of manganates with the compositions, $La_{1-x}Ca_xMnO_3$, as a function of Mn^{4+} content. Goodenough's predictions based on semicovalent exchange and the data obtained from neutron diffraction study of these manganates are in good agreement and various magnetic lattices for different kinds of magnetic order came into picture (Fig. 1.2). Even though both the end members of the series $La_{1-x}A_xMnO_3$, namely $LaMnO_3$ (x = 0.0) and $CaMnO_3$ (x = 1), are antiferromagnetic (AFM) insulators the Mn magnetic lattice are different in the two compounds. The magnetic lattice in the x = 1 composition corresponds to the G-type (Fig. 1.2a) whereas the x = 0 composition has the A-type magnetic lattice (Fig. 1.2b). The other types of magnetic lattices, found across the series as x is varied, corresponding to the antiferromagnetic ordering of Mn moments are the C and CE type. In the C-type the Mn^{3+} and Mn^{4+} ions order in alternate (111) planes (Fig. 1.2c) whereas in the CE type they order in alternate (110) planes (Fig. 1.2d). The magnetic lattice of type B (Fig. 1.2e) describes the ferromagnetic (FM) ordering of the Mn ions.

Double Exchange interaction

Zener [12] proposed a mechanism called the 'double exchange' (DE) to explain the simultaneous occurrence of ferromagnetism and metallicity, both as a function of x and temperature in the above perovskite manganates. According to this mechanism, conduction electrons in the partially filled e_g levels of the d-band are strongly coupled with

G-AF (a)   **A-AF** (b)   **C-AF** (c)

(d)

CE-AFM

(e)
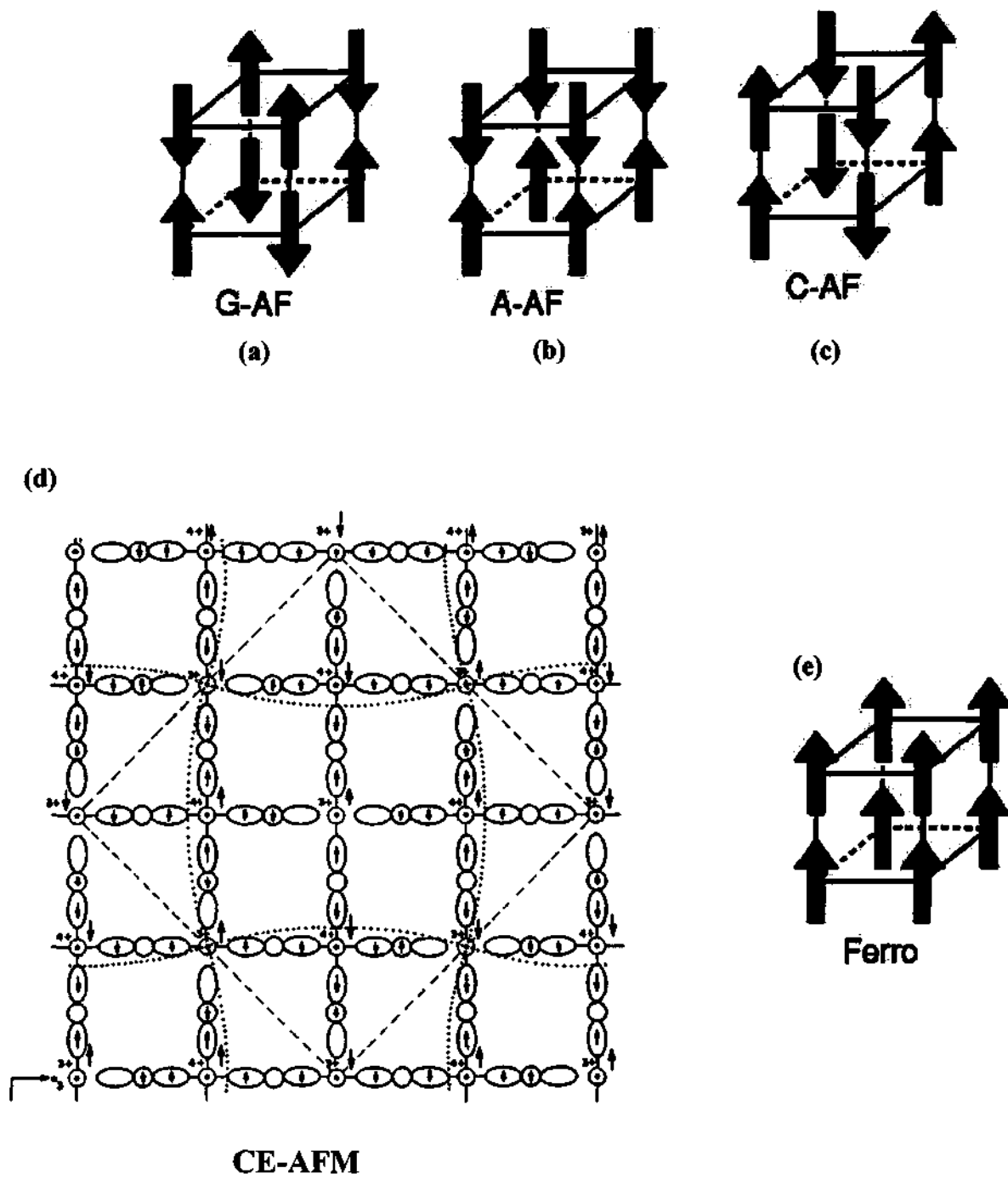
Ferro

Fig. 1.2 Various types of magnetic lattices: (a) G-type antiferromagnet (b) A-type antiferromagnet (c) C -type antiferromagnet (d) CE-type antiferromagnet and (e) B-type ferromagnet.

17

the tightly bound d electrons in the t_{2g} levels by the on-site Hund's coupling. Double exchange comes into picture only where itinerant electrons or holes are present.

In the system $La_{1-x}{}^{3+}A_x{}^{2+}MnO_3$, the migration of Mn^{4+} ion accomplished by the Mn^{4+} ion capturing an electron from a neighboring Mn^{3+} ion gives rise to electrical conductivity. The electron transfer occurs from the Mn^{3+} ion to the central O^{2-} ion simultaneously with the transfer of an electron from O^{2-} to the Mn^{4+} ion. This transfer is termed as 'double exchange'. The lowest energy of this system corresponds to a parallel alignment of the spins of the Mn^{3+} and Mn^{4+}. The exchange energy is given by the integral

$$\int \Psi_1{}^*(H-\varepsilon_0)\Psi_2 \, d\tau$$

where H is the hamiltonian of the whole system ε_0 is the energy associated with the initial states Ψ_1 and Ψ_2 and the integral extends over the coordinates and spins of all electrons. This electron hopping occurs with conservation of spin direction. Because it transfers to an unoccupied orbital that is similar to the one it occupies on the neighboring atom, it couples the moments of neighboring atom parallel to one another and hence coupling them ferromagnetically. *Anderson and Hasegawa* [13] showed that the energy of the system is stabilized by a factor of $\pm$ t $Cos(\theta/2)$ when the electron hopping is on, here θ is the angle between the directions of the neighboring ionic spins and t is the transfer integral.

De Gennes [14] further modified the double exchange mechanism. As the temperature is increased, the canting angle θ is decreased or increased until the system becomes a ferromagnet or an antiferromagnet at a certain transition temperature, T_t, according as the ferromagnetic double exchange interaction overcomes the antiferromagnetic superexchange interaction or vice-versa. The system behaves as a

simple ferromagnet above a critical concentration. But this argument ignores the effects of bound states of holes around impurity ions, an effect that cannot be neglected at low concentrations. The double exchange theory has been studied extensively by several others [15].

1.4 Colossal Magnetoresistance in Rare Earth Manganates

Although all metals have an inherent but small MR owing to the Lorenz force that a magnetic field exerts on moving electrons which had been known since 1950. In recent years there had been a great amount of research interest in understanding this phenomenon to make application-oriented materials. Metallic alloys containing magnetic atoms also can have an enhanced MR as the scattering that produces the electrical resistance in these materials is controlled by a magnetic field. Very large MR, referred to as giant magnetoresistance (GMR) was first observed in layered Fe/Cr metallic multilayers by *Baibich et al.* [16]. Also, GMR has been observed in ferromagnetic granules dispersed in paramagnetic metal films [17] and suitably doped magnetic semiconductors such as $Eu_{1-x}Gd_xSe$ and $Cd_{1-x}Mn_xSe$ [18].

Large MR was observed and known in 1970's and 1980's in bulk and single crystal forms of doped manganates of the type $Ln_{1-x}A_xMnO_3$, where Ln is a rare-earth ion and A is a divalent metal ion. But the renewed interest in these manganese oxides started with the report of observance of negative MR in bulk doped manganate, $Nd_{0.5}Pb_{0.5}MnO_3$ by *Kusters et al.* [19]. This material showed 50% MR near its ferromagnetic transition temperature (184 K). This report was followed by studies on thin films by *von Helmolt et*

19
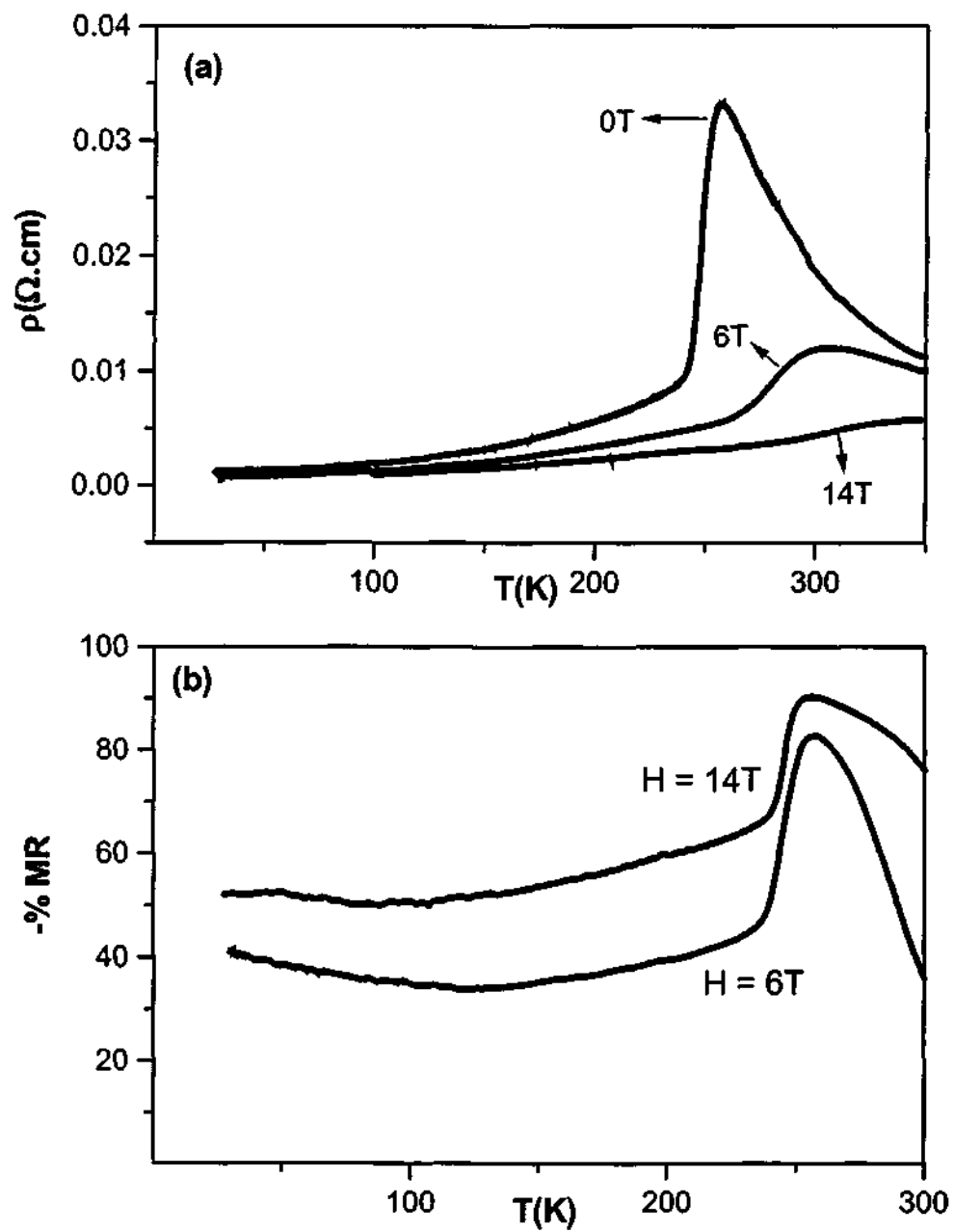
Fig. 1.3 Temperature variation of (a) the resistivity and (b) the negative magnetoresistance of polycrystalline $La_{0.7}Ca_{0.3}MnO_3$ in applied fields of 6 and 14 T.

20

al. ($La_{0.67}Ba_{0.33}MnO_3$) [20], *Chahara et al.* ($La_{0.75}Ca_{0.25}MnO_3$) [21] and *Jin et al.* [2, 22]. Though both GMR and CMR deal with the change in electrical resistance on application of a magnetic field the mechanism involved are very different. Substitution of La by divalent ions in $LaMnO_3$ generates Mn^{4+} (or holes) in the compound. When the concentration of holes is adequate in $La_{1-x}Ca_xMnO_3$ the material shows ferromagnetism and an associated insulator-metal (I-M) transition. The resistivity behavior is insulating above the ferromagnetic transition temperature, T_C and on cooling the material undergoes an I-M transition with a peak in the resistivity at a temperature, T_p close to the T_C. This behavior has been explained by double exchange mechanism of *Zener and De Gennes*. The application of a magnetic field (in Tesla) leads to a significant decrease in the resistivity of $La_{1-x}Ca_xMnO_3$, the magnitude of decrease being the maximum in the region of T_C or T_p. A typical example to show the variation of resistance as a function of temperature in an applied magnetic field is shown in Fig. 1.3. The high MR close to the T_C or T_P is due to the fact that around the T_C the magnetic energy provided by the external field is comparable with the energy due to both thermal motion and double exchange mechanism and hence leading to a decrease in the resistance. Below T_C, there is not much effect as the material is already ferromagnetically ordered and the field has negligible effect. Though CMR close to 100% has been observed at room temperature [23], the field required is very high (of the order of few tesla) making them unusable for technological applications.

The %MR varies from one composition to the other in the same series of $Ln_{1-x}A_xMnO_3$ manganates. A Mn^{4+} content of around 33% is optimal for obtaining good

ferromagnetic characteristics. Hence, cation deficient $LaMnO_3$ and oxygen deficient $LaMnO_3$ represented as $La_{1-\delta}Mn_{1-\delta}O_3$ and $LaMnO_{3-\delta}$ also exhibit MR; the ferromagnetism and insulator metal transition depending on the vacancy, δ, in these samples [24-28].

When the size of the A-site cation, $\langle r_A \rangle$ is decreased by aliovalent substitution by a smaller ion, there is a buckling of the MnO_6 octahedra and the Mn-O-Mn bond angle is reduced from $180°$. This decrease in bond angle decreases the overlap between the orbitals leading to the narrowing of the energy band formed by the e_g electrons in the highest energy level. The conductivity of these manganates is controlled by the width of the e_g band. Narrowing the e_g band weakens ferromagnetic coupling resulting in the lowering of ferromagnetic Curie temperature, T_C and an increase in the resistivity at the metal-insulator transition [29-35]. The following relationship has been derived to correlate T_C and the electronic bandwidth, W with the Mn-O-Mn bond angle, θ in the $La_{2/3}A_{1/3}MnO_3$ manganates [34],

$$T_C(\theta) \propto W(\theta) \propto Cos^2\theta$$

The maximum value of T_C, T_{IM} is when $\langle r_A \rangle = 1.23 \pm 0.01Å$ which corresponds to a tolerance factor of 0.93. MR is found to be enhanced in the rare-earth manganates by (1) shift of T_C (T_{IM}) to lower temperatures (or decrease in $\langle r_A \rangle$, Fig. 1.4 [32]), (2) a reduced mobility of the doping holes and (3) an increase of the coupling between the itinerant and localized electrons. The resistivity $\rho(H)$ is proportional to $BM^2(H)$ where the coefficient B is related to the Hund's coupling J and electronic bandwidth W as B $\approx J/W$ [33]. The relation between tolerance factor and bandwidth is clear from the study of the manganates

22
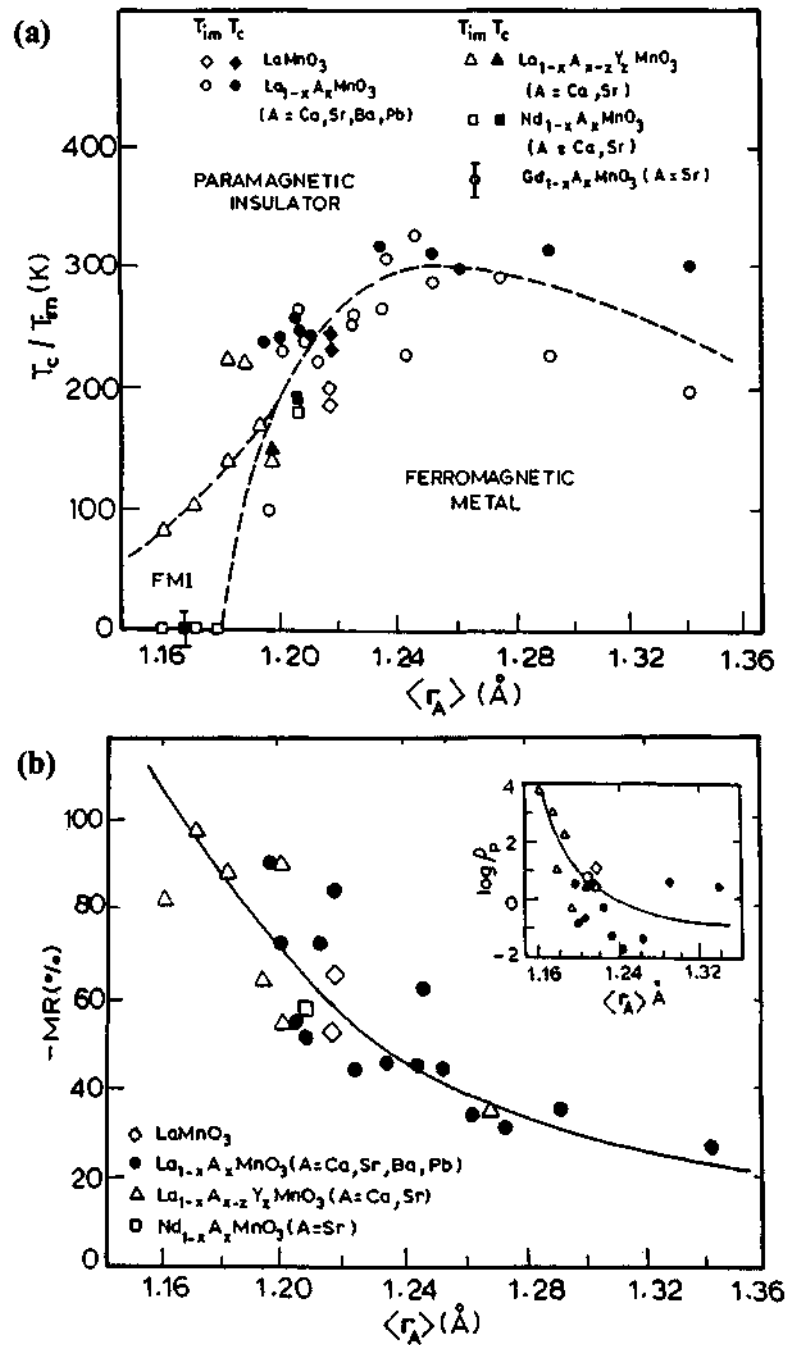
Fig. 1.4 Variation of (a) T_C (T_{IM}) and (b) magnetoresistance of $Ln_{1-x}A_xMnO_3$ with the average A-site cation radius, $\langle r_A \rangle$. The inset in (b) shows the variation of $\log \rho$ with $\langle r_A \rangle$ (from ref. [31]).

23
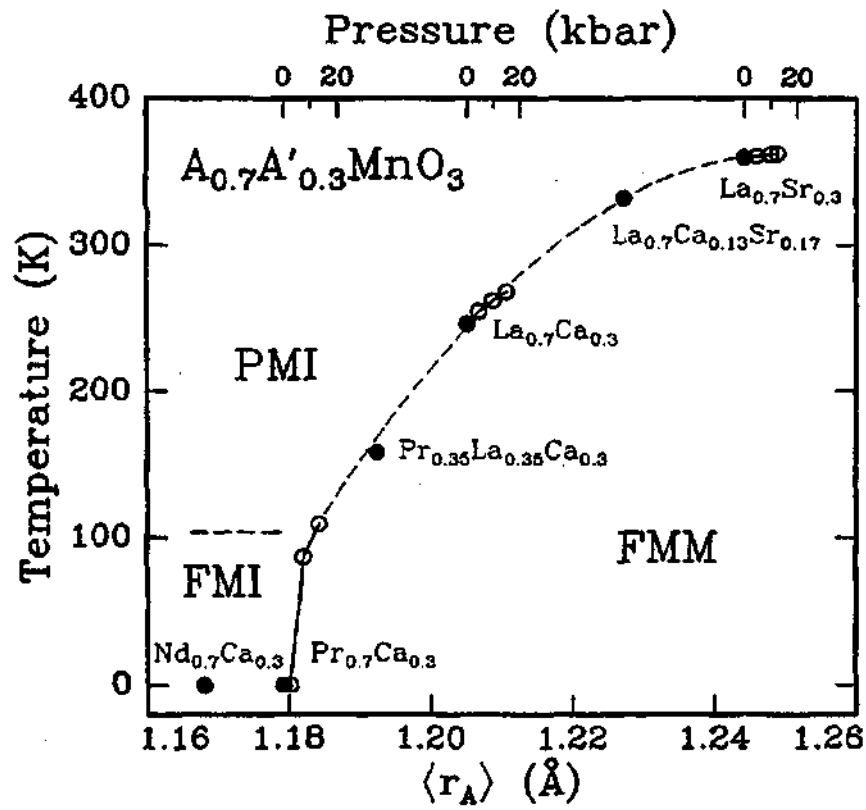
Fig. 1.5 Variation of T_C (T_{IM}) of $Ln_{0.7}A_{0.3}MnO_3$ with hydrostatic pressure and the average A-site cation radius, $\langle r_A \rangle$ (from ref. [37 (b)]).

24

with compositions $La_{0.7}A_{0.3}MnO_3$ where A = Ca or Sr and the T_C increases with t over the range $0.96 \leq t \leq 0.98$. The transition at T_C is first order and the CMR is greatest near t ≈ 0.96. Effect of hydrostatic pressure is similar to that of increase of $\langle r_A \rangle$ [36,37] as could be seen in Figure 1.5. These studies suggest that the $\langle r_A \rangle$ - T_C relationship is consistent with a transition that is driven by the kinetic energy gain of the carriers on entering the metallic state.

Although double exchange is found to be necessary for observing CMR in the perovskite manganates, double exchange alone cannot adequately explain the varied features of the CMR phenomena. The DE mechanism can predict the resistivity transition qualitatively but it cannot explain the magnitude of the change in resistivity (by several orders of magnitude) at ferromagnetic transition on application of a field. The important thing to be noted about the CMR compounds is that the resistivity at $T > T_C$ is much larger than the *Mott* limit [38] and rapidly increases as T decreases. In models involving only DE the scattering produced by spin disorder is simply not large enough to cause the insulating behavior. There is a too slow dependence on doping concentration when only the DE mechanism is considered. The understanding of the behavior and the mechanism of the conductivity of these manganates both above and below T_C have been the focus of numerous studies. The realization of the importance of electron–phonon coupling by *Millis et al.* [39,40] came as an eye opener to understand these CMR manganates. The microscopic origin of electron-phonon coupling has been tracked down to the large Jahn–Teller effect occurring in the d^4 ions (Mn^{3+}) in an octahedral ligand environment. The local distortion of the lattice due to the J-T effect produces a potential minimum leading

25

to a self-trapped state called a polaron above the T_C. Below T_C, the self-trapping disappears as the bandwidth broadens and the electrons are much more mobile. According to this theory, electron-phonon coupling should be stronger for narrower bandwidths enhancing the self-trapping effect and leading to higher resistivities. Several theories have come up to elucidate the role of electron–phonon coupling in producing CMR and have contributed to the understanding of the resistivity behavior in the CMR manganates [41]. Experimental studies of perovskite manganates involving isotopic substitution [42-47], neutron diffraction [48-54], X-ray absorption [55,56], thermopower measurements [57,58], photoemission spectroscopy [59], optical conductivity measurements [60], X-ray scattering [61] and Hall effect [62] give evidence for the electron-phonon interactions predicted by *Millis et al.*

A large oxygen isotope effect on the ferromagnetic Curie temperature, T_C of $La_{0.8}Ca_{0.2}MnO_3$ [42] supports the electron phonon coupling and polaron theory. Such a substitution invariably leads to the decrease in the ferromagnetic Curie temperature of the material (Fig. 1.6). *Babushkina* and co-workers have studied the effect of substitution of O^{16} by O^{18} on $La_{0.175}Pr_{0.525}Ca_{0.3}MnO_3$ and found a switching over from a metal to an insulator after isotopic substitution [46]. Pulsed neutron diffraction studies of $La_{1-x}Sr_xMnO_3$ ($0 \leq x \leq 0.4$) suggest that polaronic lattice distortions related to the local JT distortion exist in the paramagnetic and antiferromagnetic as well as ferromagnetic phases. The polarons are single-site small polarons above T_C or T_N, while at low temperatures they become more extended and cover three Mn sites [49,50]. *Dai et al.* has studied the structural and magnetic phase transition in the
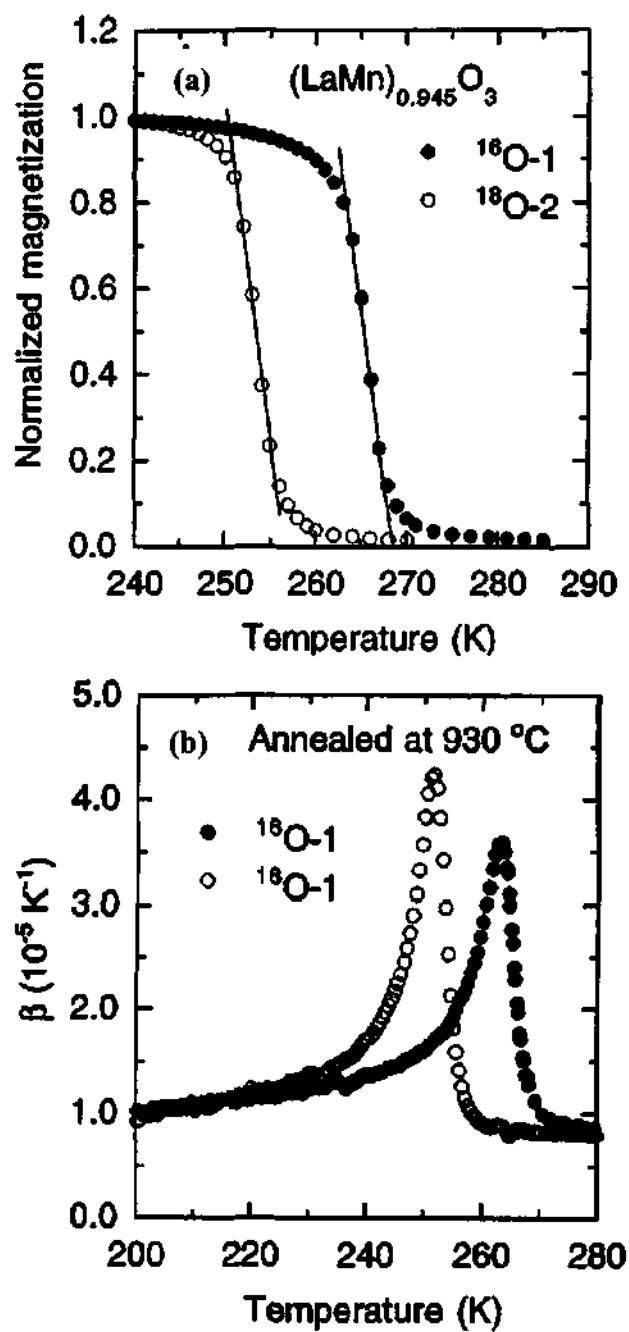
Fig. 1.6 The temperature dependence of (a) the low field magnetization for the ^{16}O and ^{18}O samples of $(LaMn)_{0.945}O_3$ and (b) linear thermal expansion coefficient $\beta(T)$ for ^{16}O and ^{18}O samples of $(LaMn)_{1-y}O_3$ (from ref. [44]).

perovskite $La_{0.65}Ca_{0.35}MnO_3$ by neutron powder diffraction. Their results show an anomalous volume, rms motion of oxygen and Mn atoms around T_C which are in good agreement with the dynamic J-T distortions theory. The work of *De Teresa et al.* [51, 52] regarding the evidence for magnetic polarons or magnons in the perovskite manganates is worth mentioning. The presence of magnetic polarons above T_C has been confirmed using a combination of volume thermal expansion (with and without field), magnetic susceptibility and small angle neutron scattering (SANS) measurements. They have interpreted the increase in thermal expansion in the range $T_C < T < 1.8T_C$ as due to the small polaron being dressed by the short-range ferromagnetic correlations forming an entity that moves as a whole. The change in the volume and SANS intensity under magnetic field indicates that the ferromagnetic cluster is associated with the lattice distortion. The observed growth in size and decrease in the number of ferromagnetic domains on application of a magnetic field above T_C implies that the field stabilizes greater ferromagnetic order. Hence, the polarons may condense into larger ferromagnetic domains containing many delocalized charge carriers. Within a ferromagnetic domain, the conductivity is presumably metallic, so the resistance decreases as the fraction of the metallic volume increases. In a recent study of the $Ln_{0.7}A_{0.3}MnO_3$ system, atomic pair distribution function analysis of pulsed neutron diffraction data suggests that the principle effect of the ionic size is to change the polaron formation energy through the change in the local elastic response [54]. Also, the polarons are stable only up to a radius of ~1.19-1.20 Å and the compositions near this crossover ionic size condition show large CMR effects.
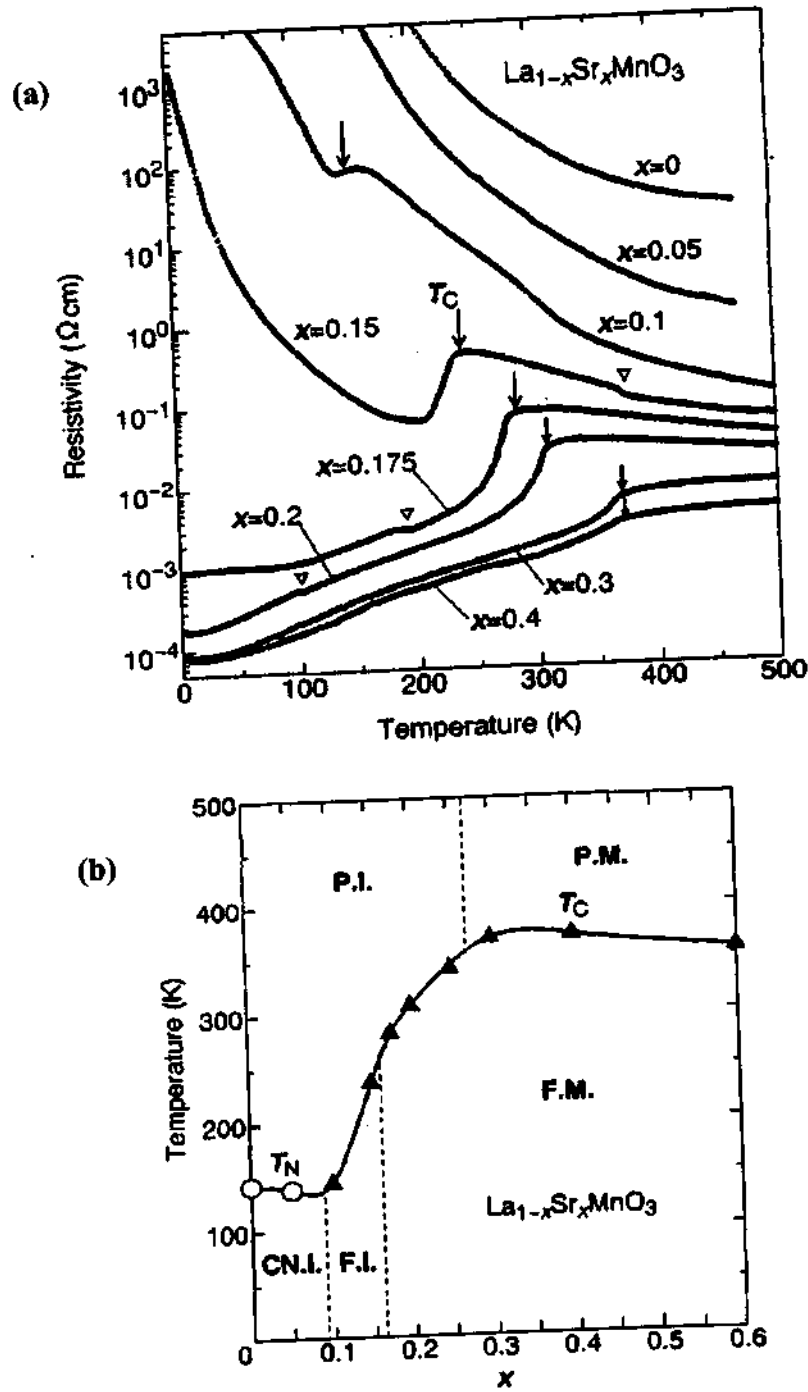
Fig. 1.7 (a) Temperature variation of the resistivity of $La_{1-x}Sr_xMnO_3$ crystals and

(b) electronic phase diagram of $La_{1-x}Sr_xMnO_3$ (from ref. [63a]).

EXAFS studies of the rare-earth manganates show the existence of local lattice distortions as predicted and support the polaronic mechanism for the electrical conduction in the paramagnetic phase [55,56]. Thermopower and transport measurements on thin films of $La_{2/3}Ca_{1/3}MnO_3$ at temperatures above T_C have shown a large field dependent difference between the activation energies for resistivity and for thermopower which supports the polaron-dominated conduction and these polaronic distortions, evident in the paramagnetic phase persist over some temperature range in the ferromagnetic phase [48,49,56,58].

Another factor which affects the properties of the rare-earth manganates, $Ln_{1-x}A_xMnO_3$ apart from the average A-site cation radius, $\langle r_A \rangle$, is the relative concentration of Mn^{3+} and Mn^{4+} (holes or electrons). This is evident from Fig. 1.7a, which shows the change in resistivity as a function of temperature for $La_{1-x}Sr_xMnO_3$ for different values of x [63]. The rare-earth manganates of the type $Ln_{1-x}A_xMnO_3$ (Ln = lanthanide, A= alkaline earth) are categorized into hole-doped and electron doped based on whether x < 0.5 or x > 0.5 respectively. The properties of the hole-doped and electron-doped manganates of the type $Ln_{1-x}A_xMnO_3$ are very different for a given Ln and A combination. This could be seen in the phase diagram of $La_{1-x}Sr_xMnO_3$ in Fig. 1.7b. However, a much clearer evidence for the difference in the behavior of the hole-doped and electron-doped manganates is the phase diagram of a few other representative manganate systems which would be discussed in a later section on charge-ordering.

The resistivity behavior and the phase diagram of $La_{1-x}Sr_xMnO_3$ (Fig. 1.7) show that with increase in x the material changes from a spin-canted insulator to a

ferromagnetic insulator at low temperatures. No ferromagnetic phase transition is observed for $x \leq 0.05$. At a critical concentration of $x = 0.16$ there is a change in the low temperature resistivity behavior from a ferromagnetic insulator to a ferromagnetic metal. The large reduction in resistivity, $\Delta\rho$ around the T_C in a magnetic field is scaled with the field induced magnetization M as $-\Delta\rho/\rho = C(M/M_s)^2$ for $M/M_S \leq 0.3$, where M_s is the saturated magnetization. Neutron diffraction studies show that the structural phase diagram and the metal insulator transition in the $(La,Sr)MnO_3$ system are linked [63]. Specific heat and low temperature resistivity study near the critical behavior of the metal-insulator transition ($x_c = 0.16$), reveal the presence of spin polarized anomalous metallic phase with strongly lattice or orbital-coupled diffuse charge dynamics. A more recent study involving magnetic X-ray dichroism (MXCD) shows that $m_{orb}(Mn)$ and $m_{spin}(Mn)$ are essentially unchanged, whereas $m_{orb}(O)$ changes dramatically for the ferromagnetic metallic and insulating phases of $La_{1-x}Sr_xMnO_3$ [64].

Other than the factors described in the previous sections, disorder arising due to the size-mismatch between the A-site cations is also found to affect the properties of the perovskite oxides [65-70]. *Rodriguez-Martinez and Attfield* quantified this effect by the parameter σ^2, called the variance (the second moment) of the A-cation radius distribution. The ferromagnetic metal to paramagnetic insulator transition temperature, T_m in the rare-earth manganates of the type $Ln_{0.7}A_{0.3}MnO_3$ is found to decrease linearly with the increase in size mismatch, σ^2, (Fig. 1.8a) according to the relation, $T_m = T_m(0) - p_1Q^2$, (p_1 is the negative slope and Q is the oxide ion displacement) where $T_m(0)$, the intercept is the experimental estimate of the ideal transition temperature that would be
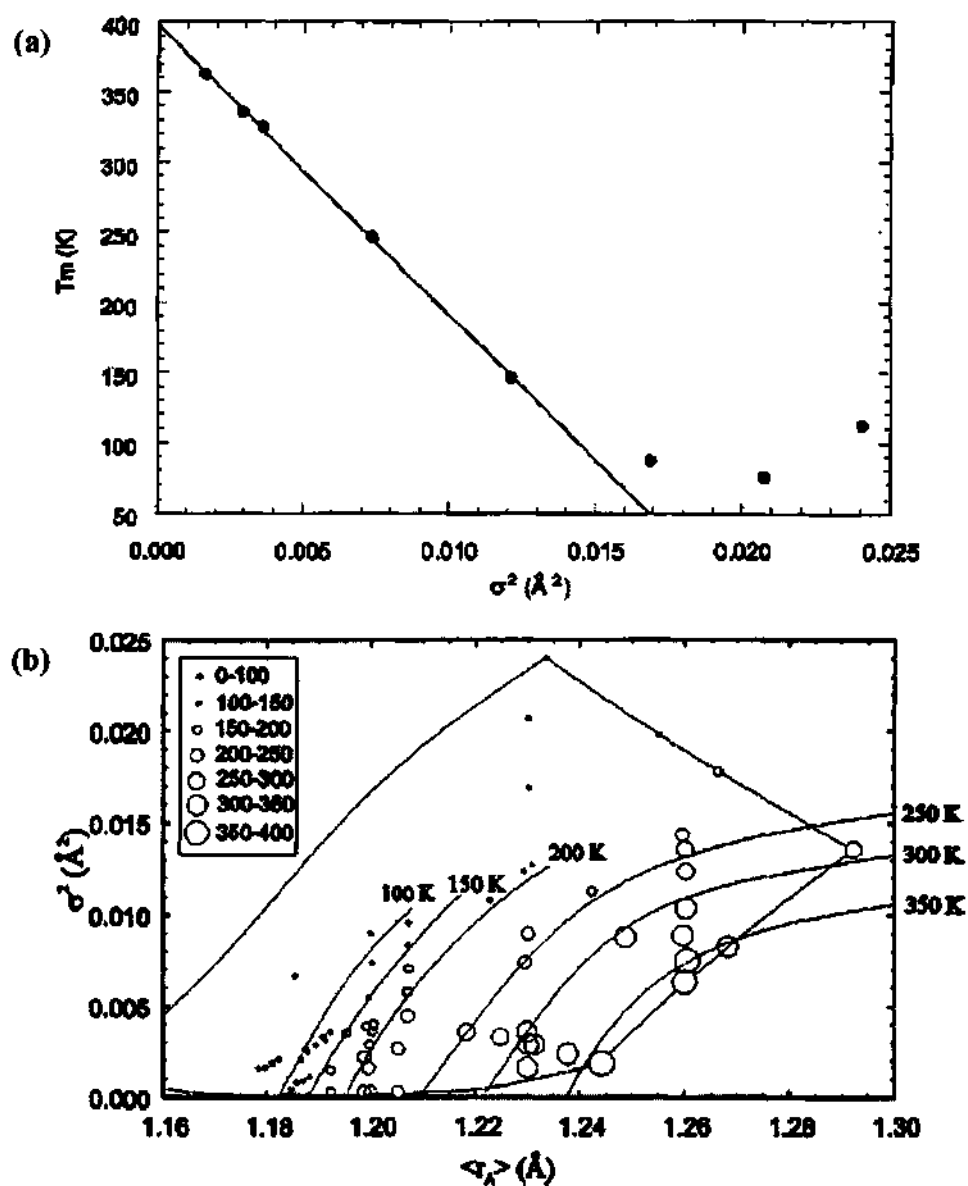
Fig. 1.8 (a) Variation of T_m with A-cation size variance σ^2, showing the linear dependence (from ref. [65]. (b) Phase diagram for $Ln_{0.7}A_{0.3}MnO_3$ plotted on the $\langle r_A \rangle$- σ^2 plane (from ref. [70]).

observed if cation size disorder is absent for a given value of $\langle r_A \rangle$. The value of $T_m(0)$ was found to be 400 K and p = 20600 $K\text{Å}^{-2}$ for the $Ln_{0.7}A_{0.3}MnO_3$ system with a fixed $\langle r_A \rangle$ of 1.23 Å. Similar linear correlations between T_m and σ^2 are also evident for $Ln_{0.5}A_{0.5}MnO_3$ systems [66]. *Damay et al.* have deduced a σ^2-$\langle r_A \rangle$ diagram for the $Ln_{0.5}A_{0.5}MnO_3$ compositions which shows that the low temperature magnetic phases in these manganates lie within distinct regions in the $\langle r_A \rangle$-σ^2 plane. Following the linear relationship between T_m and σ^2, disorder-corrected variation of T_m with $\langle r_A \rangle$ was estimated and it was found that the experimental estimate of the T_m for an ideal, disorder free $Ln_{0.7}A_{0.3}MnO_3$ perovskite is ~530 K which is higher than the experimentally observed value. These quadratic relations for $\langle r_A \rangle$ and σ^2 show the strong influence of local, incoherent lattice strains on the metal-insulator transition in these manganates. Based on these relationships, a phase diagram for $Ln_{0.7}A_{0.3}MnO_3$ system has been derived by *Rodriguez-Martinez and Attfield* (Fig. 1.8b).

Size disorder due to A-site cation size mismatch is also evidenced to affect the magnetotransport properties of the pervoskite manganates. Increase in size disorder for the $Ln_{0.7}A_{0.3}MnO_3$ compositions is seen to suppress the magnetoresistance.

Magnetoresistance in layered manganates

The Ruddlesden-Popper (RP) manganates with the general formula $(Ln,A)_{n+1}Mn_nO_{3n+1}$ (n = dimensionality) have also been examined for high MR. In the case of $SrO(La_{1-x}Sr_xMnO_3)_n$ series, the n =1 member is an insulator with the two dimensional K_2NiF_4 structure and does not show ferromagnetism with a well defined

T_C [71]. The n =2 member exhibits a sharp insulator metal transition and high MR [72, 73]. T_C and T_{IM} increase with n in this family. In $La_{1.4}Sr_{1.6}Mn_2O_7$, the current perpendicular to the MnO_2 planes is large, close to T_C and the barrier to transport provided by the intervening, insulating SrO rock salt layers can be removed by the application of a magnetic field; the interlayer transport appears to occur through tunneling [74]. Large MR has also been observed in $La_{2-2x}Ca_{1+2x}Mn_2O_7$ [75].

1.5 Magnetoresistance in other materials

Other than the rare-earth perovskite manganates CMR had been observed in many other materials also. The compound $Tl_2Mn_2O_7$ with the pyrochlore structure which has neither mixed-valence for a double exchange mechanism nor a J-T cation such as Mn^{3+} shows CMR [76]. Doping of this compound with Sc decreases the T_C by 15% but the MR in a field of 6T grows by a factor of 60 [77,78]. Another compound is the ordered double perovskite Sr_2FeMoO_6 which exhibits tunneling-type MR (TMR) at room temperature [79]. Many other double perovskites have been investigated on the lookout for CMR [80]. CMR has also been reported in Cr chalcogenide spinels $Fe_{1-x}Cu_xCr_2S_4$ by *Ramirez et al.* [81] and in Cr_2S_{3-x} (x = 0.08) by *Vaqueiro et al.* [82]. Cobaltates of the type $La_{1-x}A_xCoO_3$ (A = Ba, Sr, Ca) are also known to exhibit MR [83].

1.6 Charge ordering in manganates

Transition metal oxides with differently charged cations of the same element show the phenomenon of charge-ordering wherein the cations order on specific lattice
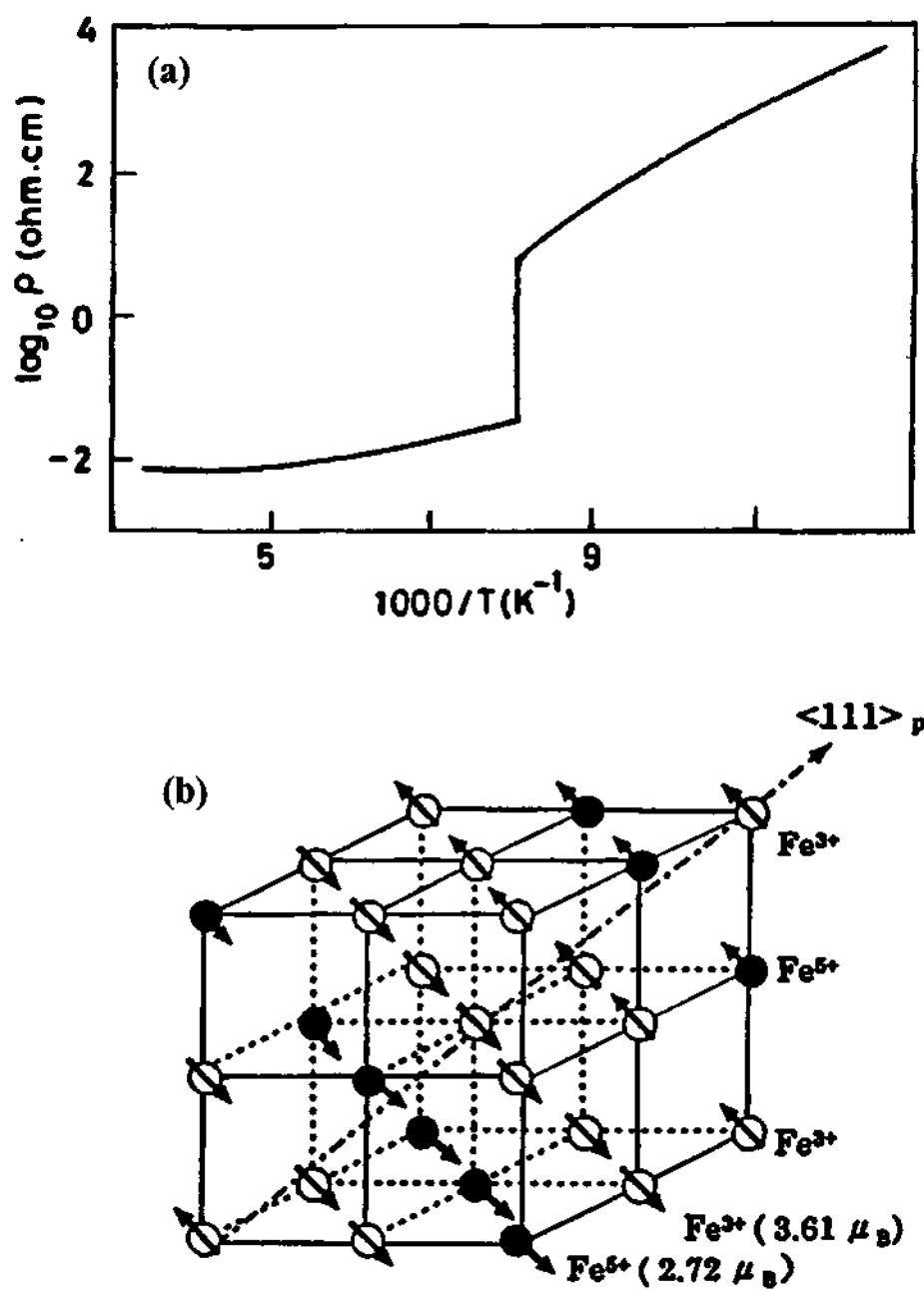
Fig. 1.9 (a) Resistivity data of Fe_3O_4 as a function of 1000/T showing the resistivity anomaly at the Verwey transition (from ref. [84]) and (b) Charge and spin ordering as observed in $La_{0.33}Sr_{0.67}FeO_3$ (from Ref. [87b])

sites. Such an ordering of the cations leads to the localization of the electrons rendering the material insulating in the charge-ordered (CO) state and is often accompanied by a change in crystal symmetry. Charge-ordering competes with double exchange and hence when the potential energy of the electrons overcome the kinetic energy, they get localized resulting in an increase in the resistance of the material in the charge-ordered state. The Jahn-Teller effect aids in the localization of electrons by inducing lattice distortion.

The phenomenon of charge-ordering is known since 1939 in the spinel Fe_3O_4 though called by a different name, the Verwey transition [84]. Fe_3O_4 is a ferrimagnet below 858 K (T_N) and on cooling shows a resistivity increase around 120 K, the Verwey transition temperature, T_V (Fig. 1.9a). This increase in resistivity is attributed to the ordering of Fe^{2+} and Fe^{3+} ions. However, recent studies [85, 86] show that the ordering in Fe_3O_4 is more complicated and it is difficult to have a clear picture regarding the ordering below T_V. Fig. 1.9b shows the charge and spin ordering as observed in $La_{0.33}Sr_{0.67}FeO_3$ [87].

Because of the electrons occupying the d-orbitals in the transition metal ions charge-ordering in transition metal oxides is closely related to the spin and orbital ordering. However, the spin (antiferromagnetic) ordering and orbital ordering may or may not occur at the same temperature as the charge-ordering temperature, T_{CO}. Orbital ordering generally accompanies spin ordering as explained by *Goodenough* [5]. Charge and spin ordering have been observed in cuprate superconductors [88] and a few other transition metal oxides like $La_{1-x}Sr_xFeO_3$ [87,89], $La_{2-x}Sr_xNiO_4$ [90,91] and $LiMn_2O_4$
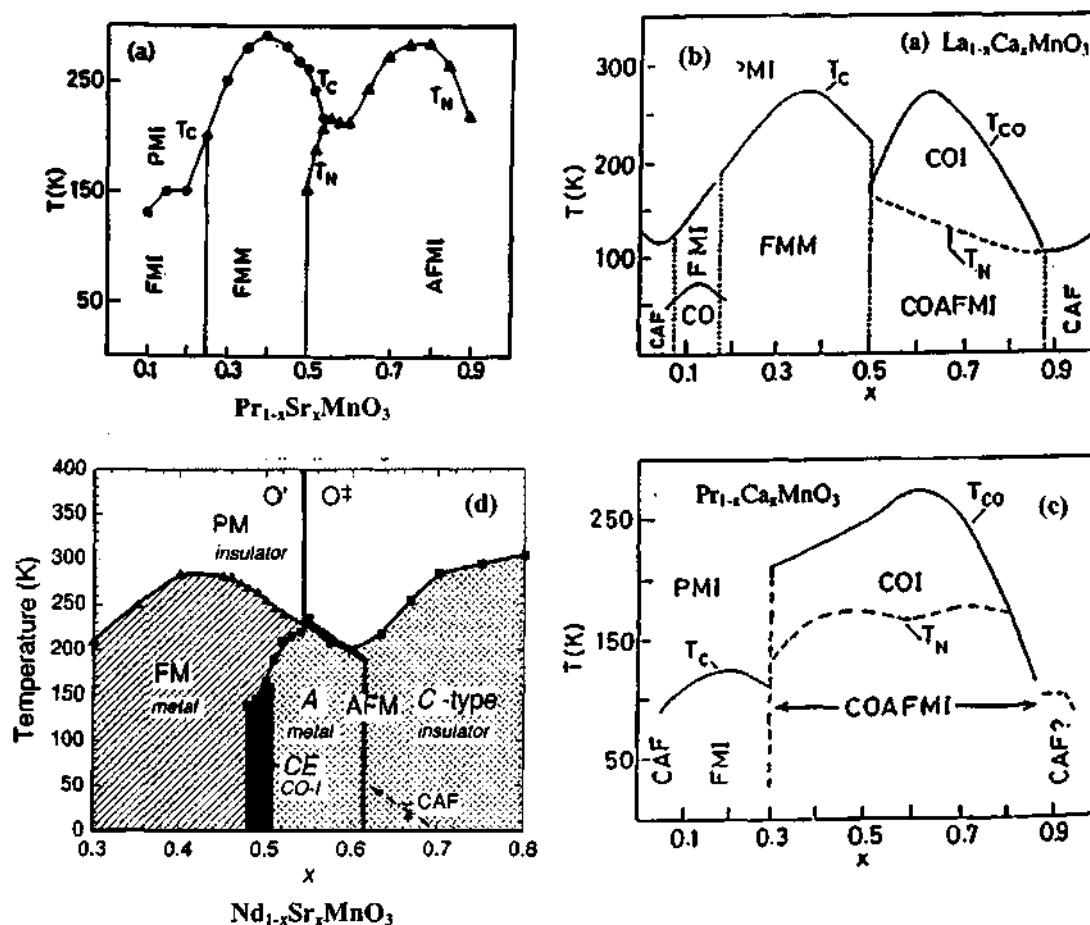
Fig. 1.10 Phase diagram of (a) $Pr_{1-x}Sr_xMnO_3$ (b) $La_{1-x}Ca_xMnO_3$ (c) $Pr_{1-x}Ca_xMnO_3$ and (d) $Nd_{1-x}Sr_xMnO_3$. T_C, T_N and T_{CO} represent the ferromagnetic Curie, Neel and the charge-ordering temperatures, respectively. The abbreviations mean paramagnetic insulator (PMI), ferromagnetic insulator (FMI), ferromagnetic metal (FMM), antiferromagnetic insulator (AFMI), charge-ordered insulator (COI), charge-ordered antiferromagnetic insulator (COAFMI) and canted antiferromagnet (CAF) (from references [94-99]).
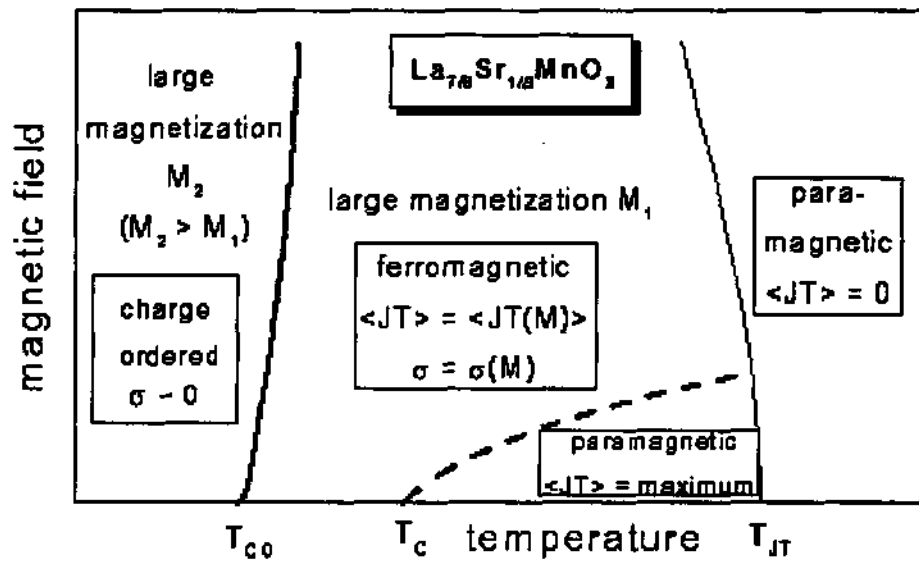
Fig. 1.11 Schematic phase diagram for $La_{0.875}Sr_{0.125}MnO_3$ showing the stabilization of the charge-ordered phase in an applied magnetic field at low temperatures (from ref. [100]).

[92,93]. However, the study of charge-ordering in the rare-earth manganates, $Ln_{1-x}A_xMnO_3$ has received more attention as the charge-ordering occurs through a fairly wide range of compositions provided the average A-site cation radius, $\langle r_A \rangle$ is not too large. Charge-ordering in the rare-earth manganates have been observed by *Wollan and Koeller, and Goodenough* in the 1950's [4,5] and in 1985 by *Jirak et al.* [94].

Charge-ordering in the rare-earth manganates of the type $Ln_{1-x}A_xMnO_3$ is very sensitive to the average A-site cation radius, $\langle r_A \rangle$. Large $\langle r_A \rangle$ favors ferromagnetism and metallicity as could be seen in the case of $La_{1-x}Sr_xMnO_3$ and $Pr_{1-x}Sr_xMnO_3$. To understand the evolution of charge-ordering in the rare-earth manganates as a function of $\langle r_A \rangle$ and doping it is appropriate to look at the temperature-composition phase diagrams of $Ln_{1-x}A_xMnO_3$ systems (Fig 1.10) [94-99]. Fig 1.10a shows the phase diagram of $Pr_{1-x}Sr_xMnO_3$ where the $\langle r_A \rangle$ varies in the range 1.192-1.297 Å. This system shows no charge ordering in the entire $\langle r_A \rangle$ and composition region. The $Pr_{1-x}Ca_xMnO_3$ system, on the other hand, exhibits charge-ordering over a wide composition range, namely x $\approx 0.3 - 0.8$. Similar kind of behavior is evident on comparing the higher $\langle r_A \rangle$ system $La_{1-x}Sr_xMnO_3$ [Fig. 1.7b] with that of the lower $\langle r_A \rangle$ system $La_{1-x}Ca_xMnO_3$ [95]. No charge-ordering is evident in $La_{1-x}Sr_xMnO_3$ system according to the phase diagram in Fig 1.7b [63a]. However, a recent report show the presence of a charge-ordered state stabilized by an applied magnetic field at low temperatures in $La_{0.875}Sr_{0.125}MnO_3$ [Fig 1.11][100]. Also, evidence for orbital ordering in $La_{0.88}Sr_{0.12}MnO_3$ has been found using resonant X-ray scattering [101].
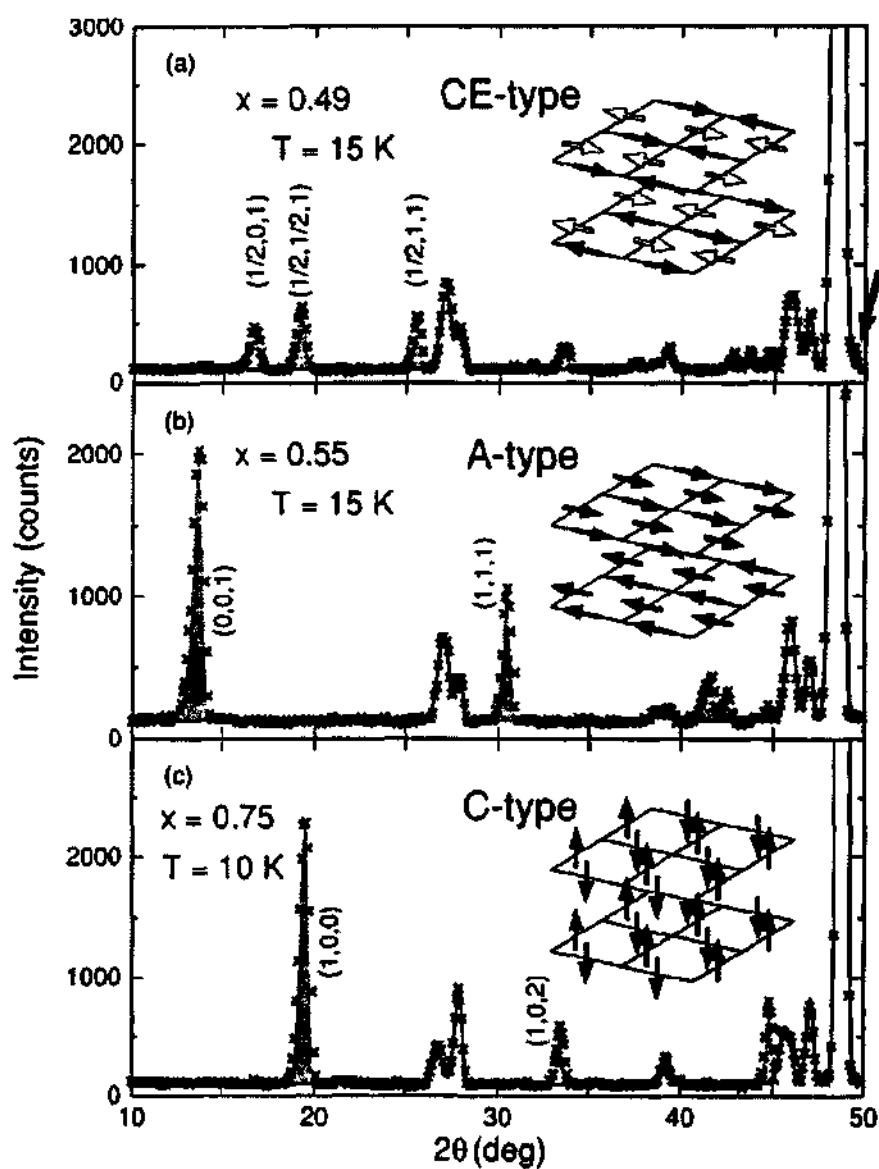
Fig. 1.12 Low scattering angle portion of the powder neutron diffraction patterns of $Nd_{1-x}Sr_xMnO_3$ for different x values, showing the superlattice reflections (hatched peaks) indicative of different types of magnetic (AFM) ordering (from Ref. [97b]).

The phase diagram of $La_{1-x}Ca_xMnO_3$ shows charge-ordering mainly for $x \geq 0.5$. Both the $Pr_{1-x}Ca_xMnO_3$ and $La_{1-x}Ca_xMnO_3$ systems show charge-ordering for the compositions with $x \geq 0.5$ i.e. in the electron-doped regime. However, there are certain differences between the hole-doped compositions in these manganates. Thus, $Pr_{0.7}Ca_{0.3}MnO_3$ charge-orders around 230 K (T_{CO}) in the paramagnetic state, becoming antiferromagnetic at 170 K; it is an insulator and does not show ferromagnetism in the absence of a strong magnetic field. $La_{0.7}Ca_{0.3}MnO_3$, on the other hand, is a FM metal below the Curie temperature $(T_C \approx 260$ K$)$ and a paramagnetic insulator above T_C. The system $Nd_{1-x}Sr_xMnO_3$ falling in the intermediate region of $\langle r_A \rangle$ between $(La),(Pr)SrMnO_3$ and $(La),(Pr)CaMnO_3$ systems shows an altogether different phase diagram. Upon hole doping the ground state spin ordering varies from that of a ferromagnetic metal to that of charge-ordered (CO) CE-type antiferromagnet, to that of a metallic A-type antiferromagnet and finally to that of an insulating C-type antiferromagnet in the this system. The CE-type charge (spin) ordering is seen to occur in a very narrow composition window around $x = 0.5$ in $Nd_{1-x}Sr_xMnO_3$. The superlattice reflections in the neutron diffraction profiles give indication of the type of magnetic ordering as could be seen in Fig. 1.12 [97b]. The $Nd_{1-x}Ca_xMnO_3$ system also exhibits charge-ordering over a large-composition range of $0.30 \leq x \geq 0.80$ [102]. This is clearly evident from temperature variation of resistivity and magnetization data [Fig. 1.13]. The phase diagrams clearly illustrate the presence of electron-hole asymmetry in these manganates. Despite these differences, one could see that the hole and electron-doped regime in $Pr_{1-x}Ca_xMnO_3$ show some similarities. The charge-ordering transition

temperature, T_{CO} increases with hole concentration in the $0.30 \geq x \geq 0.50$ regime and with electron concentration in $0.30 \geq x \geq 0.80$ regime in the (PrCa)MnO$_3$ system [103]. The charge ordered states in the manganates discussed above are associated with a CE-type AFM ordering [4,5] where the Mn^{3+} and Mn^{4+} ions are arranged as in a checker board and the Mn^{3+} sites are J-T distorted. The zig-zag ferromagnetic chains stack antiferromagnetically along the c-axis. The spin ordering (AFM) temperature, T_N in the charge ordered manganates, may or may not coincide with T_{CO}. The type of e_g orbital, $3x^2$-r^2 or $3y^2$-r^2 at the Mn^{3+} site determines the exchange coupling between the Mn^{3+} and Mn^{4+} ions and the CE-type CO state in Ln$_{1-x}$A$_x$MnO$_3$ is associated with ordering of these orbitals at the Mn^{3+} site. The J-T distortion associated with such an orbital ordering stabilizes the CE-type AFM state relative to the ferromagnetic metallic (FMM) state. Complete orbital ordering is achieved when there is both charge and spin ordering. In manganates showing A-type antiferromagnetism, orbital and spin ordering occur without charge ordering. Charge, spin and orbital ordering in CE-, A- and C-type AFM phases is shown in Fig 1.14 [97b]. The arrangement of spins in the A-type allows for some electron transfer between Mn cations in the ab plane. This is clear from the comparison of the variation of resistivity as a function of temperature of Pr$_{0.5}$Sr$_{0.5}$MnO$_3$ and Nd$_{0.5}$Sr$_{0.5}$MnO$_3$ [Fig 1.15][104]. As seen from the figure, the resistivity behavior is the same for the two manganates except for the fact that the magnitude of change in resistivity at T_N is less in the case of Pr$_{0.5}$Sr$_{0.5}$MnO$_3$. This is because Pr$_{0.5}$Sr$_{0.5}$MnO$_3$ transforms from the FMM state to a A-type AFM state on cooling at T_N unlike Nd$_{0.5}$Sr$_{0.5}$MnO$_3$ which goes to a CE-type CO state on cooling below T_N (T_{CO}).
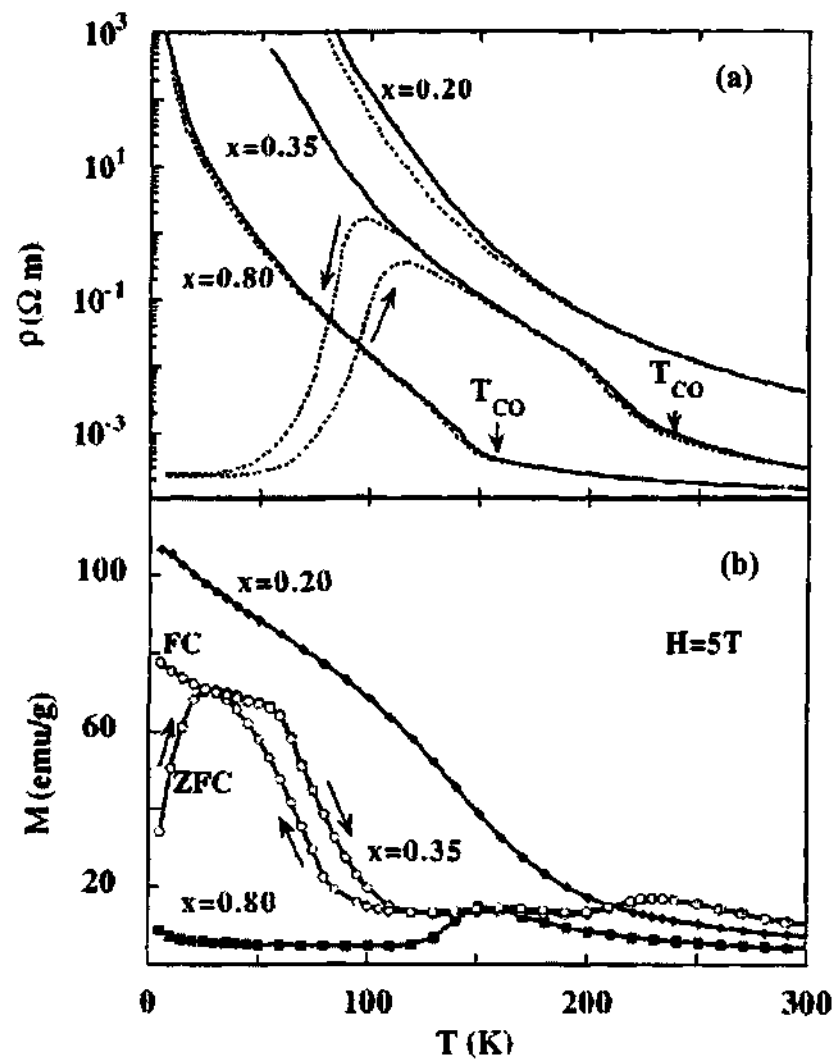
Fig. 1.13 Temperature variation of (a) resistivity in field of zero (solid line) and 5T (dotted line) and (b) magnetization in a field of 5T for $Nd_{1-x}Ca_xMnO_3$ (x = 0.20, 0.35 and 0.80) (from Ref. [102]).
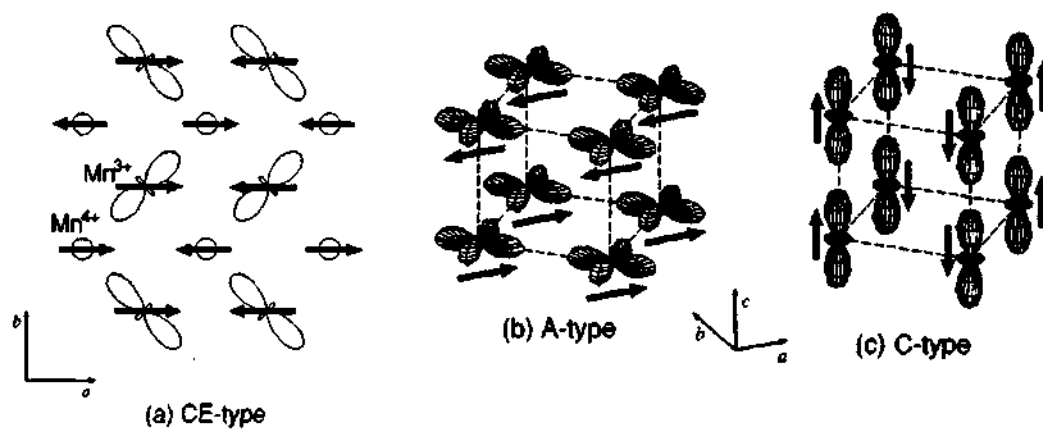
Fig. 1.14 Charge, spin and e_g orbital ordering in various AFM phases (from ref. [97b]).
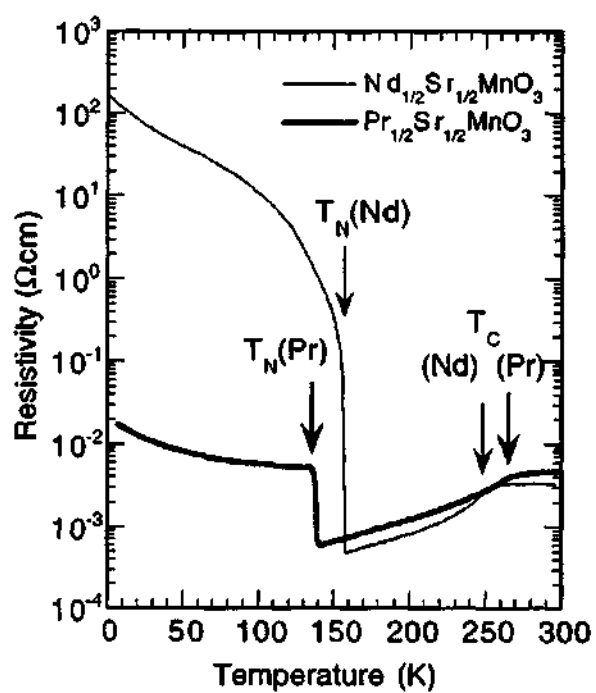
Fig. 1.15 Temperature dependence of the resistivity of $Pr_{0.5}Sr_{0.5}MnO_3$ and $Nd_{0.5}Sr_{0.5}MnO_3$ (from ref. [104]).
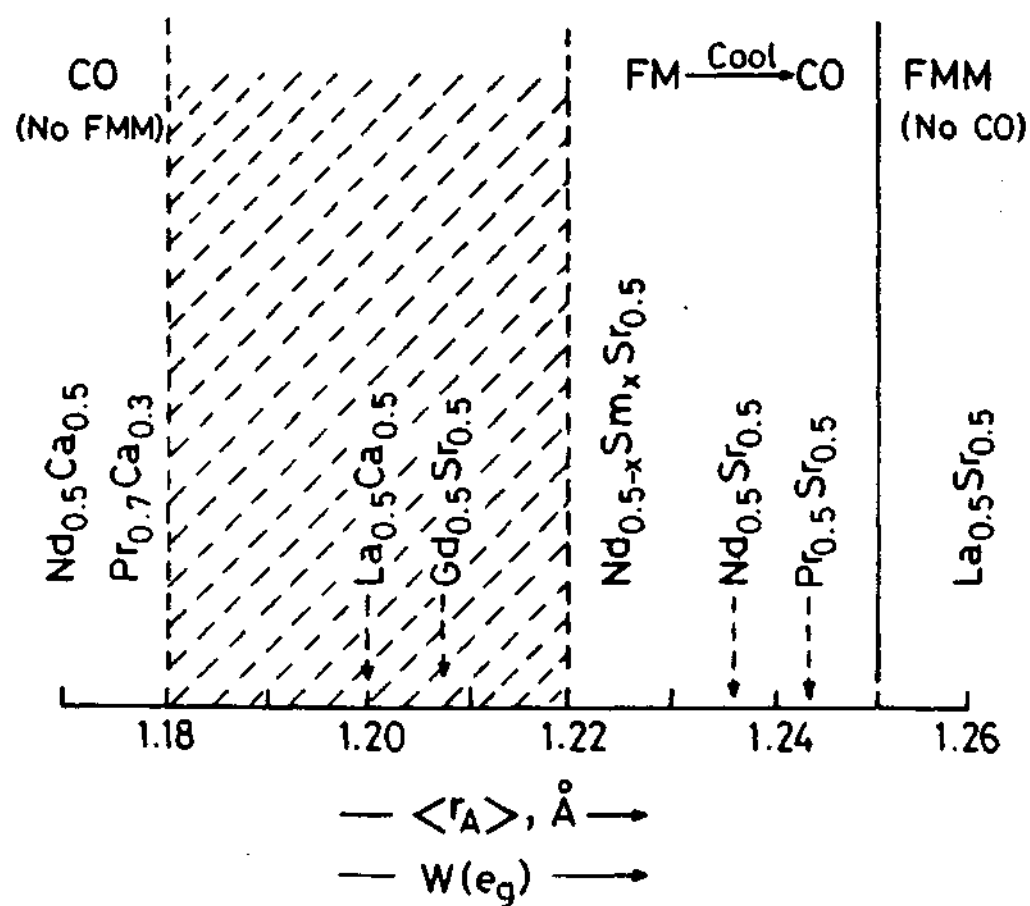
Fig. 1.16 Schematic phase diagram for the $Ln_{0.5}A_{0.5}MnO_3$ as a function of the average

A-site cation radius, $\langle r_A \rangle$ or the e_g bandwidth (from ref. [110]).

Like the ferromagnetic Curie temperature T_C, the charge ordering temperature T_{CO} in the rare earth manganates, $Ln_{1-x}A_xMnO_3$ is highly sensitive to $\langle r_A \rangle$. For $x \leq 0.5$, T_{CO} generally increases with decrease in $\langle r_A \rangle$. Charge-ordering in the $Ln_{0.5}A_{0.5}MnO_3$ systems have been investigated extensively [105-112]. Structural investigations for the $Ln_{0.5}Sr_{0.5}MnO_3$ and $Ln_{0.5}Ca_{0.5}MnO_3$ [107] show that the Mn-O(eq)-Mn angle is significantly larger (by 2-6°) than the Mn-O(ax)-Mn angle for all the $Ln_{0.5}Sr_{0.5}MnO_3$ and $Ln_{0.5}Ca_{0.5}MnO_3$ compounds. There is a change in the crystal symmetry from Pnma to I4/mcm through Imma in the $Ln_{0.5}Sr_{0.5}MnO_3$ manganates with increase in $\langle r_A \rangle$ whereas all the $Ln_{0.5}Ca_{0.5}MnO_3$ compounds crystallize in the orthorhombic Pnma symmetry. The decrease in the $\langle r_A \rangle$ leads to the increased tilting of the MnO_6 octahedra thereby localizing the electrons and charge-ordering is favored. The change in the octahedral tilt system affects the low temperature magnetic structure [107,108]. The apparent one-electron bandwidth estimated on the basis of the experimental Mn-O-Mn angles and Mn-O distances in $Ln_{0.5}A_{0.5}MnO_3$ do not vary significantly with $\langle r_A \rangle$ suggesting that other factors may be responsible for the sensitivity of the CO state to $\langle r_A \rangle$. One possibility is the competition between A and B site cations for covalent mixing with O(2p) orbitals [106b]. A schematic diagram (Fig. 1.16) showing the prevalence of CO and ferromagnetic states as a function of $\langle r_A \rangle$ in the $Ln_{0.5}A_{0.5}MnO_3$ manganates have been constructed based on the variation in the ferromagnetic and antiferromagnetic exchange couplings J_{FM} and J_{AFM} by *Kumar and Rao* [110].

The CO state can be transformed into FMM state by the application of magnetic fields [112-115] or by pressure. The sensitivity of the CO state to the applied magnetic

field in different charge-ordered manganates depends on the average A site cation radius $\langle r_A \rangle$ [114, 115]. Hence, the field required to melt the charge-ordered state in $Pr_{0.6}Ca_{0.4}MnO_3$ is higher than what is required to melt the CO state in $Nd_{0.5}Sr_{0.5}MnO_3$. $Nd_{0.5}Sr_{0.5}MnO_3$ undergoes a transition to the ferromagnetic metallic state at a $T_c \sim 250$ K and exhibits CE type AFM ordering at about 150K (T_{CO}). The transition from a charge-ordered insulator to a metal on application of a magnetic field is first order, showing hysteresis. The temperature-magnetic field phase diagram of a few representative manganates is shown in Fig 1.17. The field required to melt the CO state in manganates with smaller $\langle r_A \rangle$ is high and in the case of $Y_{0.5}Ca_{0.5}MnO_3$ even a field of 100 T does not induce a ferromagnetic transition [114]. The magnetic field induced metal-insulator transition has been studied using neutron diffraction, optical spectroscopy, magnetostriction and specific heat measurements [113, 116-119]. In the case of $Pr_{0.7}Ca_{0.3}MnO_3$, an applied field enforces a ferromagnetic spin alignment and drives the material into the metallic phase by actuating the double exchange mechanism and destroying charge-ordering. This is evident in the drastic suppression of the superlattice intensity at (2,1.5,0) which is the characteristic superlattice reflection due to charge-ordering [113a]. Magnetothermal studies suggest that the field-induced transition is associated with an enormous release of energy, which accounts for its strong irreversibility [113c]. There is a huge change in the optical spectra of $Pr_{0.6}Ca_{0.4}MnO_3$ in an applied magnetic field of 6.5T over a wide photon-energy (0.05eV-3eV) due to the melting of the CO state [116] and the change in the anisotropy of the optical spectra suggests a continuous change in the electronic structure from the
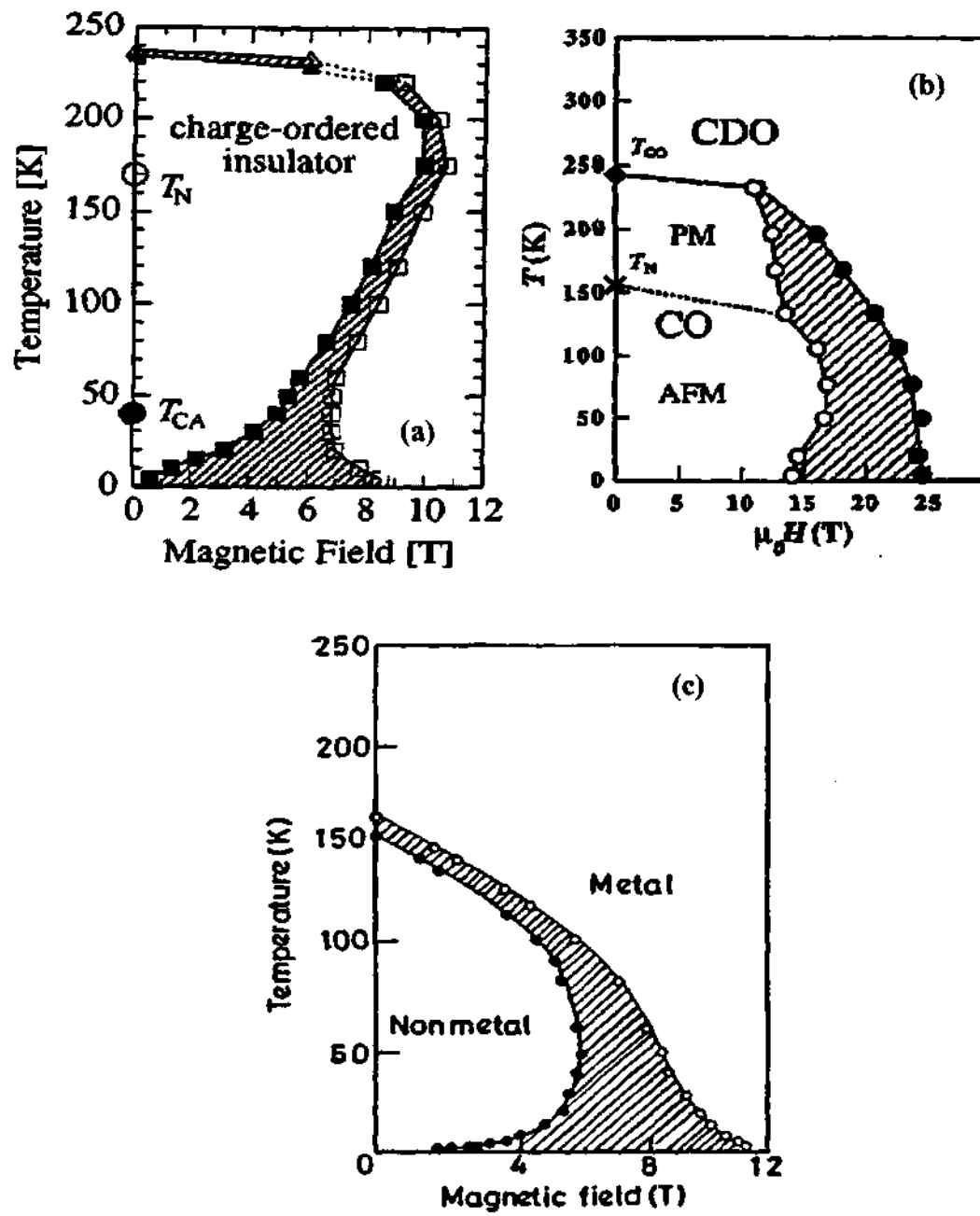
Fig. 1.17 Temperature-magnetic field phase diagram of (a) $Pr_{0.6}Ca_{0.4}MnO_3$ (b) $Nd_{0.5}Ca_{0.5}MnO_3$ and (c) $Nd_{0.5}Sr_{0.5}MnO_3$ (from references [113b, 114a]).

anisotropic CO state to the isotropic FMM state with increasing magnetic field. Low temperature specific heat measurement of $Pr_{1-x}Ca_xMnO_3$ ($0.3 \leq x \leq 0.5$) and $La_{0.5}Ca_{0.5}MnO_3$ in a magnetic field just sufficient to induce the transition from CO state to FMM state suggests that the charge-ordering is not completely destroyed by a 'melting' magnetic field and CO and metallic regions coexist in the sample [117]. The melting of the CO state in $Nd_{0.5}Sr_{0.5}MnO_3$ as studied by optical conductivity suggests that the melting of the charge-orbital ordered state in this manganate occurs through the percolation of ferromagnetic metal domains [118]. Huge positive magnetovolume effect observed over a wider temperature range in $Nd_{0.5}Sr_{0.5}MnO_3$ is attributed to the field induced structural transition [119]. This is further confirmed by the anomalies in the anisotropic magnetostriction at the field-induced transition as seen in Fig 1.18 [119]. Hence, three different types of CO manganates can be delineated based on the effect of magnetic fields.

1. Manganates that are ferromagnetic and become CO at low temperatures (e.g. $Nd_{0.5}Sr_{0.5}MnO_3$) which could be transformed to an FMM state on application of a magnetic field.

2. Manganates that are CO in the paramagnetic state and do not exhibit a FMM state, but transform to a FMM state under a magnetic field (e.g. $Pr_{1-x}Ca_xMnO_3$) and

3. Manganates which are CO in the PM state as in (2), but are unaffected by magnetic fields upto ~ 5T (e.g $Y_{0.5}Ca_{0.5}MnO_3$).

The $x = 0.5$ manganates with $\langle r_A \rangle = 1.17$Å seem to belong to the third category.
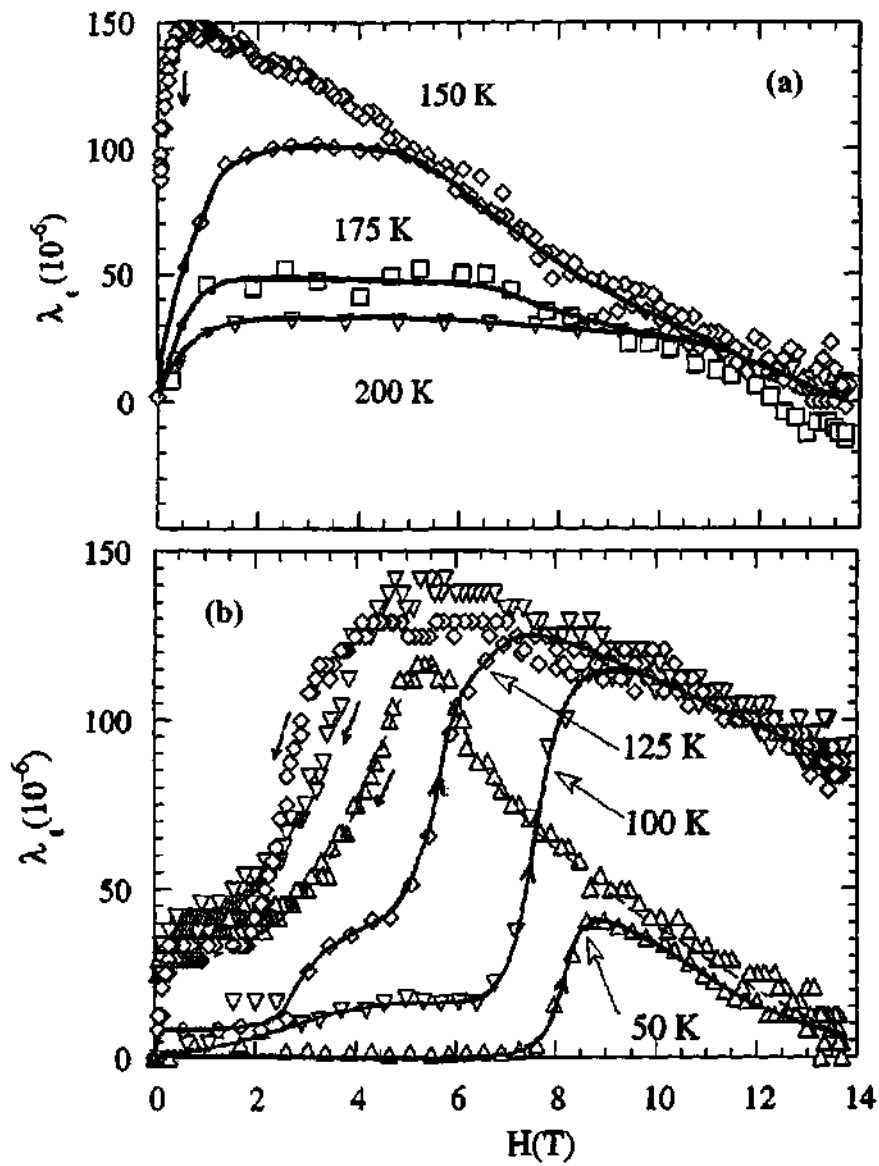
Fig. 1.18 Anisotropic magnetorestriction of $Nd_{0.5}Sr_{0.5}MnO_3$ in (a) the ferromagnetic

state and (b) the CO state (from ref. [119]).
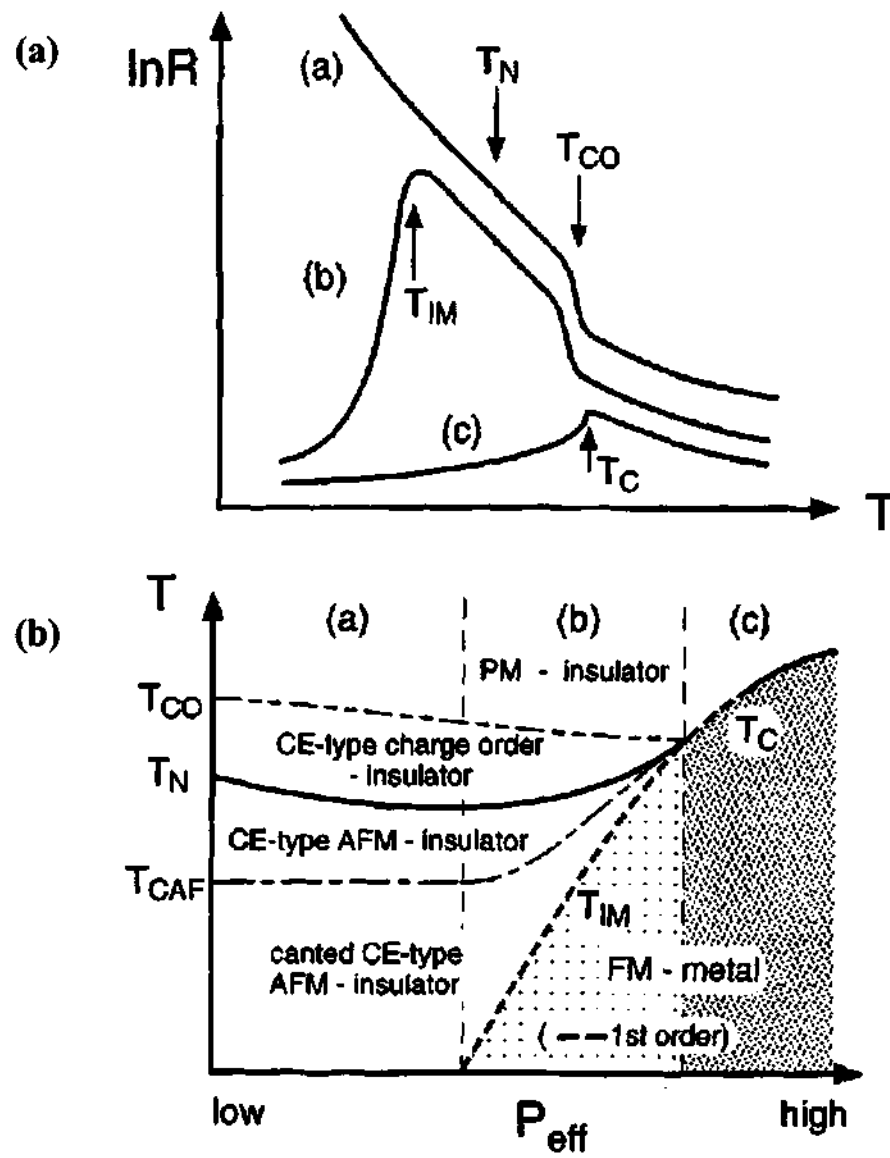
Fig. 1.19 (a) Schematic behavior of the resistivity for three regions in the $Pr_{1-x}Ca_xMnO_3$ system and (b) schematic phase diagram on effective pressure Vs temperature for a CO system (from ref. [120].

51

Effect of chemical and external pressures on the two types of charge-ordered systems falling into category (1) and (2) as mentioned above has been investigated [120,121]. Application of external pressure and resultant enhanced carrier itinerancy suppresses the CO transition for $Pr_{1-x}Ca_xMnO_3$ x ($0.3 \leq x \leq 0.7$) and for x = 0.3 produces a metallic phase from the low temperature. As a function of effective pressure, three different pressure regions for the low temperature state in $Pr_{1-x}Ca_xMnO_3$ have been identified [Fig. 1.19] [120]. Increase of chemical pressure by substituting a bigger ion such as La in place of Nd in $Nd_{0.5}Sr_{0.5}MnO_3$, increases the one-electron bandwidth (W) thereby suppressing the CO state and finally disappears above z = 0.6 for $(Nd_{1-z}La_z)_{0.5}Sr_{0.5}MnO_3$. In a narrow window of z ($0.4 \leq z \leq 0.6$) another type of AFM phase replaces the AFM-CE state due to the subtle balance between the competing interactions.

The effect of pressure on the manganates $(Nd_{1-y}Sm_y)_{0.5}Sr_{0.5}MnO_3$ with a controlled one-electron bandwidth have also been studied [122-124]. The competition between the ferromagnetic double exchange interaction and the antiferromagnetic charge-ordering instability in these compositions gives rise to thermally as well as magnetic field induced insulator metal transition. The T_C decreases from 225 to 115 K as y increases from 0.0 to 0.875 in this system as expected for a decrease in $\langle r_A \rangle$. Also, the T_{CO} decreases from 158 to 0 K with the increase in x. This unusual behavior wherein T_{CO} is suppressed as T_C approaches T_{CO} is interesting.

Other than magnetic field, internal and external pressures, the CO state in the manganates could be melted by other stimuli also [125-128]. X-ray irradiation of the

charge-ordered insulator $Pr_{0.7}Ca_{0.3}MnO_3$ at low temperatures induces a transition from the insulating AFM to metallic FM state [125]. This transition is accompanied by significant changes in the lattice structure and can be reversed by the thermal cycling. Similar effect is also seen on application of an electric current to this manganate [126]. Visible-IR pulse laser irradiation also induces an insulator-metal transition in the CO phases of $Pr_{0.7}Ca_{0.3}MnO_3$ by photocarrier generation [127]. The light induced insulator-metal transition in $Pr_{0.7}Ca_{0.3}MnO_3$ is shown to generate a well-localized conducting path while the bulk of the sample remains insulating which could be visualized through a change of reflectivity accompanying the phase transition [128]. A more recent report on the spectroscopic study of photoinduced charge-gap collapse in $Pr_{1-x}Ca_xMnO_3$ suggests that the laser irradiation excites localized electrons to destroy the charge gap, which may be general behavior not only of CO insulators but also of strongly correlated insulators in general. Electron irradiation of $Pr_{0.7}Ca_{0.3}MnO_3$ at 92K leads to a complete charge-disordering, the disordered state remaining stable at this temperature even in the absence of irradiation [129]. Films of charge-ordered $Nd_{0.5}Ca_{0.5}MnO_3$, $Gd_{0.5}Ca_{0.5}MnO_3$, $Y_{0.5}Ca_{0.5}MnO_3$ and $Nd_{0.5}Sr_{0.5}MnO_3$ show insulator-metal transitions on the passage of small electrical current [130]. What is noteworthy is that such an electric-field induced transition occurs even in films of $Y_{0.5}Ca_{0.5}MnO_3$, where the CO state is not affected by high magnetic fields in the polycrystalline sample [Fig 1.20]. The transition is attributed to the depinning of the randomly pinned charge solid.

Substitution of ^{16}O by ^{18}O in the manganates affects the charge-ordering transition temperature, T_{CO}. The T_{CO} in $La_{0.5}Ca_{0.5}MnO_3$ increases by 9K by such a

substitution. The isotope shift increases with the magnetic field in $La_{0.5}Ca_{0.5}MnO_3$ as well as in $Nd_{0.5}Sr_{0.5}MnO_3$ [131]. Also, the substitution of ^{16}O by ^{18}O in $(La_{1-y}Pr_y)_{0.7}Ca_{0.3}MnO_3$ for y = 0.75 results in the reversible transition from a FMM to CO insulator at zero magnetic field [132]. This effect is caused due to the modification of the effective hopping integrals and the resulting electron bandwidth due to isotope substitution, which shifts the relative stability of the CO versus ferromagnetic states and leads to a transition between these phases. In ^{18}O substituted $Pr_{0.67}Ca_{0.33}MnO_3$, the magnetic field induced insulator-metal transition occurs at a higher field since the heavier isotope favors the insulating state [133]. T_{CO} is affected to a greater extent in $Nd_{0.5}Sr_{0.5}MnO_3$ than $Pr_{0.5}Ca_{0.5}MnO_3$ due to ^{18}O substitution [134] hence delineating the role of $\langle r_A \rangle$. Theoretical studies based on a combination of the double exchange and interacting lattice polaron mechanism suggest that the isotope effect on T_C in the metallic phase and T_{CO} in the CO-phase of manganates is due to the polaron formations originating from the strong electron phonon interactions [135].

Other than neutron and X-ray diffraction, electron diffraction has been used widely to study and image the crystallographic superstructures arising from charge ordering. $La_{0.5}Ca_{0.5}MnO_3$ shows a ferromagnetic transition around 225K followed by a first-order transition to an antiferromagnetic CE state at ~135 K. The first order FM-AFM transition is characterized by a substantial thermal hysteresis in the temperature dependent resistivity and magnetization measurements. This latter transition from FM to AFM state is structurally associated with a incommensurate to commensurate charge-ordering phase transition as evident from electron diffraction and real space
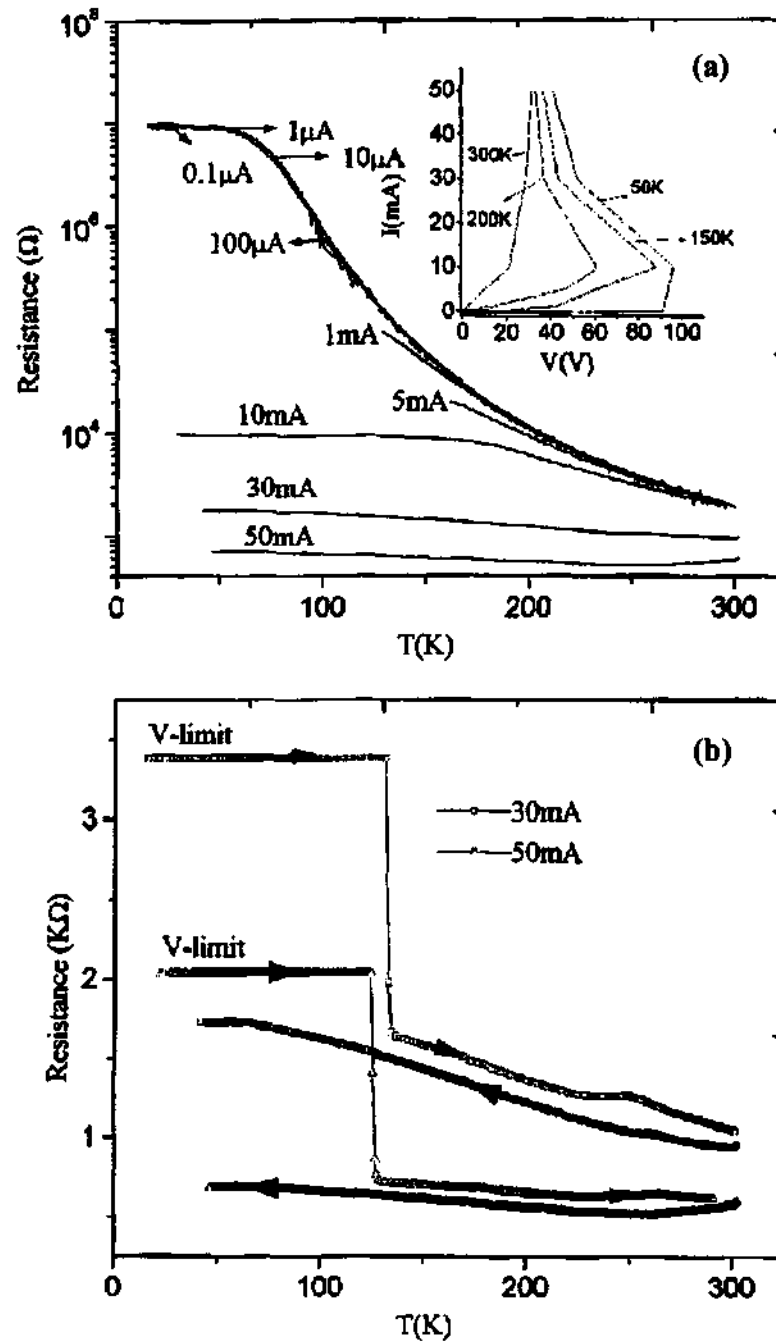
Fig. 1.20 (a) Temperature variation of the resistance of $Y_{0.5}Ca_{0.5}MnO_3$ film deposited on LAO(110) for different values of current and (b) Cooling and heating curves for different current values indicative of memory effect (from ref. [130]).

imaging [136]. This is clear in Fig. 1.21 showing the variation in the incommensurability of charge-ordering, ε as a function of temperature. Synchrotron X-ray and Neutron powder diffraction study of $La_{0.5}Ca_{0.5}MnO_3$ suggests that commensurate long-range charge-ordering coexists with quasicommensurate orbital ordering in this compound [109]. The coexistence of ferromagnetism and charge-ordering in the narrow temperature range 220-135K is due to an inhomogeneous spatial mixture of incommensurate CO and FM (charge disordered) microdomains. High-resolution lattice images of the incommensurate charge-ordered microdomains indicate a charge-ordered state with a fine mixture of paired and unpaired J-T distorted Mn^{3+} stripes [137].

The $La_{1-x}Ca_xMnO_3$ compositions in the electron doped region ($0.63 \leq x \leq 0.67$) undergo charge-ordering transition at 260K which is accompanied by an increase in sound velocity, anomalies in the heat capacity and the activation energy for conduction as shown in Fig 1.22 [138(a)]. The transmission electron microscope images of the x = 0.67 composition ($T_N = 160K$) show pairs of $Mn^{3+}O_6$ octahedra [Fig 1.23][139]. The periodicity are between two and five times the lattice parameters of the orthorhombic unit cell, corresponding to the compositions x = 1/2, 2/3, 3/4 and 4/5. A mixture of adjacent configurations is seen for other values of x. Paired Jahn-Teller distorted stripes (JTS) or bi-stripes are suggested to be the basic building block of the CO state. A structural model of the CO state has been proposed with a crystallographic unit cell of 3a x b x c of the high temperature unit cell and same symmetry [138(c)].
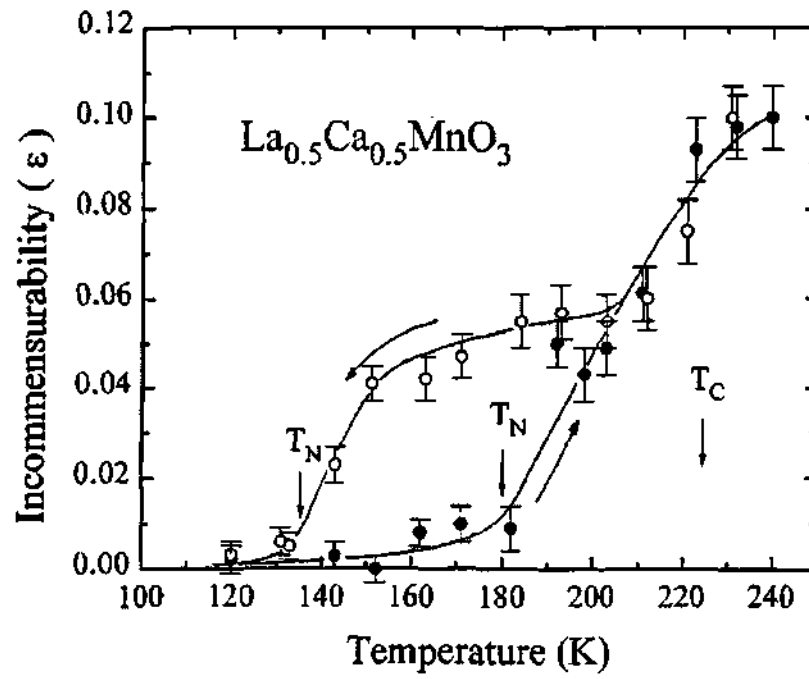
Fig. 1.21 Variation of superlattice wave-vector incommensurability, ε as a function of temperature on cooling and heating for $La_{0.5}Ca_{0.5}MnO_3$ (from ref. [136]).
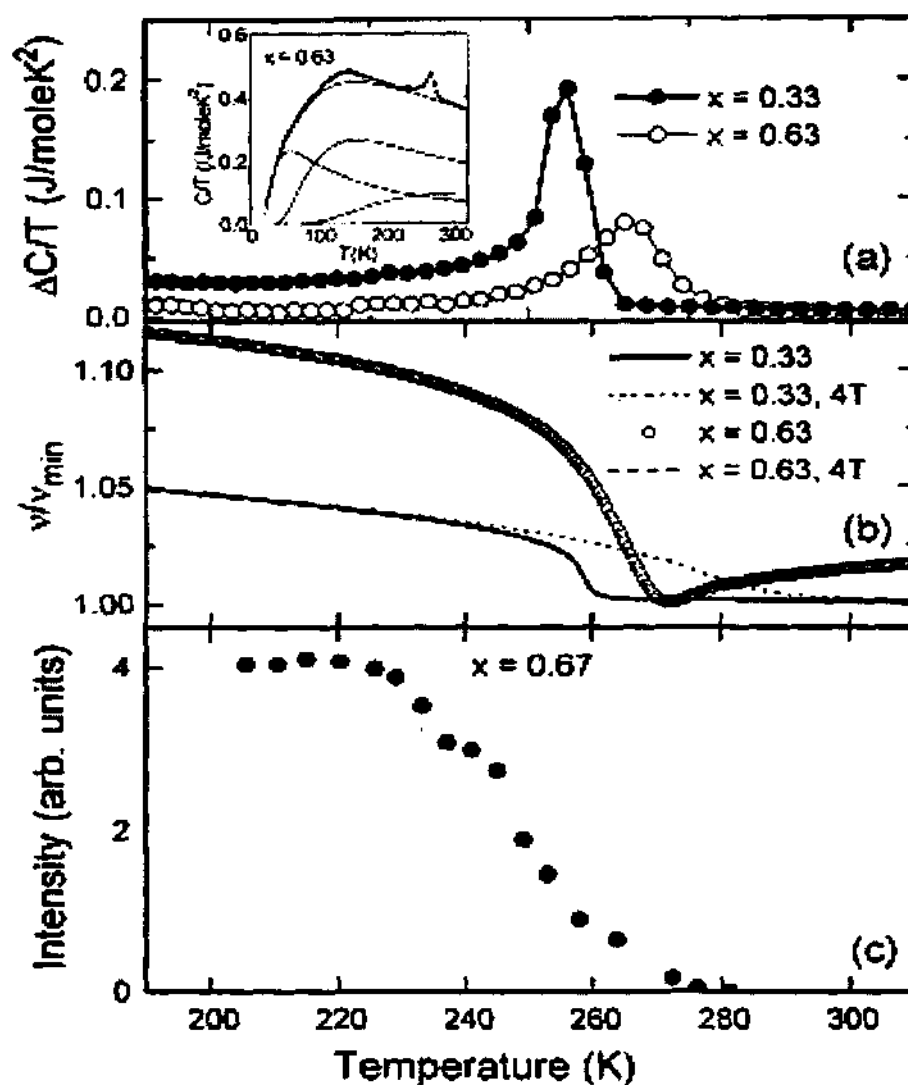
Fig. 1.22 Evidence of charge-ordering in various compositions of $La_{1-x}Ca_xMnO_3$ seen in the temperature variation of (a) Specific heat divided by temperature, $\Delta C/T$, (b) sound velocity and (c) variation in intensity of the superlattice Bragg spots in electron diffraction. (from ref. [138a]).
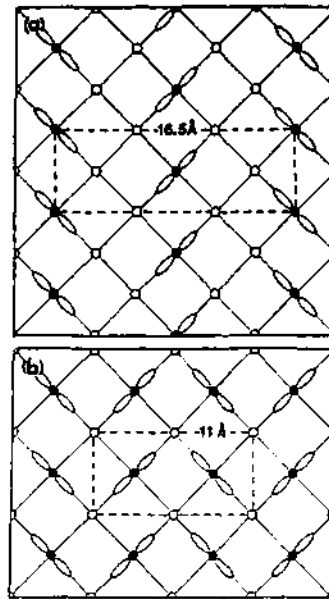
Fig. 1.23 Schematic real-space charge-ordering of Mn^{4+} (open circles) and Mn^{3+} (closed circles) for $La_{1-x}Ca_xMnO_3$ compositions with (a) x =0.67 and (b) x =0.5, demonstrating the 16.5 Å and 11 Å periodic stripes respectively (from ref. [139]).

The crystallographic (CO) and magnetic superstructure of $La_{0.33}Ca_{0.667}MnO_3$ have been studied by high-resolution synchrotron X-ray and neutron powder diffraction [140]. The lattice parameter is tripled and the c lattice parameter is doubled in the AFM structure with respect to the average crystallographic unit cell. The d_z^2 orbitals of the Jahn-Teller distorted $Mn^{3+}O_6$ octahedra order in the orthorhombic ac plane. The Mn^{3+} ions order as far as possible in the ac plane to reduce strains on the system and the $Mn^{4+}O_6$ are displaced in the c direction. All these structural features are more consistent with a Wigner-crystal model rather than the bi-stripe pattern. Fig. 1.24 compares the two models. One possibility is that the electron microscopic data are not representative of the bulk sample. A recent electron diffraction and high resolution imaging study of this compound in combination with calculations based on the two models supports the Wigner-crystal model [141]. Infrared absorption measurements show that the $La_{1-x}Ca_xMnO_3$ samples with x = 0.5 and x = 0.66 both have gaps at a temperature below T_N, providing an explanation for the coexistence of ferromagnetism and CO in the x = 0.5 composition [142]. High temperature studies of $La_{1-x}Ca_xMnO_3$ [143(a)] show the decoupling and coupling of the FM zigzags for x ~ 3/8 and 1/2 respectively. This provides evidence for the presence of short-range charge ordering correlation at high temperature possibly in the form of a FM "zigzag", a small segment of the CE-type CO state. Inelastic light scattering experiments on $La_{1-x}Ca_xMnO_3$ (0.45 ≤ x ≤ 0.76) show that the presence of enhanced fluctuations persisting upto temperatures of atleast $2T_{CO}$ for x ~ 0.50 [143 (b)].

Wigner-crystal
model
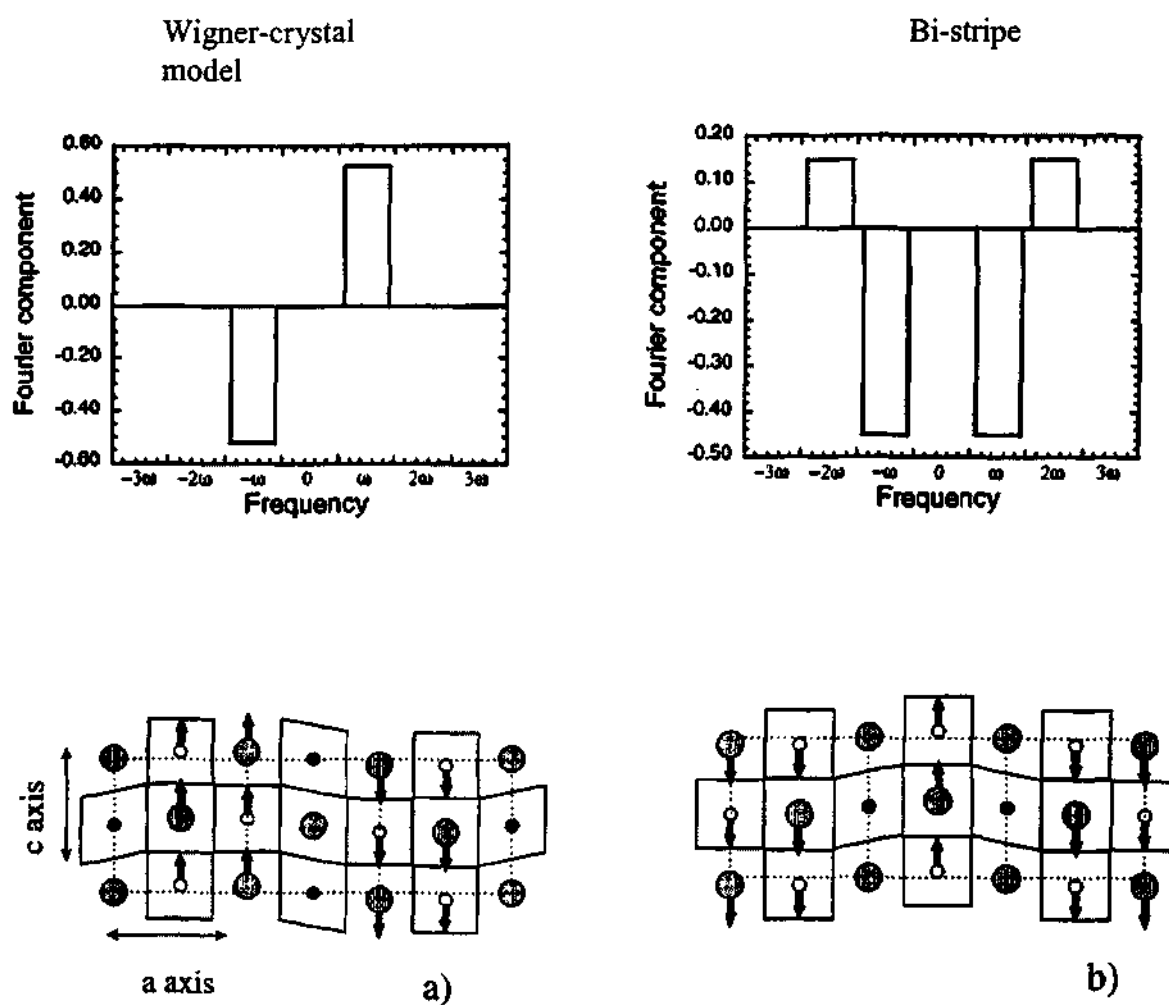
Bi-stripe

Fig. 1.24 Comparison of the Wigner-crystal and Bi-stripe models. The upper panel

shows the fourier transform of the displacement patterns depicted in the lower panel

(from ref. [140]).

Nd$_{0.5}$Sr$_{0.5}$MnO$_3$ with an $\langle r_A \rangle$ of 1.24Å undergoes a transition from a paramagnetic to ferromagnetic metal around 250 K (T$_c$) followed by a transition to the CE type insulating state at 150K. The latter transition is accompanied by spin (AFM) and orbital ordering and has been investigated by various experimental techniques. Vacuum tunneling spectroscopy of Nd$_{0.5}$Sr$_{0.5}$MnO$_3$ has shown that a gap opens up in the density of state around fermi level, E$_f$ on cooling the sample below T$_{CO}$ [144]. This CO gap of 250 meV collapses on the application of a magnetic field suggesting that a gap in the DOS at E$_F$ is necessary for the stability of the CO state [145]. However, photoemission studies give an estimate of 100 meV for the gap [146]. These estimates of the gap are considerably larger that T$_{CO}$ (12meV) raising more interest as to how a magnetic field of 6T (1.2meV) destroys the CO state. Apart from the huge positive magneto volume effect [119] observed in this compound, high resolution X-ray and neutron diffraction studies also suggest that Nd$_{0.5}$Sr$_{0.5}$MnO$_3$ phase separates into three macroscopic phases at low temperatures depending on the synthesis conditions. The evolution of the three phases namely, FMM high temperature (Imma), the orbitally ordered AFM (A-type) and the charge and orbitally ordered AFM (CE-type) as a function of temperature is shown in Fig. 1.25 [147]. Ultrasonic studies of Nd$_{0.5}$Sr$_{0.5}$MnO$_3$ show pronounced acoustic-mode hardening around T$_{CO}$ and softening of the acoustic mode in the vicinity of the I-M transition induced by a magnetic field [148].

Muon spin relaxation spectroscopy has been used to study the magnetic ion spin dynamics in single crystals of Nd$_{0.5}$Sr$_{0.5}$MnO$_3$ and Nd$_{0.45}$Sr$_{0.55}$MnO$_3$ [149]. The
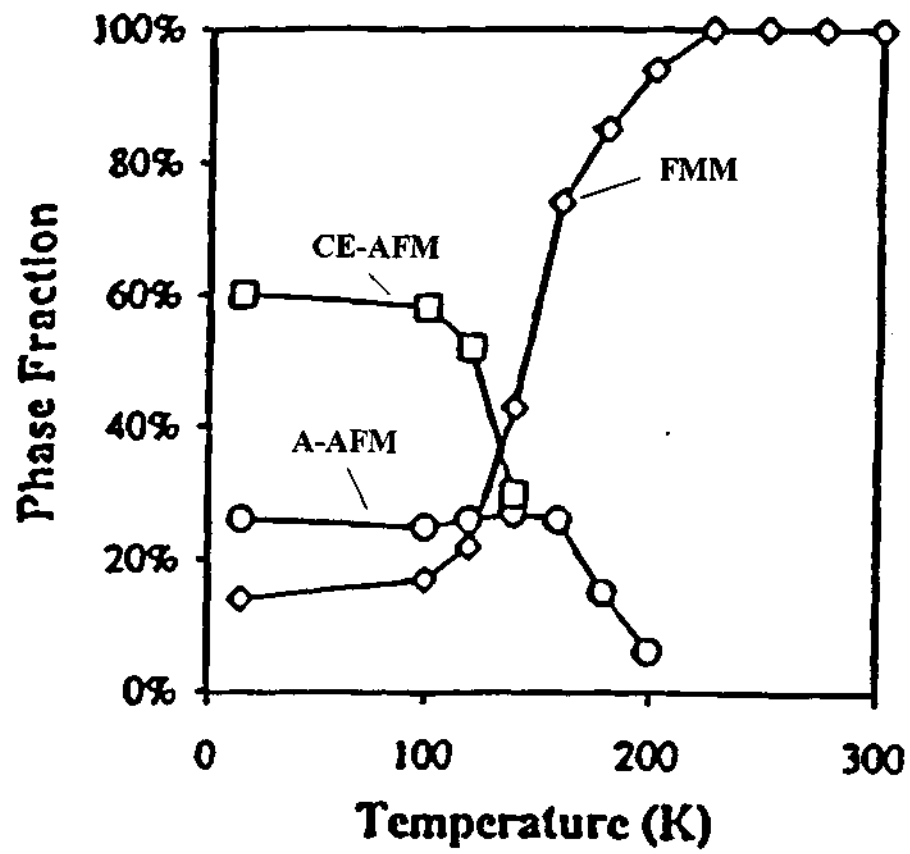
Fig. 1.25 Variation in the percentage of the different phases of $Nd_{0.5}Sr_{0.5}MnO_3$ with temperature (from ref. [147]).

critical-slowing down of Mn ion spin fluctuations have been observed above the FM ordering temperature of 250 K in $Nd_{0.5}Sr_{0.5}MnO_3$. These studies suggest the formation of spin-glass type regions into magnetically ordered states of $Nd_{1-x}Sr_xMnO_3$ around $x = 0.5$. Magnetic relaxation study behavior of $La_{0.5}Ca_{0.5}MnO_3$ and $Nd_{0.5}Sr_{0.5}MnO_3$ suggests that the general temperature dependence of the long time logarithmic relaxation rate (LTLRR) in the two manganates are independent of the particular CO system considered [150]. However, the lower temperature of the LTLRR minimum in $Nd_{0.5}Sr_{0.5}MnO_3$ compared to $La_{0.5}Ca_{0.5}MnO_3$ provides evidence for the stronger FM interactions in $Nd_{0.5}Sr_{0.5}MnO_3$ when compared to $La_{0.5}Ca_{0.5}MnO_3$.

Specific heat measurements on a single crystal of $Pr_{0.63}Ca_{0.37}MnO_3$ in a magnetic field of 8T have been used to get an estimate of the entropy and latent heat at the first-order CO transition [151]. The total entropy change at the CO transition, which is ~ 1.8 J/mol K at 0 T decreases to ~ 1.5 J/mol K in the presence of a magnetic field of 8T. The latent field involved in the CO transition is estimated to be 235 J/mol. Raman spectroscopy study of charge ordered $Pr_{0.65}Ca_{0.35}MnO_3$ suggests strong charge-lattice and spin-lattice couplings in this manganate (152).

$Nd_{0.5}Ca_{0.5}MnO_3$ is a paramagnetic insulator in the charge-ordered phase with a $T_{CO} = 240$ K. The phase transition to a canted AFM state at 140 K [153] charge ordered insulator phase in this compound could be melted by application of magnetic field. Brillouin scattering experiments of single crystal $Nd_{0.5}Ca_{0.5}MnO_3$ had shown the presence of ferromagnetic clusters in the CO and AFM phases [154]. A recent temperature dependent EPR studies of $Nd_{0.5}Ca_{0.5}MnO_3$ [155] shows a large decrease in

the linewidth from T_N to T_{CO} which is explained in terms of motional narrowing caused by the hopping of the J-T polarons yielding an activation energy of $E_a = 0.1eV$. The continuous increase in the g-value below T_{CO} is suggestive of a gradual strengthening of the orbital ordering.

Other than the rare earth manganates, Bi doped perovskite manganates have been studied extensively. $Bi_{1-x}Ca_xMnO_3$ system is similar to the $La_{1-x}Ca_xMnO_3$ system due to the similar oxidation state and ionic size of the Bi ion. *Bao et. al.* discovered dynamic ferromagnetic spin correlation at high temperature in $Bi_{1-x}Ca_xMnO_3$ ($0.74 \leq x \leq 0.82$) which are replaced by antiferromagnetic spin fluctuations at a concomitant charge ordering and structural transition [156]. *Chiba et. al.* [157] discovered ferromagnetism and especially large MR for $x \geq 0.875$ whereas *Murakami et al.* [158] reported evidence of long range period structures associated with charge ordering for $x \sim 0.80$. X-ray scattering studies of single crystals of $Bi_{0.24}Ca_{0.76}MnO_3$ show the formation of charge stripes associated with the low temperature structural phase transition indicative of charge ordering in this compound [159]. EELS studies of $Bi_{1-x}Ca_xMnO_3$ ($x \geq 0.75$) have shown that the hybridization between oxygen 2p and Mn 3d orbitals are weakened due to the distortion of the Mn-O-Mn angle at the charge ordering temperature [160]. Anisotropic optical signatures of orbital and charge ordering have been evidenced in $Bi_{1-x}Ca_xMnO_3$ system [161] highlighting the complex interplay between charge and orbital ordering in these compounds.

The $Bi_{1-x}Sr_xMnO_3$ system shows very different behavior from the $La_{1-x}Sr_xMnO_3$ inspite of La^{3+} and Bi^{3+} having similar ionic radii [162]. With increase in x in Bi_{1-}

$_x$Sr$_x$MnO$_3$ the magnetic moment decreases rapidly and the electrical resistivity remains thermally activated and transition to a metallic state does not occur. Hence the double exchange mechanism does not seem to work in this system and the localization effect due to the local distortion arising due to lone pair on Bi could be the reason. Recently *Frontera et. al.* have reported the presence of a CE charge ordered phase in Bi$_{0.5}$Sr$_{0.5}$MnO$_3$[163]. The T$_{CO}$ and the orbital ordering temperature T$_{OO}$ coincide in this compound and is well above room temperature (T$_{CO}$ = 525K).

Charge-ordering in layered manganates

The Ruddlesden-Popper (RP) manganates with the general formula (Ln,A)$_{n+1}$Mn$_n$O$_{3n+1}$ (n = dimensionality) have been the focus of study to have a better understanding of the interplay of spin, orbital and charge-ordering with dimensionality in comparison with the rare-earth manganates (n = ∞). Charge ordering of Mn^{3+} and Mn^{4+} ions in La$_{0.5}$Sr$_{1.5}$MnO$_4$ occurs around 120 K and the material becomes AFM at 110 K [164]. This material shows anisotropic properties due to orbital ordering [165,166]. Many other studies carried out in the last two years have contributed tremendously to the understanding of the CO in the n=1 RP manganates [167-169].

Structural double layered manganates of the composition Ln$_{2-2x}$Sr$_{1+2x}$Mn$_2$O$_7$ for (0.5 ≤ x ≤ 0.75) and Ln=La, Pr, Nd, Sm, Eu, Gd, Tb, Dy, Ho, Y and Er show the existence of cation ordering between the two available cation sites with the smaller lanthanides preferring the site in between the double layer block [170]. Charge ordering

in LaSr$_2$Mn$_2$O$_7$ has been studied using Raman spectroscopy and electron diffraction [171,172].

Charge ordering in other systems

The phenomenon of charge-ordering has been observed in many other systems such as rare earth cobaltates [173-175], lanthanum nickelates [90,91], LiMn$_2$O$_4$ [92,93], LuFeO$_4$ [176], TbBaFe$_2$O$_5$ [177], rare earth ferrites [82,84], Yb$_4$As$_3$[178], sodium vanadates [179-181] Yba$_2$Cu$_3$O$_{7-\delta}$ [182] and TMTTF family of molecular conductors [183].

1.7 Phase separation and segregation in manganates

Rare earth manganates of the general formula, Ln$_{1-x}$A$_x$MnO$_3$ (Ln = rare earth, A = alkaline earth) exhibit phase separation due to the occurrence of tiny clusters or small nanometric regions of one type of magnetic phase in the matrix of another (e.g., ferromagnetic metallic clusters in an insulating antiferromagnetic matrix) or phase segregation due to the coexistence of large domains of two phases. The phenomenon is nearly universal in the manganates and crucially depends on the composition, temperature, external magnetic field, dopant substitution in the Mn site and related factors.

At low dopant levels in Ln$_{1-x}$Ca$_x$MnO$_3$ (x < 0.1), FM clusters are found to be present in the antiferromagnetic host matrix, often giving rise to a spin-glass behavior. The situation is similar when x > 0.9 [184]. Even in many of the manganates
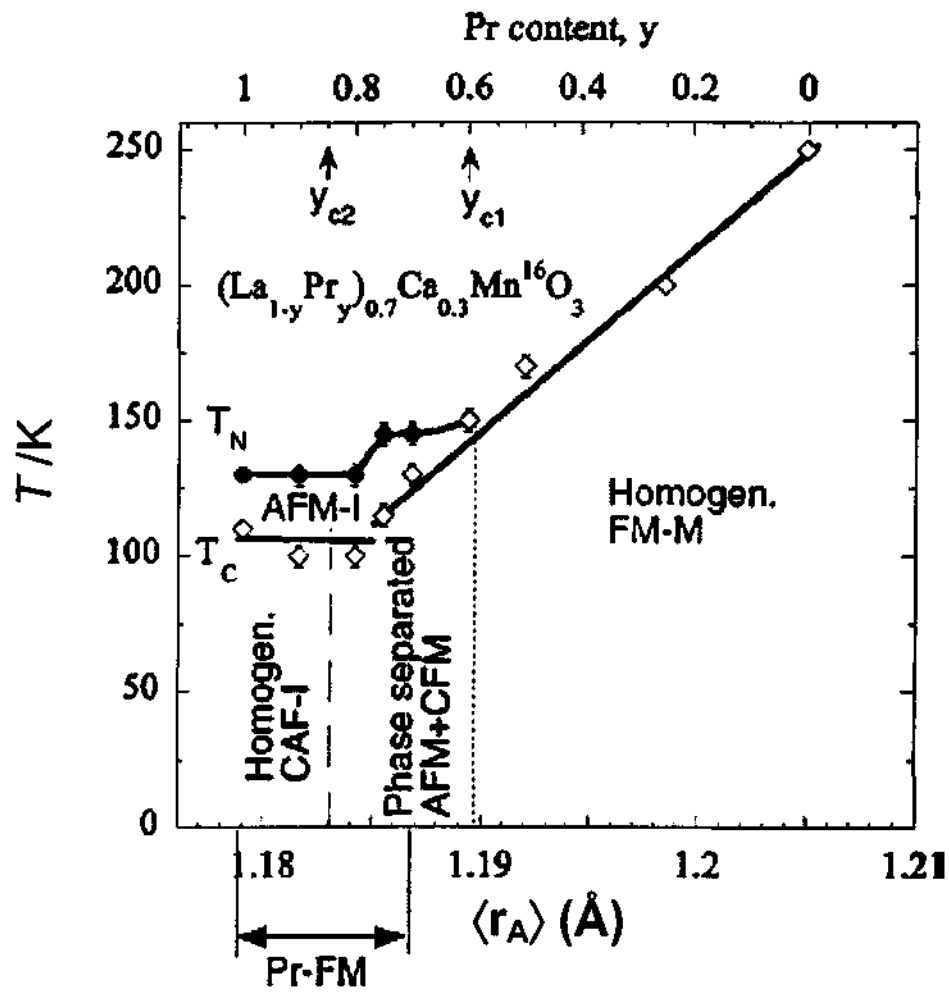
Fig. 1.26 Phase diagram of the $(La_{1-y}Pr_y)_{0.7}Ca_{0.3}MnO_3$. The diamonds and circles show the T_C and T_N values (from ref. [188]).

(exhibiting CMR) which are in the FMM state at low temperatures, charge-ordered clusters occur. In $La_{1-x-y}Pr_yCa_xMnO_3$ (x = 0.37), phase segregation into submicrometer-scale CO regions and FMM domain has been observed in electron microscopic images [185].

Phase separation or segregation implies that the different phases possess comparable free energies. The insulator-metal transition around the ferromagnetic T_C and the CMR properties in $La_{0.7}Ca_{0.3}MnO_3$ and other manganate compositions have been viewed by some workers as a percolative transition involving the two states. However, whether this requires mesoscopic phase separation or not is unclear. In the last two years, phase separation and segregation has been reported in several rare earth manganates and the phenomenon has been investigated by a variety of techniques.

The $(La_{1-y}Pr_y)_{0.7}Ca_{0.3}MnO_3$ system is one of the early examples of phase separation. A recent study [186] shows that below T_{CO} there is another insulating phase besides the CO phase and the insulator-metal transition is due to changes in the former phase. The phase diagram of this system has a region ($0.6 \leq y \leq 0.8$) where the low-temperature magnetic state is macroscopically inhomogeneous [187]. In Fig. 1.26, we show a possible phase diagram of the system. Enhancement of $1/f$ noise at the metal-insulator transition indicates that a percolation mechanism may be operative, the percolating phases being the FMM and COI phases [188].

$La_{0.7}Ca_{0.3}MnO_3$ is probably the most well studied manganate for CMR and related properties. The relation between the FM transition and polaron formation related to the insulator-metal transition in this manganate has not been clearly understood. It has been

shown recently that diffuse neutron scattering from lattice polarons develops as the Curie temperature is approached from below along with short-range polaron correlations, consistent with stripe formation [189]. Scattering due to polaron correlations and the anomalous quasielastic component of the magnetic fluctuation spectrum maximize close to T_C. An optical Jahn-Teller phonon exhibits continuous but anomalous damping with the increasing temperature in the FMM phase and collapses at T_C, due to the growing dynamic phase separation as $T \rightarrow T_C$ [190]. An electron microdiffraction study has shown temperature-dependent diffraction spots, with the intensity peaking at T_C. The results suggest the presence of nanometer-sized regions of charge ordering and charge melting [191].

Electron-doped manganates are generally charge ordered in the $x = 0.5$-0.9 region and show phase separation resulting from the strong competition between long-range AFM order and local FM order even when $1.0 > x \geq 0.8$ [192]. ^{55}Mn and ^{139}La NMR measurements on $La_{0.35}Ca_{0.65}MnO_3$ show evidence of electronic phase segregation of microscopic FM regions over an AFM background [193]. The FM clusters do not expand or increase in their population in applied fields, unlike in the hole-doped compositions. In $Pr_{1-x}Ca_xMnO_3$ ($x = 0.9, 0.95, 0.975$), coexistence of majority AFM and minority FM phases are indicated by NMR, neutron diffraction and magnetic measurements [194]. There is a reduction in the FM volume with the increase in temperature for large x. When $x = 0.9$, the FM phase is stable in the whole temperature region of its existence.

70

Similar phase separation and segregation have been observed in $Ca_{1-x}Bi_xMnO_3$ [195,196]. In the bilayered manganates, $La_{2-2x}Sr_{1+2x}Mn_2O_7$ $(0.45 \leq x \leq 0.60)$, a reentrant CO transition is observed at low temperatures. Reentrant CO melting arises from the competition between charge ordering and ferromagnetism [197]. The separation of CO and AFM phases seems to occur in $LaSr_2Mn_2O_7$, the competition between the two phases being associated with the transition to A-type antiferromagnetism [198].

Several theories have been proposed to explain phase separation and related phenomena. It has been suggested that instability towards phase separation and the formation of inhomogeneous states is an intrinsic property of many of the correlated electron systems such as the manganates [199]. Based on a simple model of CO, it has been proposed that at any deviation from half filling, the manganate system is unstable with respect to phase separation into CO regions and metallic region with a smaller carrier density [200]. In order to explain the observance of large domains or clusters it has been proposed that there is disorder in the regime of competing FM and CO states, disorder playing an important role in phase separation [201]. Considering the manganates as an inhomogeneous mixed-valent system, it is pointed out that it is necessarily unstable with respect to phase separation into AFM and CO FM domains, the latter increasing at the expense of AFM domains in the presence of magnetic field [202]. Clearly, phase separation and segregation have to be taken into account in understanding transport and magnetic properties of the manganates.

References

1. C. N. R. Rao and B. Raveau, *Transition Metal Oxides: Structure, Properties and Synthesis of Ceramic Oxides*, 2nd edition, Wiley-VCH (1998).

2. S. Jin, T. H. Tiefel, M. McKormak, R. A. Fastnacht, R. Ramesh and L. H. Chen, Science, 264, 413 (1994).

3. G. H. Jonker and J. A. van Santen, Physica, 16, 337 (1950).

4. E. O. Wollan and W. C. Koeller, Phys. Rev. 100, 545 (1955).

5. (a) J. B. Goodenough, Phys. Rev. 100,564 (1955).(b) J. B. Goodenough, A. Wold, R. J. Arnott and N. Menyuk, Phys. Rev. 124, 373 (1961).

6. (a) C. N. R. Rao and B. Raveau (Eds.), *Colossal Magnetoresistance, Charge Ordering and Related Properties of Manganese oxides*, World Scientific (1998) Singapore. (b) C. N. R. Rao and P. V. Vanitha, Curr. Opin. Solid State Mater. Sci. 6, 97 (2002).

7. H. A. Kramers, Physica 1, 182 (1934).

8. P. W. Anderson, Phys. Rev. 79, 350 (1950).

9. J. H. Van Vleck, J. Phys. Radium 12, 262 (1951).

10. J. B. Goodenough J. Phys. Chem. Solids 6, 287 (1958).

11. J. Kanamori, J. Phys. Chem. Solids 10, 87 (1959).

12. C. Zener, Phys. Rev. 81, 440 (1951).

13. P. W. Anderson and H. Hasegewa, Phys. Rev. 100, 675 (1955).

14. P. G. de Gennes, Phys. Rev. 118, 141 (1960).

15. K. Kubo and N. Ohata, J. Phys. Soc. Jpn. 33, 21 (1972); K. Kubo and N. Ohata, J. Phys. Soc. Jpn. 921, 21 (1972).

16. M. N. Baibich and J. M. Broto, A. Fert, F. Nguyen van Dan, F. Petroff, P. Eitenne, C. Creuzet, A. Friederich and J. Chazelas, Phys. Rev. Lett. 61, 2472 (1988).

17. J. Q. Xiao, J. S. Jiang and C. L. Chein, Phys. Rev. Lett. 68, 3749 (1992).

18. N. B. Brandt and V. V. Moschalkov, Adv. Phys. 33, 193 (1984).

19. R. M. Kusters, J. Singleton, D. A. Keen, R. McGreevy and W. Hayes, Phys. Rev. B55, 362 (1989).

20. R. M. von Helmolt, J. Wecker, B. Holzapfel, L. Schultz and K. Samwer, Phys. Rev. Lett. 71, 2331 (1993).

21. K. Chahara, T. Ohno, M. Kasai and Y. Kozomo, Appl. Phys. Lett. 63, 1990 (1993).

22. S. Jin, M. O' Bryan, T. H. Tiefel, M. McKormak and W. W. Rhodes, Appl. Phys. Lett. 66, 382 (1995).

23. R. Mahendiran, R. Mahesh, A. K. Raychaudhuri, C. N. R. Rao, J. Phys. D, Appl. Phys. 28, 1743 (1995).

24. R. Mahendiran, R. Mahesh, N. Rangavittal, S. K. Tewari, A. K. Raychaudhuri, T. V. Ramakrishnan and C. N. R. Rao, Phys. Rev. B53, 3348 (1996).

25. R. Mahesh, K. R. Kannan and C. N. R. Rao, J. Solid State Chem. 114, 294 (1995).

26. A. Arulraj, R. Mahesh, G. N. Subbanna, R. Mahendiran, A. K. Raychaudhuri and C. N. R. Rao, J. Solid State Chem. 127, 87 (1996).

27. J. Topfer and J. B. Goodenough, Chem. Mater. 9, 1467 (1997).

28. J. A. M. van Roosmalen, E. H. P. Cordfunke, R. B. Helmholdt and H. W. Zandbergen, J. Solid State Chem. 110, 109 (1994).

29. H. Y. Hwang, S.-W. Cheong, P. G. Radaelli, M. Marezio and B. Batlogg, Phys. Rev. Lett. 75, 914 (1995).

30. (a) B. Raveau, A. Maignan and V. Caignaert. J. Solid State Chem. 117, 424 (1995).

(b) V. Caignaert, S. Maignan and B. Raveau. Solid State Commun. 95, 357 (1995).

31. R. Mahesh, R. Mahendiran, A. K. Raychaudhuri and C. N. R. Rao, J. Solid State Chem. 120, 204 (1995).

32. J. Fontcuberta, B. Martinez, A. Seffar, S. Pinol, J. L. Garcia-Munoz and X. Obradors, Phys. Rev. Lett. 76, 1122 (1996).

33. J. L. Garcia-Munoz, J. Fontcuberta, M. Suaaidi and X. Obradors, J. Phys: Condens. Matter 8, L787 (1996).

34. V. Lankin, J. Fontcuberta, J. L. Garcia-Munoz and X. Obradors, Phys. Rev. B56, R10009 (1997).

35. R. Mahendiran, R. Mahesh, A. K. Raychaudhuri and C. N. R. Rao, Phys. Rev. B53, 12160 (1996).

36. Y. Moritomo, A. Asamitsu and Y. Tokura, Phys. Rev. B51, 16491 (1995).

37. (a) J. J. Neumeier, M. F. Hundley, J. D. Thompson and R. H. Heffner, Phys. Rev. B52, R7006 (1995); (b) H. Y. Hwang, T. T. M. Plastra, S.-W. Cheong and B. Batlogg, Phys. Rev. B52, 15046 (1995).

38. N.F.Mott, *Metal Insulator Transitions*, Taylor and Francis, London, (1990).

39. A. J. Millis, P. B. Littlewood and B. I. Shraiman, Phys. Rev. Lett 74, 5144 (1995).

40. (a) A. J. Millis, P. B. Littlewood and B. I. Shraiman, Phys. Rev. B54, 5389 (1996).

    (b) A. J. Millis, P. B. Littlewood and B. I. Shraiman, Phys. Rev. B54, 5405 (1996).

41. (a) H. Roder, J. Zang and A. R. Bishop, Phys. Rev. Lett. 76, 1356 (1996). (b) L.

    Sheng, D. Y. Xing, D. N. Sheng and C. S. Ting, Phys. Rev. Lett. 79, 1710 (1997).

42. G. Zhao, K. Conder, H. Keller and K. A. Muller, Nature 381, 676 (1996).

43. A. Shengelaya, G. Zhao, H. Keller and K. A. Muller, Phys. Rev. Lett. 77, 5296

    (1996).

44. G. Zhao, M. B. Hunt, H. Keller and K. A. Muller, Phys. Rev. Lett. 78, 955 (1997).

45. J. P. Frank, I. Isaac, W. Chen, J. Chrzanowski and J. C. Irwin, Phys. Rev. B58,

    5189 (1998).

46. N. A. Babushkina, L. M. Belova, O. Yu. Gorbenko, A. R. Kaul, A. A. Bosak, V. I.

    Ozhogin and K. I. Kugel, Nature 391, 159 (1998).

47. G. Zhao, K. Conder, H. Keller and K. A. Muller, Phys. Rev. B60, 11914 (1999).

48. S. J. L. Billinge, R. G. Difrancesco, G. H. Kurei, J. J. Neumeier and J. D.

    Thompson, Phys. Rev. Lett. 77, 715 (1996).

49. (a) D. Louca, T. Egami, E. L. Brousha, H. Roder and A. R. Bishop, Phys. Rev. B56,

    R8475 (1997). (b) D. Louca and T. Egami, J. Appl. Phys. 81, 5484 (1997).

50. D. Louca, T. Egami, Phys. Rev. B59, 6193 (1999)

51. J. M. de Teresa, M. R. Ibarra, J. Blasco, J. Garcia, C. Marquina, P.A. Algarabel, Z.

    Arnold, K. Kamenev, C. Ritter and R. von Helmolt, Phys. Rev. B 54, 1187 (1996).

52. J. M. de Teresa, M. R. Ibarra, P.A. Algarabel, C. Ritter, C. Marquina, J. Blasco, J.

    Garcia, A. del Moral and Z. Arnold, Nature 386, 256 (1997).

53. P. Dai, J. Zhang, H.A. Mook, A.-H.Liou, P.A. Dowben and E.W. Plummer, Phys. Rev. B 54 R3694 (1996).

54. D. Louca, T. egami, W. Dmowski and J. F. Mitchell, Phys. Rev. B 64, 180403 (2001).

55. G. Subias, J. Garcia, J. Blasco and M.G. Proietti, Phys. Rev. B 57, 748 (1998).

56. C. H. Booth, F. Bridges, G. H. Kwei, J. M. Lawrence, A.L. Cornelius and J. J. Neumeier, Phys. Rev. Lett. 80, 853 (1998).

57. M. Jaime, M. B. Salamon, M. Rubinstein, R. E. Treece, J. S. Horwitz and D. B. Chrisey, Phys. Rev. B 54, 11914 (1996).

58. M. Jaime, P. Lin, S. H. Chun, M. B. Salamon, P. Dorsey and M. Rubinstein, Phys. Rev. B 60 1028 (1999).

59. J.-H. Park, C.T. Chen, S.-W. Cheong, W. Bao, G. Meigs, V. Chakarian and Y. U. Idzerda, Phys. Rev. Lett. 76, 4215 (1996).

60. M. Quijada, J. Cerne, J. R. Simpson, H. D. Drew, K. H. Ahn, A. J. Millis, R. Shreekala, R. Ramesh, M. Rajeshwari and T. Venkatesan, Phys. Rev. B 58, 16093 (1998).

61. S. Shimomura, N. Wakabayashi, H. Kuwahara and Y. Tokura, Phys. Rev. Lett. 83, 4389 (1999).

62. M. Jaime, H. T. Hardner, M. B. Salamon, M. Rubistein, P. Dorsey and D. Emin, Phys. Rev. Lett. 78, 951 (1997).

63. (a) A. Urushibara, Y. Moritomo, T. Arima, A. Asamitsu, G. Kido and Y. Tokura, Phys. Rev. B51, 14103 (1995). (b) J. F. Mitchell, D. N. Argyriou, C. D. Potter, D. G. Hinks, J. D. Jorgensen and S. D. Bader, Phys. Rev. B54, 6172 (1998).

64. T. Koide, H. Miyauchi, J. Okamoto, T. Shidara, T. Sekine, T. Saitoh, A. Fujimori, H. Fukutani, M. Takano and Y. Takeda, Phys. Rev. Lett. 87, 246404 (2001).

65. L. M. Rodriguez-Martinez and J. P. Attfield, Phys. Rev. B54, R15622 (1996).

66. F. Damay, C. Martin, A. Maignan and B. Raveau, J. Appl. Phys. 82, 6181 (1997).

67. L. M. Rodriguez-Martinez and J. P. Attfield, Phys. Rev. B58, 2426 (1998).

68. J. P. Attfield, Chem. Mater. 10, 3239 (1998).

69. L. M. Rodriquez-Martinez, H. Ehrenberg and J. P. Attfield, J. Solid State Chem. 148, 20 (1999).

70. L. M. Rodriquez-Martinez and J. P. Attfield, Phys. Rev. B63, 024424 (2001).

71. R.A. Mohan Ram, P. Ganguly and C. N. R. Rao, J. Solid State Chem. 70, 82 (1987).

72. (a)Y. Moritomo, A. Asamitsu, H. Kuwahara and Y. Tokura, Nature 380, 141 (1996). (b) R. Mahesh, R. Mahendiran, A. K. Raychaudhuri and C. N. R. Rao, J. Solid State Chem. 122, 448 (1996).

73. P.D. Battle, S.J. Blundell, M.A. Green, W. Hayes, M. Honold, A.K. Klehe, N.S. Laskey, J.E. Millburn, L. Murphy, M.J. Rosseinsky, N.A. Samarin, J. Singleton, N.A. Sluchanko, S.P. Sullivan and J.F. Vente, J. Phys.: Condens. Matter, 8, L427 (1996).

74. T. Kimura, Y. Tomioka, H. Kuwahara, A. Asamitsu, M. Tamura and Y. Tokura, Science 76, 1122 (1996).

75. H. Asano, J. Hayakawa and M. Matsui, Appl. Phys. Lett. 68, 3638 (1996).

76. M. A. Subramanian, B. H. Toby, A. P. Ramirez, W. J. Marshall, A. W. Sleight and G. H. Kwei, Science 273, 81 (1996).

77. A. P. Ramirez and M. A. Subramanian, Science 277, 546 (1997).

78. D-K. Seo, M-H. Whangbo and M. A. Subramanian, Solid State Commun. 98, 163 (1997).

79. K. J. Kobayashi, T. Kimura, H. Sawada, K. Terakura and Y. Tokura, Nature 395, 677 (1998).

80. H. Kato, T. Okuda, Y. Okimoto, Y. Tomika, K.Oikawa, T. Kamiyama and Y. Tokura, Phys. Rev. B65, 144404 (2002).

81. A. P. Ramirez, R. J. Cava and J. Krajewski, Nature 387, 268 (1997).

82. P. Vaqueiro, A. V. Powell, A. I. Coldea, C. A. Steer, J. M. Marshall. S. J. Blundell, J. Singleton and T. Ohtani, Phys. Rev. B64, 132402 (2001).

83. G. Briceno, H. Chang, X. Sun, P. G. Schultz and X-D. Xiang, Science 270, 273 (1995).

84. E. J. W. Verwey, Nature 144, 327 (1939).

85. (a) M. L. Rudee, J. D. Smith and D. T. Margulies, Phys. Rev. B59, R11633 (1999).
    (b) M. L. Rudee, J. D. Smith and D. T. Margulies, Microscopy Microanal. 6, 400 (2000).

86. J. Garcia, G. Subias, M. G. Proietti, J. Blasco, H. Renevier, J. L. Hodeau and Y. Joly, Phys. Rev. B63, 054110 (2001).

87. (a)M. Takano and Y. Takeda Bull. Inst. Chem. Res. 61, 406 (1983). (b) P. D. Battle, T. C. Gibb and P. J. Lightfoot, J. Solid State Chem. 84, 271 (1990).

88. (a) J. M. Tranquada, B. J. Sternleib, J. D. Axe, Y. Nakamura and S. Uchida, Nature 375, 561 (1995).(b) S. A. Kivelson, E. Fradkin and V. J. Emery, Nature 393, 550 (1998).

89. J. Q. Li, Y. Matsui, S. K. Park and Y. Tokura, Phys. Rev. Lett. 79, 297 (1997).

90. (a) J. M. Tranquada, J. E. Lorenzo, D. J. Buttrey and V. Sachan, Phys. Rev. B52, 3581 (1995). (b) J. M. Tranquada, J. E. Lorenzo, D. J. Buttrey and V. Sachan, Phys. Rev. B54, 12318 (1996).

91. J.H. Jung, D.-W.Kim, T. W. Noh, H.C. Kim, H.-C. Ri, S.J. Levett, M.R. Lees, D. Mck Paul and G. Balakrishnan, Phys. Rev. B64, 165106 (2001).

92. (a) J. Rodriguez-Carvajal, G. Rouse, C. Masquelier and M. Hervieu, Phys. Rev. Lett. 81, 4660 (1998). (b) A. S. Willis, N. P. Raju and J. E. Greedan, Chem. Mater. 11, 1510 (1999).

93. I. Tomeno, Y. Kasuya and Y. Tsunoda, Phys. Rev. B64, 094422 (2001).

94. Z. Jirak, S. Krupicka, Z. Simsa, M. Dlouka and S. Vratislav, J. Magn. Magn. Mater. 53, 153 (1985).

95. P. Schiffer, A. P. Ramirez, W. Bao and S.-W. Cheong, Phys. Rev. Lett .75, 3336 (1995).

96. H. Kuwahara, Y. Tomioka, A. Asamitsu, Y. Moritomo and Y. Tokura, Science 270, 961 (1995).

97. Y. Tokura, Y. Tomioka, H. Kuwahara, A. Asamitsu, Y. Moritomo and M. Kasai, J. Appl. Phys. 79, 5288 (1996). (b) R. Kajimoto, H. Yoshizawa, H. Kawano, H. Kuwahara, Y. Tokura, K. Ohoyama and M. Ohashi, Phys. Rev. B60, 9506 (1999).

98. C. Martin, A. Maignan, M. Hervieu and B. Raveau, Phys. Rev. B60, 9506 (1999).

99. C. N. R. Rao, J. Phys. Chem. B104, 5877 (2000).

100. S. Uhlenbruck, R. Teipen, R. Klingeler, B. Buchner, O. Friedt, M. Hucker, H. Kierspel, T. Niemoller, L. Pinsard, A. Revcolevschi and R. Gross, Phys. Rev. Lett. 82, 185 (1999).

101. Y. Endoh, K. Hirota, S. Ishihara, S. Okamoto, Y. Murakami, A. Nishizawa, T. Fukuda, H. Kimura, H. Nojiri, K. Kaneko and S. Maekawa, Phys. Rev. Lett. 82, 4328 (1999).

102. K. Liu, X. W. Wu, J. H. Ahn, T. Shuchek and C. L. Chien, Phys. Rev. B54, 3007 (1996).

103. M. R. Lees, J. Barratt, G. Balakrishnan, D. MckPaul and C. D. Dewhurst, J. Phys: Condens. Matter 8, 2967 (1996).

104. H. Kawano, R. Kajimoto, H. Yoshizawa, Y. Tomioka, H. Kuwahara and Y. Tokura, Phys. Rev. Lett. 78, 4253 (1997).

105. C. N. R. Rao, A. Arulraj, P. N. Santhosh and A. K. Cheetham, Chem. Mater. 10, 2714 (1998).

106.   A. Arulraj, P. N. Santhosh, R. S. Gopalan, A. Guha, A. K. Raychaudhuri, N. Kumar and C. N. R. Rao, J. Phys: Condens. Matter. 10, 8497 (1998).

107.   P. M. Woodward, T. Vogt, D. E. Cox, A. Arulraj, C. N. R. Rao, P. Karen and A. K. Cheetham, Chem. Mater. 10, 3652 (1998).

108.   M. V. Zimmermann, C. S. Nelson, Y.-J. Kim, J. P. Hill, D. Gibbs, H. Nakao, Y. Wakabayashi, Y. Murakashi, Y. Tokura, Y. Tomioka, T. Arima, C.-C. Kao, D. Casa, C. Venkatraman and Th. Gog, Phys. Rev. B64, 064411 (2001).

109.   P. G. Radaelli, D. E. Cox, M. Marezio and S.-W. Cheong, Phys. Rev. B55, 3015 (1997).

110.   (a) N. Kumar and C. N. R. Rao J. Solid. State. Chem. 129, 363 (1997). (b) C. N. R. Rao, A. K. Cheetham and R. Mahesh, Chem. Mater. 8, 2421 (1996).

111.   A. Arulraj, R. Gundakaram, A. Biswas, N. Gayathri, A. K. Raychaudhuri and C. N. R. Rao, J. Phys: Condens. Matter 10, 4447 (1998).

112.   T. Terai, T. Sasaki, T. Kakeshita, T. Fukuda, T. Saburi, H. Kitagawa, K. Kindo and M. Honda, Phys. Rev. B61, 3488 (2000).

113.   (a) Y. Yoshizawa, H. Kawano, Y. Tomioka and Y. Tokura, Phys. Rev. B52, R13145 (1995); (b) Y. Tomioka, A. Asamitsu, H. Kuwahara, Y. Moritomo and Y. Tokura, Phys. Rev. B53, R1689 (1996).(c) M. Roy, J. F. Mitchell, A. P. Ramirez and P. Sciffer, Phys. Rev. B62, 13876 (2000).

114.   (a) M. Tokunaga, N. Miura, Y. Tomioka and Y. Tokura, Phys. Rev. B57, 5259 (1998). (b) M. Tokunaga, N. Miura, Y. Tomioka and Y. Tokura, Phys. Rev. B60, 6219 (1999).

115.   M. Respand, A. Llobet, C. Frontesa, C. Ritter, J. M. Broto, H. Rakoto, M. Goiran and J. L. Gracia-Munoz, Phys. Rev. B61, 9014 (2000).

116.   Y. Okimoto, Y. Tomioka, Y. Onose, Y. Otsuka and Y. Tokura, Phys. Rev. B57, 9377 (1998).

117.   V. N. Smolyaninova, A. Biswas, X. Zhang, K. H. Kim, Bog-Gi Kim, S.-W. Cheong and R. L. Greene, Phys. Rev. B62, R6093 (2000).

118.   J. H. Jung, H. J. Lee, T. W. Noh, E. J. Choi, Y. Moritomo, Y. J. Wang and X. Wei, Phys. Rev. B62, 481 (2000).

119.   R. Mahendiran, M. R. Ibarra, A. Maignan, F. Millange, A. Arulraj, R. Mahesh, B. Raveau and C. N. R. Rao, Phys. Rev. Lett. 82, 2191 (1999).

120.   H. Yoshizawa, R. Lajimoto, H. Kawano, Y. Tomioka and Y. Tokura, Phys. Rev. B55, 2729 (1997).

121.   (a) Y. Moritomo, H. Kuwahara, Y. Tomioka and Y. Tokura, Phys. Rev. B55, 7549 (1997). (b) C. N. R. Rao, P. N. Santhosh, R. S. Singh and A. Arulraj, J. Solid State Chem. 135, 169 (1998).

122.   Y. Tokura, H. Kuwahara, Y. Moritomo, Y. Tomioka and A. Asamitsu, Phys. Rev. Lett. 76, 3184 (1996).

123.   H. Kuwahara, Y. Moritomo, Y. Tomioka, A. Asamitsu, M. Kasai, R. Kumar, Y. Tokura, Phys. Rev. B56, 9386 (1997).

124.   S. Kuriki, Y. Moritomo, A. Machida, E. Nishibori, M. Takata, M. Sakata, Y. Ohishi, O. Shimomura and A. Nakamura, Phys. Rev. B65, 113105 (2002).

125. V. Kiryukhin, D. Casa, J. P. Hill, B. Keimer, A. Vigliante, Y. Tomioka and Y. Tokura, Nature 386, 813 (1997).

126. A. Asamitsu, Y. Tomioka, H. Kuwahara and Y. Tokura, Nature 388, 50 (1997).

127. K. Miyano, T. Tanaka, Y. Tomioka and Y. Tokura, Phys. Rev. Lett. 78, 4257 (1997).

128. (a) M. Fiebig, K. Miyano, Y. Tomioka and Y. Tokura, Science 280, 1925 (1998). (b) T. Tanogai, T. Satoh, K. Miyano, Y. Tomioka and Y. Tokura, Phys. Rev. B62, 13903 (2000).

129. M. Hervieu, A. Barnabe, C. Martin, A. Maignan and B. Raveau, Phys. Rev. B60, R726 (1999).

130. C. N. R. Rao, A. R. Raju, V. Ponnambalam, S. Parashar and N. Kumar, Phys. Rev. B61, 594 (2000).

131. G. Zhao, K. Ghosh and R. L. Greene, J. Phys: Condens. Matter 10, L737 (1998).

132. N. A. Babushkina, L. M. Belova, V. I. Ozhogin, O. Yu. Gorbenko, A. R. Kaul, A. A. Bosak, D. I. Khomskii and K. I. Kugel, J. Appl. Phys. 83, 7369 (1998).

133. B. Garcia Landa, M. R. Ibarra, J. M. de Teresa, G. Zhao, K. Couder and H. Keller, Solid State Commun. 105, 567 (1998).

134. R. Mahesh and M. Itoh, J. Solid State Chem. 144, 232 (1999).

135. U. Yu, Yu. V. Skrypnyk and B. J. Min, Phys. Rev. B61, 8936 (2000).

136. C. H. Chen and S. -W. Cheong, Phys. Rev. Lett. 76, 4042 (1996).

137. C. H. Chen and S.-W. Cheong, Phys. Rev. Lett. 81, 3972 (1998).

138. (a) A. P. Ramirez, P. Schiffer, S. -W. Cheong, C. H. Chen, W. Bao, T. T. M. Palstra, P. L. Gammel, D. J. Bishop and B. Zegarski, Phys. Rev. Lett. 76, 3188 (1996). (b) S. Mori, C. H. Chen and S.-W. Cheong, Nature 392, 473 (1998). (c) M. T. Fernandez-Diaz, J. L. Martinez, J. M. Alonso and E. Herrero, Phys. Rev. B59, 1277 (1999).

139. C.H. Chen, S.-W. Cheong and H.Y. Hwang, J. Appl. Phys. 81, 4326 (1997).

140. P. G. Radaelli, D. E. Cox, L. Capogna, S.-W. Cheong and M. Marezio, Phys. Rev. B59, 14440 (1999).

141. R. Wang, J. Gui, Y. Zhu and A. R. Moodenbaugh, Phys. Rev. B61, 11946 (2000).

142. P. Calvani, G. de. Marzi, P. Dore, S. Liysi, P. Maselli, F. D'. Amore, S. Galiardi and S.-W. Cheong, Phys. Rev. Lett. 81, 4504 (1998).

143. (a) K. H. Kim, M. Uehara and S.-W. Cheong, Phys. Rev. B62, R11945, (2000). (b) S. Naler, M. Rubhausen, S. Yoon, S. L. Cooper, K. H. Kim and S.-W. Cheong, Phys. Rev. B65, 092401 (2002).

144. A. Biswas, A. K. Raychaudhuri, R. Mahendiran, A. Guha, R. Mahesh and C. N. R. Rao, J. Phys: Condens. Matter 9, L355 (1997).

145. A. Biswas, A. Arulraj, A. K. Raychaudhuri and C. N. R. Rao, J. Phys: Condens. Matter 12, L101 (2000).

146. A. Sekiyama, S. Suga, Fujikawa, S. Imada, T. Iwasaki, K. Matsuda, T. Matsushita, K. V. Kaznacheyev, A. Fujimori, H. Kuwahara and Y. Tokura, Phys. Rev. B59, 15528 (1999).

147.   P. M. Woodward, D. E. Cox, T. Vogt, C. N. R. Rao and A. K. Cheetham, Chem. Mater. 11, 3528 (1999).

148.   S. Zvyagin, H. Schwenk, B. Luthi, K. V. Kamenev, G. Balakrishnan, D. McK. Paul, V. I. Kamenev and Yu. G. Pashkevich, Phys. Rev. B62, R6104 (2000).

149.   V. V. Krishnamurthy, I .Watanabe, K. Nagamine, H. Kuwahara and Y. Tokura, Phys. Rev. B61, 4060 (2000).

150.   J. Lopez, P. N. Lisboa-Filho, W. A. C. Passos, W. A. Ortiz, F. M. Araujo-Moreira, O. F. de Lima, D. Schaniel and K. Ghosh, Phys. Rev. B63, 224422 (2001).

151.   A. K. Raychaudhuri, A. Guha, J. Das, R. Rawat and C. N. R. Rao, Phys. Rev. B64, 165111 (2001).

152.   V. Dediu, C. Ferdeghini, F. C. Matacotta, P. Nozar and G. Ruani, Phys. Rev. Lett. 84, 4489 (2000).

153.   T. Vogt, A. K. Cheetham, R. Mahendiran, A. K. Raychaudhuri, R. Mahesh and C. N. R. Rao, Phys. Rev. B54, 15303 (1996).

154.   P. Murugavel, C. Narayana, A. K. Sood, S. Parashar, A. R. Raju and C. N. R. Rao, Europhys. Lett. 52, 461 (2000).

155.   J. P. Joshi, R. Gupta, A. K. Sood, S. V. Bhat, A. R. Raju and C. N. R. Rao, Phys. Rev. B65, 024410 (2002).

156.   W. Bao, J. D. Axe, C. H. Chen and S.-W. Cheong, Phys. Rev. Lett. 78, 543 (1997).

157.   H. Chiba, M. Kikuchi, K. Kusaba, Y. Muraoka and Y. Syono, Solid State Commun. 99, 499 (1996).

158. Y. Murakami, D. Shindo, H. Chiba, M. Kikuchi and Y. Syono, Phys. Rev. B55, 1, (1997).

159. Y. Su, C.-H. Du, P. D. Hatton, S. P. Collins and S.-W. Cheong, Phys. Rev. B59, 11687 (1999).

160. Y. Murakami, D. Shindo, H. Chiba, M. Kikuchi and Y. Syono, Phys. Rev. B59, 6395 (1999).

161. M. Rubhausen, S. Yoon, S. L. Cooper, K. H. Kim and S.-W. Cheong, Phys. Rev. B62, R4782 (2000).

162. H. Chiba, T. Atou and Y. Syono, J. Solid State Chem. 132 (1997)

163. (a) J. L. Garcia-Munoz, C. Frontera, M. A. G. Aranda, A. Llobet and C. Ritter, Phys. Rev. B63, 064415 (2001). (b) C. Frontera, J. L. Gracia-Munoz, M. A. G. Aranda, C. Ritter, A. Llobet, M. Respand and J. Vanacken, Phys. Rev. B64, 054401 (2001).

164. T. Ishikawa, K. Ookura and Y. Tokura Phys. Rev. B59, 8367 (1999).

165. M. Tokunaga, N. Miura, Y. Moritomo and Y. Tokura, Phys. Rev. B59, 11151 (1999).

166. C. Hess, B. Buchner, M. Hucker, R. Gross and S.-W. Cheong, Phys. Rev. B59, R10397 (1999).

167. B. Garcia-Landa, C. Marquina, M. R. Ibbara, G. Balakrishnan, M. R. Lees and D. Mck Paul, Phys. Rev. Lett. 84, 995 (2000).

168. T. Ogasawara, T. Kimura, T. Ishikawa, M. Kuwata-Gonokami and Y. Tokura, Phys. Rev. B63, 113105 (2001).

169. T. Nagai, T. Kimura, A. Yamazaki, T. Asaka, K. Kimoto, Y. Tokura and Y. Matsui, Phys. Rev. B65, 060405 (2002).

170. P. D. Battle, M. A. Green, N. S. Laskey, J. E. Milburn, J. E. Murphy, M. J. Rosseninsky, S. P. Sullivan and J. F. Vente, Chem. Mater. 9, 552 (1997).

171. J. Q. Li, Y. Matsui, T. Kimura and Y. Tokura, Phys. Rev. B57, 3205 (1998).

172. D. N. Argyriou, H. N. Bordallo, B. J. Campbell, A. K. Cheetham, D. E. Cox, J. S. Gardner, K. Hanif, A. dos Santos and G. F. Strouse, Phys. Rev. B61, 15269 (2000).

173. (a) I. O. Troyanchuk, N. V. Kasper, D. O. Khalyavin, H. Szymczak, R. Szymczak and M. Baran, Phys. Rev. B58, 2418 (1998). (b) I. O. Troyanchuk, N. V. Kasper, D. D. Khalyavin, H. Szymczak, R. Szymczak and M. Baran, Phys. Rev. Lett 80, 3380 (1998).

174. T. Vogt, P. M. Woodward, P. Karen, B. A. Hunter, P. Henning and A. R. Moodenbough, Phys. Rev. Lett. 84, 2969 (2000).

175. E. Suard, F. Fauth, V. Caignaert, I. Mirebeau and G. Baldinozzi, Phys. Rev. B61, R11871 (2000).

176. Y. Yamada, K. Kitsuda, S. Nohdo and N. Ikeda, Phys. Rev. B62, 12167 (2000).

177. P. Karen, P. M. Woodward, J. Linden, T. Vogt, A. Studer and P. Fischer, Phys. Rev. B64, 214405 (2001).

178. T. Goto, Y. Nemoto, A. Ochiai and T. Suzuki, Phys. Rev. B59, 269 (1999).

179. (a)T. Ohama, H. Yasuoka, M. Isobe and Y. Ueda, Phys. Rev. B59, 3299 (1999). (b) A. I. Smirnov, M. N. Popava, A. B. Sushkov, S. A. Golubchik, D. I. Khomskii,

M. V. Mostovoy, A. N. Vasilev, M. Isobe and Y. Ueda, Physica B284-288, 1653 (2000).

180. P. N. Rogers and R. N. Shelton, Solid State Commun 114, 607 (2000).

181. M. J. Konstantinovic, J. Dong, M. E. Ziaei, B. P. Clayman, J. C. Irwin, K. Yakushi, M. Isobe and Y. Ueda, Phys. Rev. B63, 121102 (2001).

182. S. Kramer and M. Mehring, Phys. Rev. Lett. 83, 396 (1999).

183. D. S. Chow, F. Zamborszky, B. Alavi, D. J. Tantillo, A. Baur, C. A. Merlic and S. E. Brown, Phys. Rev. Lett. 85, 1698 (2000).

184. B. Raveau, M. Hervieu, A. Maignan and C. Martin, J. Mater. Chem.11,29 (2001).

185. M. Uehara, S. Mori, C.H. Chen and S-W.Cheong, Nature 399, 560 (1999).

186. V. Kiryukhin, B.G. Kim, V. Podzorov, S-W. Cheong, T.Y. Koo, J. P. Hill, I. Moon and J. H. Jeong, Phys. Rev. B63, 024420 (2001).

187. A. M. Balagurov, V. Yu. Pomjakushin, D. V. Sheptyakov, V. L. Aksenov, P. Fischer, L. Keller, O.Yu. Gorbenko, A. R. Kaul and N. A. Babushkina, Phys. Rev. B64, 024420 (2001).

188. V. Podzorov, M. E. Gershenson, M. Uehara, S-W. Cheong, Phys. Rev. B64, 115113 (2001).

189. C. P. Adams, J. W. Lynn, Y. M. Mukovskii, A. A. Arsenov and D. A. Shulyatev, Phys. Rev. Lett. 85, 3954 (2000).

190. J. Zhang, P. Dai, J. A. Fernandez-Baca, E.W. Plummer, Y. Tomioka and Y.Tokura, Phys. Rev. Lett.86, 3823 (2001).

191.   J. M. Zuo and J.Tao, Phys. Rev. B63, 060407 (2001).

192.   J.J. Neumeier and J. L. Cohn, Phys. Rev. B61, 14319 (2000).

193.   Cz. Kapusta, P. C. Riedi, M. Sikora and M. R. Ibarra, Phys. Rev. Lett. 84, 4216
(2000).

194.   M. M. Savosta, P. Novak, M. Marysko, Z. Jirak, J. Hejtmanek, J. Englich, J.
Kohout, C. Martin and B.Raveau, Phys. Rev. B62, 9532 (2000).

195.   P. N. Santhosh, J. Goldberger, P. M. Woodward, T. Vogt, W. P. Lee, A. J.
Epstein, Phys. Rev. B62, 14928 (2000).

196.   A. Llobet, C. Frontera, J. L. García-Muñoz, C. Ritter and M. A. G. Aranda,
Chem. Mater. 12, 3648 (2000).

197.   J. Q. Li, C. Dong, L. H. Liu and Y. M. Ni, Phys. Rev. B64, 174413 (2001).

198.   D. N. Argyriou, H. N. Bordallo, B. J. Campbell, A. K. Cheetham, D. E. Cox, J.
S. Gardner, K. Hanif, A. dos Santos and G. F. Strouse, Phys. Rev. B61, 15269
(2000).

199.   D. Khomskii, Physica B280, 325 (2000).

200.   M. Yu. Kagan, K. I. Kugel, D. I. Khomskii and A. L. Rakhmanov, Physica
C364-365, 643 (2001).

201.   E. Dagotto and A. Moreo, J. Magn. Magn. Mater. 226-230, 763 (2001).

202.   P. Schlottmann, J. Appl. Phys. 87, 5022 (2000).

2. SCOPE OF THE PRESENT INVESTIGATIONS

This thesis presents the results of investigations of rare earth manganates and related systems. In particular the phenomenon of charge ordering in rare earth manganates and the factors that influence charge ordering form the major part of these investigations. The various aspects studied involve effects of cation disorder, B-site (Mn site) doping by other ions and effect of magnetic fields. Mössbauer spectroscopy also has been used to study the charge ordered rare earth manganates. The re-entrant ferromagnetic transition in rare earth manganates with relatively small size A-site cations has also been investigated. Charge ordering and related aspects of electron doped manganates has been investigated in some detail. The effect of cation size and disorder on the properties of rare earth cobaltates has been discussed in the last section.

2.1 Effect of cation size disorder on charge ordering in rare-earth manganates, $Ln_{0.5}A_{0.5}MnO_3$ (Ln = rare-earth, A = alkaline earth)

Two of the important features of rare-earth manganates, $Ln_{1-x}A_xMnO_3$ (Ln = rare-earth, A = alkaline earth), are the ferromagnetic metallic and the charge-ordered insulating states exhibited by them [1,2]. The ferromagnetic Curie temperature, T_C, around which an insulator-metal transition occurs in the manganates has been shown to be sensitive to (a) the Mn^{3+}/Mn^{4+} (b) the average size of the A-site cation, $\langle r_A \rangle$ and (c) the mismatch in the sizes of the A-site cations. While the T_C and the insulator-metal transition temperature T_M increase with the

increase in the average size of the A-site cation $\langle r_A \rangle$, the value saturates at high $\langle r_A \rangle$

values probably because many of these manganates have A-site cations with a large

size mismatch [3]. In order to account for the effects due to the strain arising from

the size mismatch of the A-site cations on T_C or T_M, *Rodriguez-Martinez and*

Attfield [4,5] employed the variance in the distribution of $\langle r_A \rangle$. The variance σ^2 is

defined by

$$\sigma^2 = \sum x_i r_i^2 - \langle r_A \rangle^2 \qquad \ldots\ldots\ldots\ldots (1)$$

where x_i is the fractional occupancy of A site ions and r_i is the corresponding ionic

radii. *Rodriguez-Martinez and Attfield* [4,5] as well as *Damay et al.* [6] have studied

several series of manganates of the type $Ln_{1-x}A_xMnO_3$ for fixed values of $\langle r_A \rangle$ and

have found a linear relation between T_C and σ^2, with the T_C decreasing with the

increase in σ^2. Since the charge-ordering behavior of the rare-earth manganates is

very sensitive to $\langle r_A \rangle$, [1,2,7], we considered it important to quantify how the

charge-ordering transition temperature, T_{CO}, depends on the size mismatch between

the A-site cations. For this purpose, we have studied charge-ordering in several

manganates of the type $Ln_{0.5}A_{0.5}MnO_3$. In order to understand the dependence of

T_{CO} on σ^2, we have determined T_{CO} in two series of manganates with fixed $\langle r_A \rangle$

values of 1.24Å and 1.17Å, albeit in a few members of each series, because of the

difficulty in realizing compositions which permit reliable measurements.

2.2 Effect of Mn site doping in rare-earth manganates, $Ln_{0.5}A_{0.5}MnO_3$ (Ln = rare-earth, A = alkaline earth)

Rare earth manganates of the type $Ln_{0.5}A_{0.5}MnO_3$ (Ln = rare earth, A = Ca, Sr) undergo charge-ordering wherein there is a real space ordering of differently charged cations on specific lattice sites. In the charge-ordered (CO) state, the hopping of electrons is unfavorable and the material is an insulator. The charge-ordered state in these compounds is very sensitive to the average ionic radius of the A-site cations, $\langle r_A \rangle$ [8, 9]. In $Nd_{0.5}Sr_{0.5}MnO_3$ with $\langle r_A \rangle$ = 1.24Å, the ground state which is a ferromagnetic metal (FMM) ($T_C \sim 250$ K) transforms to a charge-ordered (CO) state on cooling to ~ 150 K [10]. When $\langle r_A \rangle$ is small, as in $Y_{0.5}Ca_{0.5}MnO_3$ ($\langle r_A \rangle$ =1.13 Å), the ground state is a charge-ordered insulator even at room temperature and the material does not show ferromagnetism at any temperature [11]. Furthermore the charge-ordered states of $Nd_{0.5}Sr_{0.5}MnO_3$ and $Y_{0.5}Ca_{0.5}MnO_3$ show completely different sensitivities to magnetic fields. Thus, the application of a magnetic field of 6T transforms the CO state in $Nd_{0.5}Sr_{0.5}MnO_3$ to a metallic state, but has no effect on the CO state of $Y_{0.5}Ca_{0.5}MnO_3$. The CO state in $Y_{0.5}Ca_{0.5}MnO_3$ is quite robust and even a field of 100 T cannot induce an insulator-metal transition in this compound [12]. Clearly there are two types of charge-ordered states in the manganates depending on the $\langle r_A \rangle$ regime [8]. Substitution of different ions in the A-site varies the internal pressure and markedly affects the CO and FMM states, an increase in $\langle r_A \rangle$ or internal pressure lowering the T_{CO} and increasing the ferromagnetic T_C [13].

We were interested in investigating whether it is possible to melt the charge-ordered states in the manganates by chemical means, by ion substitution in the B-

site and if so, whether the two types of CO states show differences. In this context, we notice the work of *Raveau et al.* [14] who reported that the antiferromagnetic insulator $Pr_{0.5}Ca_{0.5}MnO_3$ shows a insulator-metal (I-M) transition on the substitution of Mn by Cr and Co. *Damay et al.* [15] substituted $Pr_{0.6}Ca_{0.4}MnO_3$ by several ions on the B-site and found that the metallic state is induced when Mn is substituted by Fe^{3+}, Al^{3+}, Ga^{3+} and Mg^{2+}. *Barnabe et al.* [16], on the other hand, have reported that an I-M transition is induced in charge-ordered $Ln_{0.5}Ca_{0.5}MnO_3$, most effectively by Cr. *Maignan et al.* [17] report a similar disappearance of charge-ordering in $Ln_{0.5}Ca_{0.5}MnO_3$ substituted by Ni. Encouraged by these reports, we felt that it should be possible to systematically examine the two different types of CO states, in the different $\langle r_A \rangle$ regimes, by investigating the effect of appropriate ion substitutions in the B-site. For this purpose, we have investigated the effect of substitution of Mn by both transition and non-transition metal ions in $Ln_{0.5}A_{0.5}MnO_3$ compositions, with widely differing $\langle r_A \rangle$ values, on charge ordering and related properties. The manganates investigated are, $Y_{0.5}Ca_{0.5}MnO_3$ ($\langle r_A \rangle$ = 1.13 Å), $Nd_{0.5}Ca_{0.5}MnO_3$ ($\langle r_A \rangle$ = 1.17 Å) and $Nd_{0.5}Sr_{0.5}MnO_3$ ($\langle r_A \rangle$ = 1.24 Å). The various substituents are Al, Ga, Ti, Fe, Cr, Co, Ni, Ge, Zr and Ru.

2.3 Re-entrant ferromagnetic transitions in rare-earth manganates

One of the important factors that affect the properties of the manganates is the average radius of the A-site cations, $\langle r_A \rangle$ [1,2]. In the charge ordered manganates, the role of $\langle r_A \rangle$ is indeed profound in that those with very small $\langle r_A \rangle$ (say < 1.18Å)

93

have a robust charge-ordered antiferromagnetic state, which is not affected by magnetic fields or impurity doping at the B-site [2,3,8]. $Nd_{0.5}Ca_{0.5}MnO_3$ with a $\langle r_A \rangle$ of 1.17 Å exhibits a T_{CO} of 240 K followed by a transition to the CE type antiferromagnetic state on cooling to 150 K and the CO state can be melted on application of high magnetic fields or doping at the B-site [18]. $La_{0.5}Ca_{0.5}MnO_3$ ($\langle r_A \rangle = 1.198$ Å) has a T_C of 225 K and undergoes a transition to the antiferromagnetic CO state (CE type) at 135 K. This transition coincides with a change from incommensurate to nearly commensurate charge-ordering [19]. There is a two-phase narrow temperature regime where the ferromagnetic and CO phases coexist. Clearly, the $\langle r_A \rangle$ regime between 1.17 and 1.22 Å is a complex one with competing ferromagnetic and charge-ordering interactions. $Nd_{0.25}La_{0.25}Ca_{0.5}MnO_3$ with a $\langle r_A \rangle$ of 1.185 Å has been investigated in some detail [20]. This manganate shows an incipient charge-ordered state below ~ 200 K which becomes unstable on cooling to ~150 K, with the material undergoing a transition to a charge delocalized FM state. The transition has been considered to be a re-entrant transition since the CO insulating state reverts back to a FMM state. This is in a direction opposite to that normally found in the CMR manganates where a FMM state goes to a CO AFM state on cooling. It is noteworthy that the AFM correlations in this manganate are short-range. At the CO-FM transition, there is a sharp decrease in the electrical resistivity and an increase in the magnetization characteristic of a ferromagnetic ordering. It appears that two phases exist over a region of at least 50 K near the transition. The $(La_{1-z}Nd_z)_{1-x}Ca_xMnO_3$ system has

94

been studied by *Moritomo* [21] who finds that the ground state at a fixed x value changes the FMM state to a CO insulating state with increase in z. He reports an electronic phase separation which dominates in a wide x-z parameter regime around the FM-CO phase boundary. We considered it important to study the nature of the CO state and the re-entrant ferromagnetic state in the manganates in $\langle r_A \rangle$ regime 1.17-1.20 Å where the competition between the two interaction is prominent, giving rise to interesting magnetic and electrical properties. In particular, we wanted to examine the role of $\langle r_A \rangle$ as well as of the site disorder arising from size mismatch of the A-site cations, on the ferromagnetism and charge-ordering in these manganates. It is indeed well established that both ferromagnetic T_C and the T_{CO} are strongly affected by site disorder [4-6]. We were curious if the same kind of re-entrant ferromagnetic state is evident in the single crystals of manganates in this $\langle r_A \rangle$ regime. Hence, we tried growing single crystals of the type $Nd_{0.5-x}La_xCa_{0.5}MnO_3$ by the floating zone technique and were successful in growing good quality crystals of $Nd_{0.25}La_{0.25}Ca_{0.5}MnO_3$ and $Nd_{0.35}La_{0.15}Ca_{0.5}MnO_3$. We have also investigated polycrystalline samples of the two series of manganates, $Nd_{0.5-x}La_xCa_{0.5}MnO_3$ and $Pr_{0.5-x}La_xCa_{0.5}MnO_3$, with $\langle r_A \rangle$ values in the range 1.172-1.198Å. To understand the effect of size disorder, σ^2, we have also examined a series of manganates with a fixed $\langle r_A \rangle$ value of 1.185Å corresponding to $Nd_{0.25}La_{0.25}Ca_{0.5}MnO_3$. The study delineates the effects of $\langle r_A \rangle$ and σ^2 on the re-entrant ferromagnetic transition in the manganates with $\langle r_A \rangle$ values in the complex regime of competing CO and FM interactions.

2.4 ^{57}Fe Mössbauer spectroscopic studies of charge-ordered rare-earth manganates

^{57}Fe Mössbauer spectroscopy provides a microscopic probe to investigate magnetic structure, phase transitions and other properties of transition metal oxide systems. We would therefore expect Mössbauer spectroscopy to throw light on the charge ordered manganates. To carry out Mössbauer spectroscopic studies of rare earth manganates, we have doped two typical charge ordered systems, $Nd_{0.5}Sr_{0.5}MnO_3$ and $Nd_{0.5}Ca_{0.5}MnO_3$ with ^{57}Fe. After ensuring that the small doping does not change the structure or the phase transitions, we have carried out ^{57}Fe Mössbauer studies as a function of temperature from 300 to 4.2 K. The results obtained from these studies do indeed throw some light on the charge ordering phenomena and phase separation in these two systems.

2.5 A study of electron doped manganates, $Ca_{1-x}Ln_xMnO_3$ (x < 0.5)

Investigations of colossal magnetoresistance and related phenomena in the rare-earth manganates reported extensively in the last few years, by and large, pertain to solids of the composition $Ln_{1-x}A_xMnO_3$ (Ln = rare-earth, A = Ca, Sr) which involve hole-doping (x < 0.5). The hole-doped manganates exhibit charge-ordering particularly when x = 4/8 or 5/8 and the charge-ordering transition is highly sensitive to the average radius of the A-site cations, $\langle r_A \rangle$ [1,2]. Generally, the charge ordering transition temperature, T_{CO}, decreases with increase in $\langle r_A \rangle$ unlike

the ferromagnetic T_C which increases with $\langle r_A \rangle$. Furthermore, the strain arising from the size mismatch between A-site cations affects the T_C which generally decreases with the variance, σ^2, which is the measure of the mismatch between the A-site cations [4-6]. There has been some interest recently in studying the properties of electron-doped manganates of the type $Ca_{1-x}T_xMnO_3$ where T is a tri - or a tetra - valent cation. These studies [22,23] have shown that electron concentration determines the magneto-transport properties in these materials, besides the mismatch between the sizes of the A-site cations. A study of $Ca_{1-x}Bi_xMnO_3$ (x = 0.18) has shown the occurrence of charge-ordering accompanied by a structural transition [24]. We considered it important to investigate charge-ordering in the electron-doped systems to examine the similarities, if any, with the hole-doped manganates. For this purpose, we have investigated manganates of the type, $Ca_{1-x}Ln_xMnO_3$ (Ln = La, Pr, Nd, Gd or Y), in particular the composition corresponding to x = 0.36 where charge-ordering should be favored. Also, we have studied the effect of substitution of Cr, Ga and Ge at the Mn site in few of these electron-doped manganates. The effect of the size mismatch between the A-site cations on the properties, mainly the charge-ordering transition of these electron-doped manganates have also been investigated. For this purpose, we have carried out studies on two series of electron-doped manganates, $Ca_{0.04}Ln_{0.36}MnO_3$, with fixed $\langle r_A \rangle$ values of 1.174 and 1.18 Å.

2.6 Effect of cation size and disorder on the structure and properties of rare earth cobaltates, $Ln_{0.5}A_{0.5}CoO_3$ (Ln = Rare Earth, A = Sr, Ba)

Rare earth cobaltates of the formula $Ln_{0.5}Sr_{0.5}CoO_3$ (Ln = rare earth) are known as metallic ferromagnets and their electrical and magnetic properties have been described adequately in the literature [25-27]. The ferromagnetic Curie temperature, T_C, in these materials decreases significantly with the decrease in the size of the rare earth ion. The magnetic and electrical properties of the barium-substituted cobaltates of the formula $Ln_{0.5}Ba_{0.5}CoO_3$ are different from those of the strontium analogues. Recent studies show that the barium-substituted cobaltates exhibit a insulator-metal transition when the radius of the rare earth ion is small [28,29]. Thus, $Gd_{0.5}Ba_{0.5}CoO_3$ is a charge-ordered insulator, although there are some differences in the published reports regarding its electrical properties [28,29]. Structures of the $Ln_{0.5}A_{0.5}CoO_3$ (A = Sr, Ba) compounds also vary with Ln and A, although there are conflicting structural assignments in the literature. Thus, $Ln_{0.5}Sr_{0.5}CoO_3$ have generally been considered to be cubic, although the possible orthorhombicity has been indicated recently [30]. In the corresponding Ba compounds, cubic, tetragonal and orthorhombic structures have been assigned depending on the Ln [28,29]. An examination of the electrical and magnetic properties of the various rare earth cobaltates, $Ln_{0.5}A_{0.5}CoO_3$ (A = alkaline earth), suggests that the properties are likely to be affected by both the average radius of the A-site cation and the cation disorder arising from size mismatch. In the manganates, the size variance has a marked effect on the ferromagnetic properties

of $Ln_{0.7}A_{0.3}MnO_3$, but appears to affect charge-ordering in $Ln_{0.5}A_{0.5}MnO_3$ only marginally [4-6]. We considered it worthwhile to study the structure-property relations in the cobaltates, $Ln_{0.5}A_{0.5}CoO_3$. Hence, we investigated the structures of several members of the $Ln_{0.5}A_{0.5}CoO_3$ family with A = Sr and Ba, based on Rietveld analysis of powder X-ray diffraction patterns. In order to understand the dependence of the ferromagnetic Curie temperature of $Ln_{0.5}A_{0.5}CoO_3$ on $\langle r_A \rangle$ as well as cation disorder, we have examined the magnetic and electrical properties of several of these materials. In particular, we have investigated the variation of the properties of the cobaltates with constant $\langle r_A \rangle$, but variable σ^2. Two series of rhombohedral cobaltates of the general formula $Ln_{0.5-x}Ln'_xA_{0.5-y}A'_yCoO_3$ with constant $\langle r_A \rangle$ values of ~ 1.357Å and 1.369Å were prepared in order to study the effect of the A-site cation size mismatch on the properties.

References

1. (a) A. P. Ramirez, J. Phys: Condens. Matter $\underline{9}$, 8171 (1997). (b) C. N. R. Rao and A. K. Cheetham, Adv. Mater. $\underline{9}$, 1009 (1997).

2. (a) C. N. R. Rao and B. Raveau (Eds.), *Colossal Magnetoresistance, Charge Ordering and Related Properties of Manganese oxides*, World Scientific (1998) Singapore. (b) C. N. R. Rao, J. Phys. Chem. $\underline{B104}$, 5877 (2000).

3. (a) R. Mahesh, R. Mahendiran, A. K. Raychaudhuri and C. N. R. Rao, J. Solid State Chem. $\underline{120}$, 204 (1995). (b)H. Y. Hwang, S.-W. Cheong, P. G. Radaelli, M. Marezio and B. Batlogg, Phys. Rev. Lett. $\underline{75}$, 914 (1995).

4. L. M. Rodriguez-Martinez and J. P. Attfield, Phys. Rev. $\underline{B54}$, R15622 (1996).

5. L. M. Rodriguez-Martinez and J. P. Attfield, Phys. Rev. $\underline{B58}$, 2426 (1998).

6. F. Damay, C. Martin, A. Maignan and B. Raveau, J. Appl. Phys. $\underline{82}$, 6181 (1997).

7. A. Arulraj, P. N. Santhosh, R. S. Gopalan, A. Guha, A. K. Raychaudhuri, N. Kumar and C. N. R. Rao, J. Phys. Condens. Matter. $\underline{10}$, 8497 (1998).

8. N. Kumar and C. N. R. Rao, J. Solid. State. Chem. $\underline{129}$, 363 (1997).

9. Y. Tokura, Y. Tomioka, H. Kuwahara, A. Asamitsu, Y. Moritomo and M. Kasai, J. Appl. Phys. $\underline{79}$, 5288 (1996).

10. H. Kuwahara, Y. Tomioka, A. Asamitsu, Y. Moritomo and Y. Tokura, Science $\underline{270}$, 961 (1995).

11. A. Arulraj, R. Gundakaram, A. Biswas, N. Gayathri, A. K. Raychaudhuri and C. N. R. Rao, J. Phys. Condens. Matter $\underline{10}$, 4447 (1998).

12. (a) M. Tokunaga, N. Miura, Y. Tomioka and Y. Tokura, Phys. Rev. B57, 5259

    (1998). (b) M. Tokunaga, N. Miura, Y. Tomioka and Y. Tokura, Phys. Rev. B60,

    6219 (1999).

13. (a) Y. Moritomo, H. Kuwahara, Y. Tomioka and Y. Tokura, Phys. Rev. B55, 7549

    (1997). (b) C. N. R. Rao, P. N. Santhosh, R. S. Singh and A. Arulraj, J. Solid State

    Chem. 135, 169 (1998).

14. B. Raveau, A. Maignan and C. Martin, J. Solid State Chem. 130, 162 (1997).

15. F. Damay, A. Maignan, C. Martin and B. Raveau, J. Appl. Phys. 82, 1485 (1997).

16. A. Barnabe, A. Maignan, M. Hervieu, F. Damay, C. Martin and B. Raveau, Appl.

    Phys. Lett. 71, 3907 (1997).

17. A. Maignan, F. Damay, C. Martin and B. Raveau, Mater. Res. Bull 32, 965 (1997).

18. P. Murugavel, C. Narayana, A. K. Sood, S. Parashar, A. R. Raju and C. N. R. Rao,

    Europhys. Lett. 52, 461 (2000).

19. (a) P. G. Radaelli, D. E. Cox, M. Marezio and S.-W. Cheong, Phys. Rev. B55, 3015

    (1997). (b) S. Mori, C. H. Chen and S.-W. Cheong, Phys. Rev. Lett. 81, 3972

    (1998).

20. A. Arulraj, A. Biswas, A. K. Raychaudhuri, C. N. R. Rao, P. M. Woodward, T.

    Vogt, D. E. Cox and A. K. Cheetham, Phys. Rev. B57, R8115 (1998).

21. Y. Moritomo, Phys. Rev. B60, 10374 (1999).

22. A. Maignan, C. Martin, F. Damay and B. Raveau, Chem. Mater. 10, 950 (1998).

23. A. Maignan, C. Martin, F. Damay, B. Raveau and J. Hejtmanck, Phys. Rev. B58,

    134 (1998).

24. W. Bao, J. D. Axe, C. H. Chen and S.-W. Cheong, Phys. Rev. Lett. 78, 543 (1997).

25. (a) G. H. Jonker and J. H. van Santen, Physica 19, 120 (1953). (b) P. M. Raccah and J. B. Goodenough, J. Appl. Phys. 39, 1209 (1968).

26. C. N. R. Rao, O. Prakash, D. Bahadur, P. Ganguly and S. Nagabhushana, J. Solid State Chem. 22, 353 (1977).

27. M. A. Senaris-Radriguez and J. B. Goodenough, J. Solid State Chem. 118, 323 (1995).

28. (a) I. O. Troyanchuk, N. V. Kasper, D. D. Khalyavin, H. Szymczak, R. Szymczak and M. Baran, Phys. Rev. B58, 2418 (1998). (b) I. O. Troyanchuk, N. V. Kasper, D. D. Khalyavin, H. Szymczak, R. Szymczak and M. Baran, Phys. Rev. Lett. 80, 3380 (1998).

29. Y. Moritomo, M. Takeo, X. J. Liu, T. Akimoto and A. Nakamura, Phys. Rev. B58, R13334 (1998).

30. H. W. Brinks, H. Fjellvag, A. Kjekshus and B. C. Hauback, J. Solid State Chem. 147, 464 (1999).

3. Experimental

3.1 Preparation of materials

(a) Polycrystalline materials

Manganates of the composition $Ln_{0.5-x}Ln'_xA_{0.5-y}A'_yMnO_3$ with $\langle r_A \rangle = 1.24$ and 1.17 Å as well as several manganates of the type $Ln_{0.5}A_{0.5}MnO_3$ with variable $\langle r_A \rangle$ were prepared by the ceramic route by heating stoichiometric quantities of the respective rare earth oxides, Mn_3O_4 and the carbonates of the respective alkaline earth elements. The final sintering temperature in the preparations was 1673- 1773 K.

The compositions, $Y_{0.5}Ca_{0.5}Mn_{1-x}M_xO_3$ (M = Al, Fe, Co, Ni and Cr), $Nd_{0.5}Ca_{0.5}Mn_{1-x}M_xO_3$ (M = Al, Ga, Ge, Fe, Co, Ni, Cr and Ru) and $Nd_{0.5}Sr_{0.5}Mn_{1-x}M_xO_3$ (M = Al, Ga, Ti, Ge, Zr, Fe, Co, Ni, Cr and Ru) with x in the range of 0.0 to 0.10 were prepared by the solid state reaction of the corresponding rare-earth oxide (from Indian Rare Earths, India), MnO_2 (from EMerck) and the oxides (Fluka grade) of the respective substituents. Mn_3O_4 was used as the Mn source to prepare all the substituted $Nd_{0.5}Sr_{0.5}MnO_3$ compositions. Mn_3O_4 was prepared by decomposing freshly prepared $MnCO_3$ at 1473 K for 12 h in air. The so prepared Mn_3O_4 was checked for phase purity before using it as the starting material. The oxides of the dopants used were Al_2O_3, Ga_2O_3, TiO_2, ZrO_2, GeO_2, Fe_2O_3, Co_3O_4, NiO, Cr_2O_3 and RuO_2. The mixtures were first heated at 1173 K for 12h in air followed by heating at 1273 K and 1473 K in air for 12h each with intermediate grindings. The final sintering temperature was in the range of 1673-1773 K depending on the compositions and the starting materials.

The electron doped samples, $Ca_{1-x}Ln_xMnO_3$ (Ln = La, Pr, Nd, Gd and Y) were prepared by the ceramic route by heating stoichiometric proportions of the respective rare-earth oxide, $CaCO_3$ and Mn_3O_4. Initial heating was done at 1173 K, 1273 K and 1473 K for 12h each with intermediate grindings. The final sintering was carried out at 1673 K. Cr_2O_3 was used to make the compositions, $Ca_{0.64}Ln_{0.36}Mn_{0.97}Cr_{0.03}O_3$ (Ln = La, Nd, Gd). Ga and Ge doped $Ca_{0.64}Pr_{0.36}MnO_3$ derivatives were prepared in the same manner by employing Ga_2O_3 and GeO_2. All the polycrystalline samples, $Ca_{0.64-x}Sr_xLn_{0.36}Ln'_xMnO_3$ with fixed $\langle r_A \rangle$ = 1.174 and 1.18 Å were prepared in a similar way by using the respective rare earth oxides, MnO_2, $CaCO_3$ and $SrCO_3$.

Polycrystalline samples $Nd_{0.5-x}La_xCa_{0.5}MnO_3$, $Pr_{0.5-x}La_xCa_{0.5}MnO_3$ and $Ln_{0.5-x}Ln'_xCa_{0.5-y}Sr_yMnO_3$ ($\langle r_A \rangle$ =1.185 Å) were prepared by the conventional ceramic method. Stoichiometric mixtures of the respective rare-earth oxides, alkaline-earth carbonates and MnO_2 were ground and heated at 1173 K in air followed by heating at 1273 K and 1473 K for 12h each in air. The powders thus obtained were pelletized and the pellets sintered at 1673 K in air.

Cobaltates of the general formula $Ln_{0.5}A_{0.5}CoO_3$ (Ln = rare earth, A = Sr or Ba) were prepared by the ceramic route. Stoichiometric quantities of the respective rare earth oxides, the carbonates of the alkaline earth elements and cobalt oxide (Co_3O_4) were ground and prefired at 1173 K for 12 h in air. The powder so obtained was ground thoroughly, heated at 1273 K for 12 h and the pellets finally sintered at 1473 K. The as-prepared samples were oxygen deficient (determined using iodometric titration). To improve the oxygen stoichiometry the samples were annealed in oxygen atmosphere at

a lower temperature. The temperature for oxygen annealing was determined by thermogravimetric analysis. The samples were cooled very slowly in oxygen to 573 K after annealing in oxygen (12-24 hours, depending upon the composition). Two series of rhombohedral cobaltates of the general formula $Ln_{0.5-x}Ln'_xA_{0.5-y}A'_yCoO_3$ with constant $\langle r_A \rangle$ values of $\sim 1.357Å$ and $1.369Å$ were also prepared in a similar manner.

(b) Single Crystalline materials

$Nd_{0.25}La_{0.25}Ca_{0.5}MnO_3$ crystal was grown by the floating zone method using a commercial Image Furnace (NEC, SC-M35HD). Upper panel of Fig. 3.1 shows the instrument along with the control panel. The lower panel in Fig. 3.1 shows the inside view of the crystal growth chamber. This apparatus is equipped with the heat source of a halogen lamp installed at one focal point of an ellipsoidal mirror. Infra red rays irradiated from the reflector are converged to the other focal point to heat and melt samples to thereby form a floating zone. There are two such lamps placed opposite to each other with the melting zone lying between them. The assembly of the mirrors, the seed and feed rod holders, tubes for atmosphere control and quartz tube is seen in the lower panel of Fig. 3.1. The reflectors are water cooled to prevent deformation and loss of reflectance caused by the lamp heat. The halogen lamp tube is air cooled by a blower to obtain good halogen cycle and increase the lamp life. The atmosphere in the crystal rearing unit is shut off from the air in the reflector by the transparent quartz tube and this enables the kind and pressure of the atmosphere to be controlled. The various stages during floating zone crystal growth are shown in Fig. 3.2.
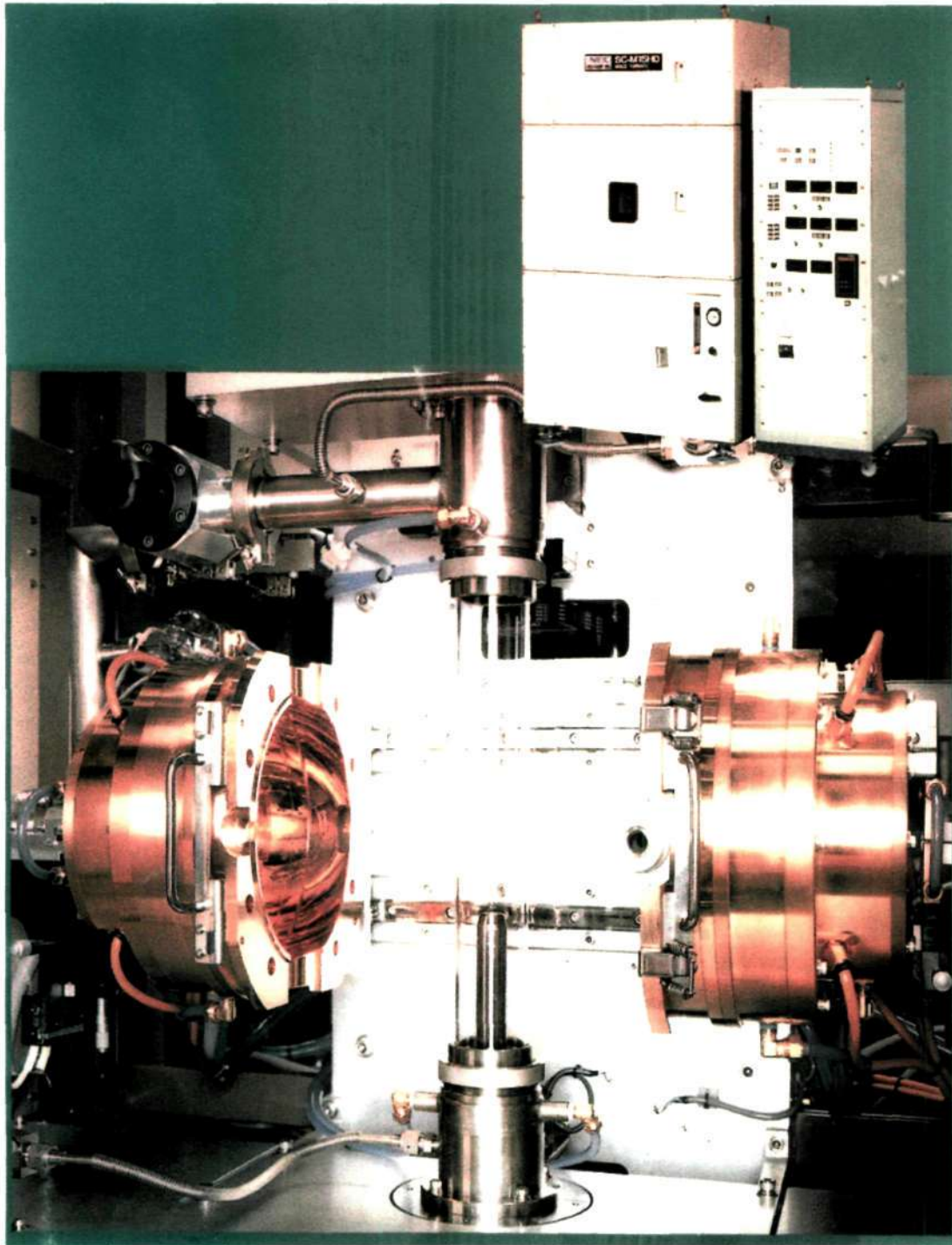
Fig 3.1 Upper Panel: The Floating Zone Crystal Growth Image Furnace with the control panel. Lower Panel: Inside view of the crystal growth chamber showing the two reflectors and other parts.
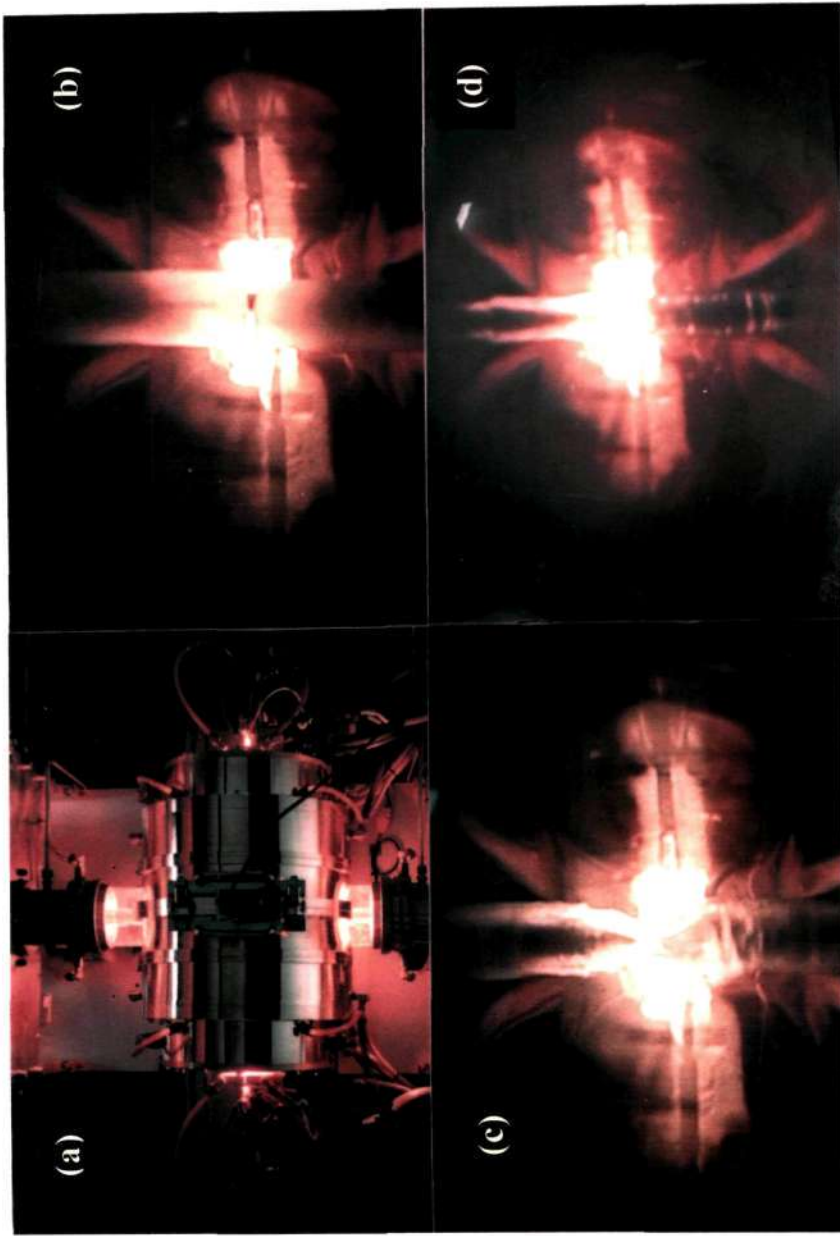
106

Fig. 3.2 Various stages during floating zone crystal growth; (a) the closed positions of the reflectors (b) position of the feed and seed rods in the melting zone (c) seeding condition and (d) growth of the crystal by downward movement.

Fig. 3.3 Picture of the as grown crystal of $Nd_{0.25}La_{0.25}Ca_{0.5}MnO_3$

A stoichiometric mixture of Nd_2O_3, La_2O_3, $CaCO_3$ and MnO_2 was ground and calcined five times at 1373 K for 12h followed by heating at 1473 K for 36h with intermediate grindings. The powder obtained was mixed with small amount of PVA (polyvinyl alcohol) as binder, dried and then pressed into rods of 8mm diameter and 9cm length using latex tubes under a hydrostatic pressure of 5 tons. The rods were sintered at 1723 K for 24h. Two polycrystalline rods of the material (feed and seed) were employed to grow the crystal. Several trials were made to grow the crystal by varying the rod diameter, growth atmosphere (gas flow and pressure), rotation rates of the seed and feed rods and growth rate. Trials to grow $Nd_{0.25}La_{0.25}Ca_{0.5}MnO_3$ crystal in compressed air, nitrogen, nitrogen-oxygen mixture and argon proved futile. Good quality $Nd_{0.25}La_{0.25}Ca_{0.5}MnO_3$ crystal (Fig. 3.3) was grown at a feeding speed of 3mm/h in oxygen pressure ($1kg/cm^2$). Polycrystalline rods of $Nd_{0.35}La_{0.15}Ca_{0.5}MnO_3$ were also prepared in a similar way and the crystal was grown in an atmosphere containing oxygen and nitrogen in the ratio of 1:10.

(c) Samples for Mössbauer Spectroscopy

$Nd_{0.5}Ca_{0.5}Mn_{0.98}{}^{57}Fe_{0.02}O_3$ and $Nd_{0.5}Sr_{0.5}Mn_{0.98}{}^{57}Fe_{0.02}O_3$ were prepared by the solid state reaction of stoichiometric quantities of Nd_2O_3, $CaCO_3/SrCO_3$, Mn_3O_4 and Fe_2O_3 (99.99% enriched). The mixture was heated at 1173 K, 1273 K and 1473K each for 12h in air with intermediate grindings. The powder so obtained was pelletized and sintered at 1673 K for 12h followed by sintering at 1773 K for 12h in air.

3.2 Characterization and Measurements

The phase purity of the samples was established by recording X-ray diffraction (XRD) patterns with a SEIFERT 3000TT diffractometer in the θ-θ geometry in the 2-theta range of 10 to 80 degrees. The polycrystalline samples were thoroughly ground and spread uniformly on a flat sample holder. The diffraction pattern was checked for reflections corresponding to impurity phase. The patterns corresponding to single phase were used to calculate the lattice parameters. Unit cell parameters were derived by least square refinement of powder diffraction data using the PROSZKI program which includes LAZY PULVERIX. Substitution at the Mn site does not have much effect on the structure (orthorhombic) of the manganates studied here. As an example, we show the diffraction patterns for $Nd_{0.5}Sr_{0.5}Mn_{1-x}Al_xO_3$ (x = 0.0, 0.01, 0.03, 0.05 and 0.1) compositions in Fig. 3.4. The diffraction patterns for $Pr_{0.36}Ca_{0.64}Mn_{1-x}Ga_xO_3$ (x = 0.0, 0.01, 0.03, 0.05 and 0.1) are shown in Fig. 3.5. Rietveld analysis of the powder X-ray data of the rare-earth cobaltates, $Ln_{0.5}A_{0.5}CoO_3$ (Ln = rare earth, A = Sr, Ba) was carried out using GSAS software suite [1]. The $\langle r_A \rangle$ values were calculated using the Shannon-radii, r_i, for 12-coordination in case of rhombohedral samples and for 9-coordination in case of orthorhombic ones [2].

The Mn^{4+} content of the samples was determined by redox titration using standard potassium permanganate and ferrous ammonium sulfate (FAS) solutions. The

[1] A. C. Larson and R. B. Von Dreele, *GSAS: General Structural Analysis System: LANSCE*, Los Alamos National Laboratory: Los Alamos, NM, 1994.

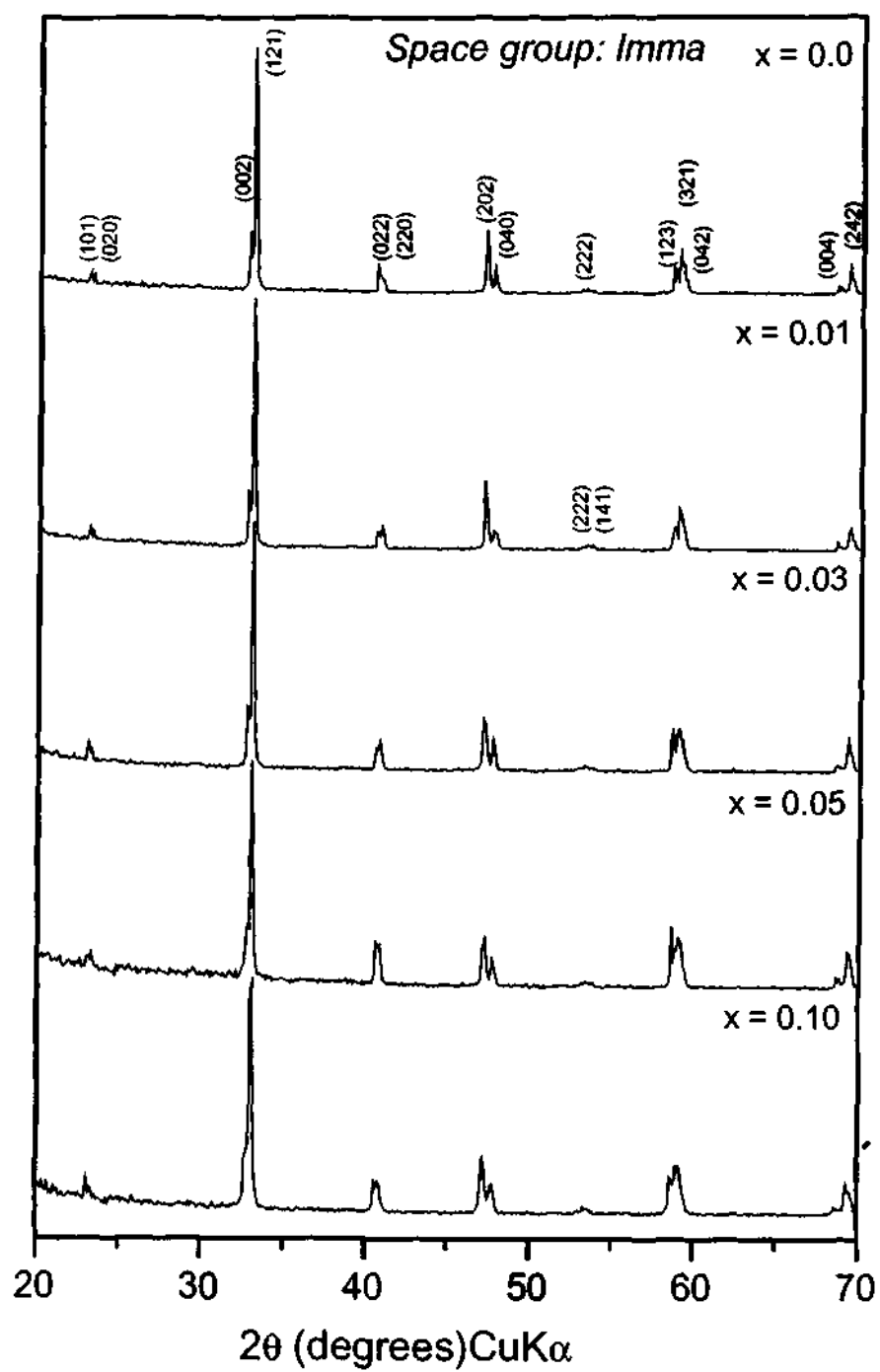[2] R. D. Shannon, Acta Crystallogr., Sect A: Cryst. Phys., Diffr., Theor. Gen. Crystallogr. 32, 751 (1976).

Fig. 3.4 Powder X-ray diffraction patterns of $Nd_{0.5}Sr_{0.5}Mn_{1-x}Al_xO_3$ compositions.

111
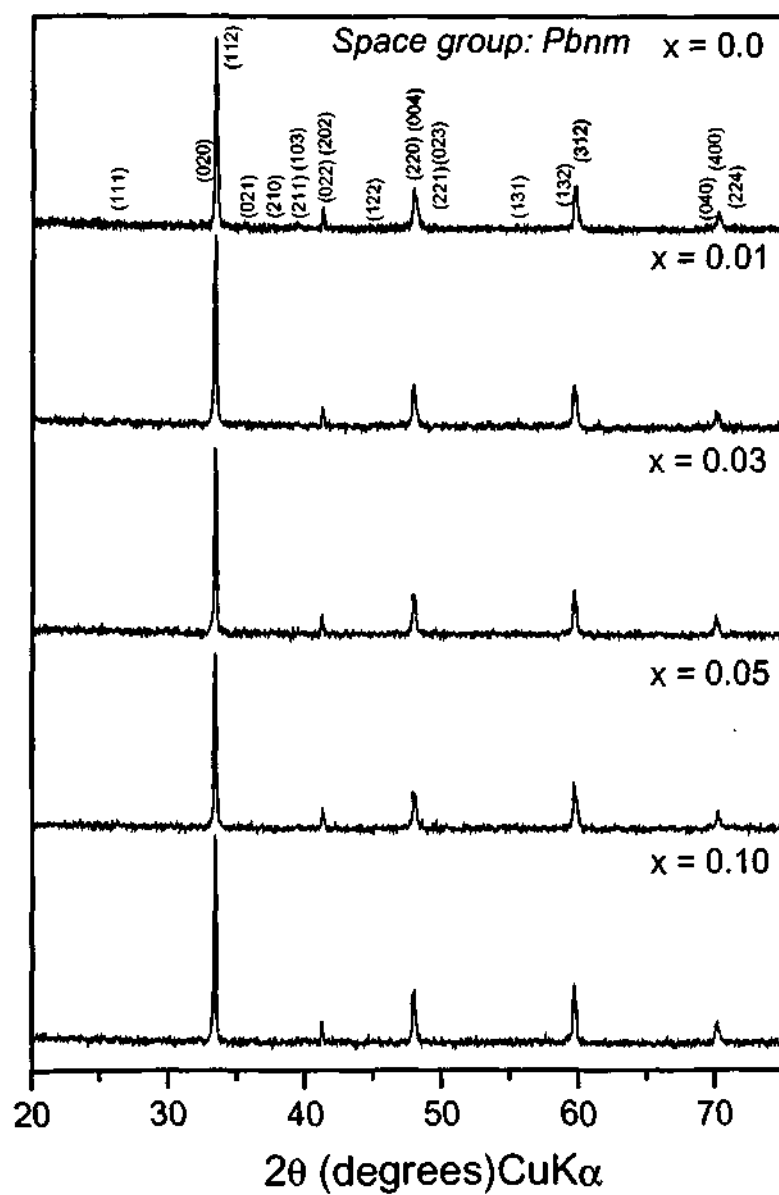
Fig. 3.5 Powder X-ray diffraction patterns of $Pr_{0.36}Ca_{0.64}Mn_{1-x}Ga_xO_3$ compositions.

sample was dissolved in a known excess of FAS solution and the excess Fe^{2+} was then titrated with potassium permanganate solution. The number of milliequivalents of iron oxidized by Mn^{3+} and Mn^{4+} was obtained by the difference between the total milliequivalents of excess iron determined by titration. A blank titration was carried out with a known volume of standard FAS and standard $KMnO_4$ solution. The oxygen stoichiometry in the cobaltates was determined by iodometric titration by employing standard sodium thiosulfate solution, potassium iodide, concentrated hydrochloric acid and freshly prepared 1% starch solution as indicator. The error in oxygen stoichiometry was ± 0.02 and the oxygen stoichiometry in the cobaltates studied by us was generally within this experimental error.

Small discs were cut out of the as-grown crystal perpendicular to the boule axis, polished and then checked for phase purity and single domain (X-ray diffraction and Scanning electron microscope). Energy dispersive analysis of X-ray (EDAX) using a LEICA S440I machine equipped with ISIS software was employed to ascertain the elemental composition of few selected samples where reliable data could be obtained. The electron diffraction pattern for $Gd_{0.5}Ba_{0.5}CoO_3$ sample was recorded using a JEOL 3010 transmission electron microscope (TEM) fitted with an ultrahigh resolution objective pole piece.

Electrical resistivity measurements were carried out from 300 to 20 K by the four-probe method on polycrystalline and single crystalline materials. Data was also collected during heating cycle to study if there were hysteresis effects in the samples. A Keithley current source meter and voltmeter was used. The temperature controller used was from Lakeshore.
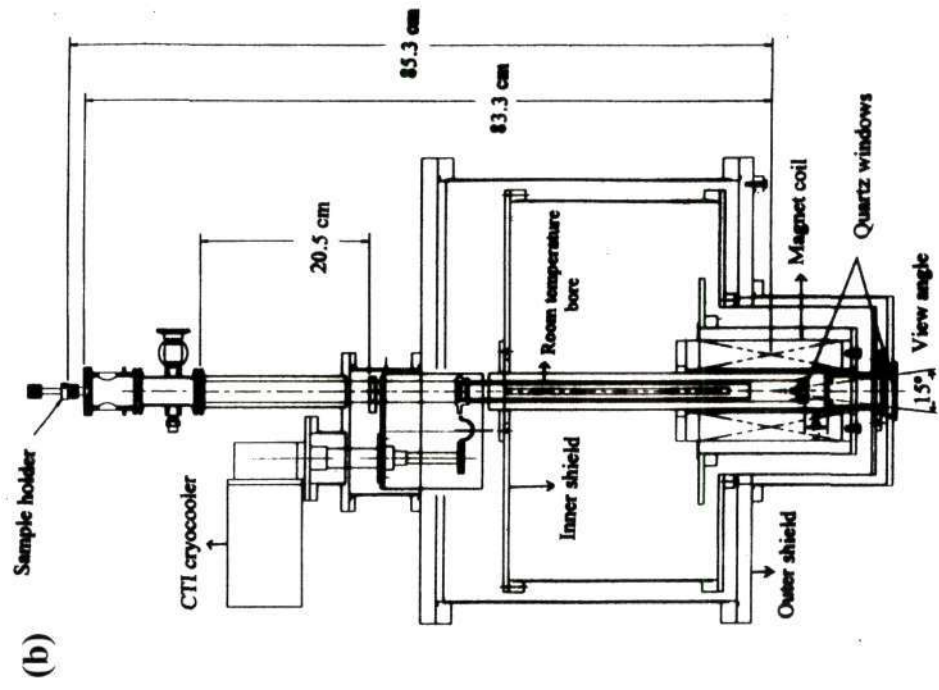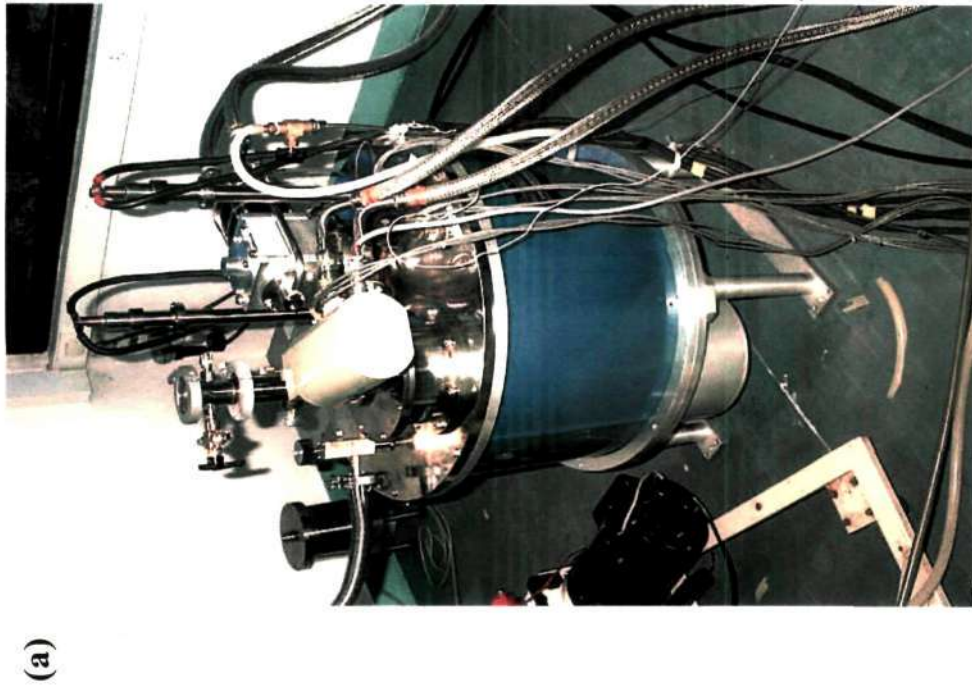
Fig. 3.6 (a) Cryocooled closed cycle superconducting magnet capable of attaining a maximum field of 15 Tesla, along with the accessories. (b) Schematic showing the various parts of the instrument.

Magnetoresistance measurements were carried out using a cryocooled closed cycle superconducting magnet capable of attaining a maximum field of 15 Tesla [3]. This magnet was designed by Prof. C. N. R. Rao and Dr. A. R. Raju in collaboration with Cryo Industries of America, Manchester, NH 03103. Fig. 3.6 shows the view of the instrument with the accessories.

The magnet consists of a single coil made from reacted multifilamentary Nb_3Sn wound on a stainless steel former and cast in epoxy resin to eliminate wire movement during energisation. The coil is supplied with a superconducting persistent mode switch to connect in parallel across the whole magnet and wired to the main input/output current terminals. Resistive heaters wound into the switch enable the switch to be either resistive or superconducting. The leads are of 2223 bismuth cuprate high-temperature superconductor. The magnet can achieve a field up to 15 Tesla and consists of a room-temperature bore of 52 mm to carry out magnetoresistance and other measurements from 12 to 500 K. Also, there is an optical window to carry out measurements under illumination with an appropriate radiation.

Magnetization measurements were carried out using a vibrating sample magnetometer (Lakeshore VSM 7300) and magnetic susceptibility measurements using a Lewis coil force magnetometer. The magnetization measurements were always done in a field of 100 Oe unless until mentioned otherwise.

Mössbauer spectra were taken in a constant acceleration drive against a 5 millicurie ^{57}Co source in Rh matrix, over the temperature range 4.2K-300K using a gas

---

[3] G. Svenconis, L. Ying, A. R. Raju and C. N. R. Rao, Curr. Sci. 77, 574 (1999).

flow liquid helium cryostat. The absorbers were prepared by spreading a thin layer of the powder on an aluminium foil and fixing the powder in position using thermally conducting GE varnish. Before spreading the sample, the sample powder was mixed with equal amount of $LiCO_3$ powder to facilitate uniform spreading of the sample over the absorber area. Having no Fe, $LiCO_3$ does not give any signal to Mössbauer spectrum and being low-density material, it acts as filler without significantly cutting gamma ray counts. The thickness of the sample used was one characteristic thickness of electronic absorption, which in this case was 19.4 mg of the material/cm^2. The sample diameter was half an inch. The sample on the Al foil was fixed on a copper ring with half-inch hole using GE varnish.

4. RESULTS AND DISCUSSION

4.1 Effect of cation size disorder on charge ordering in rare earth manganates, $Ln_{0.5}A_{0.5}MnO_3$ (Ln = rare earth, A = alkaline earth)

The manganates with a $\langle r_A \rangle$ of 1.24 Å studied here are akin to $Nd_{0.5}Sr_{0.5}MnO_3$ exhibiting distinct ferromagnetic and charge-ordering transitions both in the magnetization and resistivity data. In Table 4.1.1 and 4.1.2, the various compositions studied are listed along with the lattice parameters. Both the measurements have been employed to obtain T_{CO} values for these compositions. The T_{CO} data for manganates with $\langle r_A \rangle = 1.17$ Å were obtained from the minima in the inverse magnetization-temperature plots as well as from the maxima in $d(\ln\rho)/dT^{-1}$ plots. In Fig. 4.1.1(a) and (b), we show the typical magnetic behavior of the manganates with $\langle r_A \rangle = 1.24$ Å and 1.17 Å respectively. The method employed to determine T_{CO} is also indicated in the figure. In the other $Ln_{0.5}A_{0.5}MnO_3$ compositions with variable $\langle r_A \rangle$, T_{CO} values were obtained from the magnetization data.

In Fig. 4.1.2, we show the temperature variation of the magnetization and resistivity of the compositions listed in Table 4.1.1 corresponding to $\langle r_A \rangle = 1.24$ Å and variable size mismatch, σ^2. The ferromagnetic Curie temperature, T_C as well as the charge-ordering transition temperature, T_{CO} decrease with increase in σ^2. However, for $\sigma^2 > 0.0058$ Å^2 the samples do not show a clear transition corresponding to T_{CO} both in the magnetization and resistivity data. The magnetization and resistivity behavior as a function of temperature of a few selected compositions with $\langle r_A \rangle = 1.17$ Å (Table 4.1.2) is shown in Fig. 4.1.3. The

117

Table 4.1.1

Properties of manganates with constant $\langle r_A \rangle$ of 1.24 Å

Composition	σ^2 (Å²)	Lattice parameters (Å)[a]			%D (297 K)	Mn^{4+} (%)	T_{CO} (K)[b]	T_C (K)[b]
		a	b	c				
Pr$_{0.15}$La$_{0.35}$Ca$_{0.16}$Sr$_{0.34}$MnO$_3$	0.0030	5.436	7.644	5.459	0.34	47	175 (167)	291 (279)
Nd$_{0.15}$La$_{0.35}$Ca$_{0.145}$Sr$_{0.355}$MnO$_3$	0.0033	5.453	7.631	5.470	0.53	47	170 (154)	287 (273)
Nd$_{0.1}$Pr$_{0.4}$Sr$_{0.45}$Ca$_{0.05}$MnO$_3$	0.0045	5.431	7.623	5.466	0.47	48	168 (163)	274 (266)
Nd$_{0.5}$Sr$_{0.5}$MnO$_3$	0.0054	5.426	7.634	5.475	0.51	48	147 (149)	261 (256)
Sm$_{0.17}$Pr$_{0.33}$Sr$_{0.5}$MnO$_3$	0.0057	5.427	7.630	5.465	0.44	48	169 (156)	244 (226)
Gd$_{0.11}$Pr$_{0.39}$Sr$_{0.5}$MnO$_3$	0.0058	5.427	7.639	5.474	0.48	47	171 (159)	254 (238)
Sm$_{0.315}$La$_{0.185}$Sr$_{0.5}$MnO$_3$	0.0062	5.426	7.636	5.468	0.45	47		209 (---)
Gd$_{0.245}$La$_{0.255}$Sr$_{0.5}$MnO$_3$	0.0069	5.428	7.635	5.463	0.40	46		231 (---)

(a) *Space group: Imma*; Uncertainties in the lattice parameters are within ± 0.001 Å.

(b) T_{CO} and T_C values are from magnetization measurement; values in parenthesis are from resistivity data.

118

Table 4.1.2

Properties of manganates with constant $\langle r_A \rangle$ of 1.17 Å

Composition	σ^2 (Å²)	Lattice parameters (Å)[a]			%D (297 K)	Mn^{4+} (%)	T_{CO} (K)[b]
		a	b	c			
$Nd_{0.5}Ca_{0.5}MnO_3$	0.0001	5.401	7.610	5.396	0.67	47	240 (225)
$Pr_{0.33}Sm_{0.17}Ca_{0.5}MnO_3$	0.0003	5.437	7.623	5.374	0.42	46	234 (216)
$Pr_{0.385}Gd_{0.115}Ca_{0.5}MnO_3$	0.0006	5.423	7.592	5.383	0.38	46	225 (208)
$La_{0.255}Gd_{0.245}Ca_{0.5}MnO_3$	0.0016	5.424	7.595	5.385	0.38	47	--- (209)
$Nd_{0.25}Sm_{0.25}Ca_{0.44}Sr_{0.06}MnO_3$	0.0016	5.398	7.606	5.380	0.15	46	212 (---)
$Nd_{0.15}Sm_{0.35}Ca_{0.4165}Sr_{0.0835}MnO_3$	0.0022	5.420	7.581	5.372	0.40	47	218 (222)
$Nd_{0.25}Gd_{0.25}Ca_{0.39}Sr_{0.11}MnO_3$	0.0032	5.411	7.613	5.373	0.26	47	-- (---)
$Nd_{0.15}Gd_{0.35}Ca0_{.35}Sr_{0.15}MnO_3$	0.0043	5.422	7.593	5.377	0.39	48	---(203)
$Y_{0.2}Gd_{0.3}Ca_{0.235}Sr_{0.265}MnO_3$	0.0081	5.421	7.612	5.370	0.36	47	209 (---)

[a] *Space group: Pnma*; Uncertainties in the lattice parameters are within ± 0.001 Å.

[b] T_{CO} values are from magnetization measurement; values in parenthesis are from resistivity data.

119

anomaly in the magnetization data corresponding to the charge ordering transition is not prominent in compositions with higher σ^2.

The variation of T_{CO} with σ^2 of the $Ln_{0.5}A_{0.5}MnO_3$ series with $\langle r_A \rangle = 1.17$ Å is shown in Fig. 4.1.4(a). In Fig. 4.1.4(b), we have plotted the T_{CO} as well as the ferromagnetic T_C values of the manganate series with $\langle r_A \rangle = 1.24$ Å against σ^2. Although we could properly characterize the charge-ordered states only in a few members of each series, the data show discernible trends. The T_{CO} values from electrical resistivity data generally tend to be somewhat lower than those from magnetization data. In the $\langle r_A \rangle = 1.17$ Å series, the T_{CO} values up to a σ^2 of 0.0006 Å^2, obtained from both the magnetization and electrical resistivity data, give a slope, $p_1 = 32000 \pm 3000$ K Å^{-2}. This slope is comparable to that obtained in the metal-insulator transition data in earlier studies [1,2]. For higher values of σ^2, there is no statistically significant dependence of T_{CO} on σ^2 in the manganates of the $\langle r_A \rangle = 1.17$ Å series. Within the accuracy of our measurements, the T_{CO}-σ^2 slope is less than 4000 K Å^{-2} when $\sigma^2 \geq 0.0006$ Å^2. In effect therefore, for moderate and high values of σ^2, T_{CO} appears to be essentially independent of σ^2. This may be because there may be no long-range orbital ordering when $\langle r_A \rangle = 1.17$ Å for $\sigma^2 \geq 0.0006$ Å^2, suggesting that below this value of σ^2 the dependence of T_{CO} on σ^2 reflects the effect of cation size mismatch on the long-range structural distortion at T_{CO}. This could also make the transition rather broad as found in many manganates with $\langle r_A \rangle = 1.17$ Å (see Fig. 4.1.1(b)).

[1] (a) L. M. Rodriguez-Martinez and J. P. Attfield, Phys. Rev. B54, R15622 (1996). (b) L. M. Rodriguez-Martinez and J. P. Attfield, Phys. Rev. B58, 2426 (1998).

[2] F. Damay, C. Martin, A. Maignan and B. Raveau, J. Appl. Phys. 82, 6181 (1997).

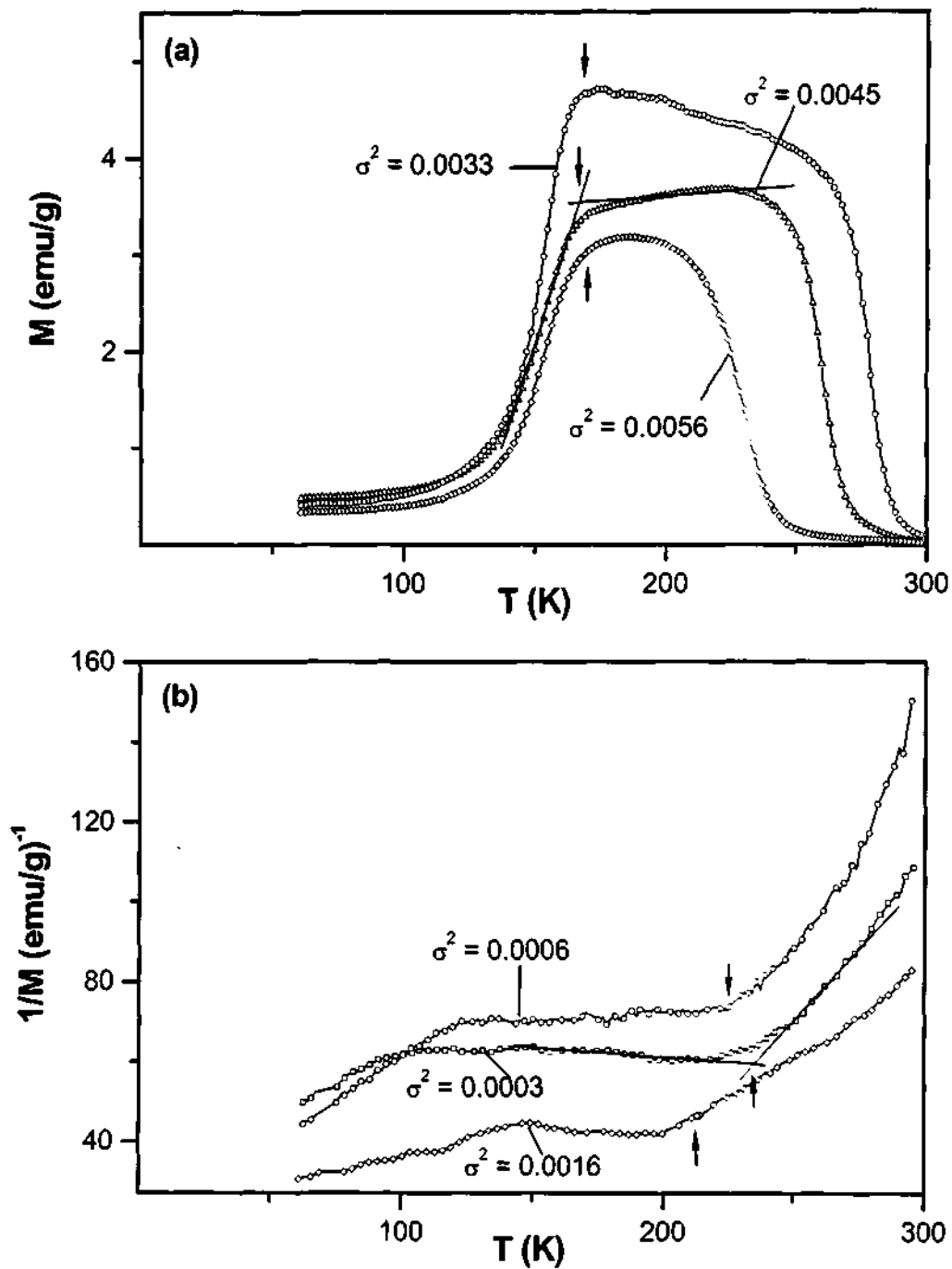Fig. 4.1.1 Temperature variation of (a) the magnetization M of the $Ln_{0.5}A_{0.5}MnO_3$ series with a fixed $\langle r_A \rangle$ of 1.24 Å and (b) of 1/M of the manganates of the series with a fixed $\langle r_A \rangle$ of 1.17 Å. T_{CO} is shown by an arrow.
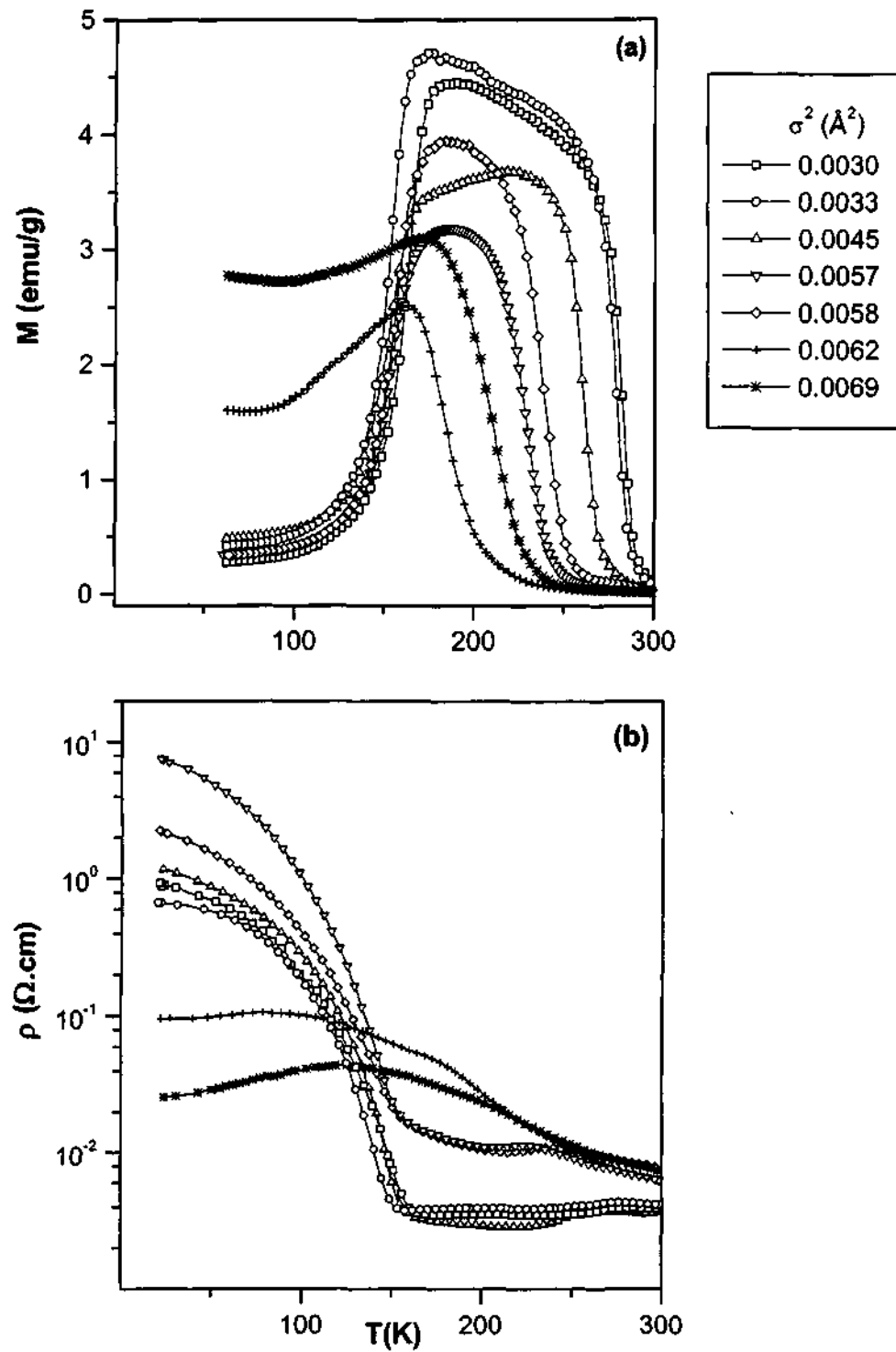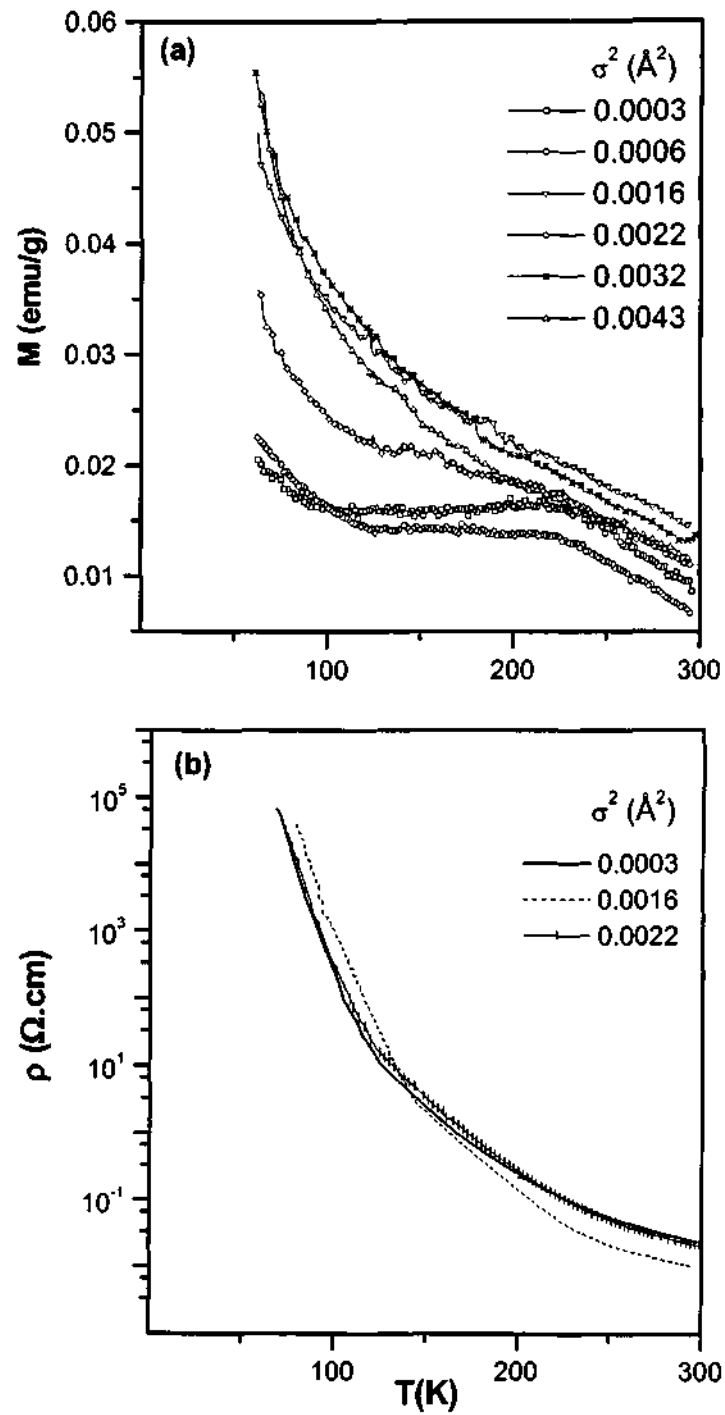
Fig. 4.1.2 Temperature variation of (a) the magnetization M and (b) the resistivity ρ of the manganates with a fixed ⟨r$_A$⟩ of 1.24 Å.

Fig. 4.1.3 Temperature variation of (a) the magnetization M and (b) the resistivity ρ of the manganates with a fixed $\langle r_A \rangle$ of 1.17 Å.
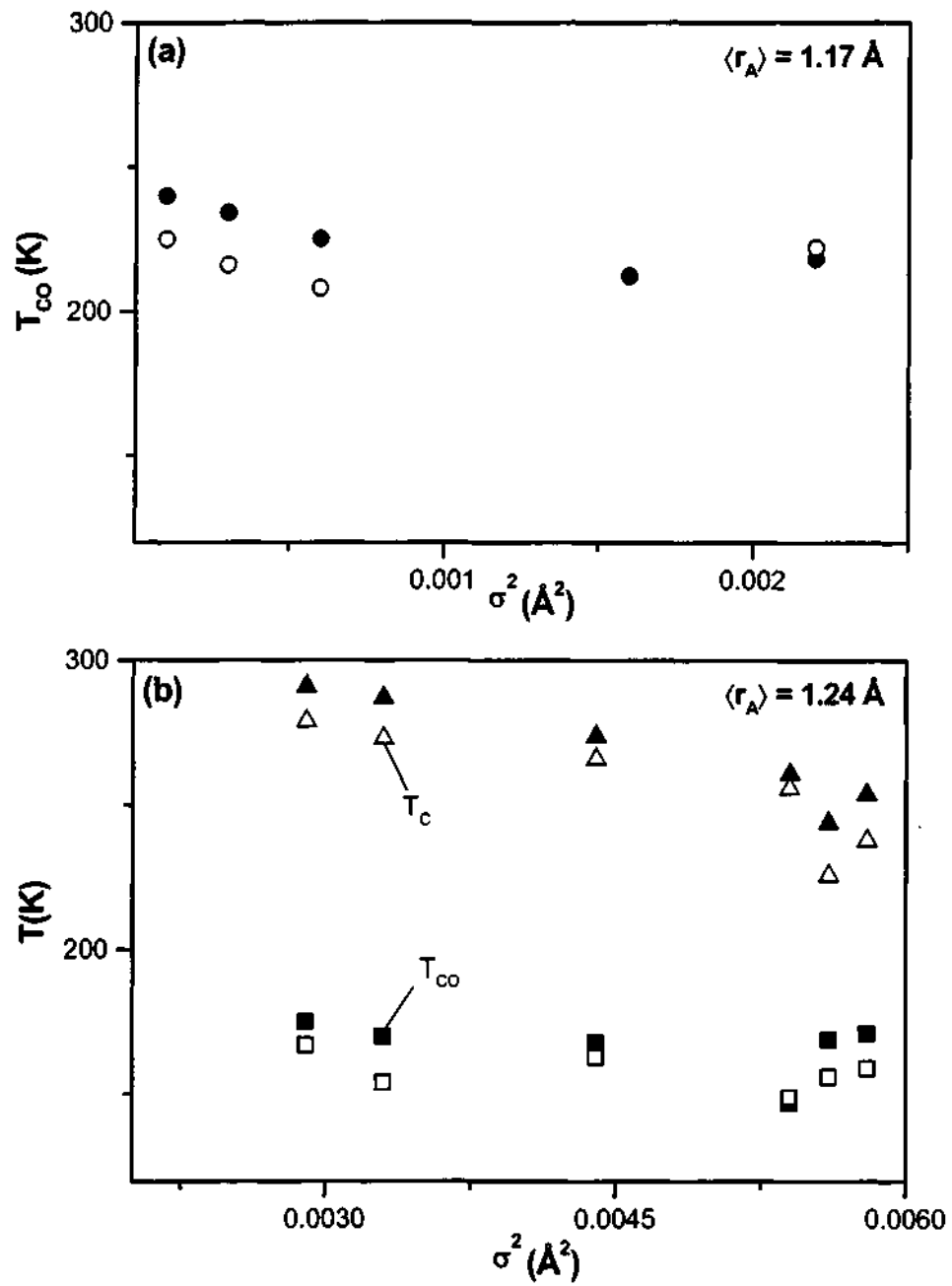
123

Fig. 4.1.4 Variation of the charge-ordering transition temperature T_{CO} with σ^2 in the

$Ln_{0.5}A_{0.5}MnO_3$ series with (a) $\langle r_A \rangle = 1.17$ Å and (b) $\langle r_A \rangle = 1.24$ Å. Filled circles, triangles,

and squares are from magnetic measurements and the corresponding open symbols are

from resistivity measurements.

124

Similarly, there is no significant dependence of T_{CO} on σ^2 in the manganates with $\langle r_A \rangle = 1.24$ Å, unlike the ferromagnetic T_C values in these materials (Fig. 4.1.4(b)). Thus, the values of T^0_{CO} and T^0_C for this series are 174 ± 13 K and 331 ± 13 K respectively and the corresponding negative slopes, p_1 are 2840 ± 270 K Å^{-2} and 15000 ± 2800 K Å^{-2}.

For the insulator-metal transition in the manganates, it has been proposed [1,2] that

$$T^0_M = T^*_M - p_2(r^0_A - \langle r_A \rangle)^2, \qquad (4.1.1)$$

where p_2 is analogous to p_1. The value of r^0_A corresponds to that of the ideal perovskite having maximum T^0_M value and a perovskite tolerance factor of 1. Oxygen atom displacements proportional to $(r^0_A - \langle r_A \rangle)$ lead to suppression of T^0_M through a changing strain energy. Unlike in metal-insulator transitions, it is difficult to fix the ideal value of $\langle r_A \rangle$ for the charge-ordered state. Experimentally, the variation of T_{CO} with $\langle r_A \rangle$ suggests that the charge-ordered state is favored for small $\langle r_A \rangle$ [3,4], as the bending of the Mn-O-Mn bond angle and the associated distortion of the MnO_6 octahedra facilitate the localization of separate Mn^{3+} and Mn^{4+} states. If we take the value of r^0_A to be the minimum observed value of $\langle r_A \rangle = 1.127$ Å, we can describe the T_{CO} data by using an expression similar to (4.1.1). The variation of T_{CO} seems to be best described by the curve in Fig. 4.1.5 with $T^*_{CO} = 260$ K and $p_2 = 6900$ K Å^{-2}.

We have explored the relationship between T_{CO} and the orthorhombic lattice distortion index, which is strongly dependent on $\langle r_A \rangle$ or $(r^0_A - \langle r_A \rangle)^2$. The lattice

[3] C. N. R. Rao and A. K. Cheetham, Adv. Mater. 9, 1009 (1997).

[4] A. Arulraj, P. N. Santhosh, R. S. Gopalan, A. Guha, A. K. Raychaudhuri, N. Kumar and C. N. R. Rao J. Phys. Condens. Matter. 10, 8497 (1998).
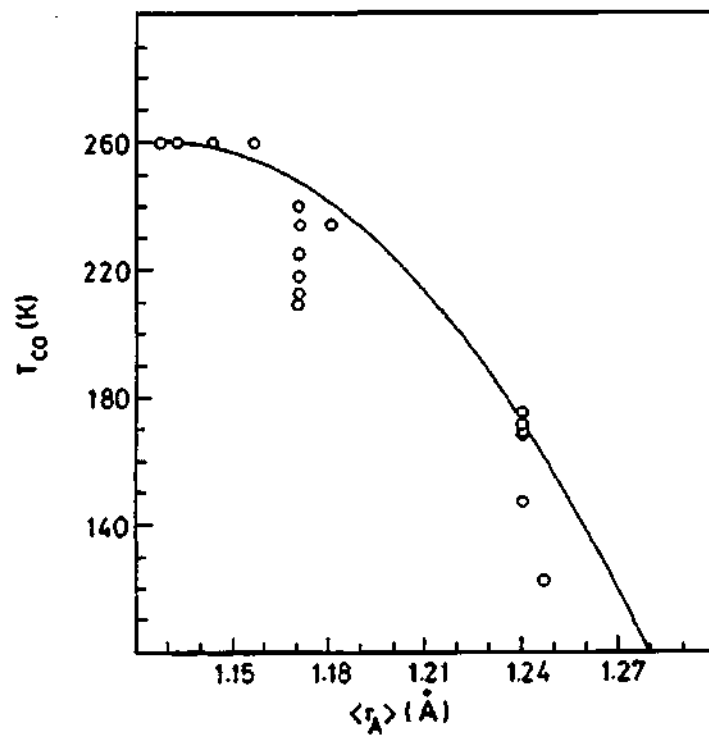
Fig. 4.1.5 A plot of T_{CO} against $\langle r_A \rangle$ in $Ln_{0.5}A_{0.5}MnO_3$.
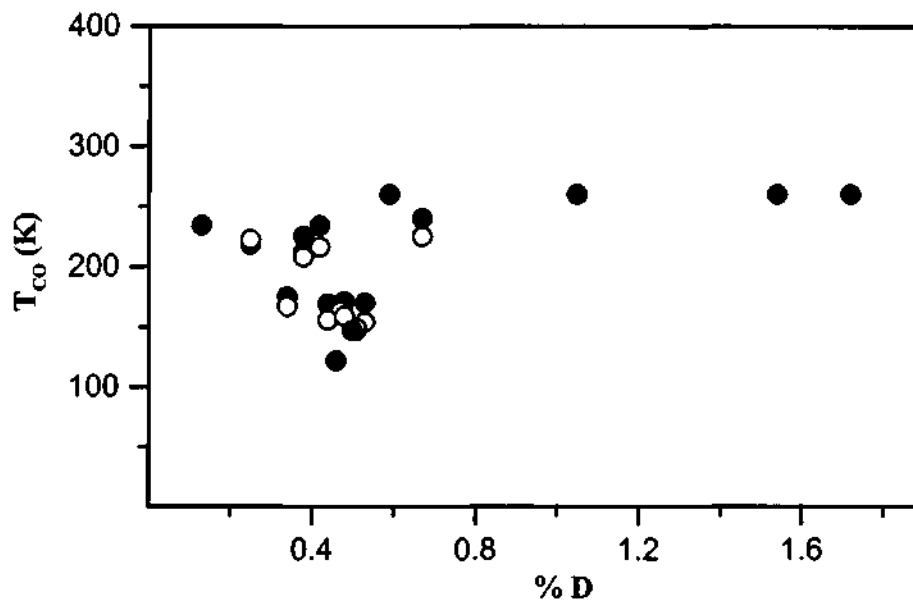

Fig. 4.1.6 Variation of T_{CO} with the orthorhombic lattice distortion index, % D. Filled

circles are from magnetic measurements and the corresponding open circles are from

resistivity measurements.

126

distortion index, % D, is defined as

$$\% D = 1/3 \left(\Sigma \, |a_i - a'|/a_i \right) \times 100, \qquad\qquad (4.1.2)$$

where $a' = (a \times b \times c/\sqrt{2})^{1/3}$. In Fig. 4.1.6, we have plotted the experimental T_{CO} values

obtained for all the manganates studied by us against % D. We see that T_{CO} does not vary

much, particularly when the distortion is high; the dependence of T_{CO} appears to be

significant at best for small values of % D.

Conclusions

In conclusion, the present study indicates that the charge-ordering transition in the

rare-earth manganates is not very sensitive to the mismatch between the sizes of the A-site

cations or to the orthorhombic lattice distortion arising from the small cation size. The

decrease in the charge-ordering transition temperature at high $\langle r_A \rangle$ [3,4] is consistent with

the observed quadratic dependence upon $(r^0_A - \langle r_A \rangle)$ where $r^0_A \approx 1.13$ Å.

4.2 Effect of Mn site doping in rare-earth manganates, $Ln_{0.5}A_{0.5}MnO_3$ (Ln = rare-earth, A = alkaline earth)

$Ln_{0.5}A_{0.5}Mn_{1-x}M_xO_3$

4.2.1 M = Al and Ga: In Table 4.2.1, we list the lattice parameters of $Nd_{0.5}Ca_{0.5}Mn_{1-x}Al_x(Ga_x)O_3$ compositions. All the materials studied here have an orthorhombic structure as shown in Table 4.2.1. The powder X-ray diffraction patterns of $Nd_{0.5}Ca_{0.5}Mn_{1-x}Al_xO_3$ compositions are shown in Fig. 4.2.1. $Nd_{0.5}Ca_{0.5}MnO_3$ with a $\langle r_A \rangle$ = 1.17 Å is a charge-ordered (CO) insulator with T_{CO} = 240 K, as evidenced from the broad peak in the magnetization data (Fig. 4.2.2, x = 0). The effect of substitution of Al^{3+} and Ga^{3+} in the place of Mn^{3+} on the magnetization of this manganate is shown in Fig. 4.2.2(a) and (b), respectively. It is evident from the graph that the substitution of Al^{3+} or Ga^{3+} in the Mn site of $Nd_{0.5}Ca_{0.5}MnO_3$ has no significant effect on the magnetization and charge-ordering. These substitutions do not destroy the charge-ordering as evident in the hump in the magnetization data in the insets of Fig. 4.2.2. However, there is a slight decrease in the charge-ordering temperature, T_{CO}. In $Nd_{0.5}Ca_{0.5}Mn_{1-x}Al_xO_3$, the charge-ordering transition is evident up to x = 0.05, but the feature corresponding to charge-ordering is rather broad for x = 0.05. In $Nd_{0.5}Ca_{0.5}Mn_{1-x}Ga_xO_3$, the transition is evident up to x = 0.03, but we do not see such a distinct signature of the transition when x > 0.03. All the Al and Ga substituted compositions are insulating as the parent compound. Fig. 4.2.3 shows the typical resistivity behavior of $Nd_{0.5}Ca_{0.5}Mn_{0.97}M_{0.03}O_3$ compositions (M = Al, Ga, Fe and Ge).

Table 4.2.1

Properties of $Nd_{0.5}Ca_{0.5}Mn_{1-x}M_xO_3$ (M = Al and Ga)

Composition	Lattice parameters (Å)*			T_{IM} (K)	T_C (K)	T_{CO} (K)
	$\underline{a}$	$\underline{b}$	$\underline{c}$			
$Nd_{0.5}Ca_{0.5}Mn_{1-x}Al_xO_3$						
0.00	5.401	7.610	5.396	-	-	240
0.01	5.407	7.627	5.382	-	-	237
0.03	5.404	7.628	5.382	-	-	234
0.05	5.416	7.601	5.378	-	-	~222
0.10	5.397	7.599	5.374	-	-	-
$Nd_{0.5}Ca_{0.5}Mn_{1-x}Ga_xO_3$						
0.01	5.408	7.604	5.388	-	-	238
0.03	5.405	7.583	5.383	-	-	233
0.05	5.398	7.606	5.373	-	-	~228
0.10	5.397	7.595	5.382	-	-	-

* *Space group: Pnma*; Uncertainties in the lattice parameters are within ± 0.001 Å.
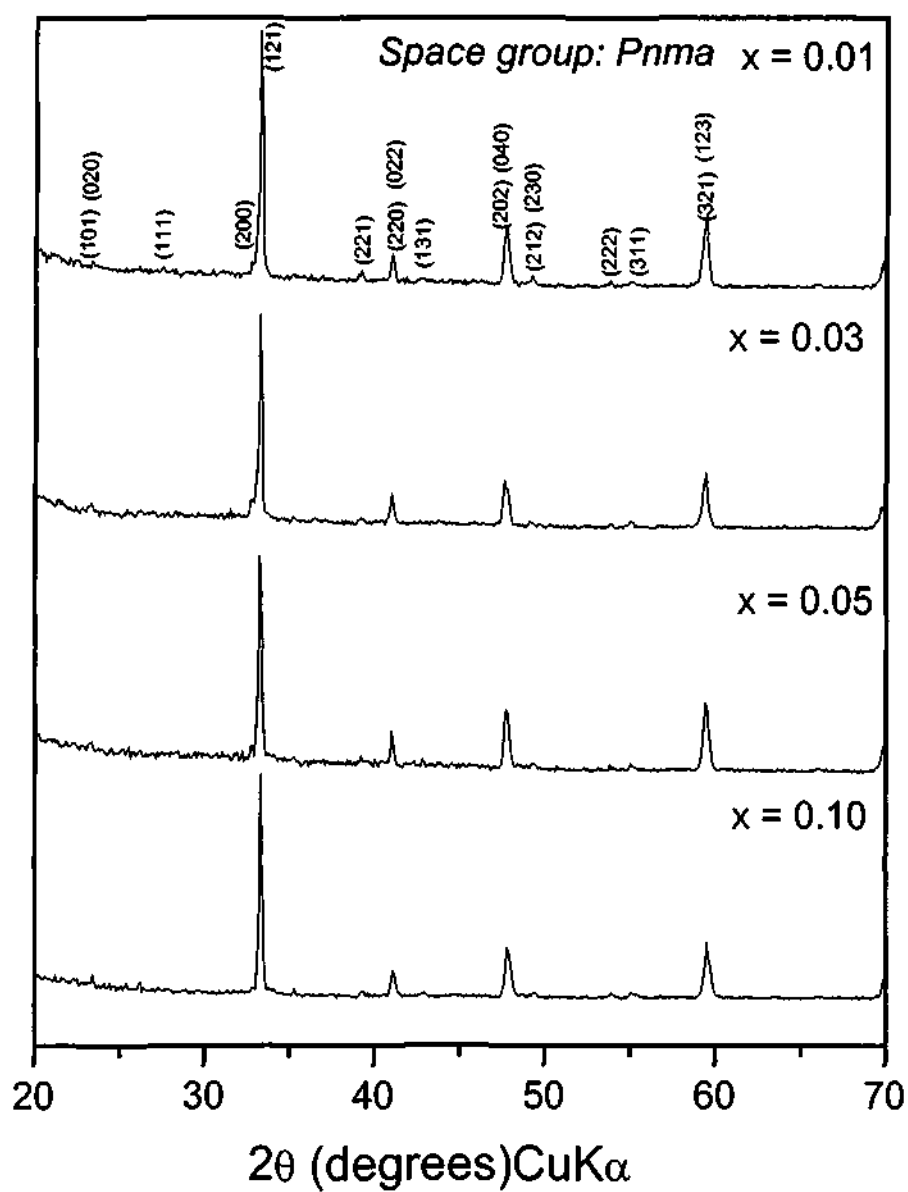
Fig. 4.2.1 Powder X-ray Diffraction patterns of $Nd_{0.5}Ca_{0.5}Mn_{1-x}Al_xO_3$ compositions.
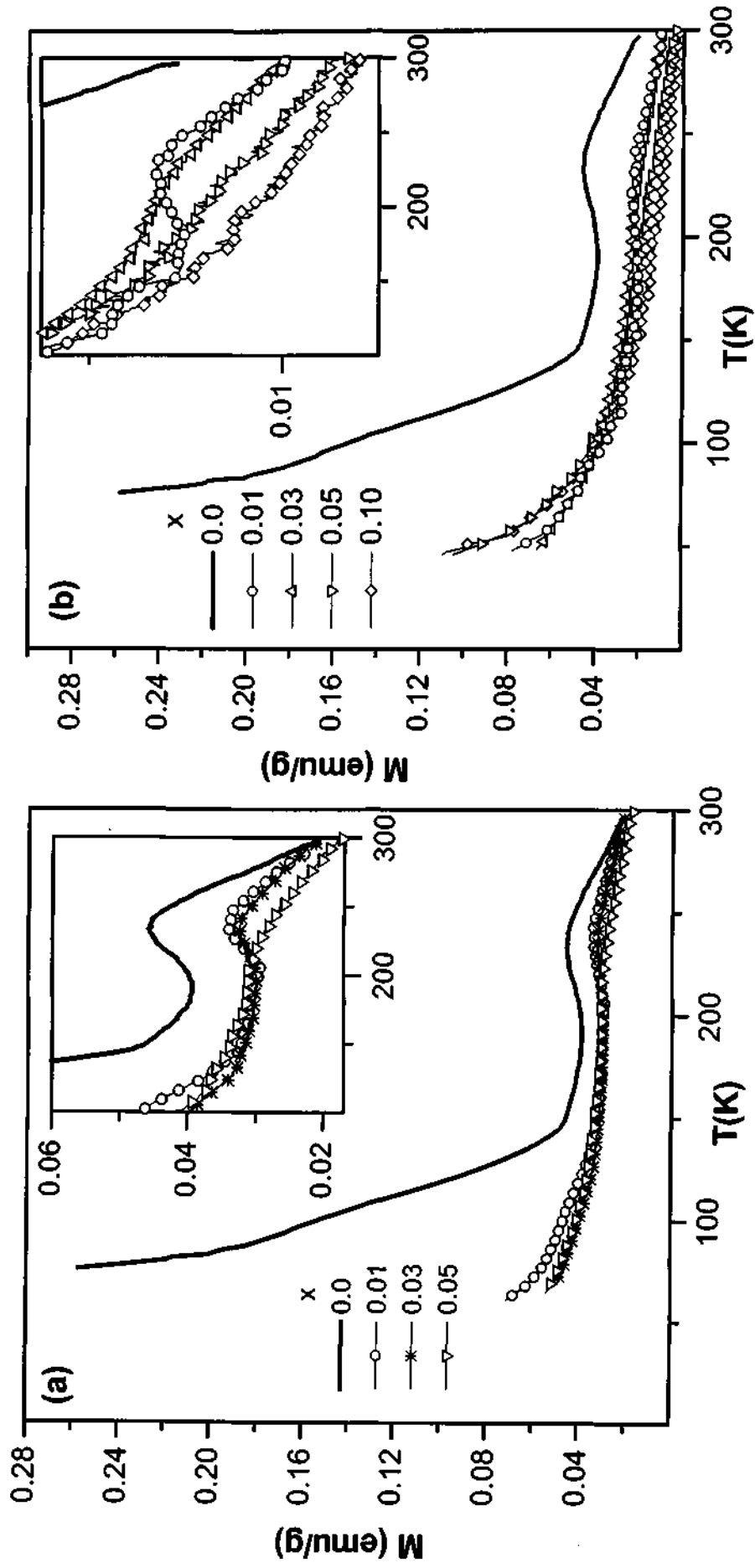
Fig. 4.2.2 Temperature variation of the magnetization of (a) $Nd_{0.5}Ca_{0.5}Mn_{1-x}Al_xO_3$ and (b) $Nd_{0.5}Ca_{0.5}Mn_{1-x}Ga_xO_3$. Inset shows the magnetization data on an enlarged scale to show the T_{CO}.

131
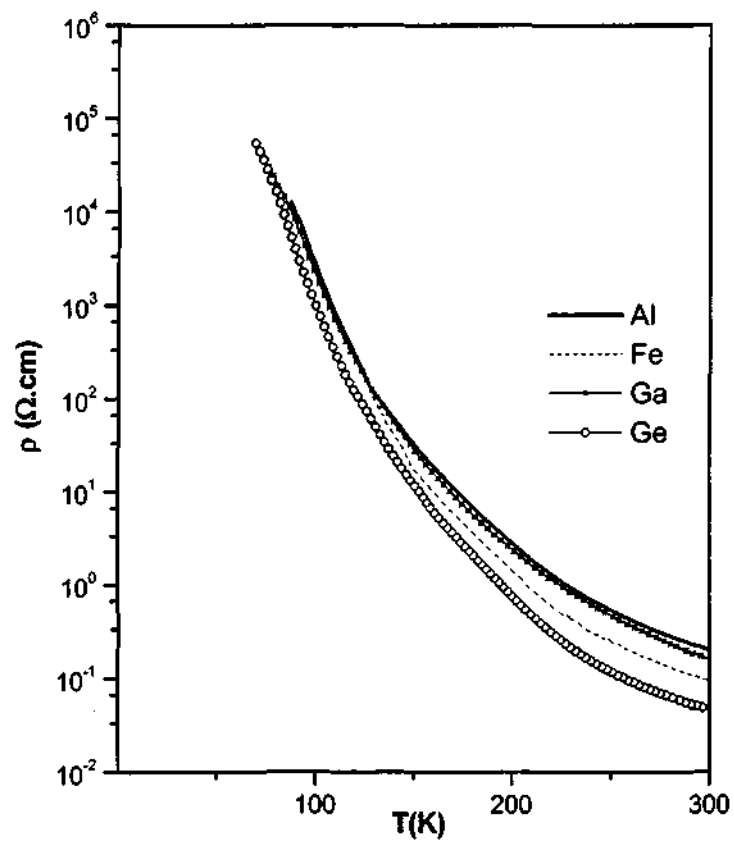
Fig. 4.2.3 Temperature variation of the resistivity of $Nd_{0.5}Ca_{0.5}Mn_{0.97}M_{0.03}O_3$ (M = Al, Ga, Fe and Ge).

Substitution of Al and Ga at the Mn site of $Nd_{0.5}Sr_{0.5}MnO_3$ has also been investigated. In Table 4.2.2, the lattice parameters of $Nd_{0.5}Sr_{0.5}Mn_{1-x}Al_x(Ga_x)O_3$ are listed. $Nd_{0.5}Sr_{0.5}MnO_3$ with $\langle r_A \rangle = 1.24$ Å, becomes ferromagnetic and metallic around 260 K and undergoes a transition to a CE-type antiferromagnetic ordering with concomitant charge-ordering around 150 K. There is a sharp metal-insulator transition around 150 K. Substitution of Al in the Mn site of this manganate is interesting. In Fig. 4.2.4, we show the temperature variation of the resistivity and magnetization of $Nd_{0.5}Sr_{0.5}Mn_{1-x}Al_xO_3$. Substitution of Al in the Mn site with x = 0.01 slightly increases T_{CO} and decreases T_C (Table 4.2.2). These changes are in a direction opposite to that of external pressure or substitution by large A-site cation [1,2]. Substitution of Al^{3+} in place of Mn^{3+} appears to have a negative pressure effect. When x = 0.03, we do not clearly see any distinction between T_C and T_{CO} in the resistivity data; the x = 0.05 composition is an insulator. When x = 0.03, T_C is close to 250 K, but the value of magnetization gradually decreases from 200 K down and it is difficult to pin down a value of T_{CO}. The x = 0.05 and 0.10 compositions show a broad hump in the magnetization data.

The resistivity and magnetization behavior of $Nd_{0.5}Sr_{0.5}Mn_{1-x}Ga_xO_3$ is presented in Fig. 4.2.5. The resistivity anomaly at the antiferromagnetic transition occurs at 136 K when x = 0.01 although the magnitude of change of resistivity is considerably reduced. The x > 0.01 compositions are insulating just as other charge-ordered manganates. The magnetization behavior of $Nd_{0.5}Sr_{0.5}Mn_{1-x}Ga_xO_3$ remains the same as that of the parent

[1] Y. Moritomo, H. Kuwahara, Y. Tomioka and Y. Tokura, Phys. Rev. B55, 7549 (1997).

[2] C. N. R. Rao, P. N. Santhosh, R. S. Singh and A. Arulraj, J. Solid State Chem. 135, 169 (1998).

Table 4.2.2

Properties of $Nd_{0.5}Sr_{0.5}Mn_{1-x}M_xO_3$ (M = Al and Ga)

Composition	Lattice parameters (Å)[*]			T_{IM} (K)	T_C (K)	T_{CO} (K)
	$\underline{a}$	$\underline{b}$	$\underline{c}$			
$Nd_{0.5}Sr_{0.5}Mn_{1-x}Al_xO_3$						
0.00	5.426	7.634	5.475	249	267	147
0.01	5.434	7.627	5.473	242	250	165
0.03	5.426	7.620	5.470	-	247	-
0.05	5.422	7.622	5.465	-	-	-
0.10	5.423	7.617	5.466	-	-	-
$Nd_{0.5}Sr_{0.5}Mn_{1-x}Ga_xO_3$						
0.01	5.425	7.633	5.472	233	248	143
0.03	5.426	7.630	5.473	-	210	-
0.05	5.425	7.630	5.470	-	-	-
0.10	5.425	7.626	5.471	-	-	-

[*] *Space group: Imma*; Uncertainties in the lattice parameters are within ± 0.001 Å.
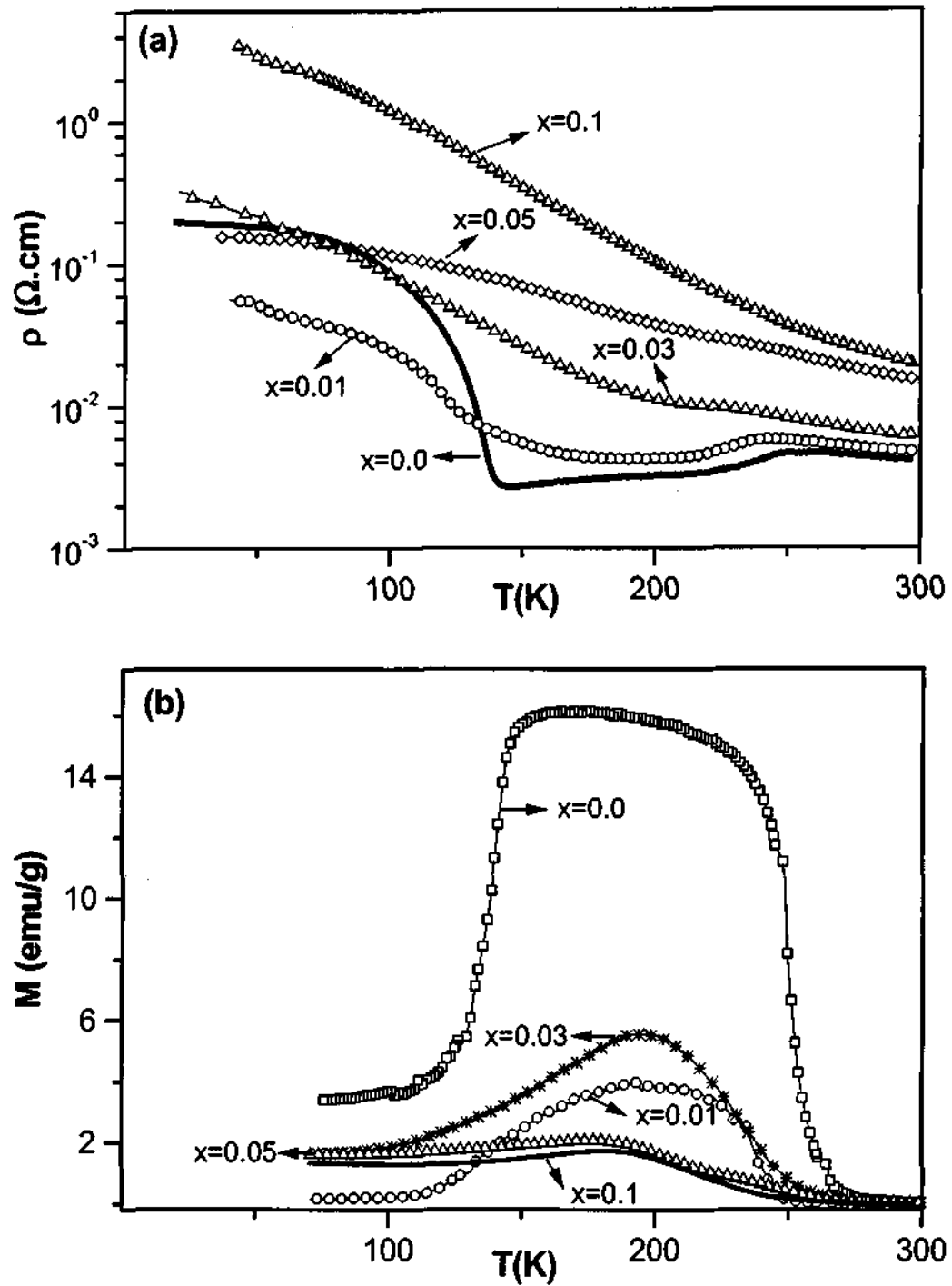
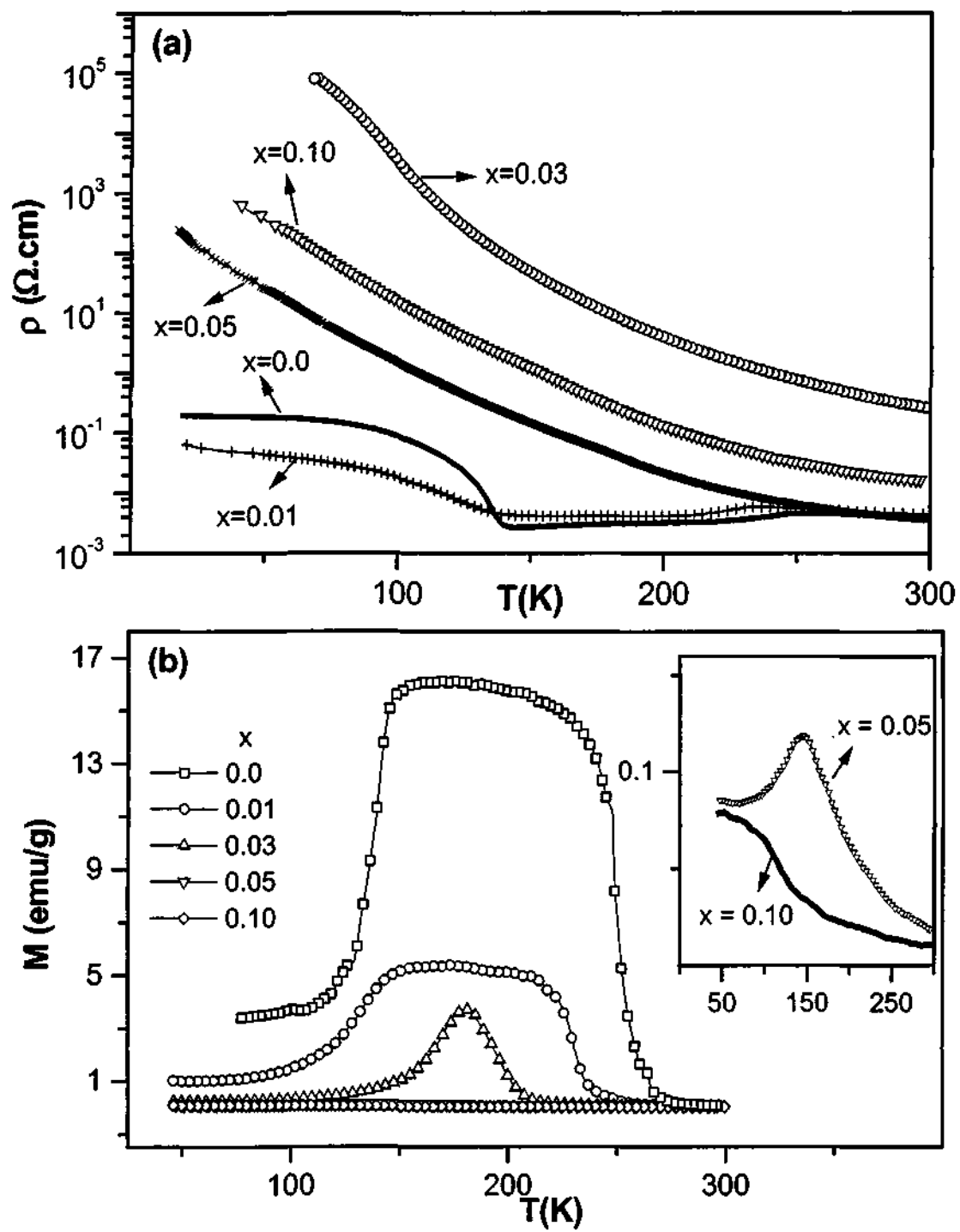Fig. 4.2.4 Temperature variation of (a) resistivity and (b) magnetization of $Nd_{0.5}Sr_{0.5}Mn_{1-x}Al_xO_3$.

Fig. 4.2.5 Temperature variation of (a) resistivity and (b) magnetization of $Nd_{0.5}Sr_{0.5}Mn_{1-x}Ga_xO_3$. Inset in (b) shows the magnetization for x = 0.05 and 0.10 on an enlarged scale.

compound when x = 0.01 except that the T_C decreases to 248 K. There is negligible effect on the T_N (T_{CO}) at ~ 150 K. The value of the saturation magnetization in the ferromagnetic region, however, decreases to a great extent. The effect of Ga substitution for x = 0.03 and 0.05 is interesting. These compositions show peaks in the magnetization curves around 180 and 145 K respectively. These peaks are reminiscent of the magnetization anomaly found in $Nd_{0.5}Ca_{0.5}MnO_3$ or other charge-ordered insulators (see Fig. 4.2.2). We consider that these anomalies as due to competition between ferromagnetism and antiferromagnetism in these compositions. In principle, we could consider the anomalies as due to charge ordering. If so, the T_{CO} decrease with increasing x. When x > 0.05, we see no anomaly in the magnetization and the material remains paramagnetic down to 50 K.

4.2.2 M = Cr, Fe, Co and Ni: In Table 4.2.3, the lattice parameters of $Nd_{0.5}Ca_{0.5}Mn_{1-x}M_xO_3$ (M = Cr, Fe, Co and Ni) are listed. Substitution of Mn site of $Nd_{0.5}Ca_{0.5}MnO_3$ by 1% Cr induces an insulator-metal (I-M) transition around 100 K as shown in Fig. 4.2.6 (a). The I-M transition temperature, T_{IM} increases with increase in Cr concentration upto x = 0.03 and thereafter decreases with further increase in the dopant concentration (Table 4.2.3). The resistivity data on $Nd_{0.5}Ca_{0.5}Mn_{1-x}Cr_xO_3$ are corroborated by the magnetization data (Fig. 4.2.6 (b)). Substitution by Cr^{3+} makes the material ferromagnetic below the ferromagnetic Curie temperature, T_C that is very close to T_{IM}. The inset in Fig. 4.2.6 (b) shows the plot of inverse magnetization as a function of temperature. The dip in the inverse magnetization data, which is the signature of charge-ordering is present for compositions up to x = 0.05 indicating that low concentration of Cr does not melt the

Table 4.2.3

Properties of $Nd_{0.5}Ca_{0.5}Mn_{1-x}M_xO_3$ (M = Cr, Fe, Co and Ni)

Composition	Lattice parameters (Å)[*]			T_{IM} (K)	T_C (K)	T_{CO} (K)
	$\underline{a}$	$\underline{b}$	$\underline{c}$			
$Nd_{0.5}Ca_{0.5}Mn_{1-x}Cr_xO_3$						
0.0	5.401	7.610	5.396	-	-	240
0.01	5.425	7.595	5.382	106	119	238
0.03	5.430	7.618	5.389	133	140	233
0.05	5.409	7.604	5.392	131	136	~202
0.10	5.450	7.622	5.339	~95	147	-
$Nd_{0.5}Ca_{0.5}Mn_{1-x}Fe_xO_3$						
0.01	5.404	7.617	5.393	-	-	238
0.03	5.409	7.599	5.389	-	-	219
0.05	5.408	7.619	5.392	-	-	~209
0.10	5.401	7.612	5.390	-	-	-
$Nd_{0.5}Ca_{0.5}Mn_{1-x}Co_xO_3$						
0.01	5.422	7.649	5.372	84	-	236
0.03	5.410	7.608	5.385	87	94	225
0.05	5.429	7.546	5.389	65	90	195
0.10	5.418	7.595	5.379	51	-	-
$Nd_{0.5}Ca_{0.5}Mn_{1-x}Ni_xO_3$						
0.01	5.412	7.608	5.385	90	103	236
0.03	5.414	7.606	5.380	96	101	221
0.05	5.409	7.619	5.381	71	95	-
0.1	5.405	7.608	5.376	59	-	-

[*] *Space group: Pnma*; Uncertainties in the lattice parameters are within ± 0.001 Å

charge-ordered state completely. Hence, compositions with $x \leq 0.05$ show charge-ordering at high temperatures and on cooling undergo a transition to a ferromagnetic metallic (FMM) state.

Fig. 4.2.7 shows the temperature variation of magnetization of $Nd_{0.5}Ca_{0.5}Mn_{1-x}Fe_xO_3$. As evident from the figure, there is no significant effect on the magnetization when we substitute Mn site with Fe. There is a decrease in magnetization at low temperature for all substituted materials when compared to the parent manganate, $Nd_{0.5}Ca_{0.5}MnO_3$. Also, the hump like feature in the magnetization data corresponding to charge-ordering is not very clear for compositions with $x > 0.03$. All the materials remain insulating as the parent manganate (see Fig. 4.2.3).

The resistivity and magnetization data of the $Nd_{0.5}Ca_{0.5}Mn_{1-x}Co_xO_3$ compositions are shown in Fig. 4.2.8. As Mn^{3+} is progressively substituted by Co^{3+}, we observe an I-M transition varying between 50 and 90 K in the x range 0.01-0.1 (Table 4.2.3). The transition temperature increases slightly and then decreases with increase in x in agreement with *Raveau et al.* [3]. The magnetization data show definitive evidence for ferromagnetism around 90 K only in the x = 0.03 and 0.05 compositions, with the magnetization increasing sharply around this temperature (Fig 4.2.8 (b)). There is only a small increase in magnetization in the x = 0.01 and 0.1 compositions. The x = 0.01 composition shows charge-ordering with the T_{CO} close to that of the parent manganate (inset of Fig. 4.2.8 (b)) and the T_{CO} decreases with increase in x (Table 4.2.3). The x = 0.1

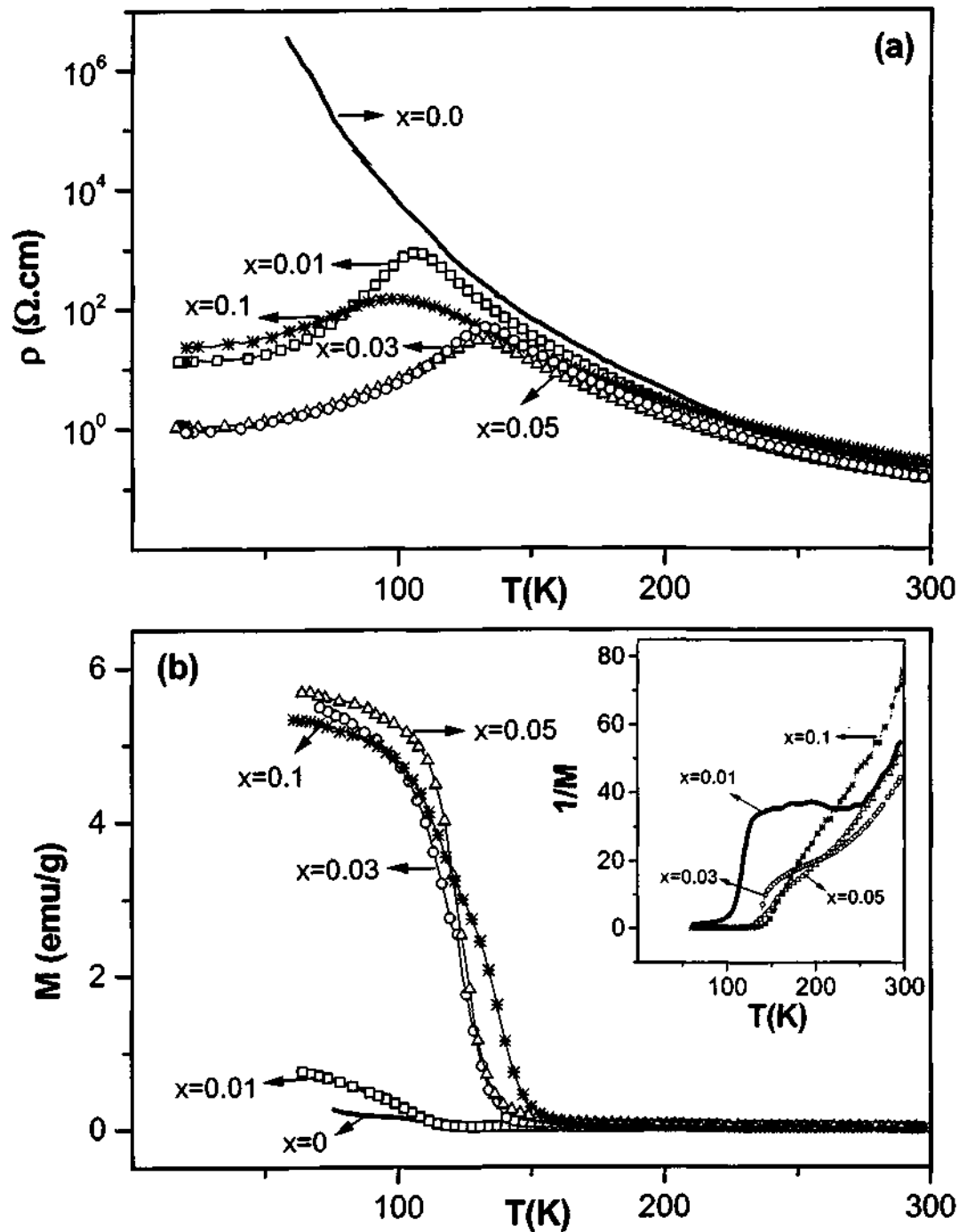[3] B. Raveau, A. Maignan and C. Martin J. Solid State Chem. 130, 162 (1997).

Fig. 4.2.6 Temperature variation of (a) resistivity and (b) magnetization of $Nd_{0.5}Ca_{0.5}Mn_{1-x}Cr_xO_3$. Inset in (b) shows the plots of the reciprocal of magnetization against temperature to show the T_{CO}.
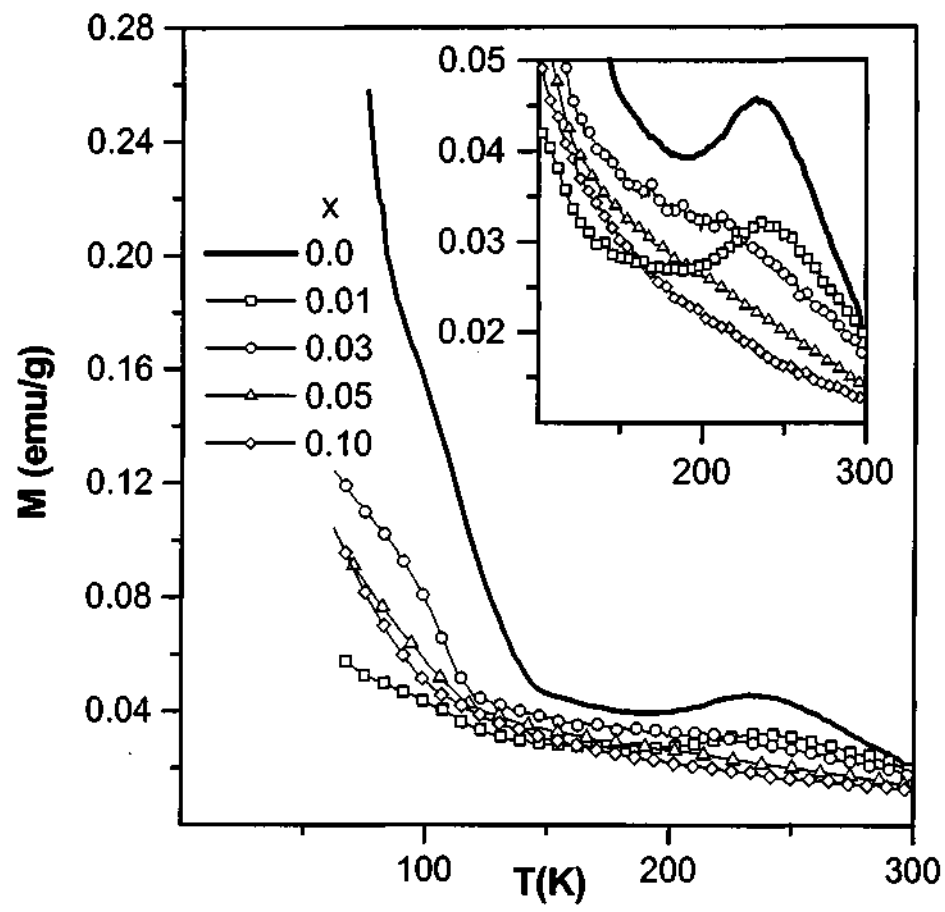
140

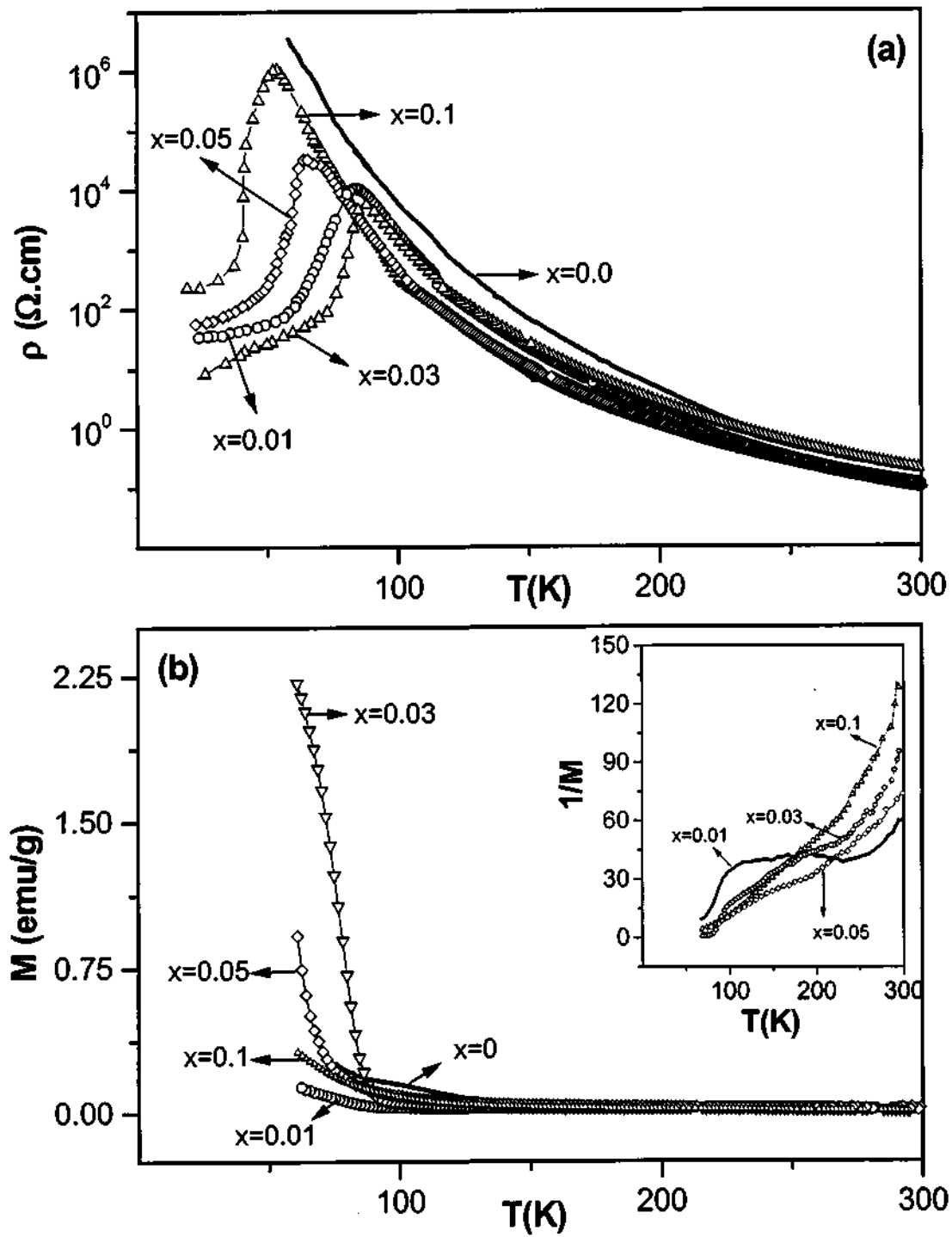Fig. 4.2.7 Temperature variation of magnetization of $Nd_{0.5}Ca_{0.5}Mn_{1-x}Fe_xO_3$. Inset shows the magnetization data on an enlarged scale to show the T_{CO}.

Fig. 4.2.8 Temperature variation of (a) resistivity and (b) magnetization of $Nd_{0.5}Ca_{0.5}Mn_{1-x}Co_xO_3$. Inset in (b) shows the plots of the reciprocal of magnetization against temperature to show the T_{CO}.
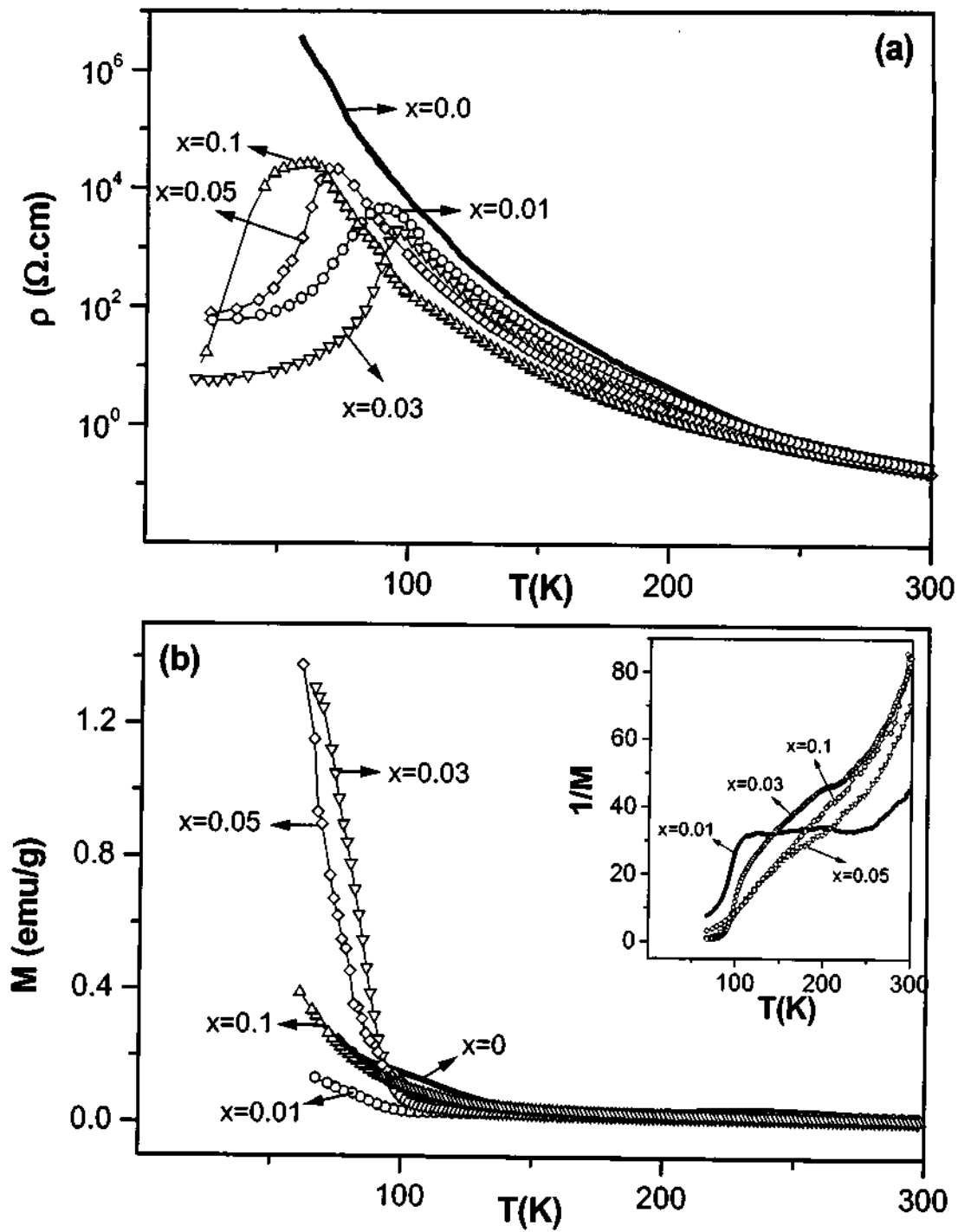
142

Fig. 4.2.9 Temperature variation of (a) resistivity and (b) magnetization of $Nd_{0.5}Ca_{0.5}Mn_{1-x}Ni_xO_3$. Inset in (b) shows the plots of the reciprocal of magnetization against temperature to show the T_{CO}.

143

composition remains paramagnetic throughout, although it shows a broad I-M transition around 50 K.

The resistivity and magnetization behaviors of $Nd_{0.5}Ca_{0.5}Mn_{1-x}Ni_xO_3$ compositions are similar to those of the corresponding Co substituted compositions (Fig. 4.2.9). However, the T_C and T_{CO} values are slightly higher than those of the corresponding $Nd_{0.5}Ca_{0.5}Mn_{1-x}Co_xO_3$ compositions. The present results on Co and Ni substituted $Nd_{0.5}Ca_{0.5}MnO_3$ are comparable to that of *Maignan et al.* [4], with the difference that these workers do not report the charge-ordering transition temperature in these manganates. *Maignan et al.* employed a magnetic field of 1.45 T, while a field of 100 G was employed in the present study. The charge-ordering transition is not easily seen in magnetic measurements when high magnetic fields are employed. It appears that in both $Nd_{0.5}Ca_{0.5}Mn_{1-x}Co_xO_3$ and $Nd_{0.5}Ca_{0.5}Mn_{1-x}Ni_xO_3$, ferromagnetic clusters are present when $x > 0.05$, although ferromagnetic transitions do not occur. The curious feature of these two systems is that when $x \leq 0.05$, the T_{CO} is higher than the T_C, unlike in $Nd_{0.5}Sr_{0.5}MnO_3$ where $T_C > T_{CO}$. The CO state is not entirely destroyed in $Nd_{0.5}Ca_{0.5}MnO_3$ by substitution of Cr, Ni and Co.

In Table 4.2.4, the lattice parameters of $Nd_{0.5}Sr_{0.5}Mn_{1-x}M_xO_3$ (M = Cr, Fe, Co and Ni) are listed. The effect of Cr^{3+} substitution on the properties of $Nd_{0.5}Sr_{0.5}MnO_3$ is indeed marked. Thus, in $Nd_{0.5}Sr_{0.5}Mn_{1-x}Cr_xO_3$, when $x = 0.01$, there is a slight decrease in the T_C but we do not see the resistance anomaly at T_{CO} as in the parent compound (Fig. 4.2.10). The material is metallic below T_C, down to low temperatures. It seems that 1% Cr

[4] A. Maignan, F. Damay, C. Martin and B. Raveau Mater. Res. Bull 32, 965 (1997).

Table 4.2.4

Properties of $Nd_{0.5}Sr_{0.5}Mn_{1-x}M_xO_3$ (M = Cr, Fe, Co and Ni)

Composition	Lattice parameters (Å)[a]			T_{IM} (K)	T_C (K)	T_{CO} (K)
	$\underline{a}$	$\underline{b}$	$\underline{c}$			
$Nd_{0.5}Sr_{0.5}Mn_{1-x}Cr_xO_3$						
0.0	5.426	7.634	5.475	249	267	147
0.01	5.427	7.638	5.476	243	253	-
0.03	5.428	7.633	5.471	242	244	-
0.05	5.425	7.635	5.472	233	230	-
0.10	5.428	7.629	5.467	210 (140)[b]	216	-
$Nd_{0.5}Sr_{0.5}Mn_{1-x}Fe_xO_3$						
0.01	5.424	7.637	5.476	213[c]	240	140
0.03	5.426	7.635	5.476	174[c]	210	160
0.05	5.444	7.643	5.472	-	-	-
0.10	5.428	7.638	5.475	-	-	-
$Nd_{0.5}Sr_{0.5}Mn_{1-x}Co_xO_3$						
0.03	5.425	7.630	5.471	201	240	-
0.05	5.425	7.630	5.475	~170	233	-
0.10	5.416	7.632	5.468	-	-	-
$Nd_{0.5}Sr_{0.5}Mn_{1-x}Ni_xO_3$						
0.01	5.420	7.633	5.477	219	257	-
0.03	5.432	7.633	5.473	212	257	-
0.05	5.426	7.627	5.469	171	245	-
0.10	5.434	7.626	5.457	-	-	-

[a] *Space group: Imma*; Uncertainties in the lattice parameters are within ± 0.001 Å

[b] Corresponds to the second hump in the resistivity data.

[c] Corresponds to the slope change in the resistivity data.

145

substitution suffices to destroy the CO state in $Nd_{0.5}Sr_{0.5}MnO_3$. The resistivity behavior of the x = 0.03 composition is similar and the FMM state occurs down to the lowest temperature. Such behavior is also found when x = 0.05. When x = 0.1, T_C appears to be around 210 K, but there is a slight hump in the resistivity around 140 K in the metallic regime. The resistivity data of $Nd_{0.5}Sr_{0.5}Mn_{1-x}Cr_xO_3$ are nicely corroborated by the magnetization data (Fig. 4.2.10(b)). Accordingly, the x = 0.03, 0.05 and 0.1 compositions show a ferromagnetic T_C (see Table 4.2.4) with the sample remaining ferromagnetic down to 50 K. There is no charge-ordering transition around 150 K, as in the parent compound (x = 0.0).

In the Fe substituted $Nd_{0.5}Sr_{0.5}MnO_3$ compositions, $Nd_{0.5}Sr_{0.5}Mn_{1-x}Fe_xO_3$ (Fig. 4.2.11), there is no sharp resistivity anomaly corresponding to charge-ordering when x = 0.01 as seen in the case of the parent compound but only a change in the slope of resistivity around 200 K. For higher concentration of the dopant, the material becomes insulating. The magnetization behavior of $Nd_{0.5}Sr_{0.5}Mn_{1-x}Fe_xO_3$, when x = 0.01 is similar to the parent manganate, but there is a decrease in the magnitude of magnetization and the T_C. The x = 0.03 and 0.05 compositions show a hump in the magnetization as seen in the case of analogous Ga substituted compositions (Fig. 4.2.5). These peaks are reminiscent of the magnetization anomaly found in $Nd_{0.5}Ca_{0.5}MnO_3$ or other charge-ordered insulators (see Fig. 4.2.2). We consider that these anomalies as due to competition between ferromagnetism and antiferromagnetism in these compositions.

The temperature variation of resistivity and magnetization of $Nd_{0.5}Sr_{0.5}Mn_{1-x}Co_xO_3$ is shown in Fig. 4.2.12. The x = 0.03 composition shows metallic behavior below 200 K in

146

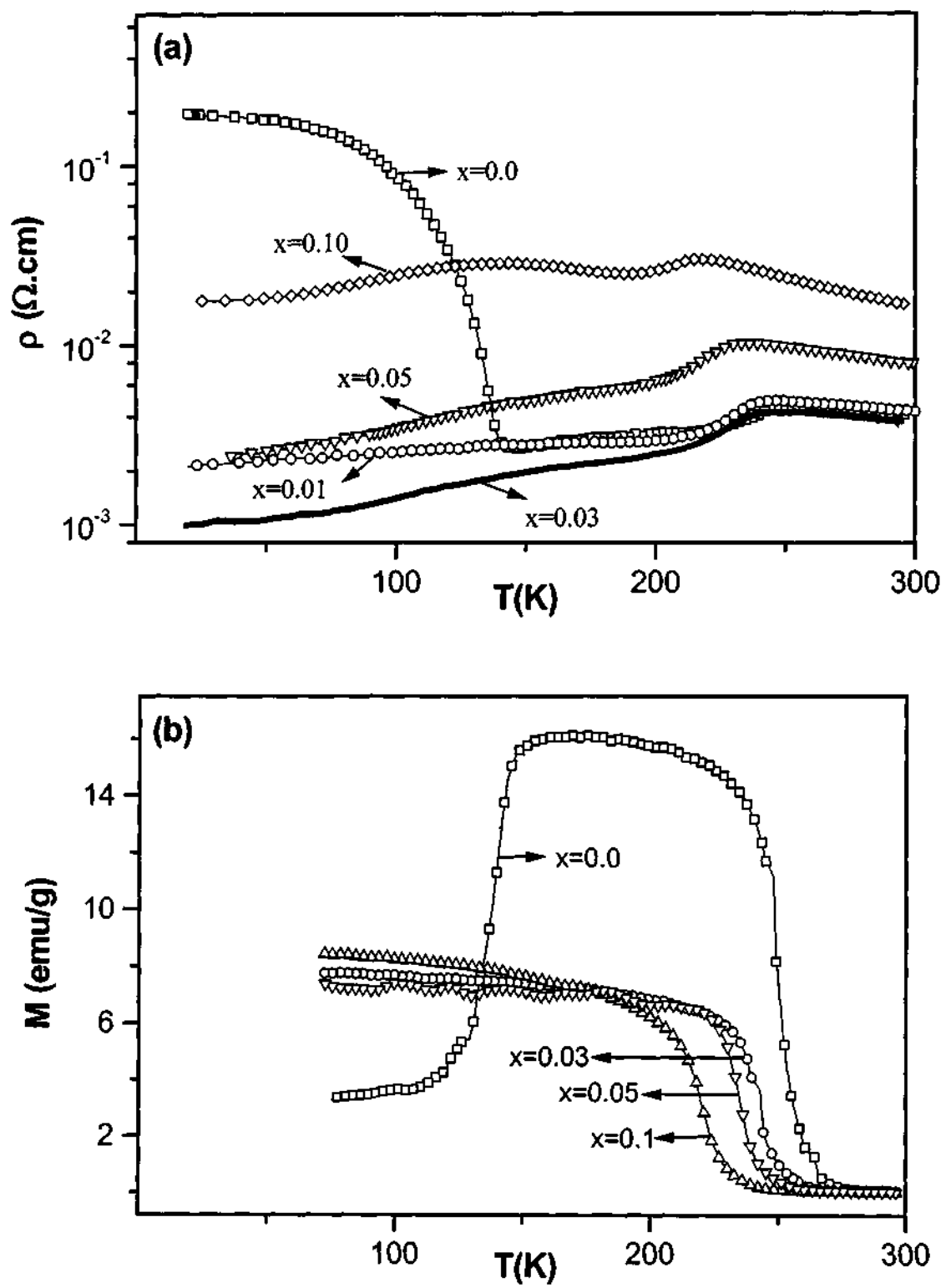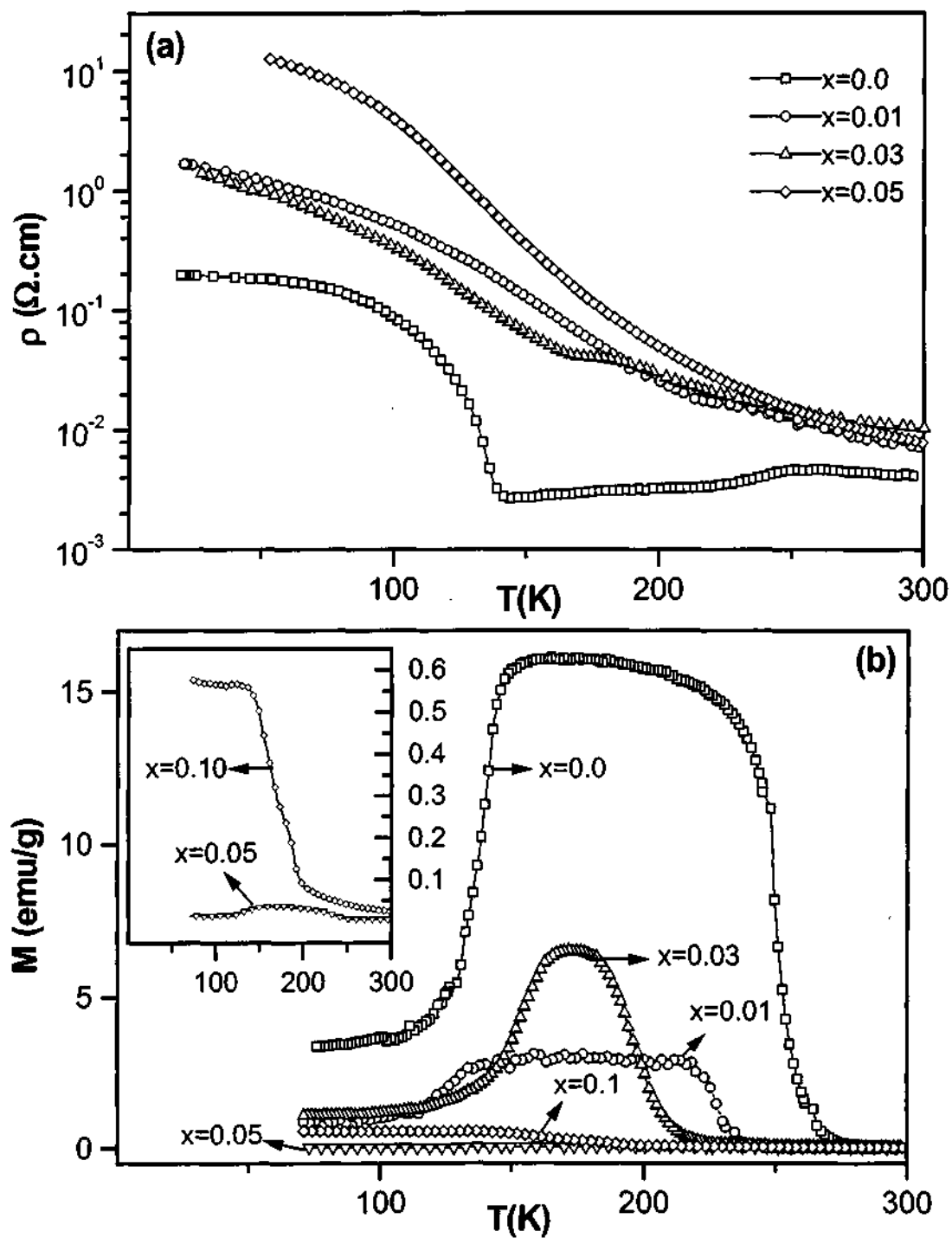Fig. 4.2.10 Temperature variation of (a) resistivity and (b) magnetization of $Nd_{0.5}Sr_{0.5}Mn_{1-x}Cr_xO_3$.

Fig. 4.2.11 Temperature variation of (a) resistivity and (b) magnetization of $Nd_{0.5}Sr_{0.5}Mn_{1-x}Fe_xO_3$. Inset in (b) shows the magnetization for $x = 0.05$ and 0.10 on an enlarged scale.
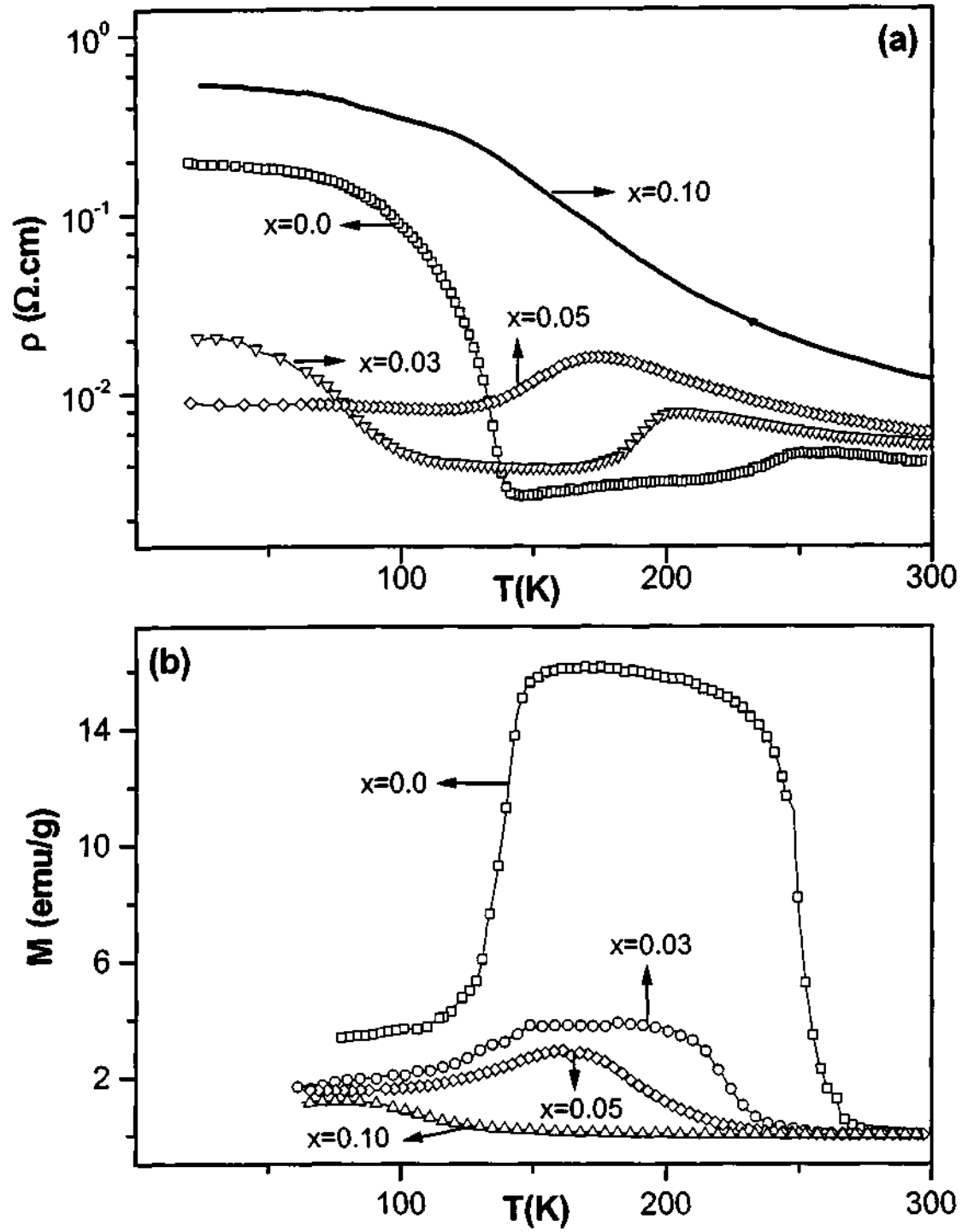
148

(a)

10^0

10^{-1}

ρ (Ω.cm)

10^{-2}

x=0.10

x=0.0

x=0.05

x=0.03

100   T(K)   200   300

(b)

14

10

M (emu/g)

6

2

x=0.0

x=0.03

x=0.05

x=0.10

100   T(K)   200   300

Fig. 4.2.12 Temperature variation of (a) resistivity and (b) magnetization of $Nd_{0.5}Sr_{0.5}Mn_{1-x}Co_xO_3$.

149
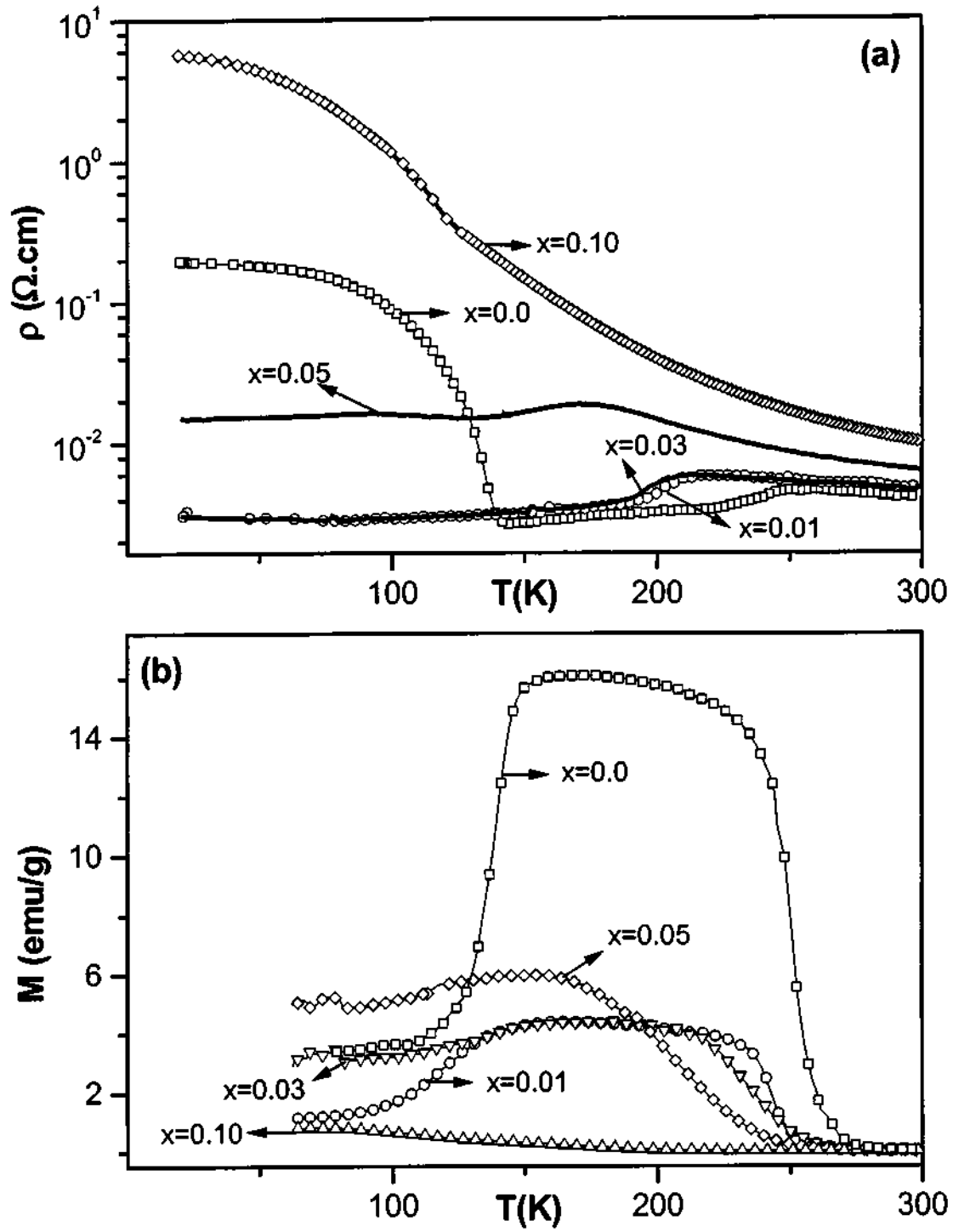
Fig. 4.2.13 Temperature variation of (a) resistivity and (b) magnetization of $Nd_{0.5}Sr_{0.5}Mn_{1-x}Ni_xO_3$.

the resistivity data, but there is a slight increase below 100 K. The magnetization data shows a lowering in the ferromagnetic T_C to ~ 240 K (Table 4.2.4), and we find no evidence for antiferromagnetism at lower temperatures. When x = 0.5, the material exhibits metal-like resistivity below 170 K and a broad maximum in the magnetization around this temperature. This composition does not show a sharp ferromagnetic transition. When x = 0.1, the material is a paramagnetic insulator throughout.

Fig. 4.2.13 shows the resistivity and magnetization as a function of temperature of $Nd_{0.5}Sr_{0.5}Mn_{1-x}Ni_xO_3$ for values of x ranging from 0.01 to 0.1. When x = 0.01 or 0.03, we see no evidence for charge-ordering in the resistivity data and the material remains metallic down to the lowest temperature, below the I-M transition. The I-M transition temperature, however, is substantially lower than that in the parent compound (Table 4.2.4). Accordingly, the magnetization data show the ferromagnetic T_C to be lower in the x = 0.01 and 0.03 composition (see Fig. 4.2.13 (b) and Table 4.2.4). There is a decrease in magnetization in the x = 0.01 composition around 140 K, but this is unlikely to be because of charge-ordering as there is no concomitant increase in resistivity around this temperature. When x = 0.05, there is a metal-like resistivity behavior below 175 K, but the magnetization only shows a broad maximum without evidence for an antiferromagnetic transition. The ferromagnetic transition is also not sharp. When x = 0.1, however, the material is a paramagnetic insulator from 300 K down to the lowest temperature studied. The main difference between the Co and Ni substituted $Nd_{0.5}Sr_{0.5}MnO_3$ compositions are in the low temperature resistivity behavior. When x = 0.03, the material is metallic down to low temperatures in the Ni case, but not so in the Co case. Ferromagnetism is found

only in x = 0.03 in both Ni and Co systems and charge ordering is absent in all the compositions with x > 0.0.

Why substitution of Cr, Co and Ni in place of Mn destroys the CO state in $Ln_{0.5}A_{0.5}MnO_3$ is worthy of comment. It is unlikely to be due to the disorder created by such substitution. Otherwise, substitution of Mn by Al^{3+} or Fe^{3+} should also have given rise to I-M transitions. The effect of substitution by Cr^{3+}, Co^{3+} and Ni^{3+} must have an electronic origin. Cr^{3+} has the same electronic configuration as Mn^{4+} ($t_{2g}^3 e_g^0$). It is possible that when Cr^{3+} is in the Mn^{3+} site, there is some electron hopping between Mn^{3+} and Cr^{3+} sites which triggers electron exchange between the Mn^{3+} and Mn^{4+} sites. The Co^{3+} and Ni^{3+} ions, in the low-spin states have empty e_g orbitals, the electronic configurations being $t_{2g}^6 e_g^0$ and $t_{2g}^6 e_g^1$ respectively. The presence of an empty e_g orbital in the substitutent ion seems to be necessary to destroy the CO state. We must recall that Fe^{3+} has the configuration $t_{2g}^3 e_g^2$ and would not favor electron jumping as Cr^{3+}, Co^{3+} and Ni^{3+} ions. We suggest that the electron jump between the substitutent transition metal ion with empty e_g orbital and Mn^{3+} ion may be the initial condition for the melting of the CO states in these materials. In the foregoing discussion, we have assumed that both Co and Ni are in the 3+ state. If they occur in the 2+ state there would be a proportionate conversion of Mn^{3+} to the 4+] state. It is not clear why such oxidation states would affect the CO states of the manganates. The present results are consistent with the 3+ state of both Co and Ni.

We have also investigated the effect of substitution of the above mentioned substitutents in the Mn site of $Y_{0.5}Ca_{0.5}MnO_3$. In Table 4.2.5, the lattice parameters of $Y_{0.5}Ca_{0.5}Mn_{1-x}M_xO_3$ (M = Cr, Fe, Co and Ni; x = 0.0, 0.03) are listed. $Y_{0.5}Ca_{0.5}MnO_3$ with

152

Table 4.2.5

Properties of $Y_{0.5}Ca_{0.5}Mn_{1-x}M_xO_3$ (M = Al, Cr, Fe, Co and Ni)

Composition	Lattice parameters (Å)[*]			T_{CO}
	a	b	c	(K)
$Y_{0.5}Ca_{0.5}MnO_3$	5.537	7.443	5.295	260
$Y_{0.5}Ca_{0.5}Mn_{0.97}Al_{0.03}O_3$	5.497	7.443	5.294	-
$Y_{0.5}Ca_{0.5}Mn_{0.97}Fe_{0.03}O_3$	5.509	7.450	5.296	-
$Y_{0.5}Ca_{0.5}Mn_{0.97}Cr_{0.03}O_3$	5.495	7.451	5.301	-
$Y_{0.5}Ca_{0.5}Mn_{0.97}Co_{0.03}O_3$	5.505	7.449	5.296	-
$Y_{0.5}Ca_{0.5}Mn_{0.97}Ni_{0.03}O_3$	5.502	7.456	5.291	-

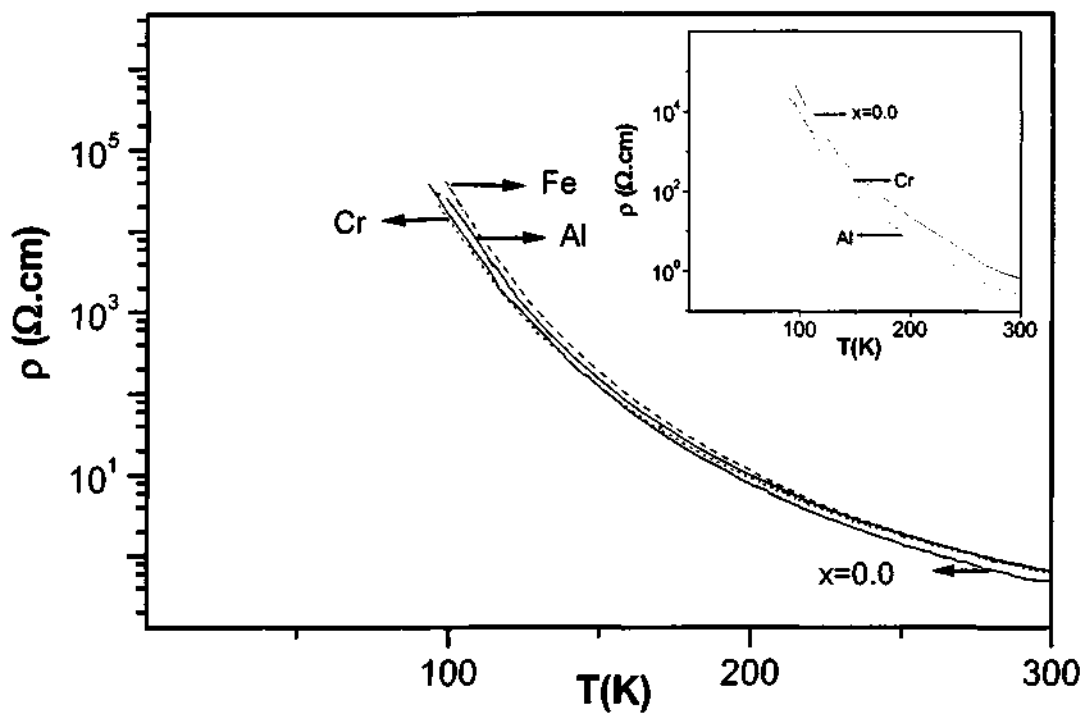[*] *Space group: Pnma*; Uncertainties in the lattice parameters are within ± 0.001 Å.

Fig. 4.2.14 Temperature variation of resistivity of $Y_{0.5}Ca_{0.5}Mn_{0.97}M_{0.03}O_3$ (M = Al, Cr and

Fe). Inset shows the data for $Gd_{0.5}Ca_{0.5}Mn_{0.97}M_{0.03}O_3$ (M = Al and Cr).

a $\langle r_A \rangle$ = 1.13 Å is a charge-ordered insulator and does not show ferromagnetism at any temperature [5]. Even pulsed magnetic field of 100 T is not able to induce a I-M transition in this manganate [6]. In Fig. 4.2.14, we show the variation of resistivity of $Y_{0.5}Ca_{0.5}Mn_{0.97}M_{0.03}O_3$ (M = Al, Fe and Cr) as a function of temperature. We see that there is almost no effect of such substitution on the resistivity of $Y_{0.5}Ca_{0.5}MnO_3$ for all M mentioned above. A decrease in the extent of substitution to x = 0.01 or an increase up to x = 0.1 showed no difference in resistivity behavior (Table 4.2.5). We found a similar result with $Gd_{0.5}Ca_{0.5}MnO_3$ (see inset of Fig. 4.2.14), where substitution of Al^{3+} or Cr^{3+} for Mn^{3+} had no effect on the resistivity. Thus, both $Y_{0.5}Ca_{0.5}Mn_{1-x}M_xO_3$ and $Gd_{0.5}Ca_{0.5}Mn_{1-x}M_xO_3$ compositions remain insulating from room temperature down to the lowest temperature for M = Al, Cr, Fe, Co and Ni. The magnetization data of the substituted compositions do not show a clear indication of charge-ordering. This extraordinary behavior of $Y_{0.5}Ca_{0.5}MnO_3$ and $Gd_{0.5}Ca_{0.5}MnO_3$ towards B-site substitution could be attributed to the rather small $\langle r_A \rangle$ (< 1.15 Å) of these two manganates.

4.2.3 M = Ge, Ti and Zr: In Table 4.2.6, the lattice parameters of $Nd_{0.5}A_{0.5}Mn_{1-x}M_xO_3$ (A = Ca, Sr; M = Ge, Ti and Zr) are listed. Substitution of Ge on the Mn site of $Nd_{0.5}Ca_{0.5}MnO_3$ does not affect the charge ordering transition to a great extent (Table4.2.6). Thus, in $Nd_{0.5}Ca_{0.5}Mn_{1-x}Ge_xO_3$ there is a clear indication of charge ordering

[5] A. Arulraj, R. Gundakaram, A. Biswas, N. Gayathri, A. K. Raychaudhuri and C. N. R. Rao, J. Phys. Condens. Matter 10, 4447 (1998).
[6] (a) M. Tokunaga, N. Miura, Y. Tomioka and Y. Tokura Phys. Rev. B57, 5259 (1998). (b) M. Tokunaga, N. Miura, Y. Tomioka and Y. Tokura, Phys. Rev. B60, 6219 (1999).

Table 4.2.6

Properties of $Nd_{0.5}A_{0.5}Mn_{1-x}M_xO_3$ (M = Ge, Ti and Zr)

Composition	Lattice parameters (Å)[*]			T_{IM}	T_C	T_{CO}
	$\underline{a}$	$\underline{b}$	$\underline{c}$	(K)	(K)	(K)
$Nd_{0.5}Ca_{0.5}Mn_{1-x}Ge_xO_3$						
0.0	5.401	7.610	5.396	-	-	240
0.01	5.407	7.596	5.387	-	-	238
0.03	5.410	7.605	5.391	-	-	239
0.05	5.399	7.604	5.387	-	-	237
0.1	5.408	7.611	5.392	-	-	-
$Nd_{0.5}Sr_{0.5}Mn_{1-x}Ge_xO_3$						
0.0	5.426	7.634	5.475	249	267	147
0.01	5.429	7.629	5.471	244	249	127
0.03	5.425	7.629	5.474	230	237	-
0.05	5.424	7.630	5.475	~145	233	-
$Nd_{0.5}Sr_{0.5}Mn_{1-x}Ti_xO_3$						
0.01	5.430	7.625	5.466	245	259	130
0.03	5.430	7.631	5.469	224	245	-
0.05	5.460	7.620	5.466	192	229	-
0.10	5.437	7.660	5.479	71	-	-
$Nd_{0.5}Sr_{0.5}Mn_{1-x}Zr_xO_3$						
0.01	5.455	7.637	5.472	239	~256	-
0.03	5.429	7.656	5.470	~165	~252	-
0.05	5.434	7.661	5.471	~159	-	-

[*]Uncertainties in the lattice parameters are within ± 0.001 Å.

156
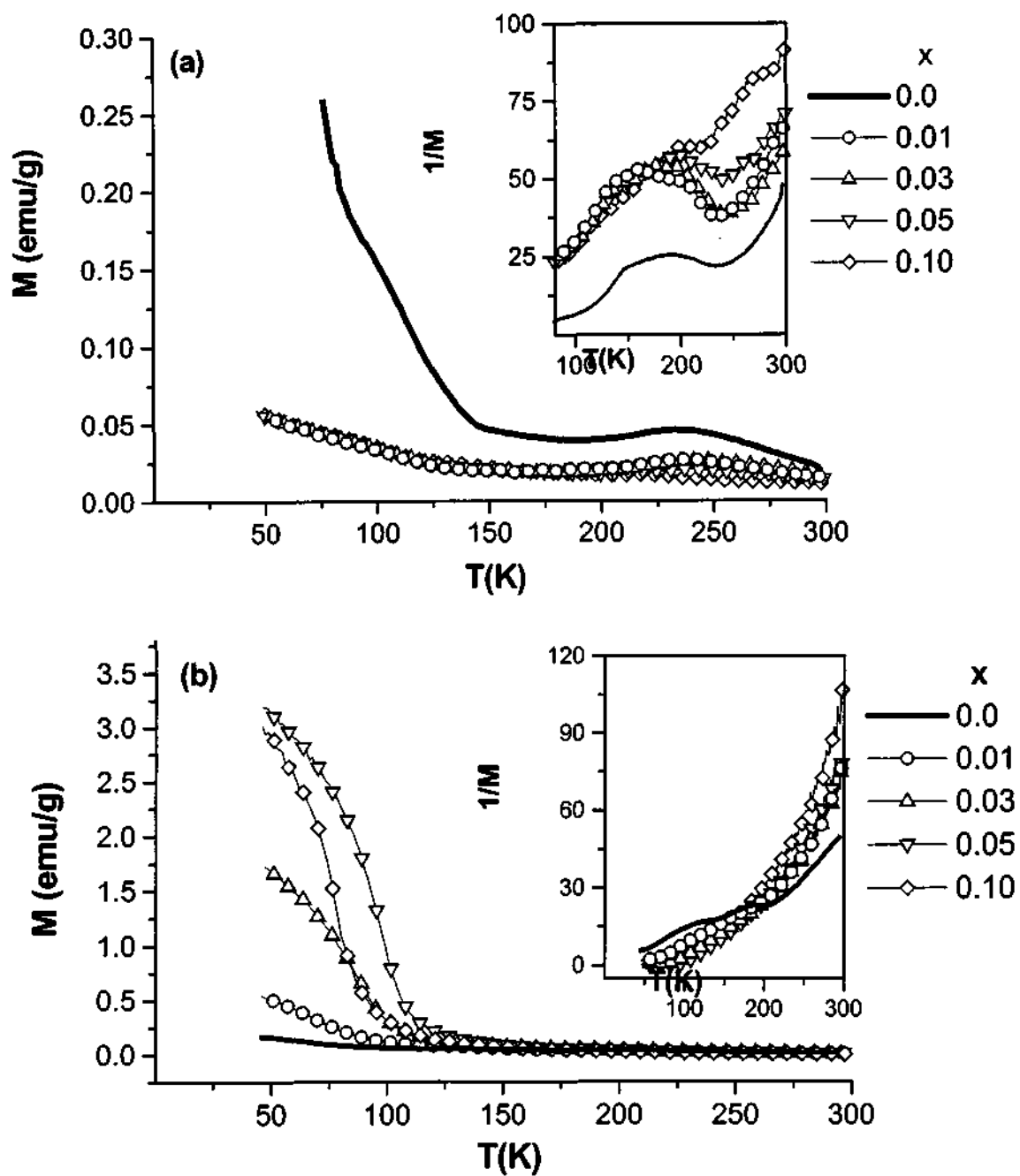
Fig. 4.2.15 Temperature variation of magnetization of (a) $Nd_{0.5}Ca_{0.5}Mn_{1-x}Ge_xO_3$ and (b) $Pr_{0.64}Ca_{0.36}Mn_{1-x}GeO_3$. The insets are the plots of inverse magnetization as a function of temperature to show the charge ordering transition.
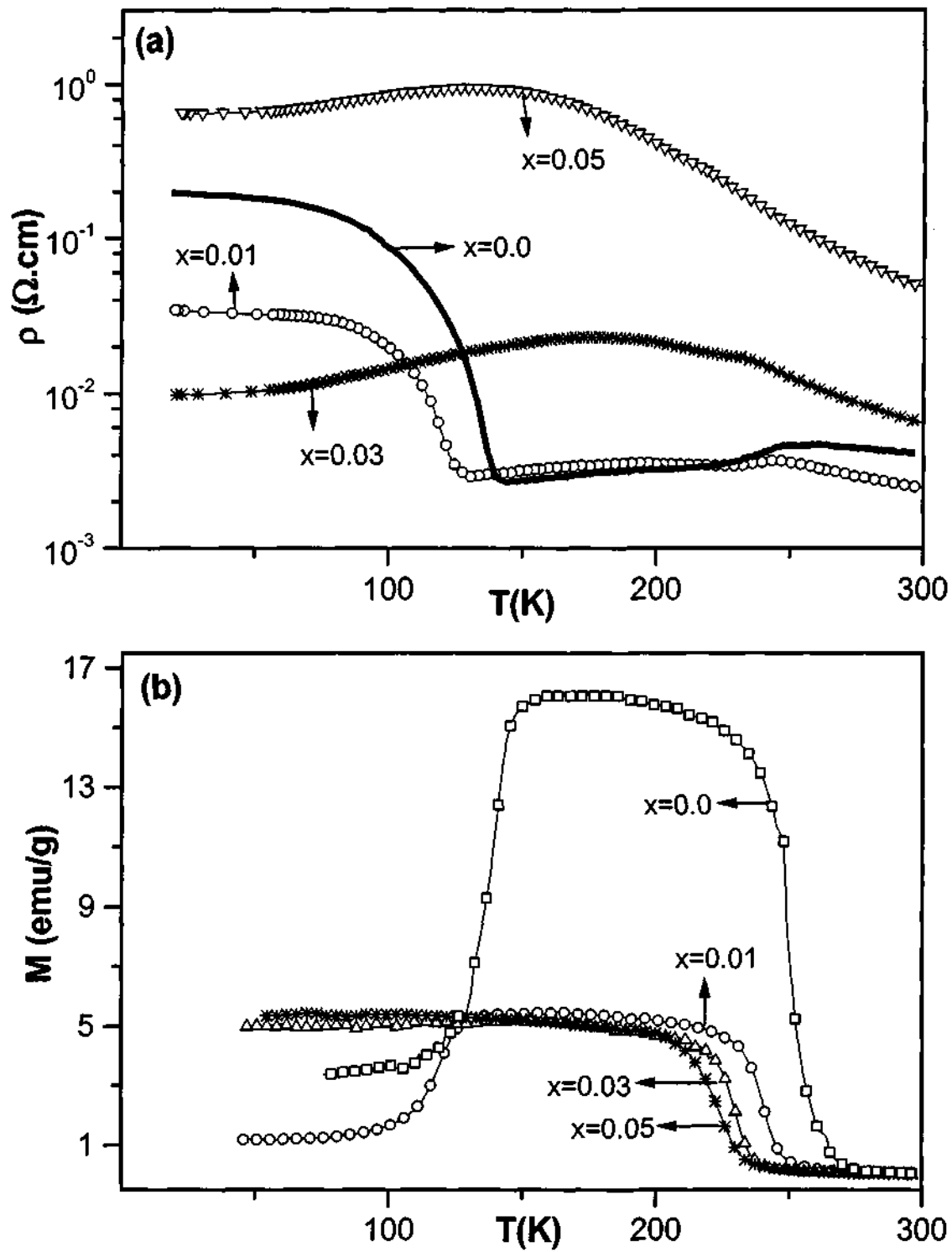
Fig. 4.2.16 Temperature variation of (a) resistivity and (b) magnetization of $Nd_{0.5}Sr_{0.5}Mn_{1-x}Ge_xO_3$.

upto x = 0.05 (Fig. 4.2.15 (a)). All the Ge substituted compositions are insulating just as the parent compound.

Damay et al. [7] have studied the effect of substitution of Ga on $Pr_{0.6}Ca_{0.4}MnO_3$ and found that such a doping not only destroys charge-ordering but also induces a transition from an antiferromagnetic insulating state to a ferromagnetic metallic state at low temperatures. We have examined the effect of Ge substitution on the properties of $Pr_{0.64}Ca_{0.36}MnO_3$. In $Pr_{0.64}Ca_{0.36}Mn_{1-x}Ge_xO_3$, even a small concentration of Ge (x = 0.01) destroys the charge ordering (Fig. 4.2. 15 (b)). With increase in x, there is an increase in the ferromagnetic component at low temperatures (T < 120 K). The parent manganate (x = 0.0) generally shows the presence of ferromagnetic clusters at low temperatures, but the size of these clusters or domains appears to increase substantially on substitution with Ge. This effect was not evident on substitution of Ge in $Nd_{0.5}Ca_{0.5}MnO_3$. All the Ge-doped $Pr_{0.64}Ca_{0.36}MnO_3$ compositions are insulating down to 70 K just as the parent compound.

In $Nd_{0.5}Sr_{0.5}Mn_{1-x}Ge_xO_3$, the x = 0.01 composition shows an electrical resistivity behavior similar to that of the parent manganate (x = 0.0) with a reduced magnitude of the change in resistivity at the metal-insulator transition. When x > 0.01, the materials show broad insulator-metal transitions (Fig. 4.2.16 (a)). The magnetization behavior of x = 0.01 composition is similar to the parent manganate, with a lowered T_C. When x > 0.01, there is no transition corresponding to antiferromagnetic ordering as in the parent compound, but a ferromagnetic transition persists even up to x = 0.10. The ferromagnetic Curie

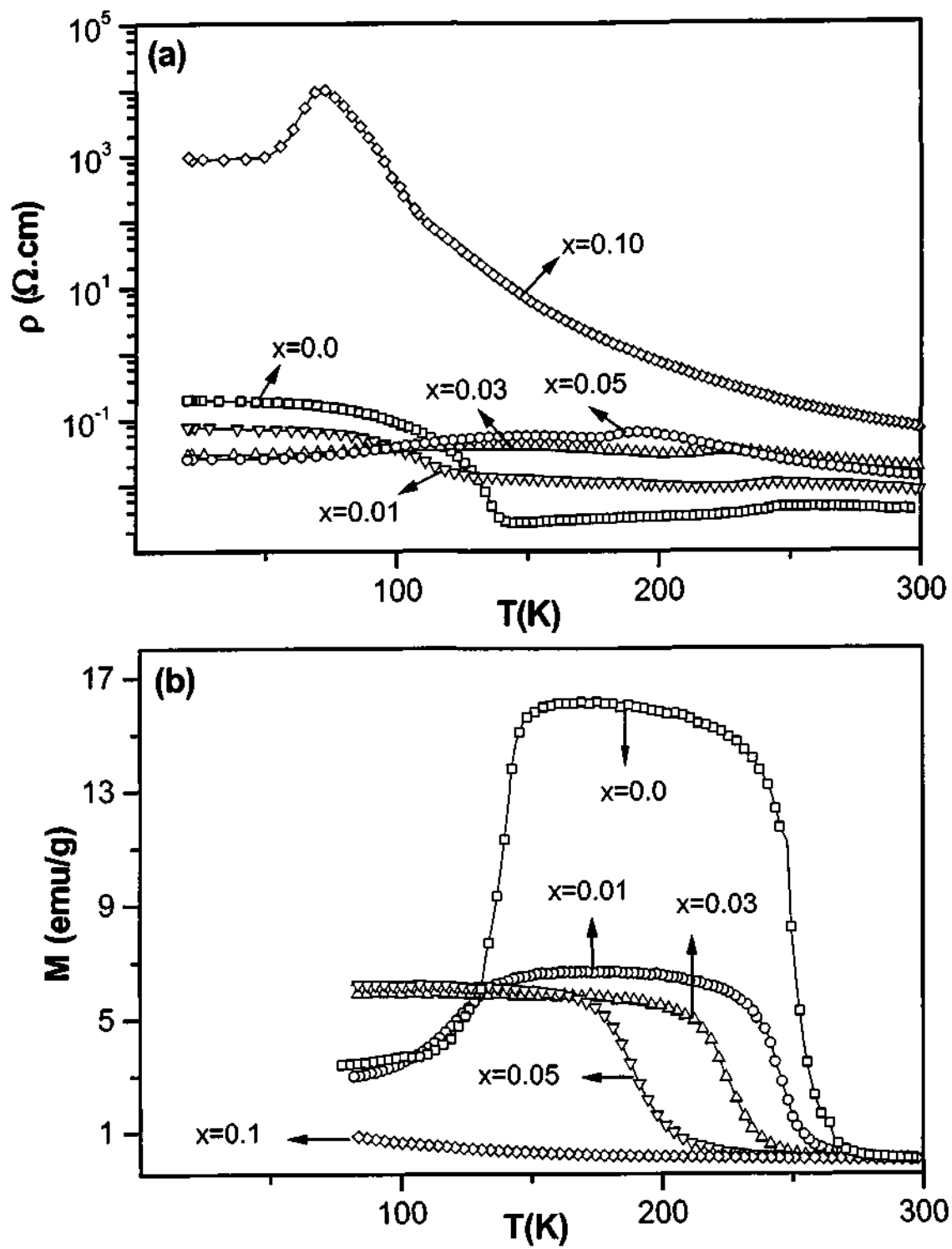[7] F. Damay, A. Maignan, C. Martin and B. Raveau J. Appl. Phys. 82, 1485 (1997).

Fig. 4.2.17 Temperature variation of (a) resistivity and (b) magnetization of $Nd_{0.5}Sr_{0.5}Mn_1$.$_xTi_xO_3$
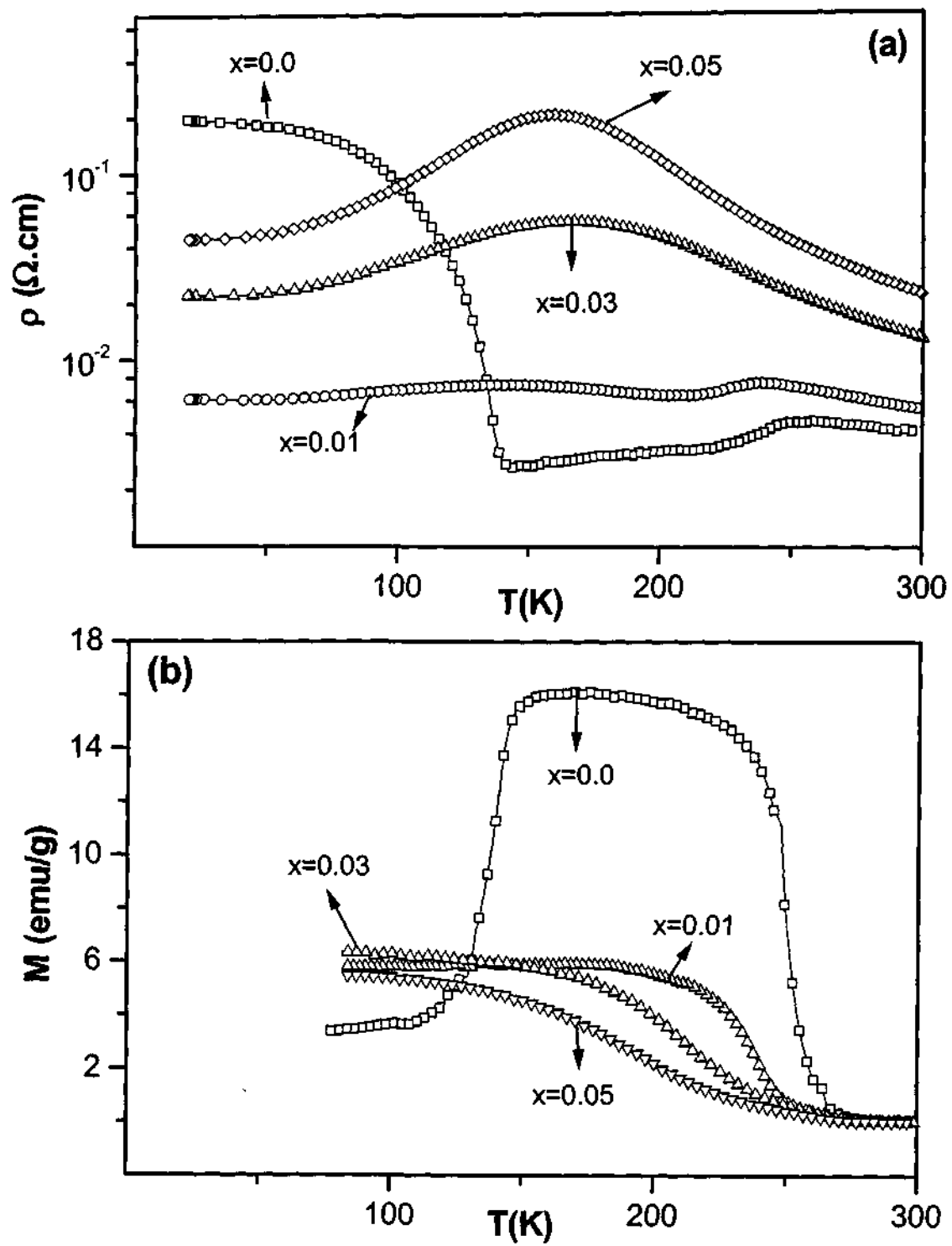
Fig. 4.2.18 Temperature variation of (a) resistivity and (b) magnetization of $Nd_{0.5}Sr_{0.5}Mn_{1-x}Zr_xO_3$.

temperature, T_C, decreases with increase in x (Table 4.2.6).

Substitution of Ti in the Mn site of $Nd_{0.5}Sr_{0.5}MnO_3$ also shows interesting magnetic and electrical transport behavior. In $Nd_{0.5}Sr_{0.5}Mn_{1-x}Ti_xO_3$, the x = 0.03 and 0.05 compositions remain metallic from 200 K to low temperatures while the x = 0.1 composition is an insulator down to 70 K (Fig. 4.2.17 (a)). Progressive substitution of Ti decreases the T_C up to x = 0.05 and the x = 0.1 composition does not exhibit ferromagnetism down to low temperatures (Fig. 4.2.17 (b)). The charge-ordering transition is seen only in the x = 0.01 composition (T_{CO} = 130 K, see Table 4.2.6). Clearly, charge-ordering is destroyed by Ti substitution (x > 0.01), although the ferromagnetism is not, suggesting thereby that charge-ordering is more sensitive to such disorder effects. Effect of Zr substitution in the Mn site of $Nd_{0.5}Sr_{0.5}MnO_3$ is similar to that of Ti substitution except that we do not see charge-ordering even for x = 0.01, probably because of the larger size of Zr (Fig. 4.2.18). The ferromagnetic T_C decreases with increase in Zr content. Insulator-metal transitions are seen in these materials around 170 K, up to x = 0.05.

4.2.4 The extraordinary effect of Ru substitution: Unlike the substitutents mentioned so far, substitution of Ru^{4+} in place of Mn^{4+} has marked effects on the properties of $Nd_{0.5}Ca_{0.5}MnO_3$ and $Nd_{0.5}Sr_{0.5}MnO_3$ (Table 4.2.7). Fig. 4.2.19 shows the powder X-ray diffraction patterns for the Ru substituted $Nd_{0.5}Sr_{0.5}MnO_3$ materials. In Fig. 4.2.20, we show the magnetic susceptibility and resistivity data of $Nd_{0.5}Ca_{0.5}Mn_{1-x}Ru_xO_3$. Substitution of Mn by even 1% Ru makes the substance ferromagnetic with a T_C at 135 K (Fig. 4.2.20 (a)). Increase in Ru content progressively increases the T_C, giving a T_C of 240 K when x =

Table 4.2.7

Properties of $Nd_{0.5}A_{0.5}Mn_{1-x}Ru_xO_3$ (A = Ca, Sr)

Composition	Lattice parameters (Å)[a]			T_{IM}	T_C	T_{CO}
	a	b	c	(K)	(K)	(K)
$Nd_{0.5}Ca_{0.5}Mn_{1-x}Ru_xO_3$						
0.01	5.404	7.635	5.404	130	135	230
0.03	5.417	7.629	5.391	149	157	217[b]
0.05	5.423	7.619	5.394	149	202	-
0.10	5.411	7.634	5.402	-	240	-
$Nd_{0.5}Sr_{0.5}Mn_{1-x}Ru_xO_3$						
0.01	5.418	7.628	5.470	263	274	-
0.03	5.425	7.631	5.472	~279	283	-
0.05	5.434	7.642	5.469	~284	290	-
0.10	5.444	7.660	5.475	-	~300	-

[a] Uncertainties in the lattice parameters are within ± 0.001 Å.

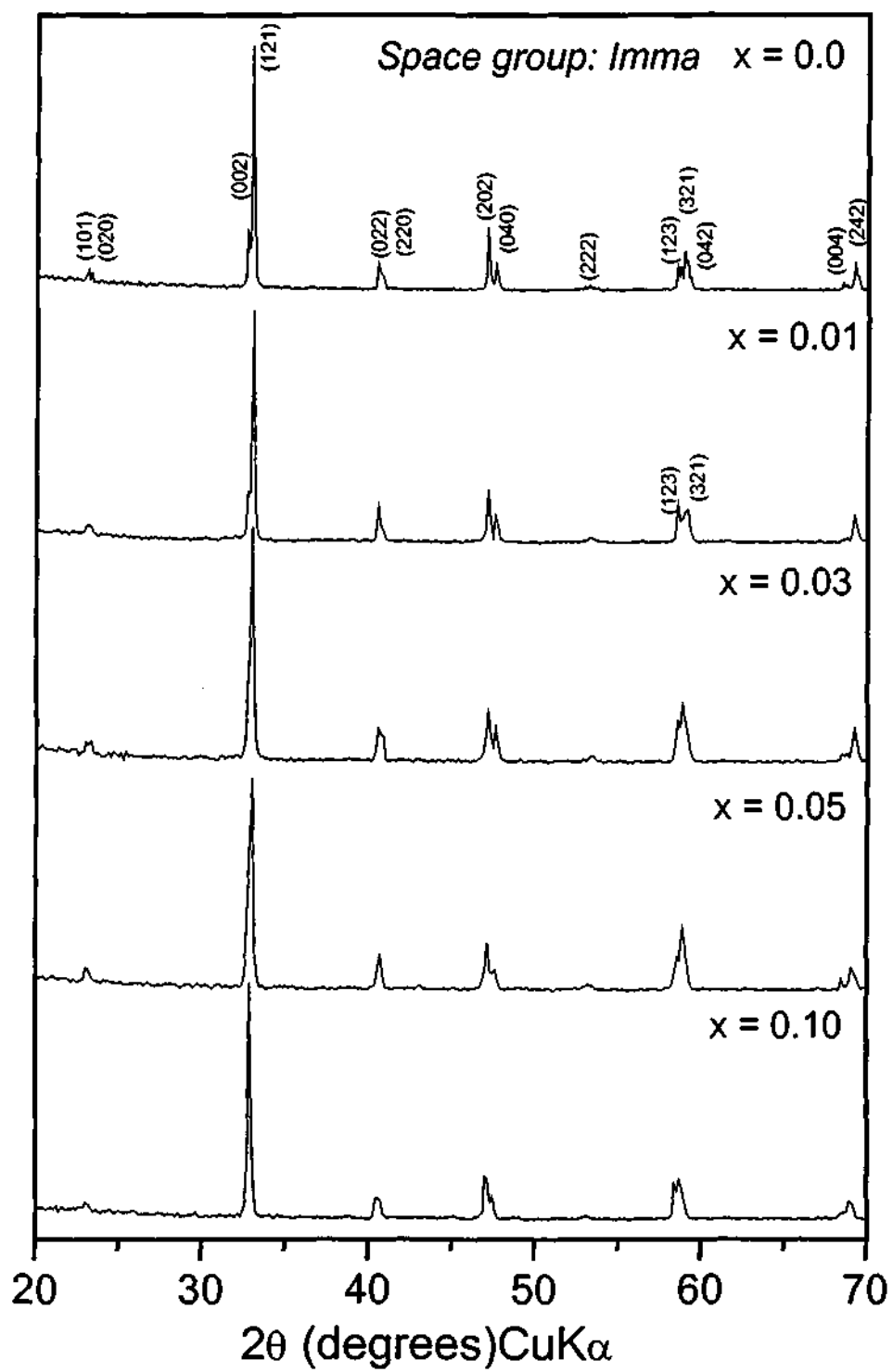[b] T_{CO} obtained from the slope change in $1/\chi$ versus T plot.

Fig. 4.2.19 Powder X-ray diffraction patterns of $Nd_{0.5}Sr_{0.5}Mn_{1-x}Ru_xO_3$ compositions.

0.1. This value of T_C is close to that of $Nd_{0.5}Sr_{0.5}MnO_3$. The material becomes metallic at $T < T_C$ in all the compositions. The progressive increase in T_C with substitution of Ru is similar to the effect of internal or hydrostatic pressure on $La_{0.7}A_{0.3}MnO_3$ [2,8], probably involving an increase in the Mn-Mn transfer integral or Mn-O-Mn angle. It must be underscored, however, that the ferromagnetic metallic state is favored by Ru substitution also because of its right electronic configuration to render the material ferromagnetic and metallic. We recall that $SrRuO_3$ is a metallic ferromagnet. Furthermore, Ru^{4+} surrounded by Mn^{3+}, is favorable for electron exchange. The susceptibility data also indicate the likely presence of clusters which may be Ru-rich when x is large. A comparison of the effective magnetic moment (μ_{eff}) above T_C with the spin-only value (assuming a low-spin configuration ($t_{2g}^4 e_g^0$) for Ru^{4+}) shows that a distribution of the magnetic clusters may be present. With the increase in the Ru content, the μ_{eff} of the system decreases.

The resistivity data of $Nd_{0.5}Ca_{0.5}Mn_{1-x}Ru_xO_3$ in Fig. 4.2.20 (b), shows that in the x = 0.01 composition an I-M transition occurs at 130 K, close to the T_C of the material. The T_{IM} increases up to x = 0.05, but the transition also becomes broad. The transition at x = 0.1 is a little broad, but the maximum is at a lower temperature than for x = 0.05. It is noteworthy that the T_{IM} does not increase with x like the T_C. It is not entirely surprising that the transport properties are affected to a greater extent by inhomogeneities and impurities than the magnetic properties. The difference between T_C and T_{IM} increases with x, possibly as a result of the presence of Ru-rich/poor clusters or small domains. The

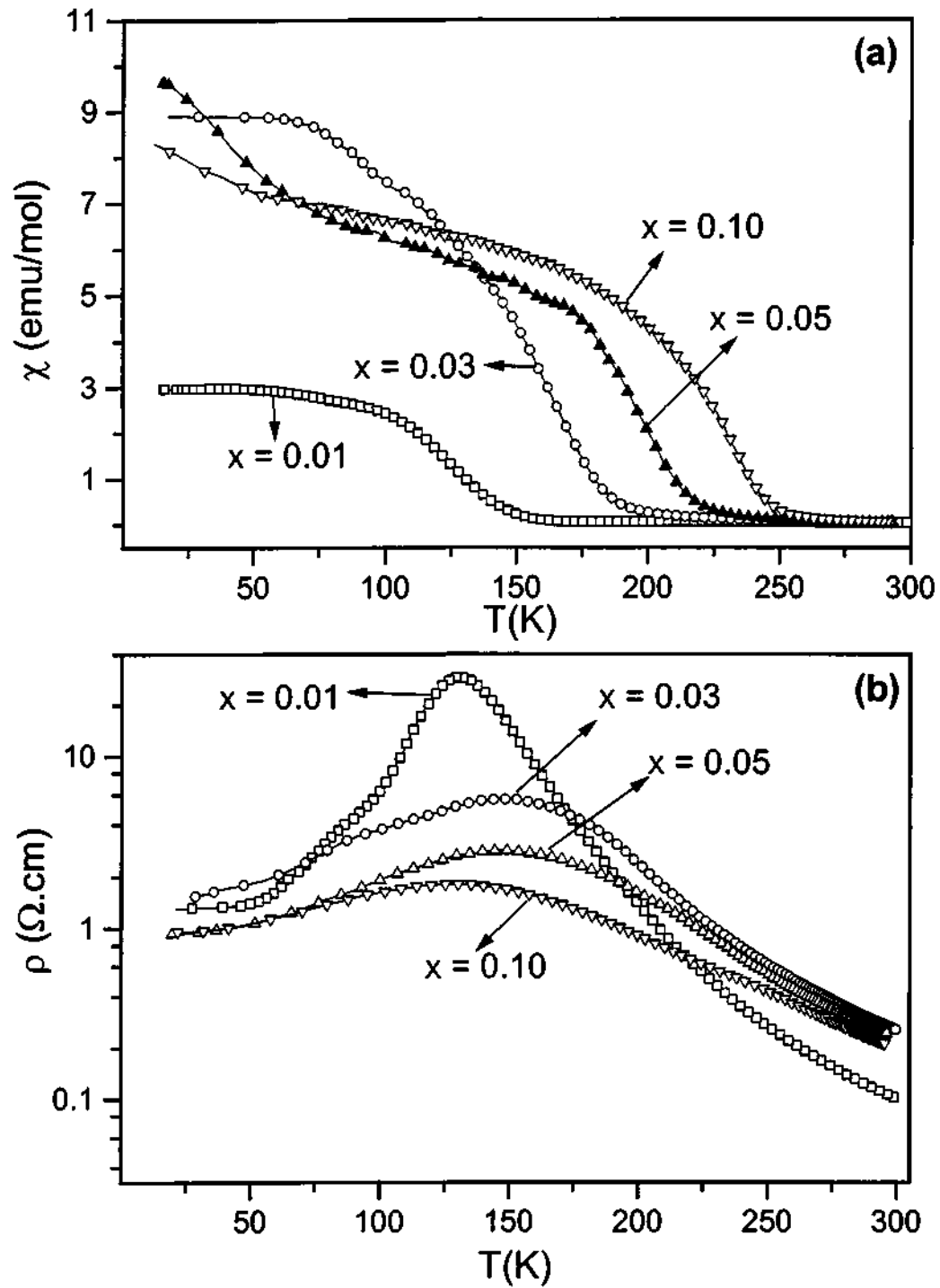[8] H. Y. Hwang, T. T. M. Plastra, S.-W. Cheong and B. Batlogg, Phys. Rev. B52, 15046 (1995).

Fig. 4.2.20 Temperature variation of (a) magnetization and (b) resistivity of $Nd_{0.5}Ca_{0.5}Mn_{1-x}Ru_xO_3$.

drastic effect of Ru doping above a critical concentration (3%) on the resistivity may imply that the carrier hopping involves quasiparticles such as magnetic polarons, which spread over a few lattice units. Of all the substitutents, both non-transition and transition ions, Ru^{4+} is the most effective in melting charge-ordering in $Nd_{0.5}Ca_{0.5}MnO_3$. Magnetoresistivity measurements show that at 1% Ru doping, the MR in the T_C (T_{IM}) region is 95% at 5 T. This value of CMR in an otherwise charge-ordered insulator is noteworthy.

In Fig. 4.2.21, we show the effect of substitution of Ru^{4+} in the B-site of $Nd_{0.5}Sr_{0.5}MnO_3$. While the other tetravalent ions like Ti^{4+}, Zr^{4+} and Ge^{4+} substitution lower the T_C and destroy the charge-ordering, Ru substitution increases the T_C up to x = 0.10, the T_C occurring above the room temperature in the x = 0.10 composition. Charge-ordering is destroyed by Ru^{4+} doping and instead a broad insulator-metal transition occurs around 165 K for $0.01 \leq x \leq 0.1$. The T_{IM} does not vary significantly with x unlike the T_C (Fig.4.2.20 (b)). Magnetoresistivity measurements (5 T) on the x = 0.01 composition show ~ 28% MR around 260 K (T_C) and 55% MR in the 20-60 K region (Fig. 4.2.22).

Conclusions

The present investigations of the effect of substitution of the B-site of the half doped rare earth manganates with different average A-site radius shows that it is possible to melt the charge-ordered state in these manganates by such a substitution. The sensitivity of the charge-ordered state in the manganates, $Ln_{0.5}A_{0.5}MnO_3$ depends on $\langle r_A \rangle$ value as well as the substitutent ion.

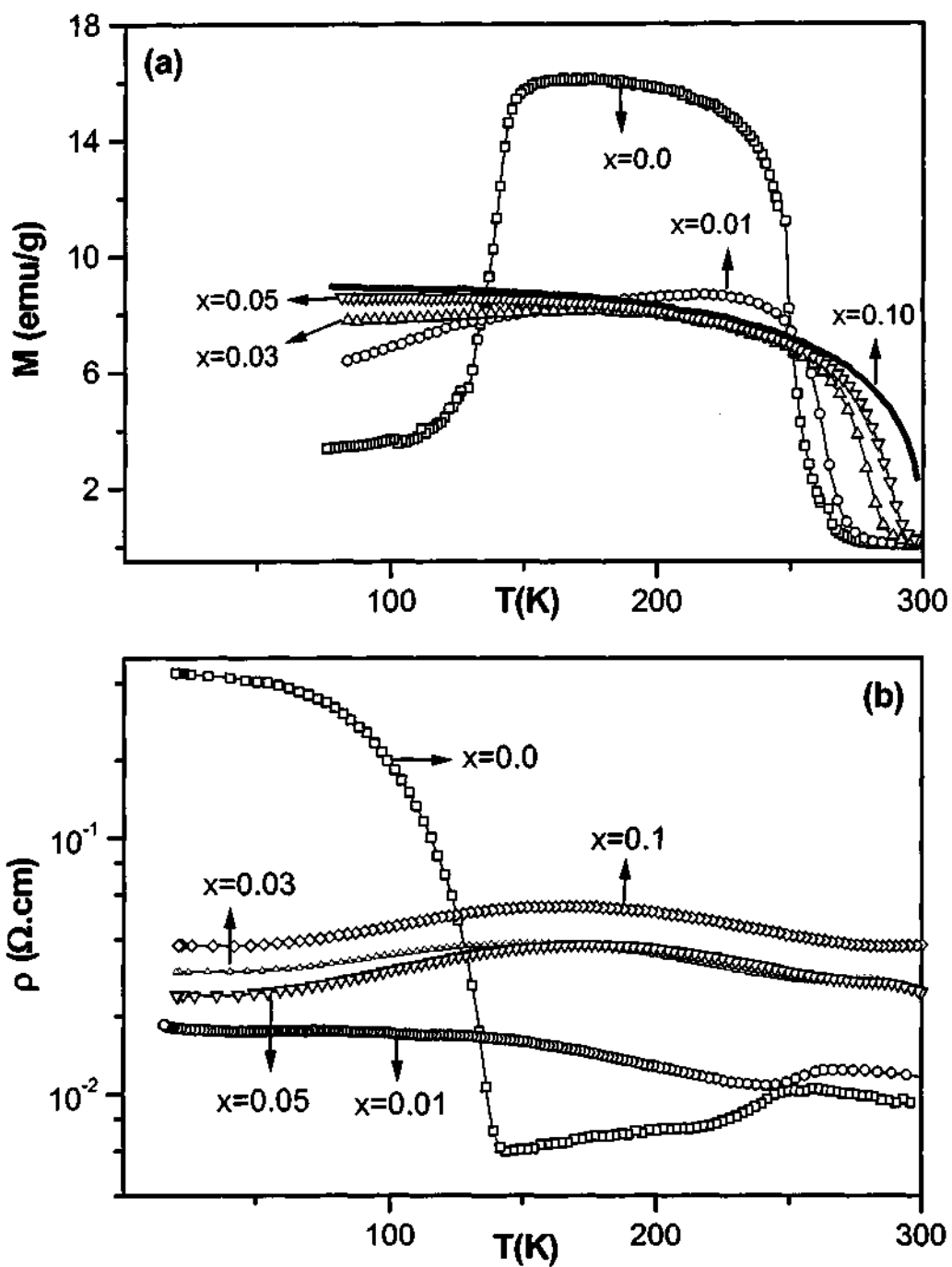Fig. 4.2.21 Temperature variation of (a) magnetization and (b) resistivity of $Nd_{0.5}Sr_{0.5}Mn_{1-x}Ru_xO_3$.

The charge-ordered state in the manganate $Y_{0.5}Ca_{0.5}MnO_3$ ($\langle r_A \rangle \sim 1.13$ Å.) is very robust and there is no effect of any substitutent on the magnetic and electrical transport properties of this manganate. $Nd_{0.5}Ca_{0.5}MnO_3$ with $\langle r_A \rangle = 1.17$ Å, on the other hand shows interesting properties on substitution with various transition and non-transition metal ions. Substitution of Al, Ga, Ge and Fe does not affect the properties of $Nd_{0.5}Ca_{0.5}MnO_3$ much. Substitution of Cr, Ni, Co and Ru introduces an insulator-metal transition in the compound and the material shows ferromagnetism. However, low concentrations of these metal ions do not destroy the charge-ordering completely (Fig. 4.2.23) and the ferromagnetic state in these substituted compositions appear to be re-entrant in nature (see Section 4.3) $T_{CO} > T_C$. The ferromagnetic and charge-ordered phases seem to coexist in the temperature range between the T_{CO} and T_C.

Substitution of Cr, Co, Ni and Ru at the B-site induces ferromagnetism in $Nd_{0.5}Ca_{0.5}MnO_3$, the best effects being observed with Ru substitution. The ferromagnetic transition temperature, T_C, increases with the increase in Ru substitution unlike that of Cr, Co or Ni.

The properties of $Nd_{0.5}Sr_{0.5}MnO_3$ ($\langle r_A \rangle = 1.24$ Å) are affected to a greater extent by substitution at the B-site by different ions. Even the substitution of the non-transition metal ions such as Al, Ga and Ge changes the properties of this manganate. Substituion of Al, Fe and Ga makes the material an insulator and the material seems to behave more like other charge-ordered insulators with smaller $\langle r_A \rangle$ like $Nd_{0.5}Ca_{0.5}MnO_3$. Substitution of Cr, Co, Ni and Ru makes the material ferromagnetic and metallic. Ru substitution gives the
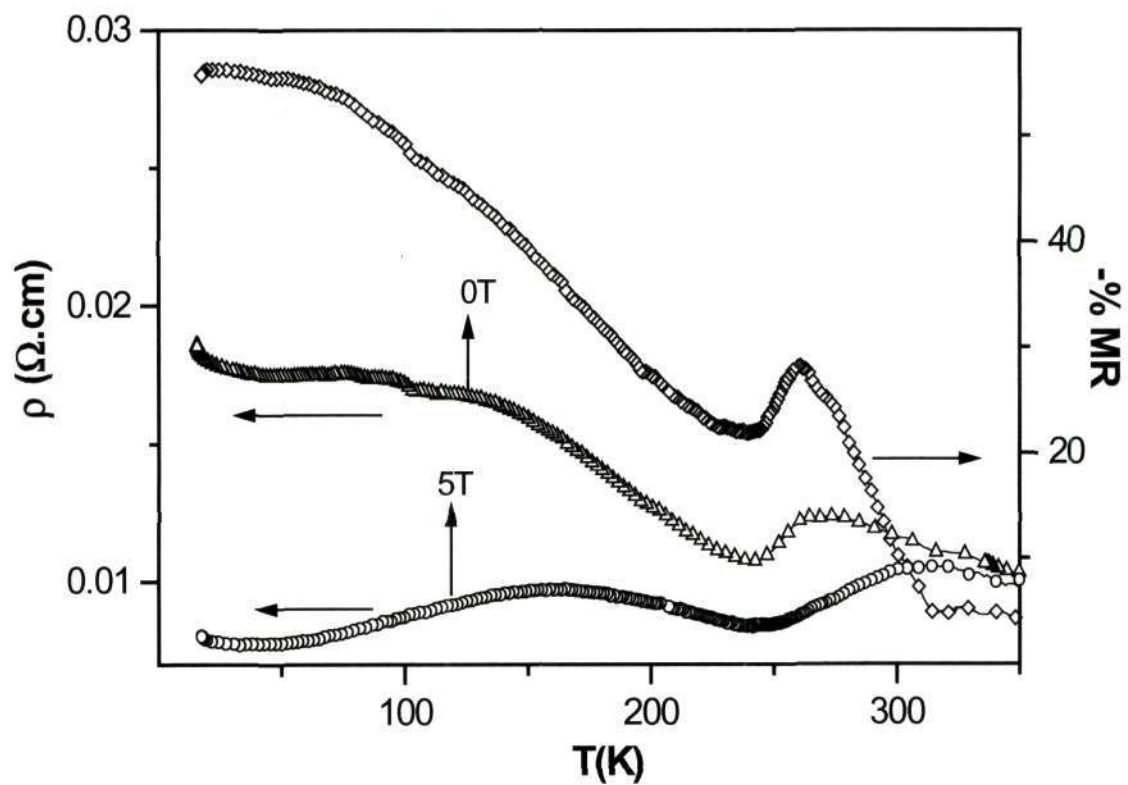
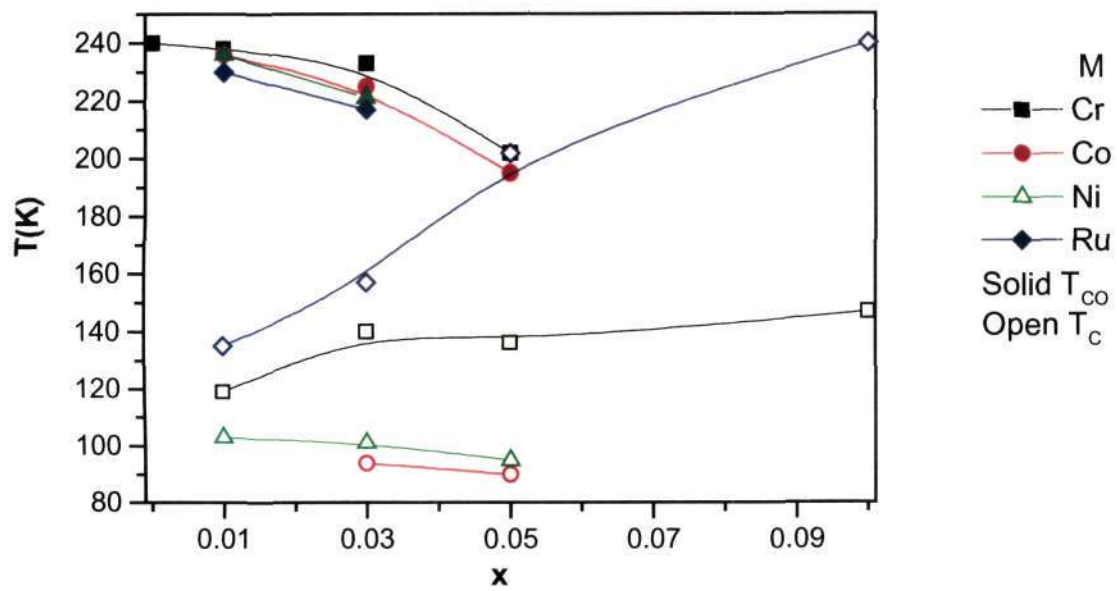Fig. 4.2.22 Resistivity of $Nd_{0.5}Sr_{0.5}Mn_{0.99}Ru_{0.01}O_3$ at 0 and 5T; -%MR is also shown.

Fig. 4.2.23 Variation of ferromagnetic Curie temperature, T_C and charge ordering temperature T_{CO} with x in $Nd_{0.5}Ca_{0.5}Mn_{1-x}M_xO_3$ (M = Cr, Co, Ni and Ru). The lines are guide to the eye.

best result and increases the ferromagnetic T_C to room temperature due to its unique electronic configuration that facilitates electron hopping.

The presence of empty e_g orbitals in the substitutent transition metal ion appears to be necessary for destroying the charge ordered state in the rare earth manganates, $Ln_{0.5}A_{0.5}MnO_3$. Also, such substitution effects delineate the different types of charge ordered states caused by differences in the average size of the A-site ions.

4.3 Re-entrant ferromagnetic transition in the rare-earth manganates, $Ln_{0.5}A_{0.5}MnO_3$, with small A-site cations

The temperature variation of magnetization and resistivity of a single crystal of $Nd_{0.25}La_{0.25}Ca_{0.5}MnO_3$ are shown in Fig. 4.3.1(a) and (b) respectively. There is a change in the saturation magnetization of the single crystal based on its orientation to the applied magnetic field. The ferromagnetic T_C of the sample is around 160 K. The inset in Fig. 4.3.1(a) shows the inverse magnetization of the single crystal as a function of temperature to show the charge ordering transition around 200 K. Fig. 4.3.1 (b) shows the electrical resistivity of the single crystal in fields of 0, 1, 5 and 10 T. The material shows an insulator-metal (I-M) transition around 150 K (Fig. 4.3.1 (b)). Application of a magnetic field decreases the resistance of the crystal and the I-M transition occurs at a higher temperature in an applied magnetic field as in the case of CMR manganates. These results confirm that the $T_{CO} > T_C$ in a single crystalline sample just as shown earlier by *Arulraj et al.* [1] in the case of polycrystalline sample. The I-M transition is higher in the case of the single crystal when compared to that of the polycrystalline sample.

In Tables 4.3.1 and 4.3.2, the lattice parameters of $Ln_{0.5-x}La_xCa_{0.5}MnO_3$ (Ln = Nd, Pr) and $Ln_{0.5-x}Ln'_xCa_{0.5-y}Sr_yMnO_3$ ($\langle r_A \rangle$ = 1.185 Å) compositions are listed. The powder X-ray diffraction patterns of a few compositions of $Nd_{0.5-x}La_xCa_{0.5}MnO_3$ are shown in Fig. 4.3.2. In Fig. 4.3.3(a), we show the temperature variation of the magnetization, M of the $Nd_{0.5-x}La_xCa_{0.5}MnO_3$ series of manganates. The material becomes ferromagnetic even for

[1] A. Arulraj, A. Biswas, A. K. Raychaudhuri, C. N. R. Rao, P. M. Woodward, T. Vogt, D. E. Cox and A. K. Cheetham, Phys. Rev. B57, R8115 (1998).
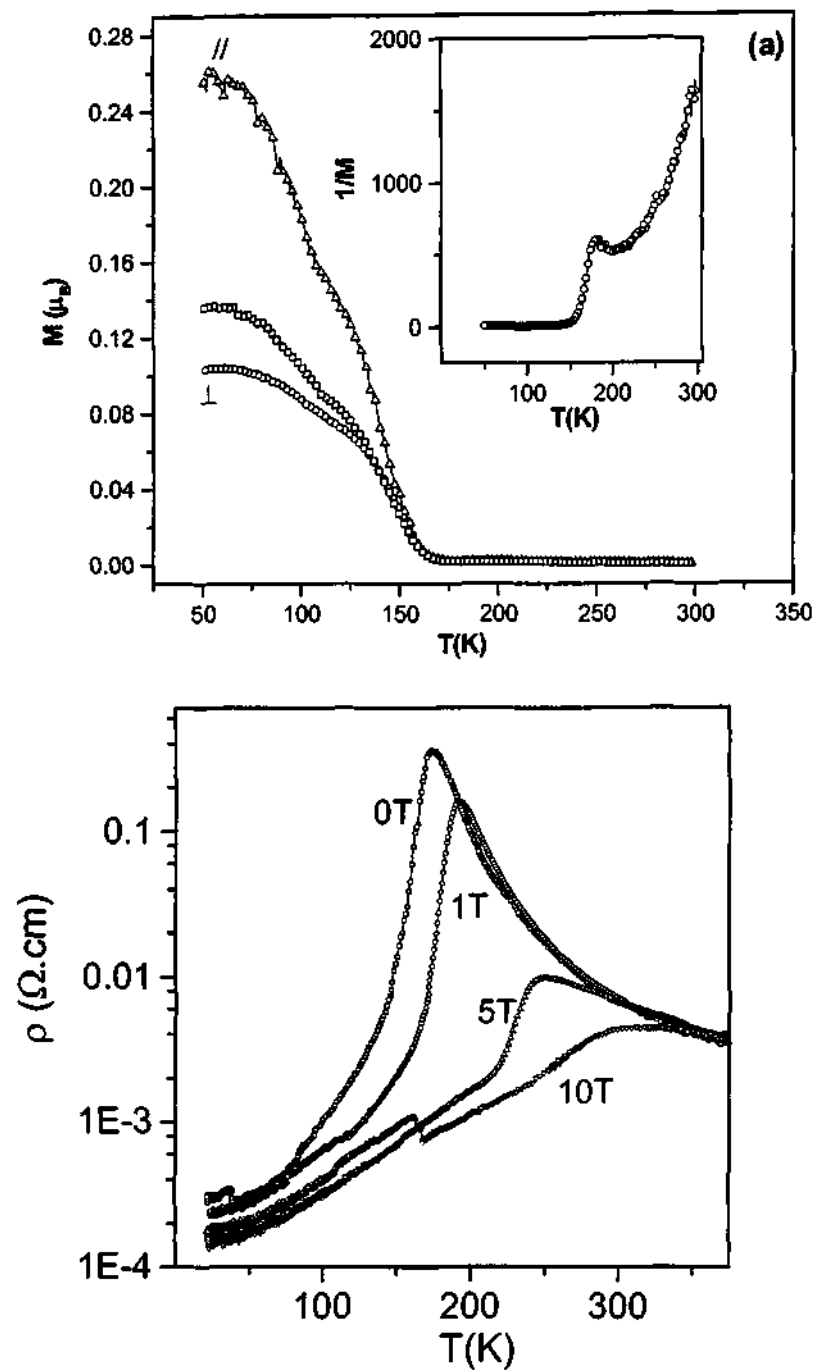
Fig. 4.3.1 (a) Temperature variation of the magnetization of single crystal of $Nd_{0.25}La_{0.25}Ca_{0.5}MnO_3$ in different orientations to the applied magnetic field. The plot of inverse of magnetization as a function of temperature in the inset shows the charge ordering transition. (b) Temperature variation of resistivity of single crystal of $Nd_{0.25}La_{0.25}Ca_{0.5}MnO_3$ in applied magnetic field of 0, 1, 5 and 10 Tesla.

Table 4.3.1

Structure and properties of $Ln_{0.5-x}La_xCa_{0.5}MnO_3$ (Ln = Nd, Pr)

Composition	$\langle r_A \rangle$ (Å)	σ^2 (Å²)	lattice parameter (Å)[a]			T_C (K)	T_{CO} (K)	T_P (K)
			a	b	c			
$Nd_{0.5}Ca_{0.5}MnO_3$	1.172	0.0001	5.392	7.589	5.376	-	240	-
$Nd_{0.4}La_{0.1}Ca_{0.5}MnO_3$	1.177	0.0002	5.400	7.603	5.397	-	~245	~100
$Nd_{0.35}La_{0.15}Ca_{0.5}MnO_3$	1.179	0.0003	5.404	7.631	5.402	~118	~245	~115
$Pr_{0.5}Ca_{0.5}MnO_3$	1.1795	0.0000	5.401	7.630	5.391	~154[b]	235	-
$Nd_{0.3}La_{0.2}Ca_{0.5}MnO_3$	1.182	0.0003	5.409	7.633	5.404	118	237	125
$Nd_{0.25}La_{0.25}Ca_{0.5}MnO_3$	1.185	0.0004	5.416	7.636	5.410	127	239	137
$Pr_{0.35}La_{0.15}Ca_{0.5}MnO_3$	1.185	0.0002	5.411	7.647	5.410	138	239	136
$Nd_{0.2}La_{0.3}Ca_{0.5}MnO_3$	1.187	0.0004	5.417	7.637	5.413	136	242	144
$Pr_{0.25}La_{0.25}Ca_{0.5}MnO_3$	1.189	0.0002	5.413	7.657	5.401	150	237	148
$Nd_{0.15}La_{0.35}Ca_{0.5}MnO_3$	1.190	0.0004	5.416	7.635	5.418	155	226	155
$Pr_{0.15}La_{0.35}Ca_{0.5}MnO_3$	1.192	0.0003	5.417	7.665	5.403	185	234	168
$Nd_{0.1}La_{0.4}Ca_{0.5}MnO_3$	1.193	0.0004	5.416	7.649	5.427	177	-	176
$La_{0.5}Ca_{0.5}MnO_3$	1.198	0.0003	5.418	7.639	5.427	225	135	-

(a) *Space group: Pnma*; Uncertainties in the lattice parameters are within ± 0.001 Å.
(b) Corresponds to T_N in this composition

174

Table 4.3.2

Structure and properties of $Ln_{0.5-x}Ln'_xCa_{0.5-y}Sr_yMnO_3$ with a fixed $\langle r_A \rangle$ of 1.185Å

Composition	σ^2 ($Å^2$)	lattice parameter ($Å$)*			T_C (K)	T_{CO} (K)	T_P (K)
		a	b	c			
$Pr_{0.35}La_{0.15}Ca_{0.5}MnO_3$	0.0002	5.411	7.647	5.410	138	239	136
$Nd_{0.25}La_{0.25}Ca_{0.5}MnO_3$	0.0004	5.416	7.636	5.410	127	239	137
$Sm_{0.15}La_{0.35}Ca_{0.5}MnO_3$	0.0008	5.414	7.636	5.408	105	238	108
$Nd_{0.3}Sm_{0.2}Ca_{0.35}Sr_{0.15}MnO_3$	0.0031	5.401	7.642	5.398	105	221	103
$Gd_{0.3}Nd_{0.2}Ca_{0.27}Sr_{0.23}MnO_3$	0.0055	5.423	7.641	5.401	79	220	78

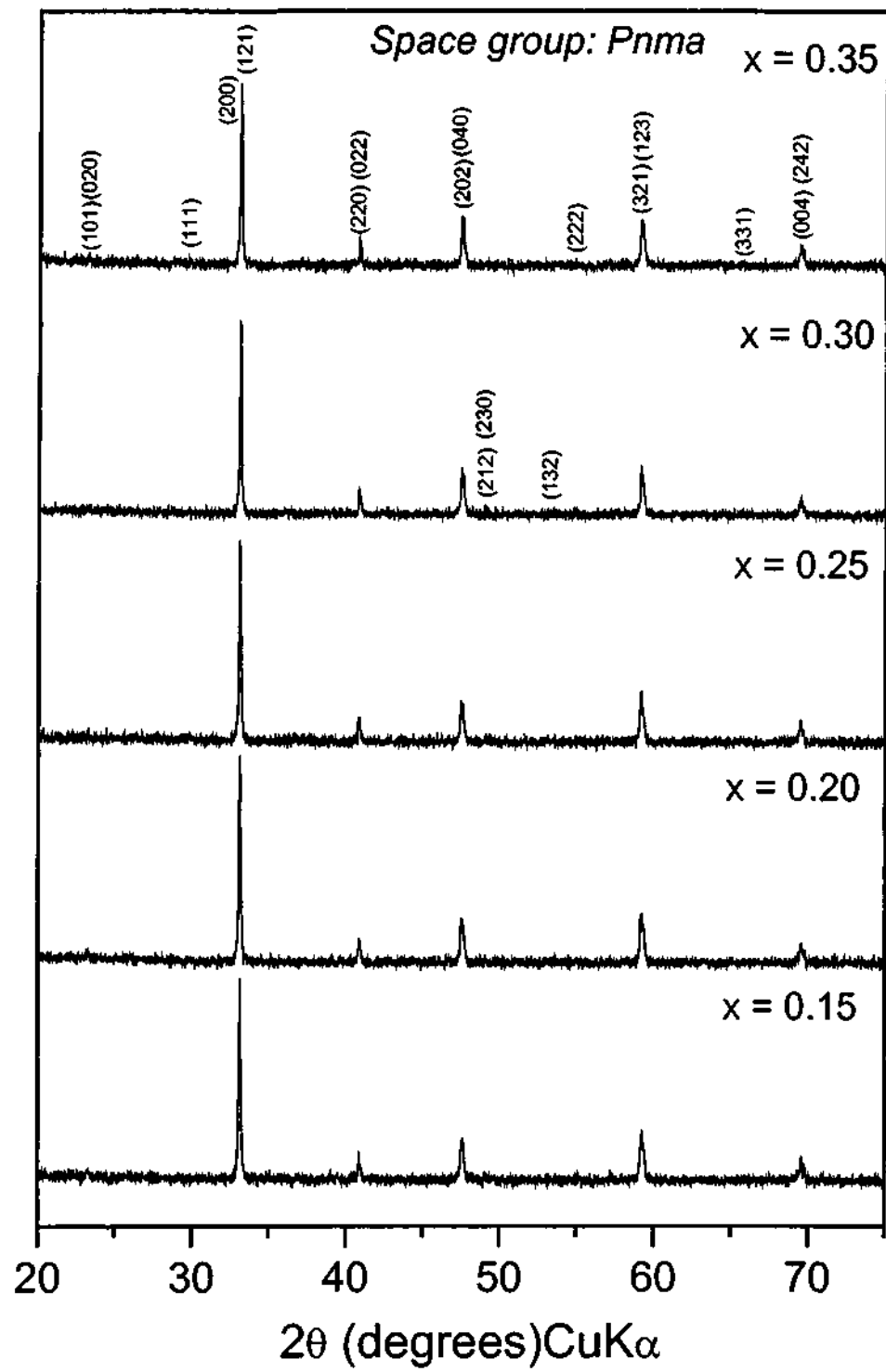* *Space group: Pnma;* Uncertainties in the lattice parameters are within ± 0.001 Å.

175

Fig. 4.3.2 Powder X-ray diffraction patterns of $Nd_{0.5-x}La_xCa_{0.5}MnO_3$ compositions.

$x = 0.15$. The ferromagnetic Curie temperature, T_C, as well as the saturation magnetization of the material increase with increase in x from ~118 K for $x = 0.15$ to 177 K when $x = 0.4$. The plot of inverse magnetization Vs temperature in the inset of Fig. 4.3.3(a) shows how the charge-ordering transition temperature, T_{CO}, as evidenced from the broad minimum in the curve varies with x. The T_{CO} of 240 K for the $x = 0.0$ composition changes only slightly as the x value is increased to 0.35. We show the electrical resistivity data of $Nd_{0.5-x}La_xCa_{0.5}MnO_3$ in Fig. 4.3.3(b), to demonstrate the effect of substitution of La in place of Nd. The $x = 0.0$ composition is an insulator down to low temperatures. As the value of x is increased, an insulator metal (I-M) transition manifests itself. The I-M transition temperature, T_p, increases with x from ~100 K for $x = 0.1$ to 176 K when $x = 0.4$. The I-M transition temperature is close to the ferromagnetic Curie temperature, T_C.

The magnetic and electrical properties of the $Pr_{0.5-x}La_xCa_{0.5}MnO_3$ series of manganates are shown in Fig. 4.3.4. Here again, the material becomes ferromagnetic on substitution of La in place of Pr, with the T_C varying from 138 K for $x = 0.15$ to 185 K for $x = 0.35$. The inset in Fig. 4.3.4(a) shows how the T_{CO} varies with x in this series of manganates. The resistivity data in Fig. 4.3.4(b) show that the I-M transition temperature, corresponding to the peak in the resistivity-temperature curve, T_p, increases with increase in x just as in the case of the $Nd_{0.5-x}La_xCa_{0.5}MnO_3$ system, with the T_p values lying close to those of T_C.

In the $Nd_{0.5-x}La_xCa_{0.5}MnO_3$ and $Pr_{0.5-x}La_xCa_{0.5}MnO_3$ series of manganates (Table 4.3.1) studied by us, the ferromagnetic transition occurs below the CO transition just as in $Nd_{0.25}La_{0.25}Ca_{0.5}MnO_3$. This is unlike the situation in the manganates with $\langle r_A \rangle > 1.20$ Å,
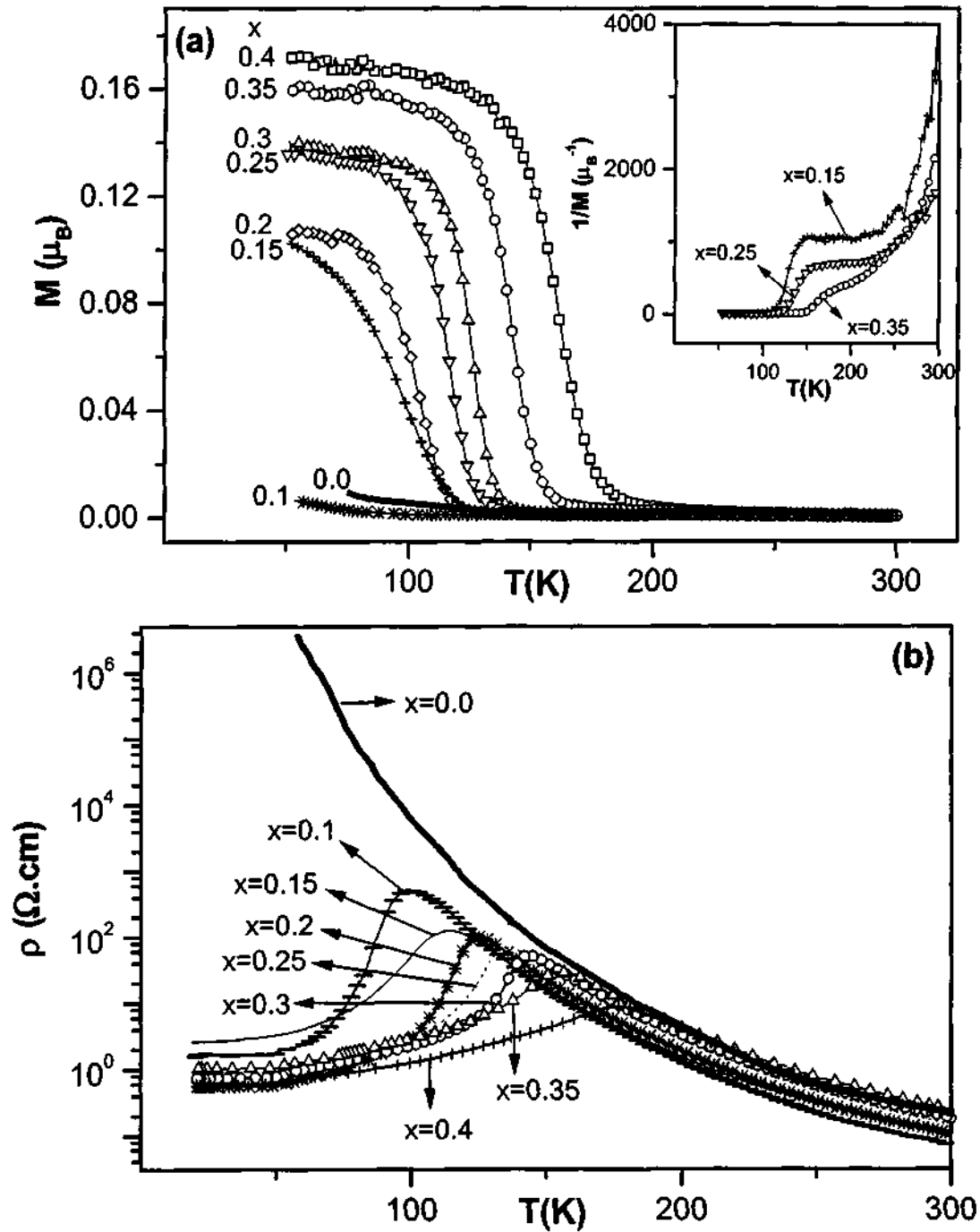
Fig. 4.3.3 Temperature variation of (a) magnetization and (b) resistivity of $Nd_{0.5-x}La_xCa_{0.5}MnO_3$. The inset in (a) shows the variation of inverse magnetization with temperature.

178

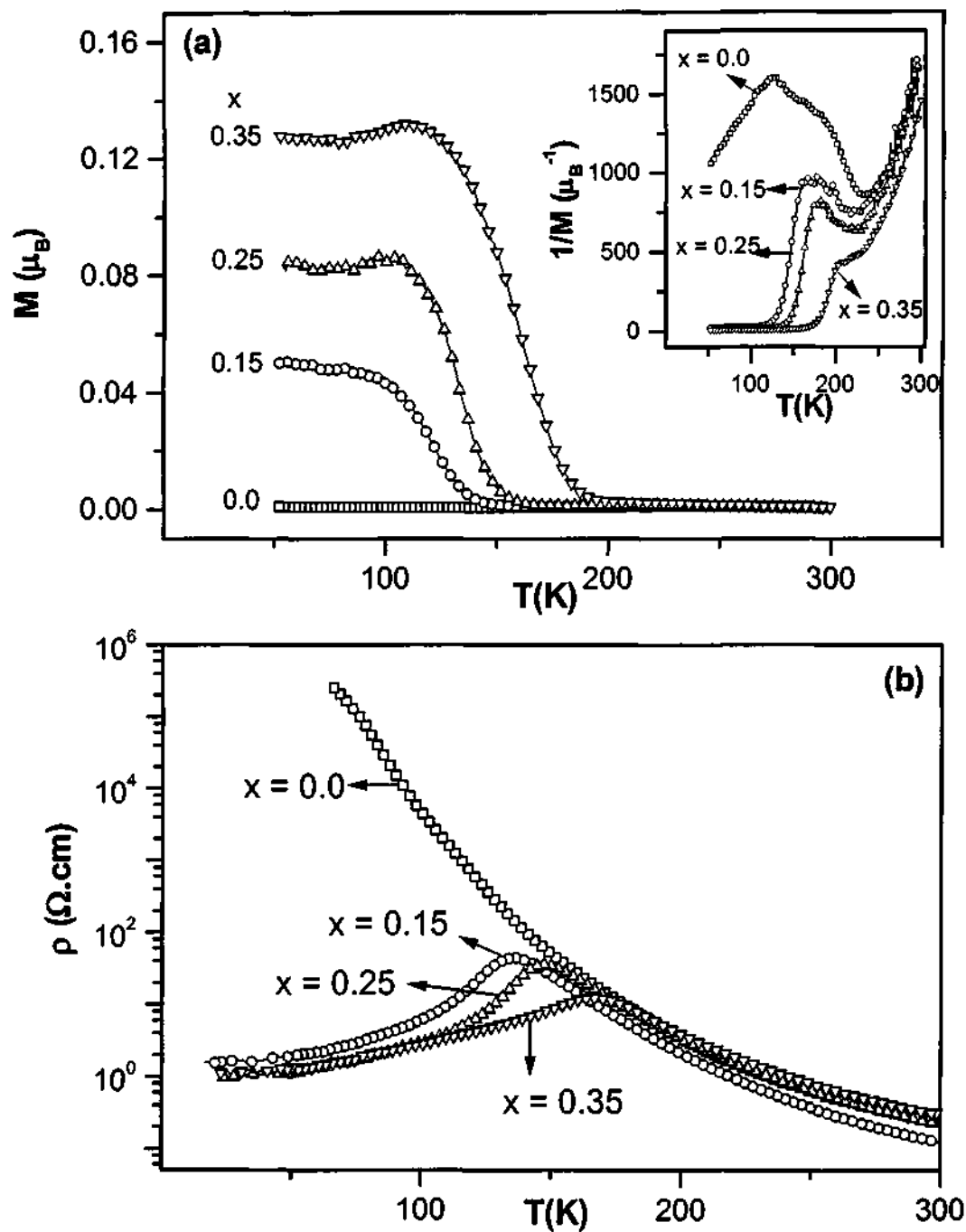Fig. 4.3.4 Temperature variation of (a) magnetization and (b) resistivity of $Pr_{0.5-x}La_xCa_{0.5}MnO_3$. The inset in (a) shows the variation of inverse magnetization with temperature.
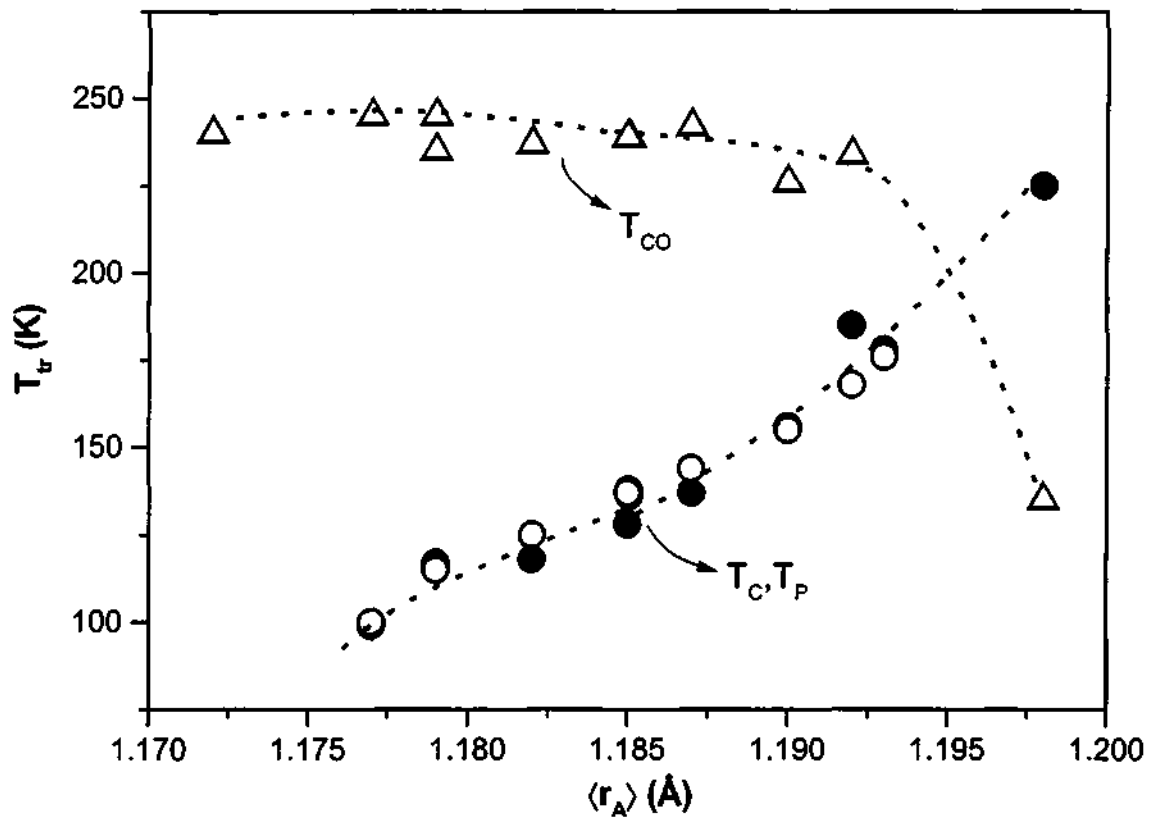
179

Fig. 4.3.5 Variation of ferromagnetic Curie temperature, T_C, the I-M transition temperature, T_p, and the CO transition temperature, T_{CO}, with $\langle r_A \rangle$ in the manganates $Ln_{0.5-x}La_xCa_{0.5}MnO_3$ (Ln = Nd, Pr). Closed and open circles represent T_C and T_p respectively. Dotted lines are guides to the eyes.

where T_C is almost always greater than T_{CO}. We have plotted the T_C and T_{CO} values as well as the I-M transition temperature, T_P, against $\langle r_A \rangle$ in Fig. 4.3.5. The T_C increases with increase in $\langle r_A \rangle$ as expected. The CO transition temperature, T_{CO}, does not vary significantly with $\langle r_A \rangle$ in this regime. When $\langle r_A \rangle$ is slightly higher, say ≥ 1.19 Å as in $La_{0.5}Ca_{0.5}MnO_3$, the CO transition occurs below the FM transition. In other words, the T_{CO} - $\langle r_A \rangle$ and T_C - $\langle r_A \rangle$ curves intersect around a $\langle r_A \rangle$ of 1.195 Å. This would mean that the nature of the ground state changes across this $\langle r_A \rangle$. This is indeed a fascinating feature of the rare earth manganates. Depending on the $\langle r_A \rangle$, the CO or the FM state can be the ground state giving rise to $T_{CO} > T_C$ or $T_C > T_{CO}$ behaviour. That there is a critical cross-over point around $\langle r_A \rangle = 1.195$ Å is noteworthy.

$Nd_{0.5}Ca_{0.5}MnO_3$ has been found to exhibit ferromagnetic excitations at low temperatures even in the AFM regime [2], eventhough it has been considered to be a pure CO material [3]. In $Nd_{0.25}La_{0.25}Ca_{0.5}MnO_3$, there would be a coexistence region between the T_{CO} (~240 K) and the T_C (~140 K). A similar coexistence region is known to occur in $La_{0.5}Ca_{0.5}MnO_3$. The temperature range of the coexistence regime appears to decrease with the increase in x in $Nd_{0.5-x}La_xCa_{0.5}MnO_3$, accompanying an increase in $\langle r_A \rangle$, as can be surmised from Fig. 4.3.5. *Moritomo* [3] found the so-called phase separation regime in $Nd_{0.5-x}La_xCa_{0.5}MnO_3$ in the composition regime of x = 0.2-0.5. The systems studied by us (Table 4.3.1) are, by and large, in this regime, although we find the $T_{CO} > T_C$ behaviour in a wider composition regime (0.1 < x < 0.5).

[2] P. Murugavel, C. Narayana, A. K. Sood, S. Parashar, A. R. Raju and C. N. R. Rao Europhys. Lett. 52, 461 (2000).
[3] Y. Moritomo, Phys. Rev. B60, 10374 (1999).

One may suspect that the results discussed above are partly from site disorder. It is to be noted, however, that in the manganates studied (Table 4.3.1), the value of σ^2 is in the range of 0.0001 - 0.0004 Å^2. We can, therefore. consider the observed variation in T_C and T_{CO} in Fig. 4.3.5 to be as almost entirely due to the effect of $\langle r_A \rangle$. In order to examine the effect of size mismatch on the magnetic and electrical properties, on the re-entrant FM transition, we have studied a series of manganates with a fixed $\langle r_A \rangle$ value of 1.185 Å (Table 4.3.2). We show the temperature variation of magnetization and electrical resistivity for these manganates in figures 4.3.6(a) and 4.3.6(b) respectively. It is remarkable that the saturation magnetization as well as the T_C decrease markedly with increase in σ^2 as shown in Fig.4.3.6 (a). Thus, the T_C of 138 K for $\sigma^2 = 0.0002$ Å^2 decreases to 79 K for $\sigma^2 = 0.0055$ Å^2. Accompanied by this change, we also see a decrease in the temperature corresponding to the I-M transition, T_p, from 136 K for $\sigma^2 = 0.0002$ Å^2 to 78 K when $\sigma^2 = 0.0055$Å^2. It appears that the re-entrant ferromagnetic transition can entirely be suppressed by increasing σ^2 sufficiently around an $\langle r_A \rangle$ of 1.19 Å. The variation of inverse magnetization as a function of temperature shown in the inset of 4.3.6(a) shows how T_{CO} decreases slightly with increase in σ^2.

In Fig. 4.3.7, we have plotted the variation of T_C (T_p) and T_{CO} against σ^2 for the series of manganates with a fixed $\langle r_A \rangle$ of 1.185 Å. There is a fairly good linear relationship of T_C (T_p) and T_{CO} with σ^2. The T_C (T_p) - σ^2 plot has a slope of 10000 ± 2600 K Å^{-2} with an intercept (T^0_C) of 132 ± 7 K. The T_{CO} - σ^2 plot has a slope of 4110 ± 870 K Å^{-2} with an intercept (T^0_{CO}) of 240 ± 2 K. The T^0_C and T^0_{CO} values represent the experimental estimates of the ideal ferromagnetic and charge ordering transition temperatures that
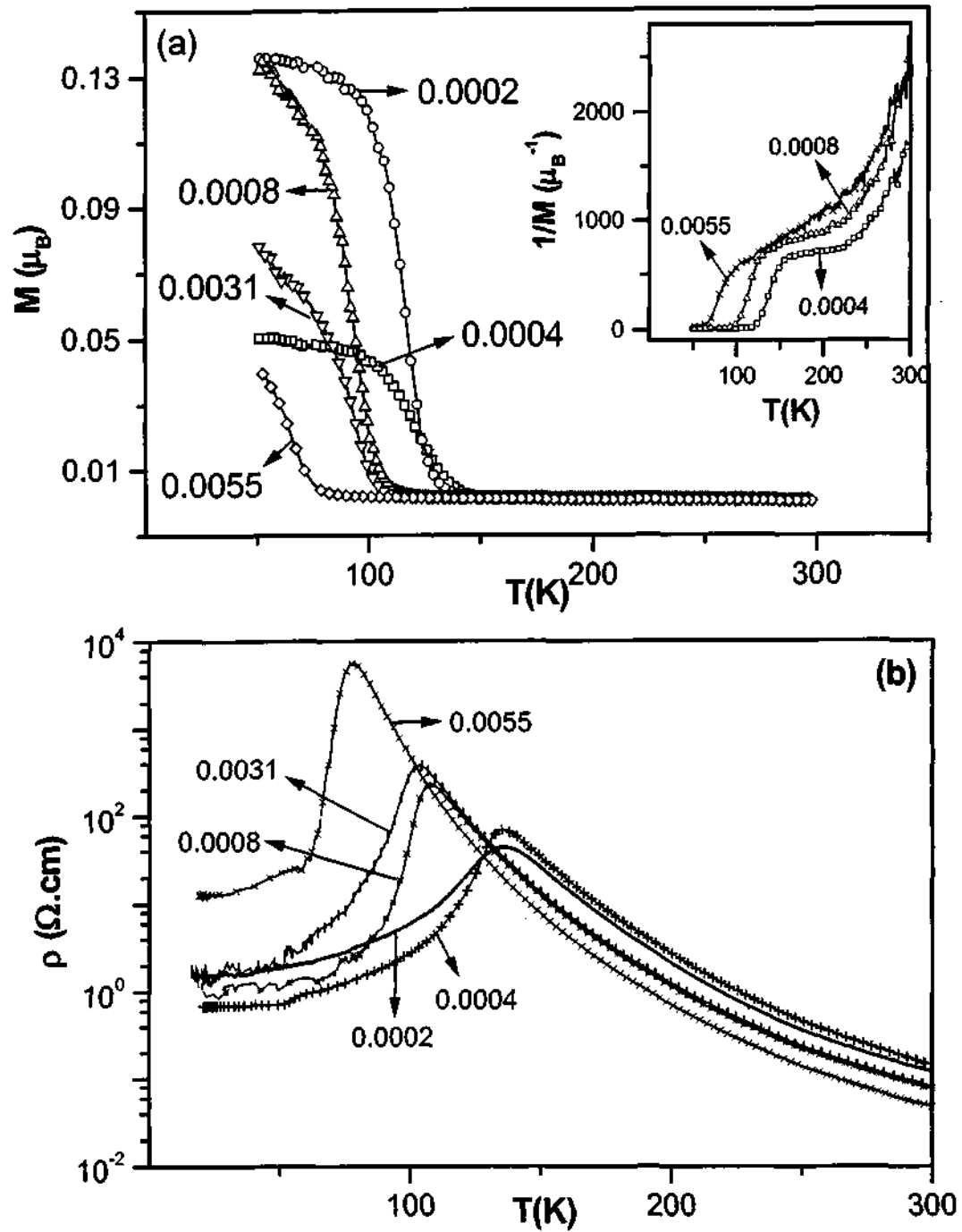
Fig. 4.3.6 Temperature variation of (a) the magnetization and (b) the resistivity of the $Ln_{0.5}A_{0.5}MnO_3$ series of manganates with a fixed $\langle r_A \rangle$ of 1.185 Å. The inset in (a) shows the variation of inverse magnetization with temperature.
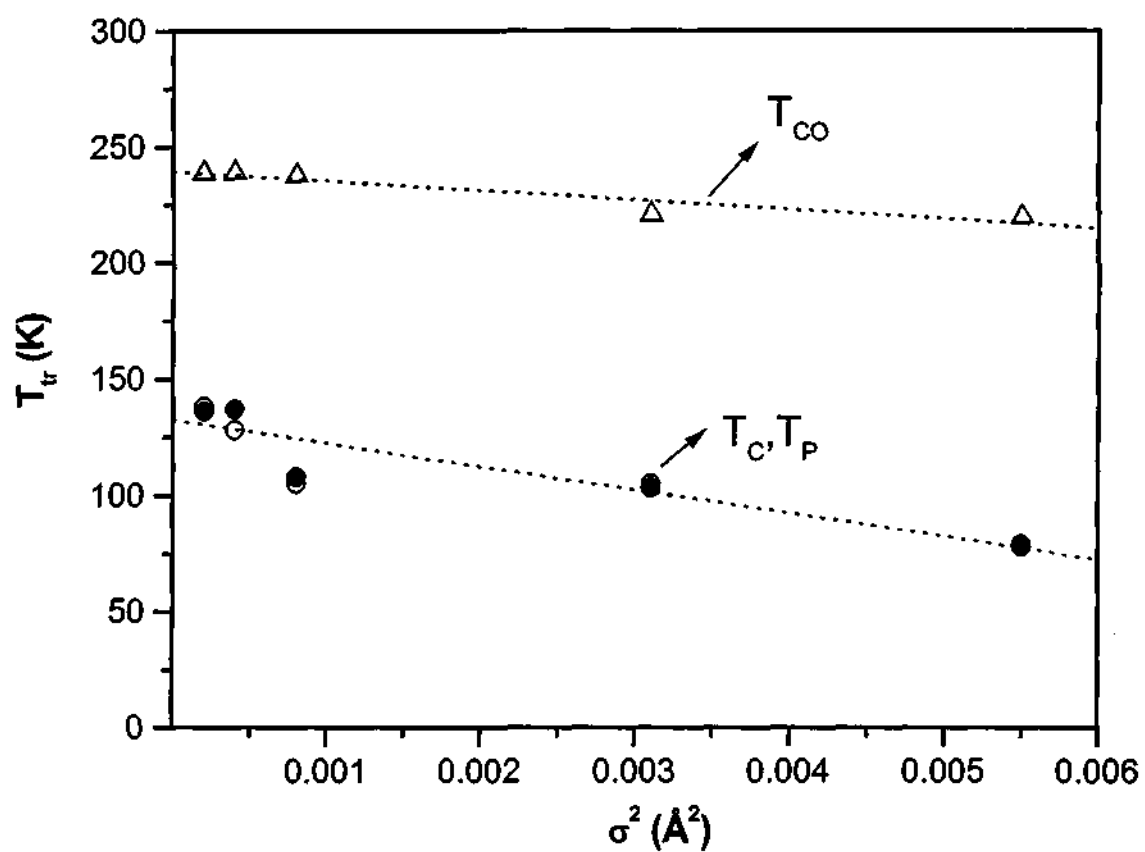
Fig. 4.3.7 Variation of ferromagnetic Curie temperature, T_C, the I-M transition temperature, T_p, and the CO transition temperature, T_{CO}, with σ^2 in the $Ln_{0.5}A_{0.5}MnO_3$ series of manganates with a fixed $\langle r_A \rangle$ of 1.185 Å.

would be observed in the manganates with $\langle r_A \rangle$ of 1.185 Å in the absence of size

mismatch. We have carried out studies on a few manganates with a fixed $\langle r_A \rangle$ of 1.189 Å

and find that the variations of T_C and T_{CO} with σ^2 in this series follow trends similar to

those in Fig. 4.3.7. Thus, for σ^2 values of 0.0007 and 0.0030 Å^2 (for $\langle r_A \rangle$ = 1.189 Å), the

T_C values are 136 and 68 K respectively while the corresponding T_{CO} values are 230 and

220 K. The estimates of T^0_C and T^0_{CO} found by us for $\langle r_A \rangle$ of 1.185 Å are in line with the

results of earlier studies on the $Ln_{0.5}A_{0.5}MnO_3$ systems with different fixed $\langle r_A \rangle$ values

[4,5, (Also see Section 4.2.1 of this thesis)]. Thus, the value of T^0_C for fixed $\langle r_A \rangle$ value of

1.24 Å is 331 ± 13 K and the corresponding value of the slope is 15000 ± 2800 K Å^{-2}. The

T^0_{CO} value for a fixed $\langle r_A \rangle$ of 1.24 Å is 174 ± 13 K with a slope of 2840 ± 270 K Å^{-2}. The

values of the slopes and the intercepts appear to be greater in a bonafide ferromagnet with

large $\langle r_A \rangle$.

Conclusions

A series of rare earth manganates with an average A-site cation radius, $\langle r_A \rangle$, in the

range 1.17 - 1.20 Å where charge ordering and ferromagnetism are competing interactions,

has been investigated. These manganates show charge ordering around 240 K and become

ferromagnetic and metallic on cooling, characteristic of a re-entrant behaviour.

Interestingly, the plots of T_{CO} and T_C against $\langle r_A \rangle$ intersect at a value of 1.195 Å, indicating

[4] (a) L. M. Rodriguez-Martinez and J. P. Attfield, Phys. Rev. B54, R15622 (1996). (b) L. M. Rodriguez-Martinez and J. P. Attfield, Phys. Rev. B58, 2426 (1998).

[5] F. Damay, C. Martin, A. Maignan and B. Raveau, J. Appl. Phys. 82, 6181 (1997).

a change in the relative stabilities of the ground states. Below a $\langle r_A \rangle$ of 1.195 Å, $T_{CO} > T_C$ and it is likely that the CO and FMM states coexist in the temperature range between T_{CO} and T_C. It is noteworthy that the width of the regime $(T_{CO}-T_C)$ decreases with increase in $\langle r_A \rangle$, becoming rather small in $La_{0.5}Ca_{0.5}MnO_3$.

Site disorder arising from size mismatch has a profound effect on the T_C corresponding to the re-entrant transition in this $\langle r_A \rangle$ regime of the manganates. Accordingly, a change in σ^2 from 0.0002 Å^2 to 0.0055 Å^2 at a fixed $\langle r_A \rangle$ of 1.185 Å brings about a vast change in T_C, although the T_{CO} is affected to a much smaller extent. Unlike with $\langle r_A \rangle$, the coexistence regime $(T_{CO}-T_C)$ increases with increase in σ^2.

4.4 ^{57}Fe Mössbauer spectroscopy study of charge-ordered rare-earth manganates

For the Mössbauer spectroscopy study of charge ordering and phase separation in rare earth manganates, we have chosen two compositions with distinctly different charge-ordering characteristics, namely $Nd_{0.5}Ca_{0.5}MnO_3$ and $Nd_{0.5}Sr_{0.5}MnO_3$. In $Nd_{0.5}Ca_{0.5}MnO_3$, charge ordering occurs in the paramagnetic phase at 240 K followed by an antiferromagnetic transition (T_N = 150 K) on cooling [1]. The presence of ferromagnetic correlations at low temperatures has been noticed in this compound [2]. On doping this manganate with ^{57}Fe to give the composition $Nd_{0.5}Ca_{0.5}Mn_{0.98}{}^{57}Fe_{0.02}O_3$, the charge ordering transition is found around 230 K and the Neel temperature at130 K as shown in Fig. 4.4.1. Below 200 K, this composition is likely to exhibit a two-phase state, one involving a larger c parameter than the other. The long c (7.5728 Å) phase is paramagnetic while the short c (7.5029 Å) phase corresponds to CE-type antiferromagnetic structure with no drastic changes in lattice parameters across the Neel temperature around 120 K [3]. $Nd_{0.5}Sr_{0.5}MnO_3$, on the other hand, becomes ferromagnetic around 250 K and undergoes a transition to the charge ordered CE-type antiferromagnetic state on cooling to 150 K [4]. On doping this material with ^{57}Fe to give the composition $Nd_{0.5}Sr_{0.5}Mn_{0.98}{}^{57}Fe_{0.02}O_3$, the ferromagnetic transition temperature is lowered (T_C ~ 215 K) and the antiferromagnetic transition occurs around 120 K (Fig. 4.4.2). Some samples of

[1] Y. Tomioka, A. Asamitsu, H. Kuwahara, Y. Moritomo and Y. Tokura, Phys. Rev. B53, R1689 (1996).

[2] P. Murugavel, C. Narayana, A. K. Sood, S. Parashar, A. R. Raju and C. N. R. Rao, Europhys. Lett. 52, 461 (2000).

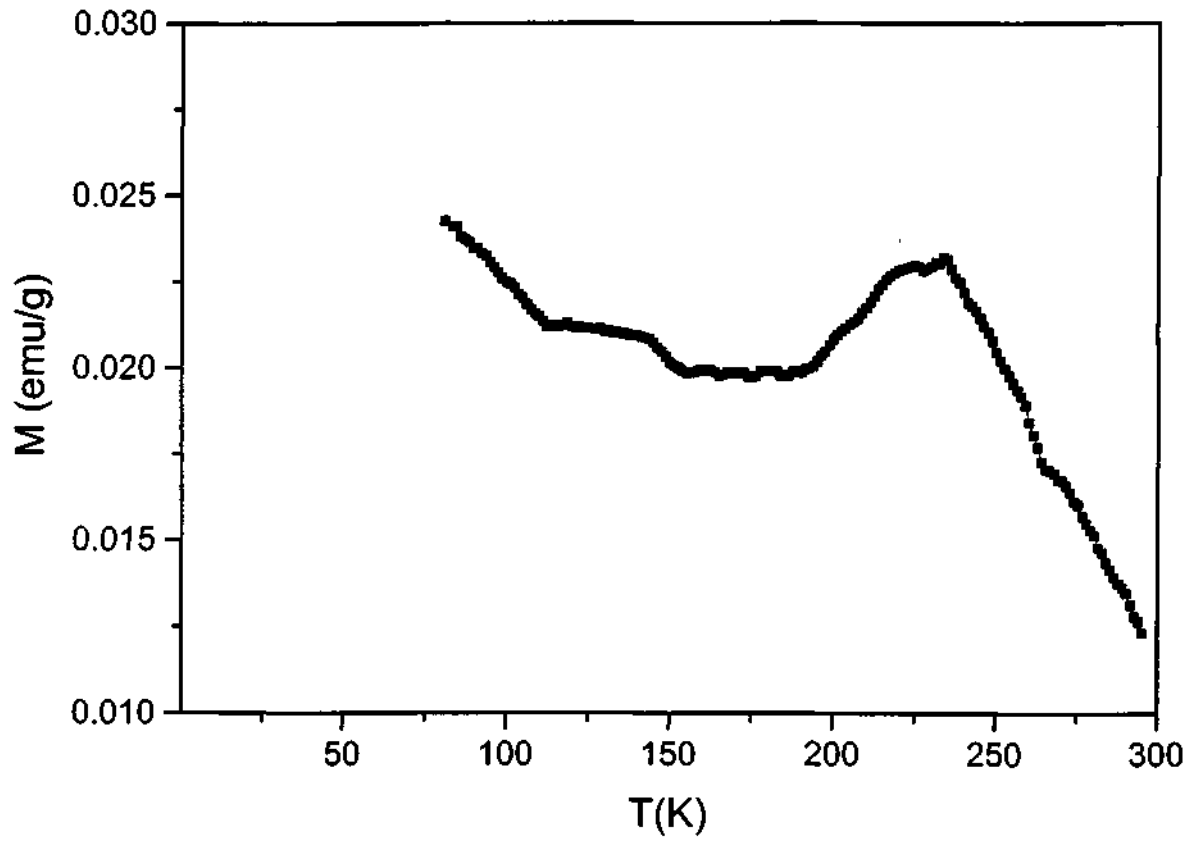[3] A. Machida, Y. Moritomo, K. Ohoyama, T. Katsufuji and A. Nakamura, Phys. Rev. B65, 064435 (2002).

Fig. 4.4.1 Temperature variation of magnetization of $Nd_{0.5}Ca_{0.5}Mn_{0.98}{}^{57}Fe_{0.02}O_3$.
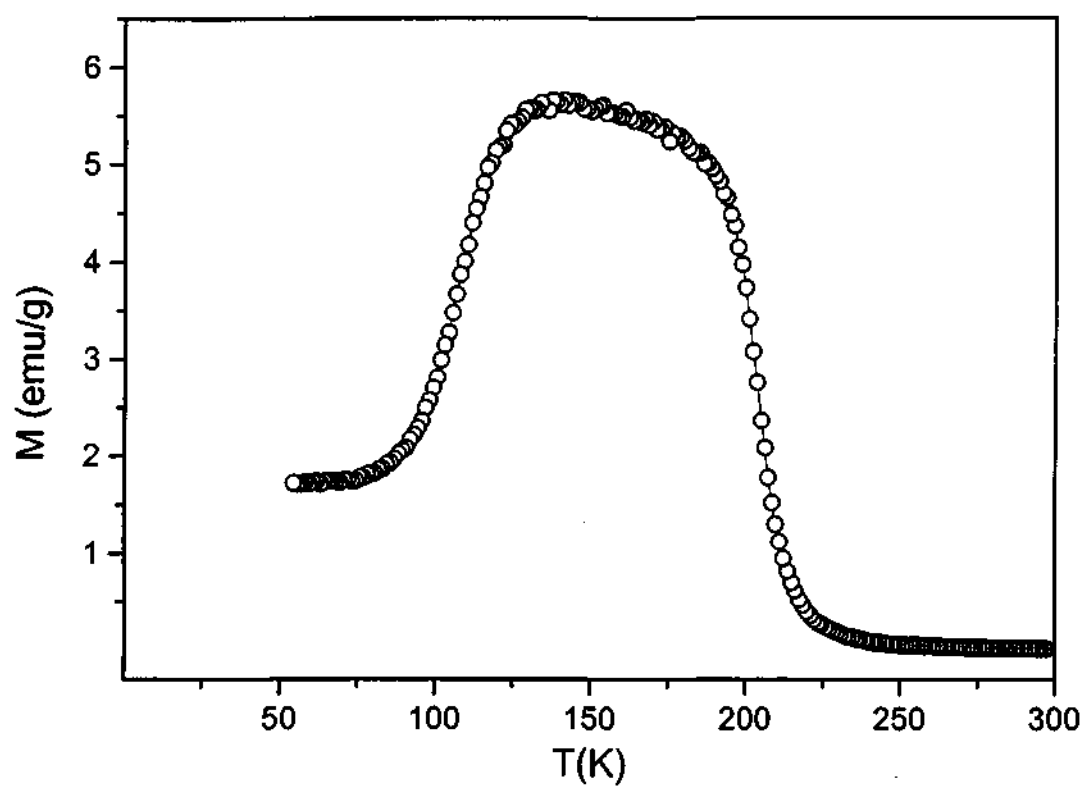
Fig. 4.4.2 Temperature variation of magnetization of $Nd_{0.5}Sr_{0.5}Mn_{0.98}{}^{57}Fe_{0.02}O_3$.

$Nd_{0.5}Sr_{0.5}MnO_3$ are found to undergo a transition to A-type antiferromagnetic state on cooling the ferromagnetic state below 225 K followed by the transition to the CE-type antiferromagnetic state below 150 K. At very low temperatures, all the three phases are reported to coexist in some samples of $Nd_{0.5}Sr_{0.5}MnO_3$ [5,6]. The residual magnetization found at 100 K and below in the magnetization data shown in Fig. 4.4.2 could arise from the presence of a small fraction of the ferromagnetic phase.

$Nd_{0.5}Ca_{0.5}Mn_{0.98}{}^{57}Fe_{0.02}O_3$: Mössbauer spectra of $Nd_{0.5}Ca_{0.5}Mn_{0.98}{}^{57}Fe_{0.02}O_3$ over the temperature range 295-100 K are shown in Fig. 4.4.3. The room temperature spectrum is a single paramagnetic doublet with an isomer shift (IS) of 0.26 ± 0.01mm/s and a quadrupole splitting (QS) of 0.20 ± 0.01mm/s. The isomer shift value is characteristic of Fe^{3+}. On cooling the sample, IS increases gradually and tends to saturate below 130 K as can be seen in Fig. 4.4.4 (a). The spectra retain the doublet character down to 90 K. The line-width increases exhibiting a definitive change below 230 K as evident from the spectra in Fig. 4.4.3. While the line broadening below 230 K suggests possible magnetic hyperfine interaction, the retention of the doublet like-feature indicates that only short-range magnetic order may exist in the 230-90 K region. The line-width becomes nearly constant around 110 K where the material is known to become antiferromagnetic. One can fit the Mössbauer spectra below 200 K to two doublets with same isomer shifts, line

---

[4] H. Kuwahara, Y. Tomioka, A. Asamitsu, Y. Moritomo and Y. Tokura, Science 270, 961 (1995).

[5] P. M. Woodward, D. E. Cox, T. Vogt, C. N. R. Rao and A. K. Cheetham, Chem. Mater. 11, 3528 (1999).

[6] C. Ritter, R. Mahendiran, M. R. Ibarra, L. Morellon, A. Maignan, B. Raveau, C. N. R. Rao, Phys. Rev. B61, R9229 (2000).
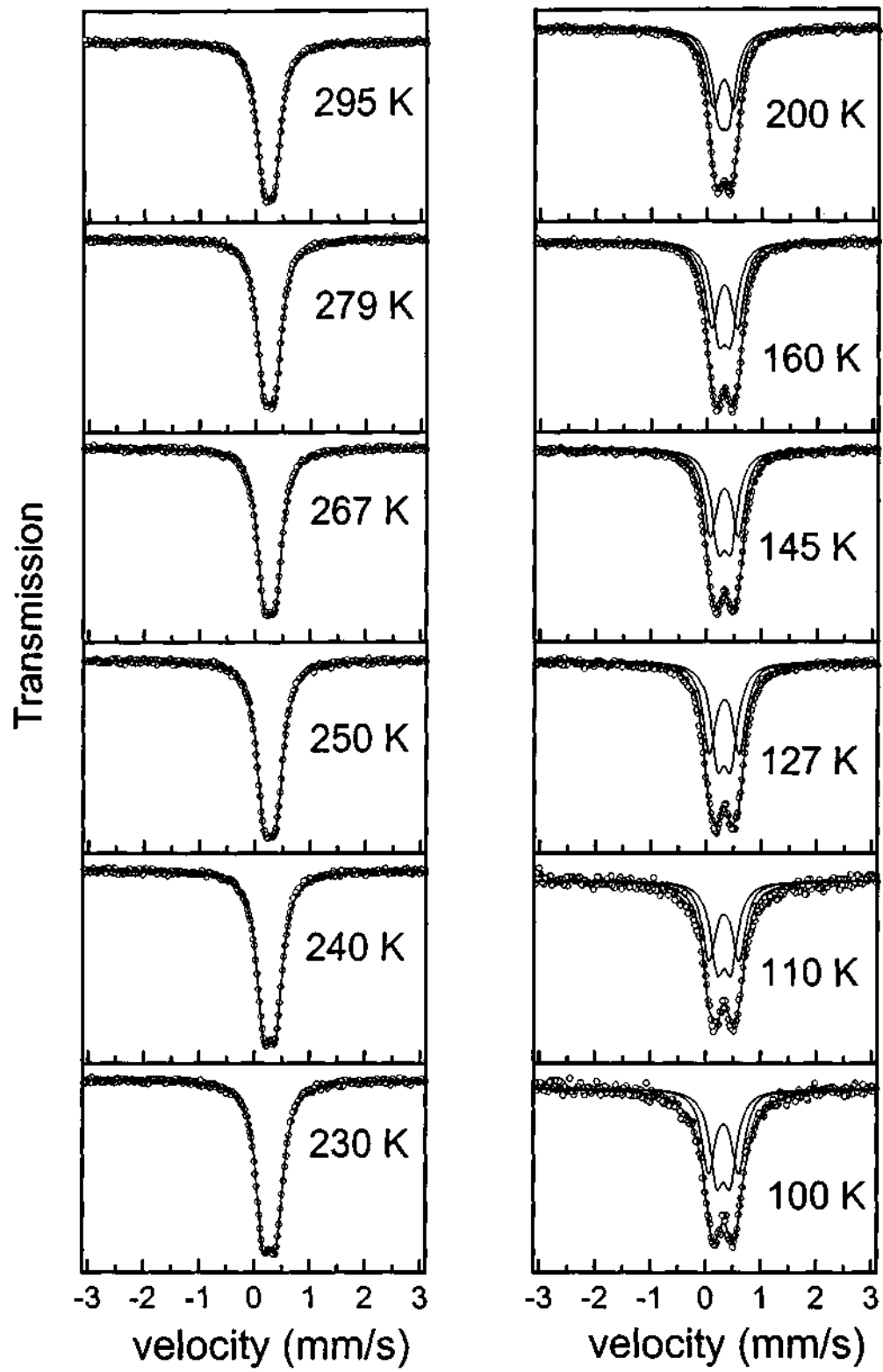
Fig. 4.4.3 Mössbauer spectra of $Nd_{0.5}Ca_{0.5}Mn_{0.98}{}^{57}Fe_{0.02}O_3$ in the 100 - 295 K range. Decomposition to two doublets in the 100-200 K range is also shown.

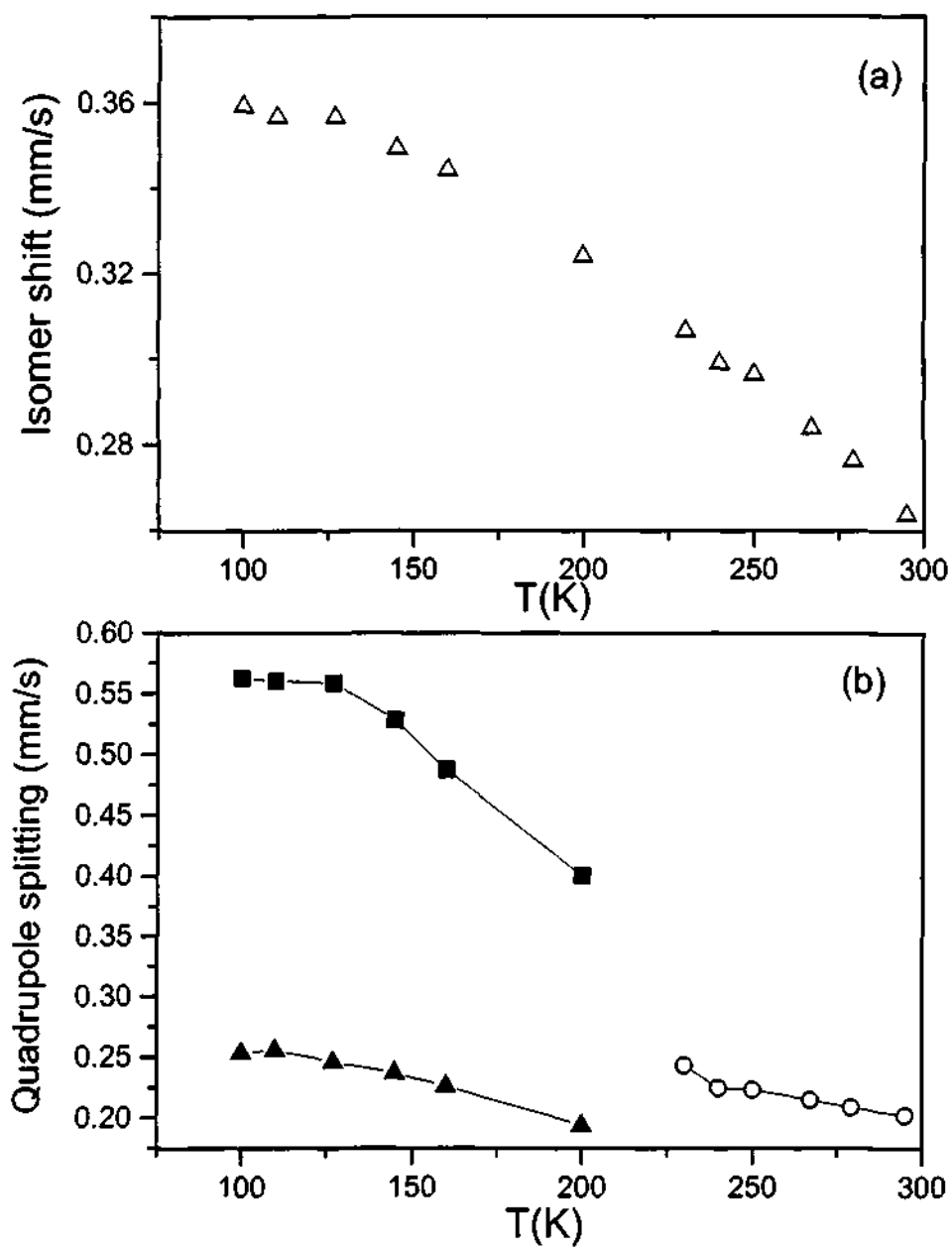Fig. 4.4.4 Temperature variation of (a) the isomer shift and (b) quadrupole splitting of $Nd_{0.5}Ca_{0.5}Mn_{0.98}{}^{57}Fe_{0.02}O_3$. The solid lines are only guide to the eye.

widths and intensities but different quadrupole splitting. The fitted subspectra are shown in Fig. 4.4.3. This fitting method was chosen based on the possibility of Fe^{3+} being located in two different manganese sites created by the ordering of Mn^{3+} and Mn^{4+} ions. In Fig. 4.4.4 (b), we show the temperature variation of the quadrupole splitting. The quadrupole splitting increases with decrease in temperature showing a jump around 230 K (T_{CO}). The quadrupole splitting is split into two components below 230 K down to 100 K, one with higher QS (QS1) than the room temperature spectrum and the other with lower QS (QS2). With the lowering of temperature, both QS1 and QS2 increase, but the increase in the value of QS1 is greater than that of QS2. Both QS1 and QS2 become a constant below ~130 K. The observation of two quadrupole splittings is consistent with the occurrence of two phases with large and small c-parameters below T_{CO} [3].

The spectrum at 60 K is broad and unresolved (Fig. 4.4.5) and indicates a disordered state. The spectrum at 40 K shows a six-finger pattern indicative of a long-range antiferromagnetic order, but disorder continues to persist. The spectrum at 4.2 K is, however, well-split with reasonably narrow lines indicating that all the Fe ions have reached saturating internal fields. Since the lines are slightly broader than the experimental line-widths for Fe-metal, we invoke the presence of more than one site for Fe. We are able to fit the spectrum to two sets of magnetically split lines of equal intensity and width and a paramagnetic doublet with a width similar to that of the room temperature spectrum. The hyperfine field, H_{int}, of the two magnetic phases are 487 and 503 kOe and their respective isomer shifts are 0.39 ± 0.01 and 0.40 ± 0.01 mm/s. The spectrum at 4.2 K does not show appreciable asymmetry and hence no appreciable quadrupole shift of the magnetic phases.
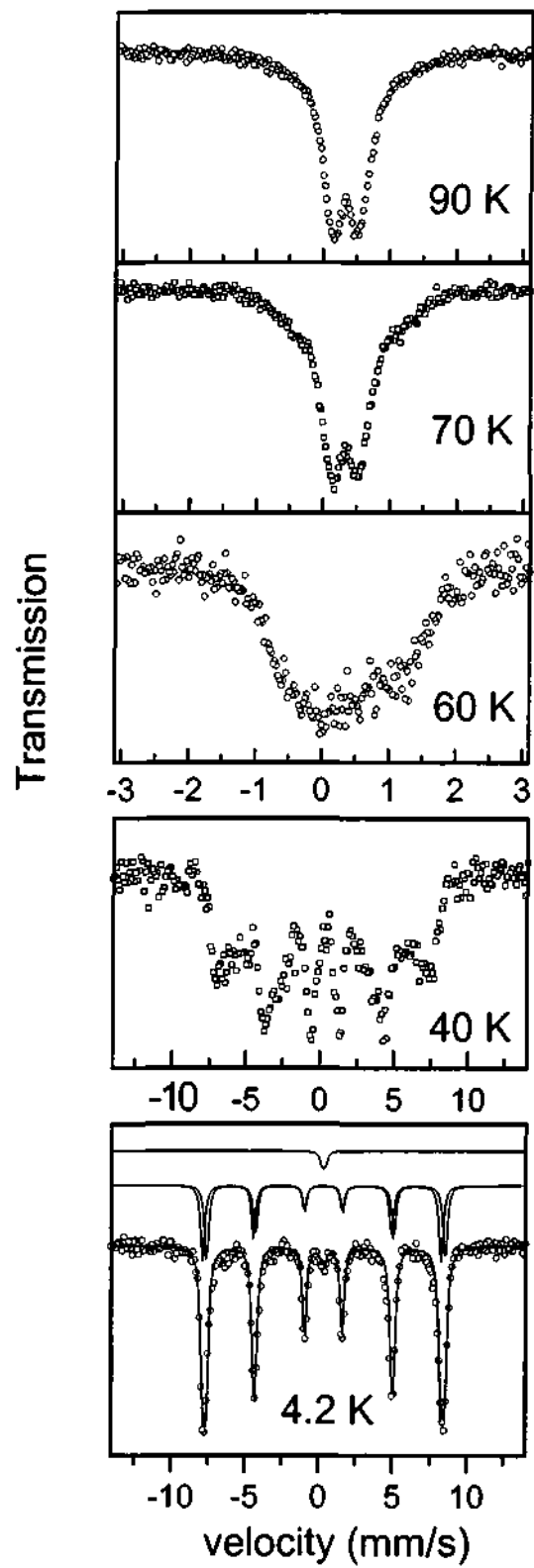
Fig. 4.4.5 Mössbauer spectra of $Nd_{0.5}Ca_{0.5}Mn_{0.98}{}^{57}Fe_{0.02}O_3$ in the 4.2 – 90 K range.

The spectrum at 4.2 K can be decomposed to three components.

We suggest that the two magnetically split spectra arise from the two paramagnetic phases (with different values of QS). Thus, our Mössbauer study shows that this manganate is phase-separated at low temperatures.

$Nd_{0.5}Sr_{0.5}Mn_{0.98}{}^{57}Fe_{0.02}O_3$: $Nd_{0.5}Sr_{0.5}Mn_{0.98}{}^{57}Fe_{0.02}O_3$ shows a single quadrupole doublet at 295 K with an isomer shift of 0.26 ± 0.01 mm/s and quadrupole splitting of 0.30 ± 0.01 mm/s (Fig. 4.4.6). The relatively large quadrupolar splitting, QS = 0.30 mm/s at room temperature has its origin in the high orthorhombic distortion of the structure (space group: Imma) [5]. We continue to see the doublet down to 200 K although the isomer shift increases below 250 K as shown in Fig. 4.4.7 (a). This clearly indicates some change taking place in the electronic environment around Fe. Accordingly, we note that the line-width is essentially constant down to 220 K and increases below this temperature as can be seen from Fig. 4.4.7 (b). This is consistent with the magnetization data (Fig. 4.4.2). The changes found in the line-width below 220 K correspond to the paramagnetic to ferromagnetic transition, although we do not see a clear six-finger spectrum as expected of a long range ferromagnetically ordered system. There is a definitive and discernible six-finger spectrum below 180 K (Fig. 4.4.8), although there is disorder. Compared to $Nd_{0.5}Ca_{0.5}Mn_{0.98}{}^{57}Fe_{0.02}O_3$, however, the magnitude of disorder may be less, as evidenced from the resolution of the spectrum at 41 K.

The transition to the CE-type antiferromagnetic state around 120 K (which is evident from the magnetization data in Fig. 4.4.2) is difficult to discern from Mössbauer spectra (Fig.4.4.8), although the hyperfine features are somewhat more obvious in the
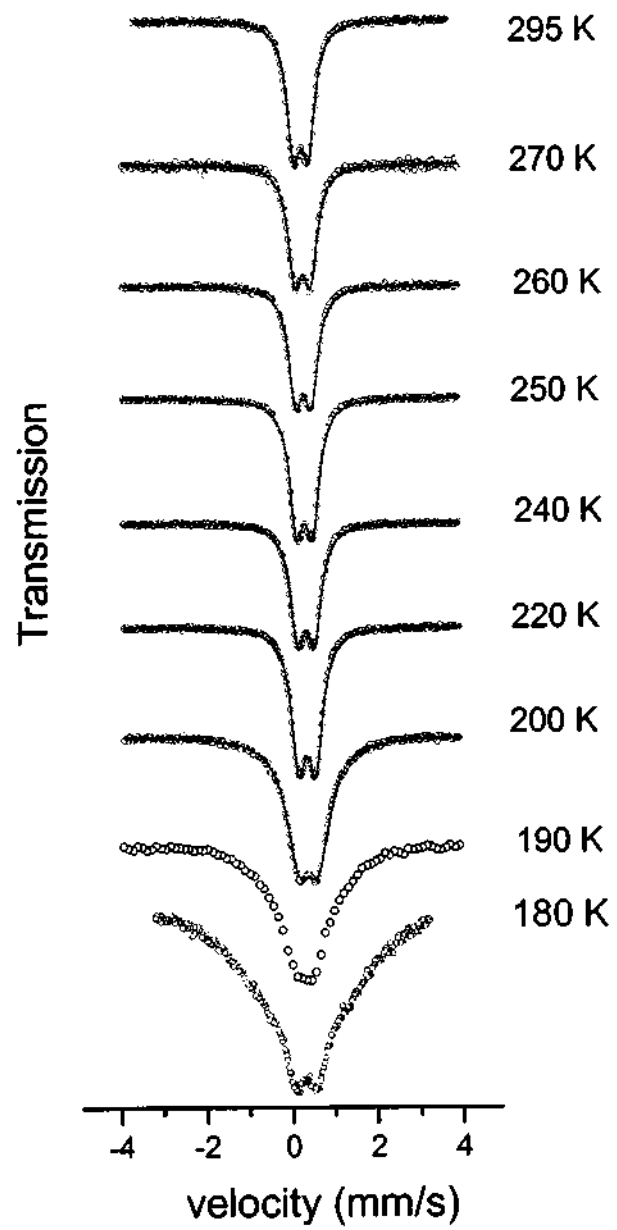
195

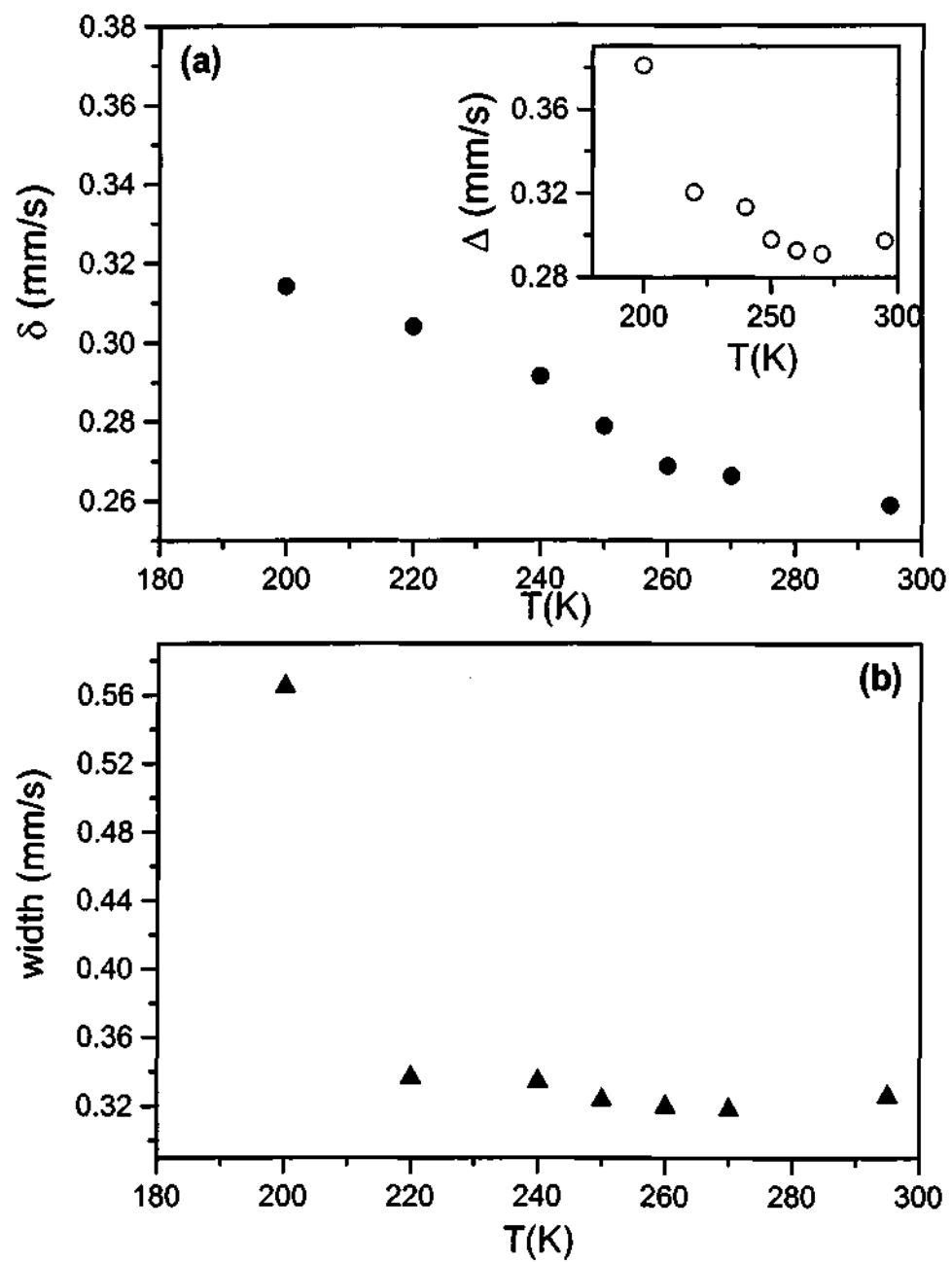Fig. 4.4.6 Mössbauer spectra of $Nd_{0.5}Sr_{0.5}Mn_{0.98}{}^{57}Fe_{0.02}O_3$ in the 180-295 K range

Fig. 4.4.7 Temperature variation of (a) the isomer shift and (b) the width of the quadrupole split spectra observed for $Nd_{0.5}Sr_{0.5}Mn_{0.98}{}^{57}Fe_{0.02}O_3$. The inset in (a) shows the variation of quadrupole splitting as a function of temperature.
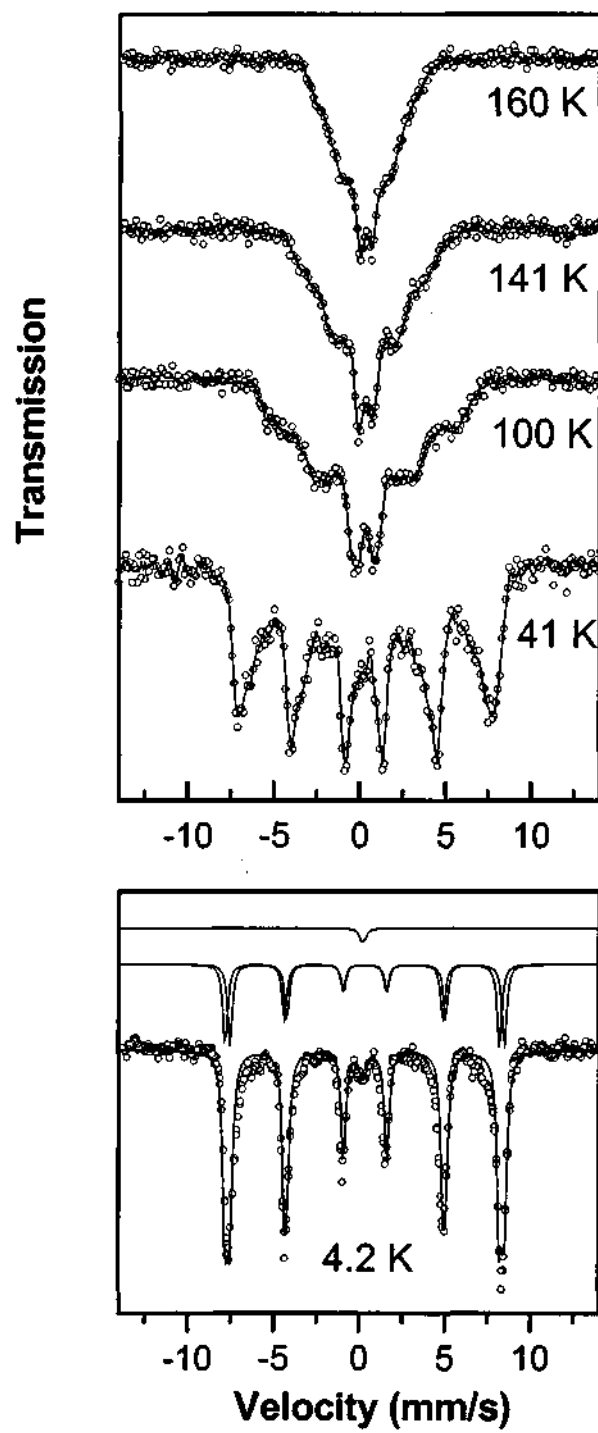
197

Fig. 4.4.8 Mössbauer spectra of $Nd_{0.5}Sr_{0.5}Mn_{0.98}{}^{57}Fe_{0.02}O_3$ in the 4.2 – 160 K range. The 4.2 K spectrum is fitted with two sextets and a weak paramagnetic doublet.

198

spectrum at 100 K. A certain feature in all the spectra below 160 K is the presence of an unresolved magnetic hyperfine spectrum with an additional central paramagnetic doublet. The evolution of the spectral line shape from 200 K downwards is typical of superparamagnetic relaxation or of the magnetic correlation evolving slowly from short range to long range. Thus, the Mössbauer spectra show that in this charge ordered manganate, long-range magnetic order does not emerge in a clean manner, just as in $Nd_{0.5}Ca_{0.5}MnO_3$. The coexistence of two or more phases, such as A- and CE-type antiferromagnets besides the ferromagnetic phase in $Nd_{0.5}Sr_{0.5}MnO_3$ has been pointed out [5]. The Mössbauer spectra show that indeed. The systems evolve in a complex manner, although it is not straightforward to assign the possible phases present in the 160 - 40 K range. At 4.2 K, however, we see a well-resolved magnetic hyperfine spectrum with reasonably narrow line-width which implies, either that the long range order sets in or that the superparamagnetic relaxation reaches its end. The slightly broad spectrum of $Nd_{0.5}Sr_{0.5}Mn_{0.98}{}^{57}Fe_{0.02}O_3$ at 4.2 K (Fig. 4.4.8) can be resolved into essentially two site magnetic six-line spectra and a weak doublet reminiscent of the paramagnetic phase. The hyperfine field, H_{int} of the two magnetic phases are 488 and 506 kOe and their respective isomer shifts are 0.38 ± 0.01 and 0.39 ± 0.01 mm/s. The 4.2 K spectrum clearly results from phase separation. It is not however, possible to unequivocally resolve the magnetic phases, as all the phases seem to have the same local field value at the Fe nuclei.

Conclusions

The study indicates that Fe exists in the 3+ state in both the manganates, namely $Nd_{0.5}Ca_{0.5}Mn_{0.98}{}^{57}Fe_{0.02}O_3$ and $Nd_{0.5}Sr_{0.5}Mn_{0.98}{}^{57}Fe_{0.02}O_3$. The evolution of the Mössbauer

spectra as a function of temperature shows that long-range magnetic order does not emerge in a clean manner in both the manganates studied. The well-resolved magnetic hyperfine Mössbauer spectra at 4.2 K of both $Nd_{0.5}Ca_{0.5}Mn_{0.98}{}^{57}Fe_{0.02}O_3$ and $Nd_{0.5}Sr_{0.5}Mn_{0.98}{}^{57}Fe_{0.02}O_3$ indicate the presence of more than one magnetic phase. A weak paramagnetic component is also evident in the spectra at 4.2 K of $Nd_{0.5}Ca_{0.5}Mn_{0.98}{}^{57}Fe_{0.02}O_3$ and $Nd_{0.5}Sr_{0.5}Mn_{0.98}{}^{57}Fe_{0.02}O_3$. Mössbauer spectroscopy of these two manganates confirms that these materials undergo phase separation at low temperatures.

4.5 A study of electron-doped manganates, $Ca_{1-x}Ln_xMnO_3$ (x < 0.5)

The lattice parameters of $Ca_{1-x}Ln_xMnO_3$ (Ln = La, Nd, Gd, Y; x = 0.2, 0.36) compositions are listed in Table 4.5.1. The compounds $Ca_{1-x}Ln_xMnO_3$ with x = 0.1 do not show evidence for charge-ordering properties in the 120-300 K range, and instead exhibit ferromagnetic interactions akin to those in spin glasses [1]. The compounds with x = 0.2 show peaks in magnetization due to charge ordering at 215, 176 and 157 K for Ln = La, Nd and Gd respectively (Fig. 4.5.1(a)). At these temperatures, there is a marked increase in electrical resistivity as can be seen in Fig. 4.5.1(b). The compounds with compositions corresponding to the optimal 3/8 doping (x = 0.36) show interesting electrical and magnetic properties. Thus, the magnetization exhibits a broad maximum at around 270 K when Ln = La, Nd or Gd (Fig. 4.5.2 (a)). Around this temperature, there is a small, but definitive, jump in resistivity (Fig. 4.5.2 (b)). An examination of the variation of T_{CO} in $Ca_{1-x}Ln_xMnO_3$ suggests that T_{CO} increase with the increase in x or the electron concentration. When x = 0.2, T_{CO} decreases significantly, although $\langle r_A \rangle$ decreases with only a marginal change in the σ^2 value (Table 4.5.1). When x = 0.36, T_{CO} is nearly constant despite the marked decrease in $\langle r_A \rangle$ and fairly high values of σ^2 when Ln = Gd. It appears that at optimal electron doping, $\langle r_A \rangle$ has no effect on T_{CO}. The yttrium substituted materials with the smallest values of $\langle r_A \rangle$ fail to exhibit high values of T_{CO} and fall in line with the manganates discussed above (Table 4.5.1). These trends for the electron-doped $Ca_{1-x}Ln_xMnO_3$ compounds are different from those for the hole-doped $Ln_{1-x}Ca_xMnO_3$

[1] (a) A. Maignan, C. Martin, F. Damay and B. Raveau Chem. Mater. 10, 950 (1998). (b) A. Maignan, C. Martin, F. Damay, B. Raveau and J. Hejtmanck Phys. Rev. B58, 134 (1998).

Table 4.5.1

Properties of electron-doped manganates showing charge-ordering

Composition	$<r_A>$ (Å)	σ^2 (Å^2)	Lattice parameters (Å)[a]			D%	T_{CO}[b] (K)
			a	b	c		
$Ca_{0.8}La_{0.2}MnO_3$	1.187	0.0002	5.333	5.316	7.546	0.15	215 (170)
$Ca_{0.64}La_{0.36}MnO_3$	1.193	0.0003	5.390	5.391	7.588	0.20	271 (254)
$Ca_{0.8}Nd_{0.2}MnO_3$	1.177	0.00005	5.317	5.316	7.495	0.13	176 (154)
$Ca_{0.64}Nd_{0.36}MnO_3$	1.174	0.00007	5.388	5.361	7.570	0.33	271 (253)
$Ca_{0.8}Gd_{0.2}MnO_3$	1.165	0.0008	5.300	5.311	7.482	0.13	157 (139)
$Ca_{0.64}Gd_{0.36}MnO_3$	1.154	0.0012	5.354	5.381	7.509	0.26	269 (252)
$Ca_{0.8}Y_{0.2}MnO_3$	1.159	0.0017	5.262	5.339	7.437	0.65	182 (141)
$Ca_{0.64}Y_{0.36}MnO_3$	1.142	0.0025	5.295	5.295	7.451	1.32	- (240)

[a] *Space group: Pbnm*; Uncertainties in the lattice parameters are within ± 0.001 Å.

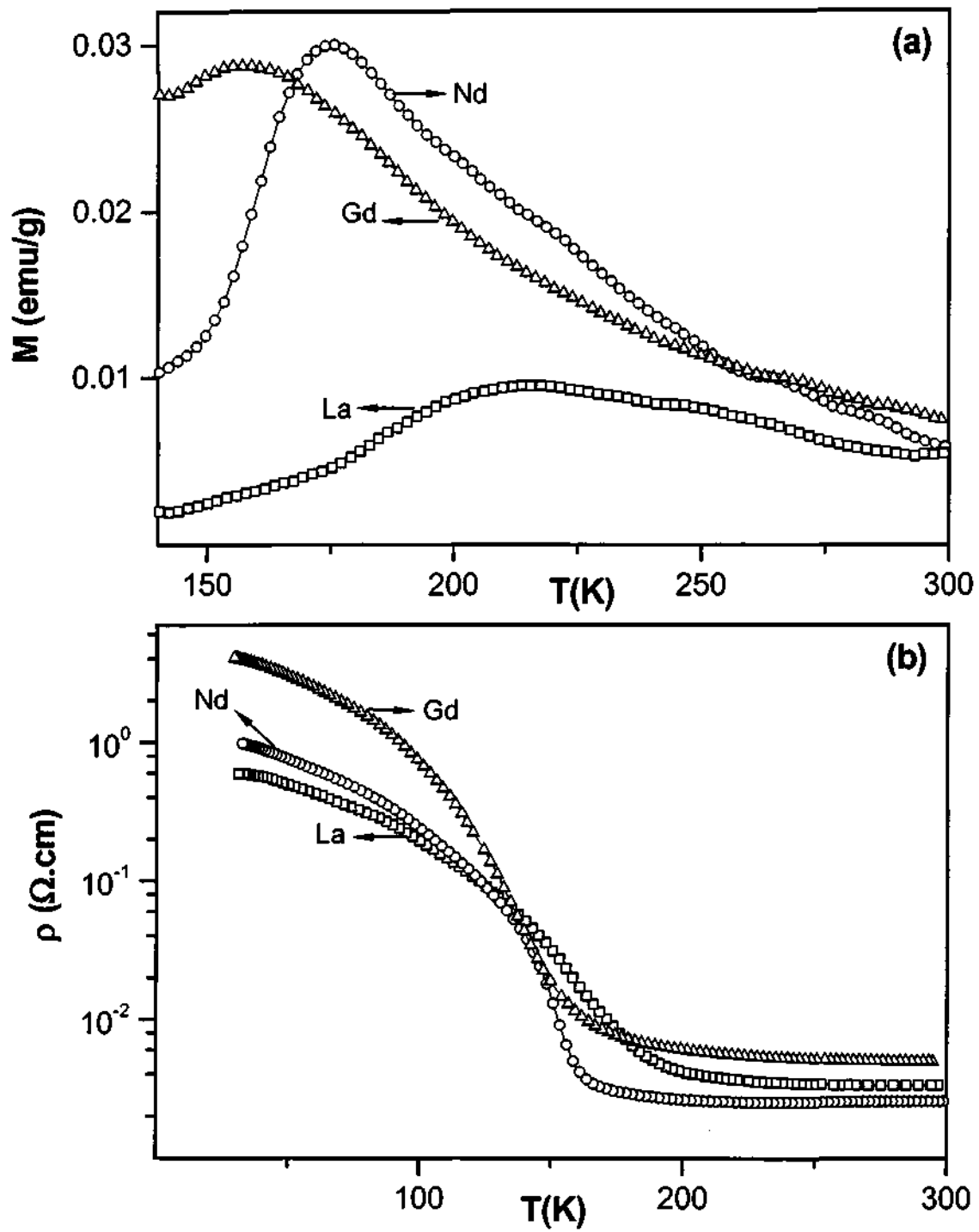[b] From magnetization measurements; values in parenthesis are from resistivity data.

Fig. 4.5.1 The temperature variation of (a) the magnetization and (b) the electrical resistivity of $Ca_{0.8}Ln_{0.2}MnO_3$ (Ln = La, Nd, Gd).

203
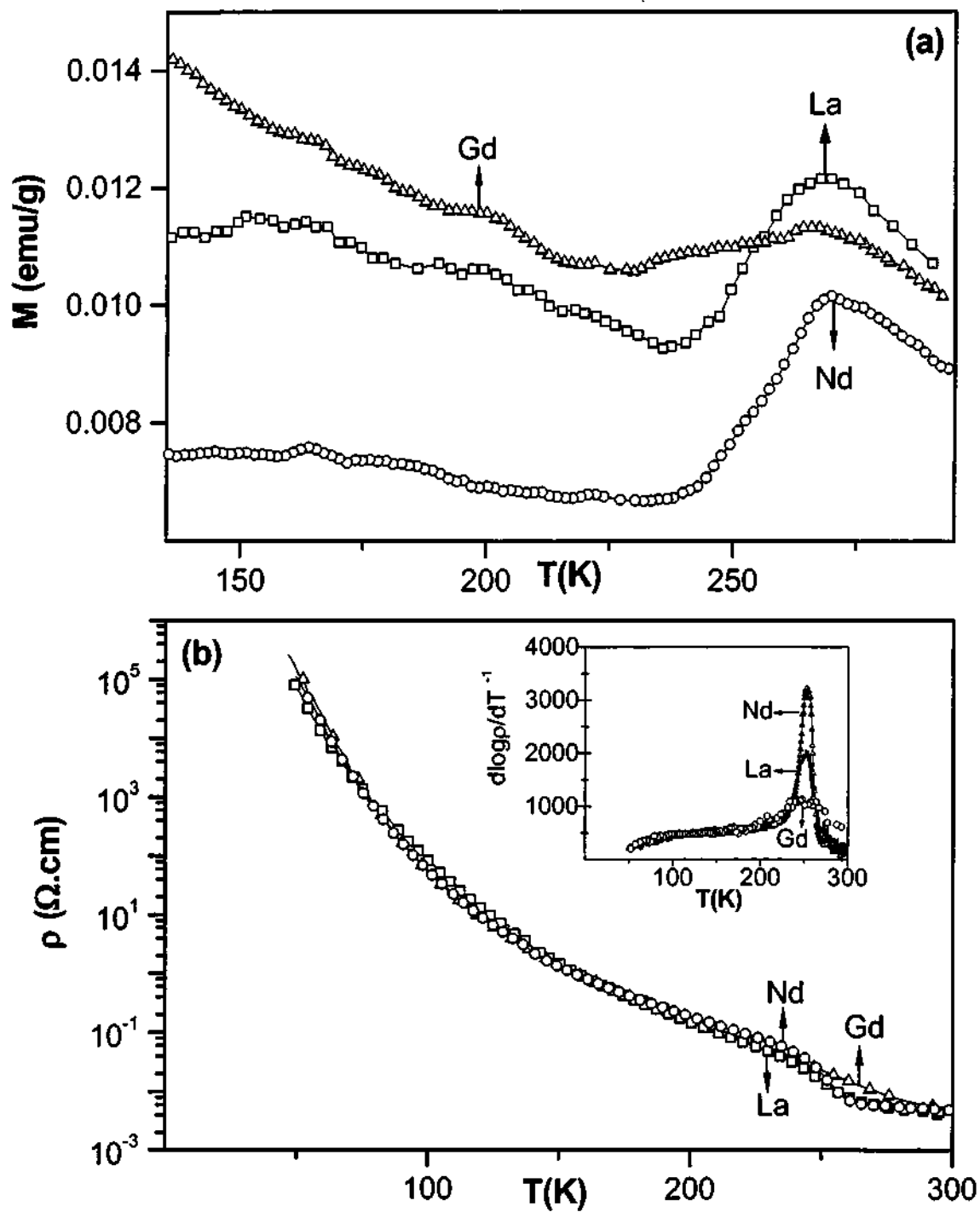
Fig. 4.5.2 The temperature variation of (a) the magnetization and (b) the electrical resistivity of $Ca_{0.64}Ln_{0.36}MnO_3$ (Ln = La, Nd, Gd). The inset in (b) shows the temperature variation of $d(log\rho)/dT^{-1}$ (or the activation energy).

204

compounds, where T_{CO} increase with decrease in $\langle r_A \rangle$ as could be seen in Fig. 4.5.3. Interestingly, the decrease in T_{CO} with $\langle r_A \rangle$ when x = 0.2 is in the same direction as the decrease in ferromagnetic interaction.

We have also studied the electron-doped manganate, $Ca_{0.64}Pr_{0.36}MnO_3$ with a negligible size mismatch between the A-site cations, i.e. Pr and Ca with 9- coordinate Shannon radii of 1.179 and 1.18 Å. The compound is a charge ordered insulator like the other analogues with a T_{CO} of 268 K (Fig. 4.5.4(a)). In Table 4.5.2, we list the atomic coordinates and lattice parameters of $Ca_{0.64}Pr_{0.36}MnO_3$ obtained from Rietveld analysis. There is no effect of an applied magnetic field of 12 T on the resistivity of this sample (Fig. 4.5.4 (b)) which suggests the robustness of the charge ordered state in this manganate.

The effect of cation size disorder on the charge-ordering transition in the electron doped manganates $Ca_{1-x}Ln_xMnO_3$ with x = 0.36 has been investigated by keeping the average radius of the A-site cation, $\langle r_A \rangle$ fixed and varying σ^2. The value of σ^2 is varied by making different combinations of the Ln and alkaline-earth ions. We have studied two series of electron-doped manganates of the type $Ca_{0.64}Ln_{0.36}MnO_3$ with fixed $\langle r_A \rangle$ of 1.174 and 1.18 Å pertaining to $Ca_{0.64}Nd_{0.36}MnO_3$ and $Ca_{0.64}Pr_{0.36}MnO_3$ as listed in Table 4.5.3. The temperature variation of the resistivity and magnetization of a few members of the two series of compounds are shown in Figures 4.5.5 and 4.5.6. As could be seen from the anomalies in the resistivity and magnetization data the T_{CO} decreases with increase in σ^2. The plots of the T_{CO} against σ^2 for the two series of manganates are shown in Fig. 4.5.7. The plots are linear, giving slopes 5813 and 6408 K$Å^{-2}$ for fixed $\langle r_A \rangle$ of 1.174 and 1.18 Å,
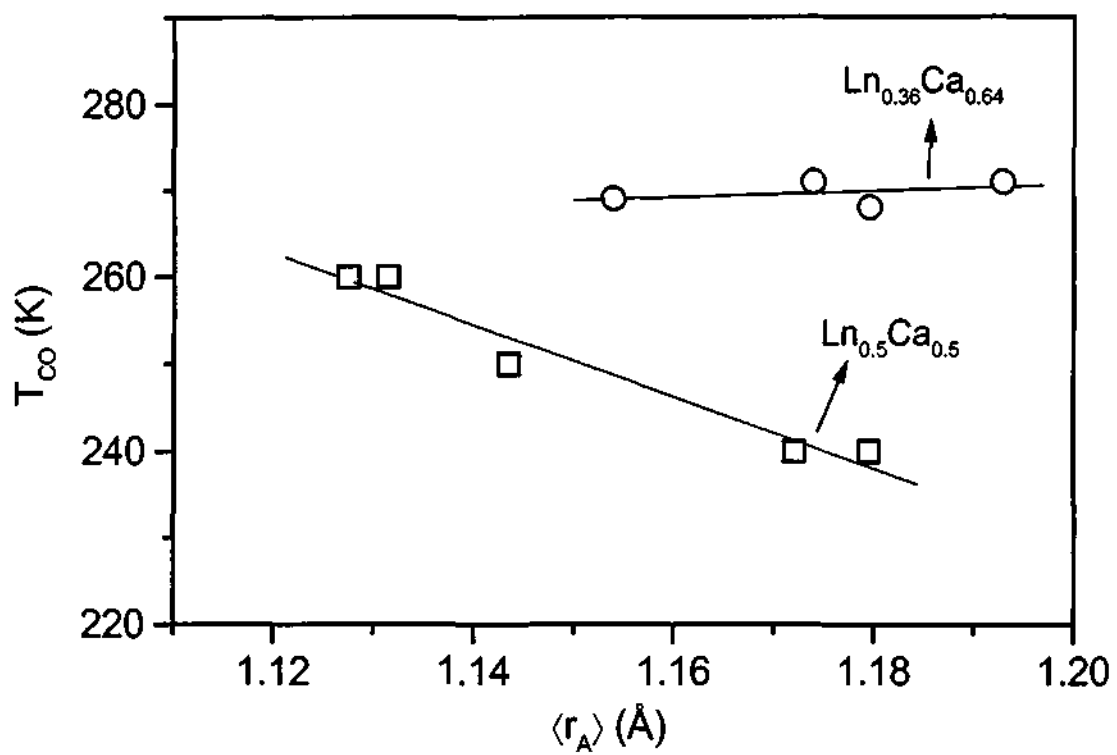
Fig. 4.5.3 Variation of the charge-ordering transition temperature, T_{CO}, with the average

size of the A-site cation, $\langle r_A \rangle$.

Table 4.5.2

Atomic coordinates and structural parameters of $Pr_{0.36}Ca_{0.64}MnO_3$

Atom	Site	x	y	z	Frac	U_{ISO}
Pr	4c	0.5027	0.4746	0.2500	0.3600	-0.0033
Ca	4c	0.5027	0.4746	0.2500	0.6400	-0.0033
Mn	4b	0.5000	0.0000	0.0000	1.0000	0.0063
O	8d	0.0544	0.5213	0.2500	1.0000	0.0901
O	4c	0.2854	0.2717	-0.0460	1.0000	-0.0367

Bond distance (Å)		Bond angle (°)	
Mn-O	2 x 1.892 2 x 1.993 2 x 1.916	Mn-O-Mn	4 x 155.6 2 x 161.2

Space group: Pbnm; $\underline{a}$ = 5.3664 Å, $\underline{b}$ = 5.3746 Å, $\underline{c}$ = 7.5603 Å; R_{wp}= 3.28%.
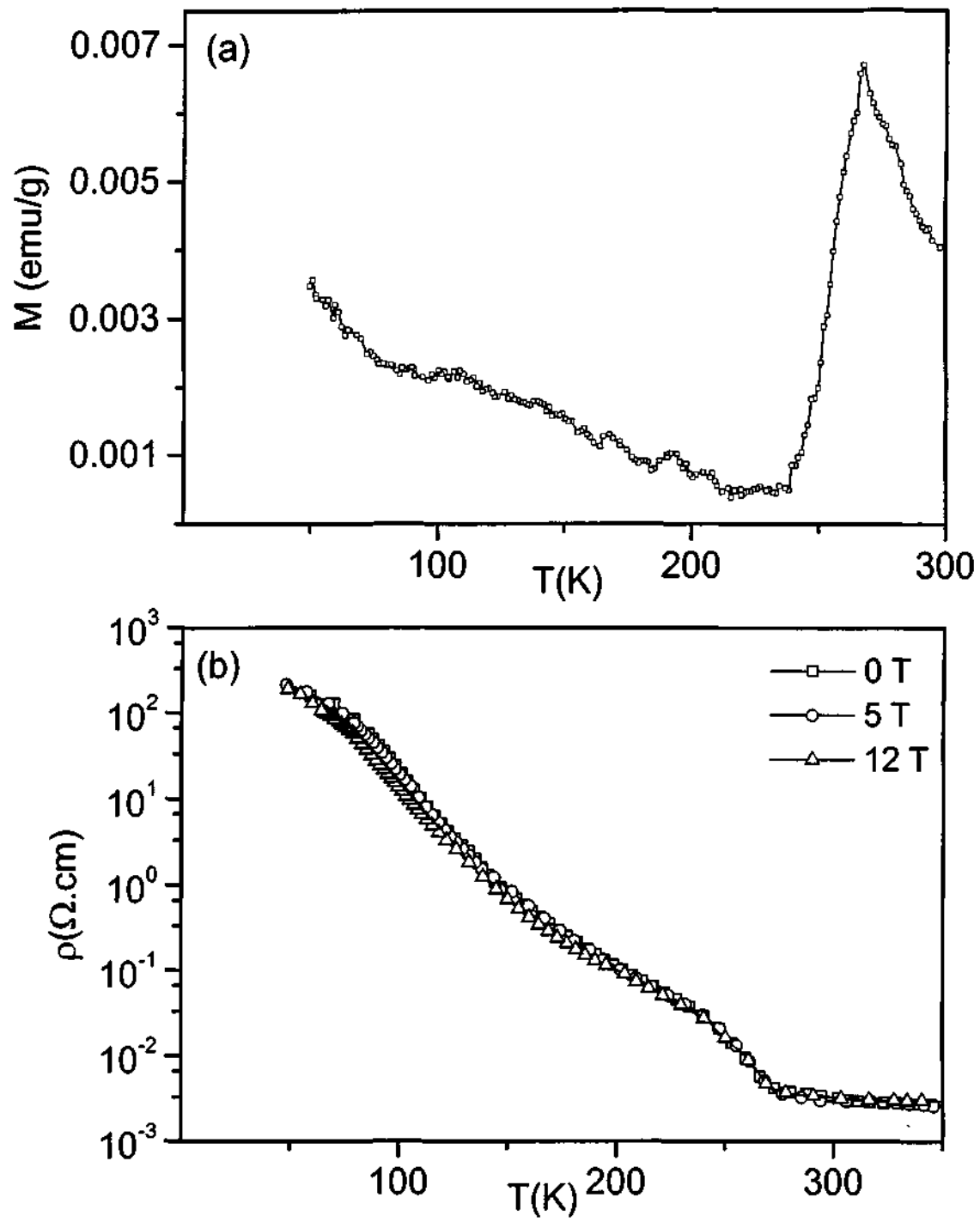
Fig. 4.5.4 Temperature variation of (a) magnetization and (b) resistivity at 0, 5 T and 12 T

of $Pr_{0.36}Ca_{0.64}MnO_3$.

Table 4.5.3

Structure and properties of $Ln_{0.36-x}Ln'_xCa_{0.64-y}Sr_yMnO_3$ with fixed $\langle r_A \rangle$ values

Composition	σ^2 ($\mathring{A}^2$)	lattice parameter ($\mathring{A}$) [a]			%D (300 K)	T_{CO} [b] (K)
		a	b	c		
$\langle r_A \rangle$ = 1.174 Å						
$Nd_{0.36}Ca_{0.64}MnO_3$	0.0001	5.388	5.361	7.570	0.33	271 (261)
$Pr_{0.28}Gd_{0.08}Ca_{0.64}MnO_3$	0.0003	5.353	5.366	7.548	0.18	279 (270)
$La_{0.185}Gd_{0.175}Ca_{0.64}MnO_3$	0.0011	5.354	5.369	7.537	0.27	257 (253)
$La_{0.225}Y_{0.135}Ca_{0.64}MnO_3$	0.0017	5.353	5.370	7.563	0.15	249 (248)
$Sm_{0.36}Ca_{0.554}Sr_{0.086}MnO_3$	0.0022	5.355	5.372	7.569	0.15	263 (258)
$Nd_{0.1}Gd_{0.26}Ca_{0.528}Sr_{0.112}MnO_3$	0.0033	5.355	5.364	7.580	0.06	245 (243)
$Gd_{0.15}Y_{0.21}Ca_{0.433}Sr_{0.207}MnO_3$	0.0066	5.346	5.374	7.567	0.21	~229 (223)
$\langle r_A \rangle$ = 1.18 Å						
$Pr_{0.36}Ca_{0.64}MnO_3$	0.0000	5.374	5.369	7.576	0.11	267 (267)
$Nd_{0.18}Sm_{0.18}Ca_{0.553}Sr_{0.087}MnO_3$	0.0019	5.369	5.370	7.580	0.07	~256 (251)
$Nd_{0.18}Gd_{0.18}Ca_{0.518}Sr_{0.122}MnO_3$	0.0031	5.363	5.376	7.573	0.14	250 (245)
$La_{0.16}Y_{0.2}Ca_{0.526}Sr_{0.114}MnO_3$	0.0043	5.364	5.370	7.578	0.07	~241 (~238)
$La_{0.1}Y_{0.26}Ca_{0.46}Sr_{0.18}MnO_3$	0.0060	5.386	5.369	7.550	0.32	234 (222)

[a] *Space group: Pbnm*; Uncertainties in the lattice parameters are within ± 0.001 Å.

[b] The values in parentheses are obtained from resistivity data.

Fig. 4.5.5 Temperature variation of (a) the resistivity and (b) the magnetization in the $Ca_{0.64}Ln_{0.36}MnO_3$ series with a fixed $\langle r_A \rangle$ of 1.174 Å.
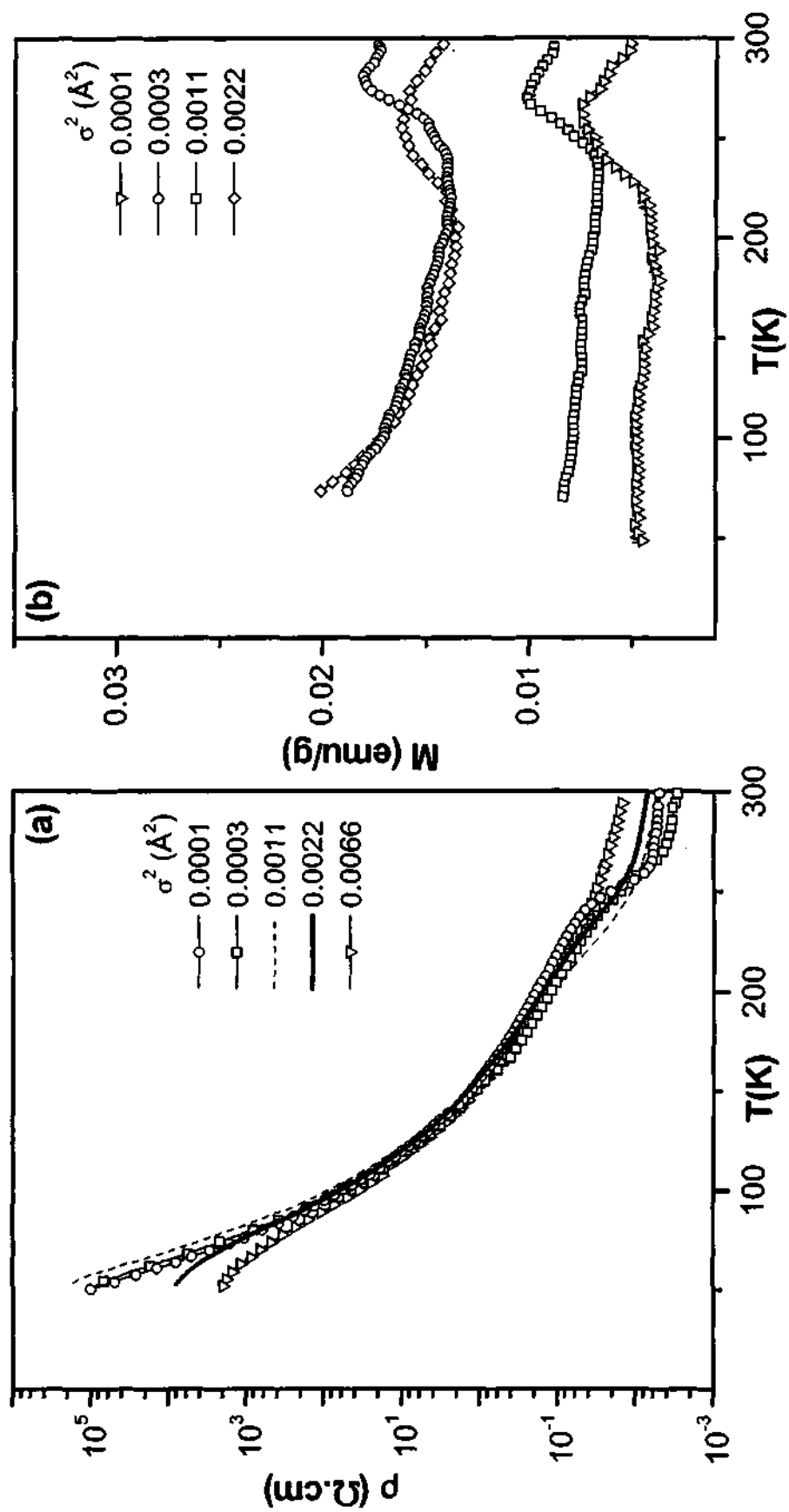
210
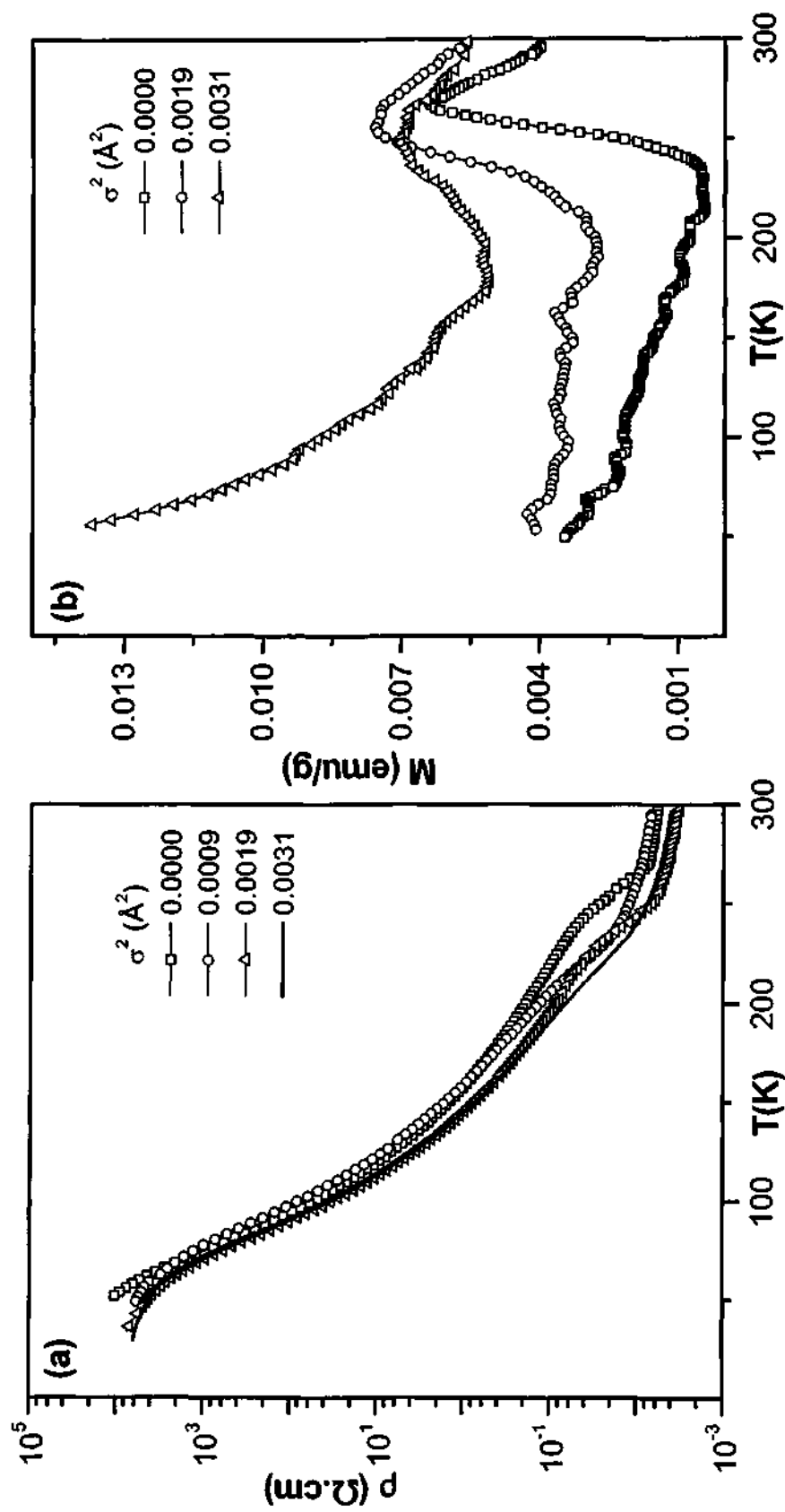
Fig. 4.5.6 Temperature variation of (a) the resistivity and (b) the magnetization in the $Ca_{0.64}Ln_{0.36}MnO_3$ series with a fixed $\langle r_A \rangle$ of 1.18 Å

211

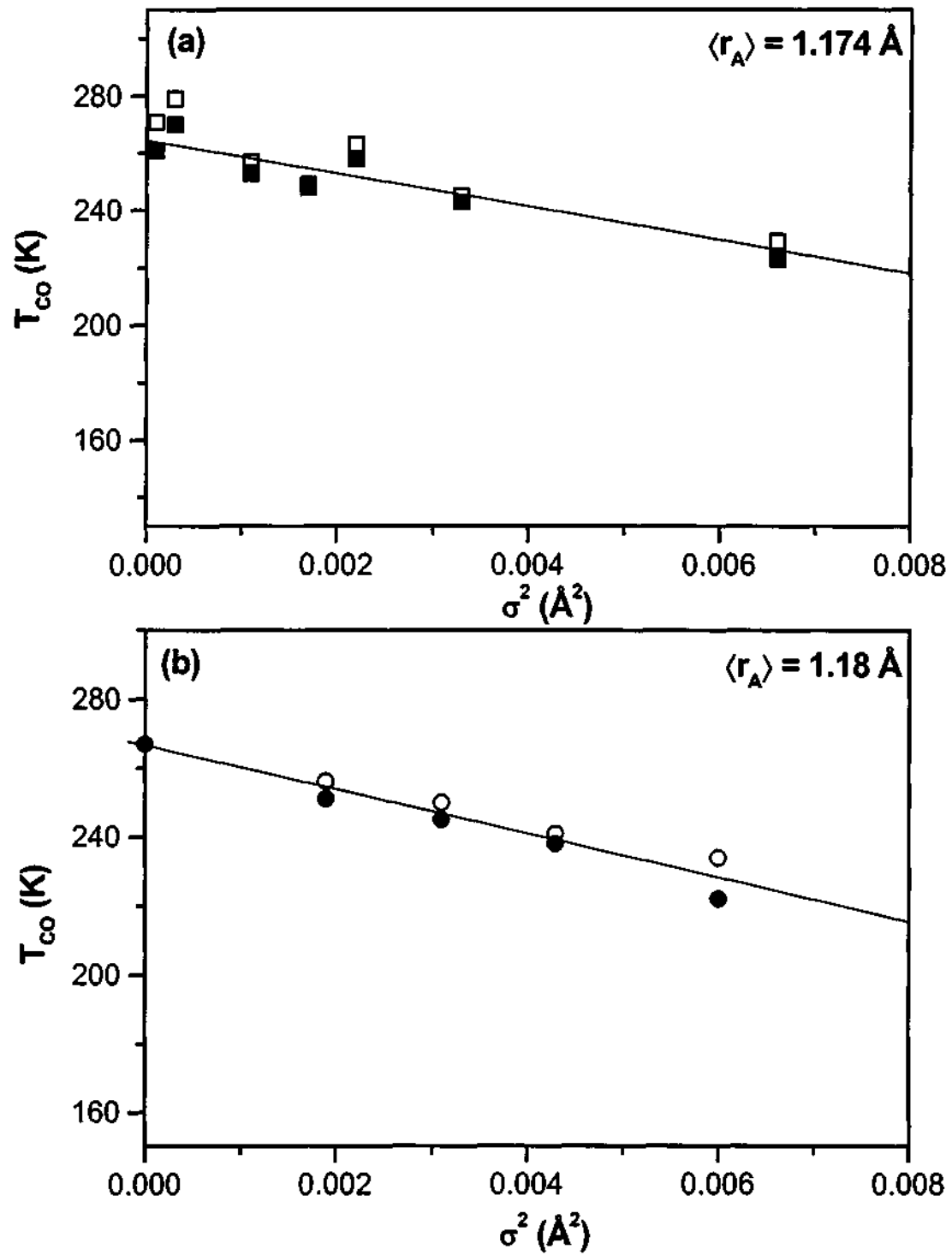Fig. 4.5.7 Variation of the charge-ordering temperature in $Ln_{0.36}Ca_{0.64}MnO_3$ with σ^2 for fixed $\langle r_A \rangle$ values. Open symbols represent data obtained from magnetic measurements, and the corresponding closed symbols are from resistivity measurements.

respectively. The intercept, T^0_{CO}, corresponding to the charge-ordering temperature for a disorder-free manganate, is around 266 K in both the cases. This value of T^0_{CO} is considerably higher than that in $Ln_{0.5}A_{0.5}MnO_3$.

The effects of substitution of Ga and Ge on the charge ordering properties of the electron-doped manganate, $Ca_{0.64}Pr_{0.36}MnO_3$, were also investigated. The magnetization anomaly corresponding to the charge ordering transition is observed in $Ca_{0.64}Pr_{0.36}Mn_{1-x}Ga_xO_3$ upto $x = 0.05$, with the charge ordering transition temperature decreasing with increasing Ga concentration (Fig. 4.5.8). When $x = 0.1$, there is no charge ordering. In the Ge-substituted compositions, there is not much change in T_{CO}, upto $x = 0.10$ as seen in Fig. 4.5.9. All the Ga and Ge substituted $Ca_{0.64}Pr_{0.36}MnO_3$ compositions remain insulating down to low temperatures just as the parent compound. However, the anomaly in the resistivity data around T_{CO} is not so evident when the dopant concentration increases. The properties of these compositions are listed in Table 4.5.4. Though both Ga and Ge have the same electronic configuration ($3d^{10}$), their substitution at the Mn site will have opposite effects on the Mn^{3+}/Mn^{4+} ratios. Also, Ge^{4+} has a six coordination ionic radius (0.54 Å), close to that of Mn^{4+} (0.53 Å) and hence the disorder induced by size would be small. The ionic radius of Ga^{3+} (0.620 Å) is slightly smaller than that of Mn^{3+} (0.645 Å). In general, Ge substitution has less effect on the properties of the parent manganate than Ga substitution. These effects of Ga and Ge substitution on $Ca_{0.64}Pr_{0.36}MnO_3$ are similar to those on $Ln_{0.5}Ca_{0.5}MnO_3$ manganates (see Section 4.2).

The electron-doped manganates with $x = 0.36$ differ from the corresponding hole-doped manganates with respect to the effect of Cr^{3+} doping. The charge-ordered state in

Table 4.5.4

Properties of $Ca_{0.64}Pr_{0.36}Mn_{1-x}M_xO_3$ (M = Ga and Ge)

Composition	Lattice parameters (Å)[a]			T_{CO} [b]
	$\underline{a}$	$\underline{b}$	$\underline{c}$	(K)
$Ca_{0.64}Pr_{0.36}Mn_{1-x}Ga_xO_3$				
0.0	5.366	5.374	7.560	268 (267)
0.01	5.359	5.378	7.545	255 (245)
0.03	5.360	5.369	7.552	237 (228)
0.05	5.360	5.374	7.546	212
0.10	5.361	5.367	7.551	-
$Ca_{0.64}Pr_{0.36}Mn_{1-x}Ge_xO_3$				
0.01	5.361	5.374	7.556	264 (244)
0.03	5.360	5.375	7.562	265 (245)
0.05	5.367	5.371	7.561	264 (242)
0.1	5.365	5.383	7.551	260

[a] *Space group: Pbnm*; Uncertainties in the lattice parameters are within ± 0.001 Å.

[b] Values in parenthesis are from resistivity measurements.

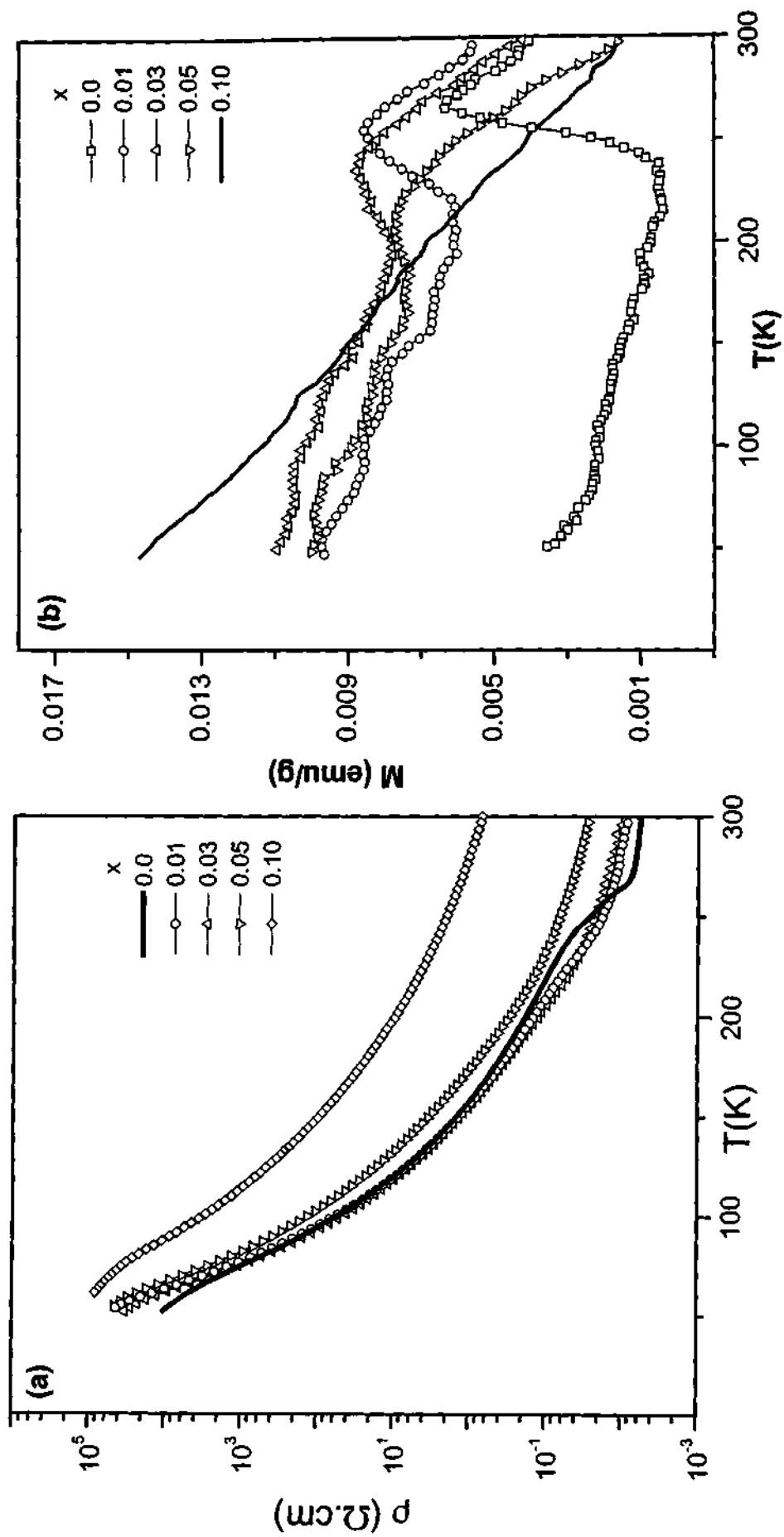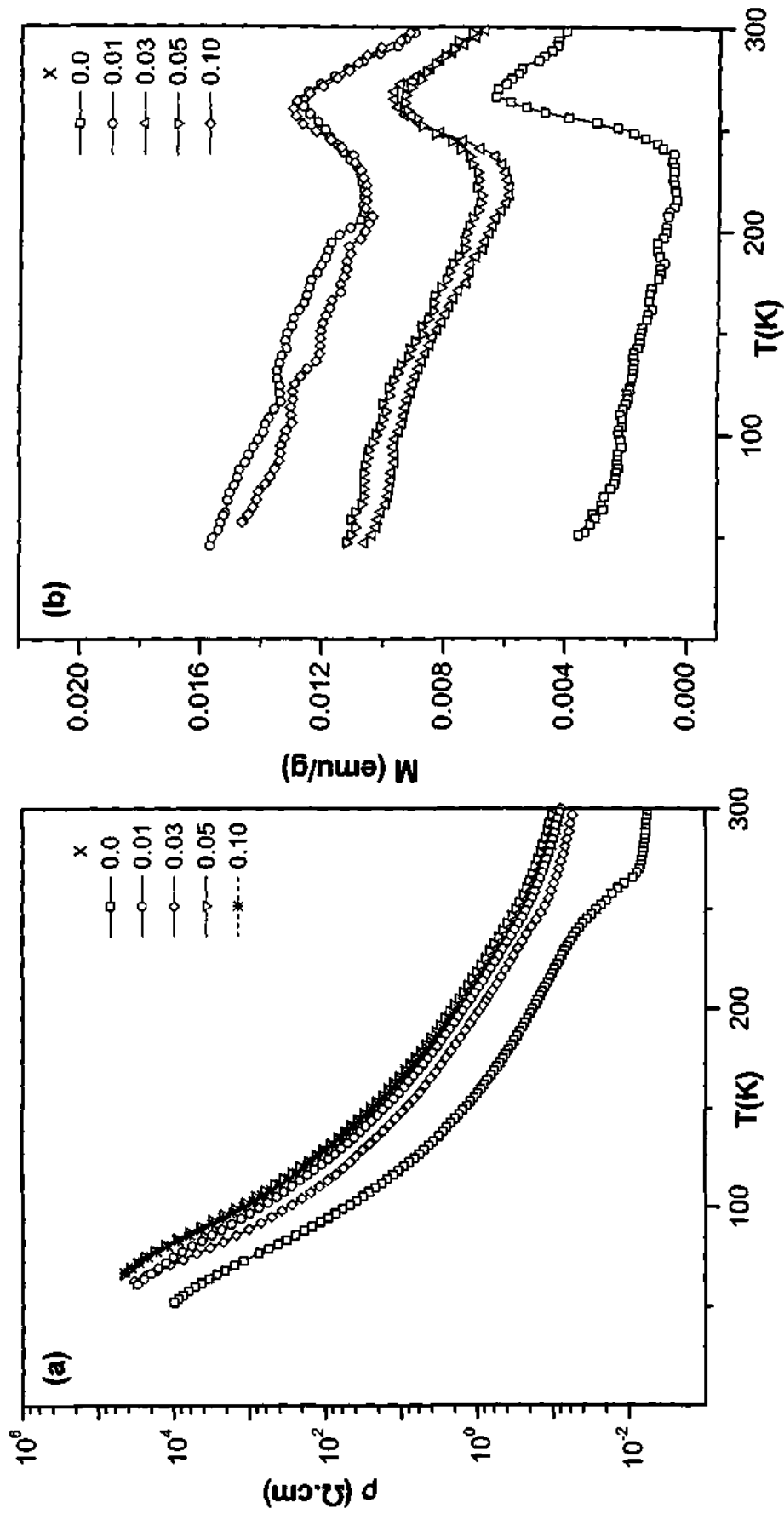Fig.4.5.8 Temperature variation of (a) the resistivity and (b) the magnetization of $Ca_{0.64}Pr_{0.36}Mn_{1-x}Ga_xO_3$.

215

Fig.4.5.9 Temperature variation of (a) the resistivity and (b) the magnetization of $Ca_{0.64}Pr_{0.36}Mn_{1-x}Ge_xO_3$.

216

hole-doped manganate like $Nd_{0.5}Ca_{0.5}MnO_3$ could be melted by appreciable *substitution* at

the B-site by Cr^{3+} or Ru^{4+} (Section 4.2). In $Ca_{1-x}Ln_xMnO_3$ ($x = 0.36$, Ln = La, Nd or Gd),

however, 3% doping with Cr does not completely destroy the charge ordering. We do not

observe an insulator-metal transition on Cr doping as in the case of some of the hole-

doped charge-ordered manganates (Fig. 4.5.10).

Conclusions

The present investigations demonstrate that charge-ordering in electron doped

manganates is distinctly different from that in the analogous hole-doped manganates. In a

given family of manganates, the charge-ordering transition temperature, T_{CO}, increases

with the electron concentration. In fact, T_{CO} decreases with decrease in $\langle r_A \rangle$, unlike in the

case for the $Ln_{0.5}A_{0.5}MnO_3$ manganates, where it increases. The T_{CO} decreases linearly

with the increase in size mismatch, σ^2. Also, the T^0_{CO} value is higher for the electron-

doped manganates, $Ca_{1-x}Ln_xMnO_3$ with $x = 3/8$ when compared to the half-doped

manganates (see Section 4.1). Substitution of the B-site in electron-doped manganate ($x =$

0.36) by Ga and Ge does not have much effect. Even substitution of a transition metal ion

such as Cr at the B-site does not affect the charge-ordering in $Ca_{0.64}Ln_{0.36}MnO_3$ (Ln = La,

Nd and Gd) manganates and the charge-ordered state in these manganates is more robust

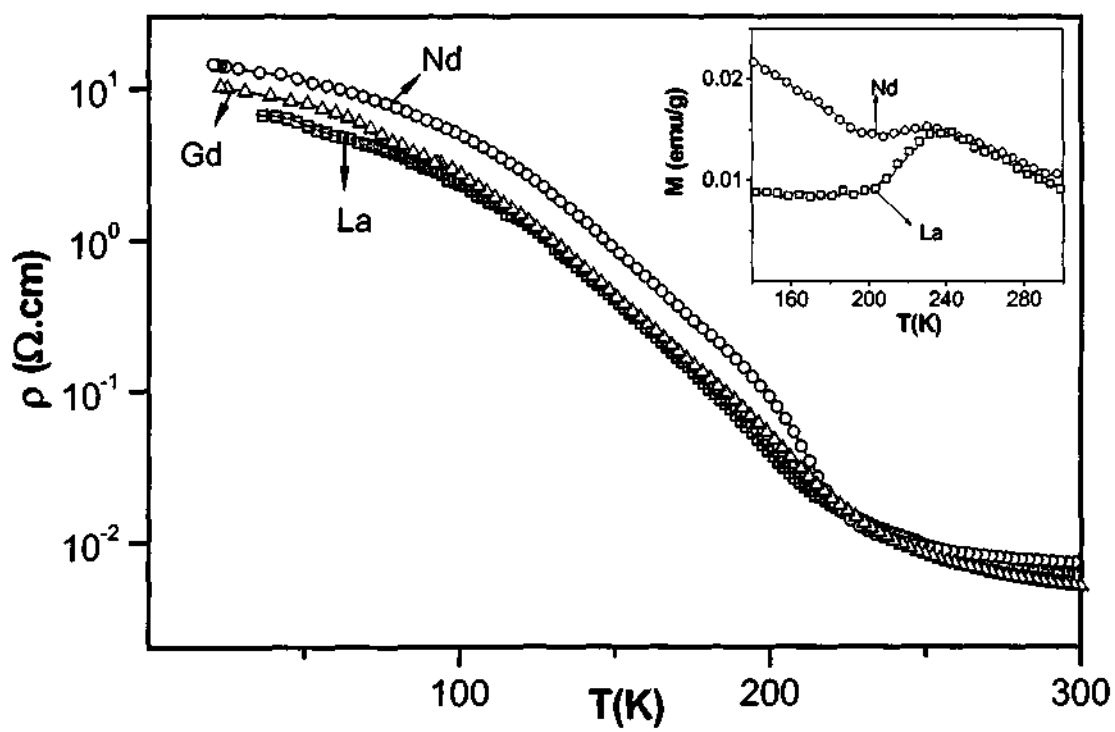than those of the half-doped manganates.

Fig. 4.5.10 The effect of 3% Cr doping on the electrical resisitivity of $Ca_{0.64}Ln_{0.36}MnO_3$
(Ln = La, Nd , Gd). In the inset, typical magnetization data showing charge-ordering
transitions are shown.

4.6 Effect of cation size and disorder on the structure and properties of rare earth cobaltates, $Ln_{0.5}A_{0.5}CoO_3$ (Ln = Rare Earth, A = Sr, Ba)

Cobaltates of the general formula $Ln_{0.5}A_{0.5}CoO_3$ (Ln = rare earth, A = Sr or Ba) were investigated and the unit cell parameters of representative cobaltates are listed in Table 4.6.1. In Table 4.6.1, we have also listed the weighted average radius, $\langle r_A \rangle$, and the σ^2 values of these materials. Rietveld analysis of the powder X-ray diffraction data of the cobaltates gave good fits as shown for five of the materials in Figures 4.6.1 and 4.6.2. The atomic co-ordinates for some of the cobaltates are given in Table 4.6.2. The structural data reveal that when A = Sr, the structure is rhombohedral (space group: $R\bar{3}c$) up to Ln = Nd. In the case of $Nd_{0.5}Sr_{0.5}CoO_3$ we could get an equally good fits for the Pnma and $R\bar{3}c$ space groups, and we have, therefore, preferred the space group with higher symmetry as per the normal practice. When Ln = Gd, the structure is orthorhombic (space group: Pnma). The corresponding Ba compounds are all however orthorhombic with the space group Pmmm. The A-site coordination number is 12 when the structure is rhombohedral and 9 when it is orthorhombic. In Fig. 4.6.3, we show rhombohedral and orthorhombic structures for purpose of illustration. In Table 4.6.3 we list some of the structural parameters. The Co-O bond distances listed in the table show how the CoO_6 octahedra are distorted in the orthorhombic structure, especially in the Pmmm space group of the Ba compounds.

In Fig. 4.6.4(a), we show the temperature-variation of the magnetization of a few compositions of $Ln_{0.5}A_{0.5}CoO_3$. The T_C values obtained from the magnetization data are listed in Table 4.6.1. In Fig. 4.6.5, T_C values obtained by us are plotted against $\langle r_A \rangle$, along

219

Table 4.6.1

Structure and Properties of $Ln_{0.5}A_{0.5}CoO_3$

Ln	A	Space group	$\langle r_A \rangle$ (Å)	σ^2 (Å^2)	Lattice parameter (Å)			T_C (K)
					a	b	c	
La	Sr	R $-\overline{3}$ c[a]	1.40	0.0016	5.4152	-	-	258
Nd	Sr	R $-\overline{3}$ c[b]	1.355	0.0072	5.3770	-	-	226
Gd	Sr	Pnma	1.329	0.0123	5.3746	7.5601	5.3723	162
La	Ba	R $-\overline{3}$ c[c]	1.485	0.0156	5.4997	-	-	219
Nd	Ba	Pmmm	1.317	0.024	11.7100	11.6778	7.6130	178
Gd	Ba	Pmmm	1.288	0.033	11.7196	11.6323	7.5392	--

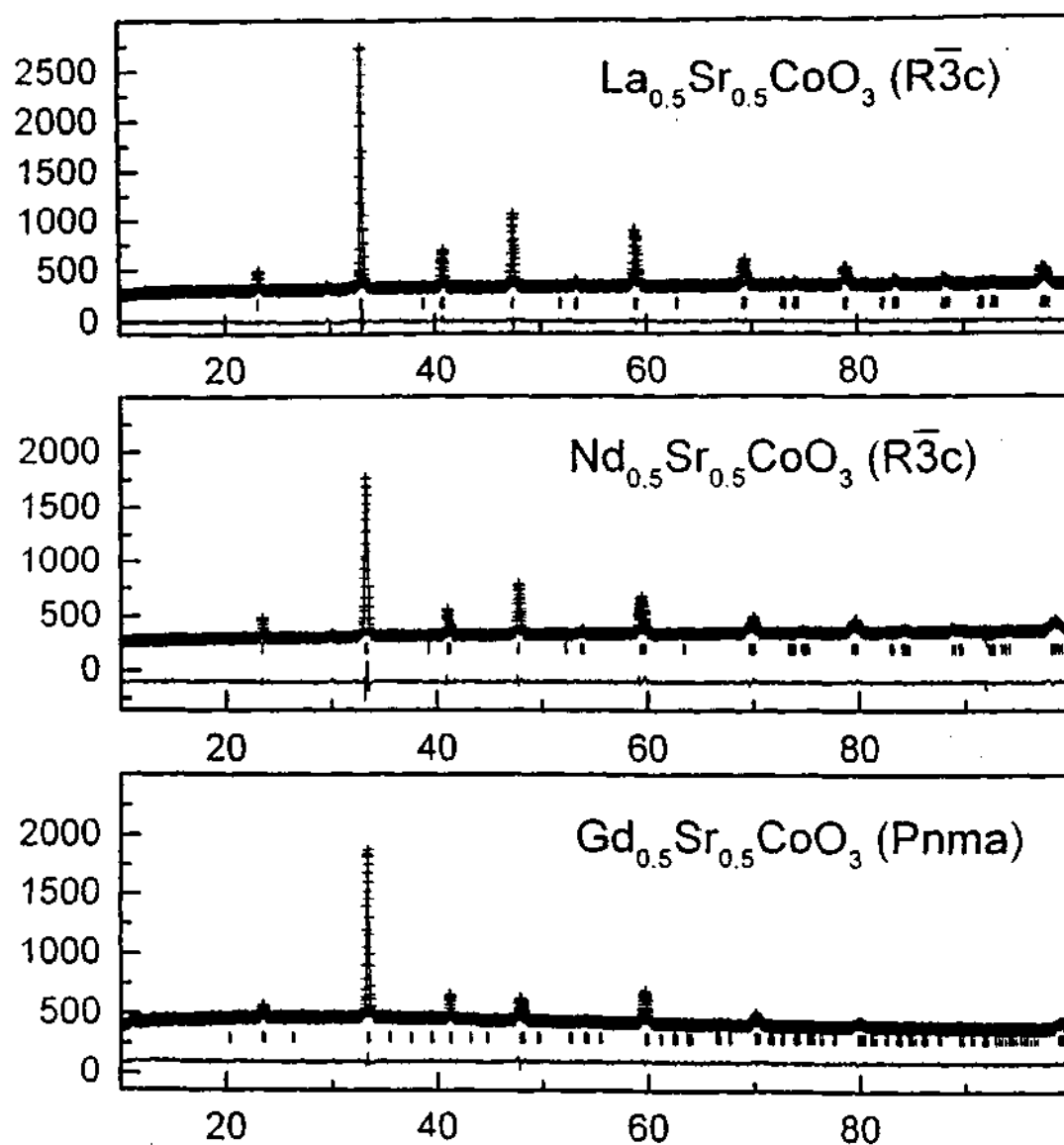(a) $\alpha = 60.17\,^\circ$

(b) $\alpha = 60.28\,^\circ$

(c) $\alpha = 60.04\,^\circ$

Fig. 4.6.1 Powder X-ray diffraction patterns for the representative members of $Ln_{0.5}Sr_{0.5}CoO_3$. The calculated profile and the difference curve obtained from Rietveld analysis are also shown.
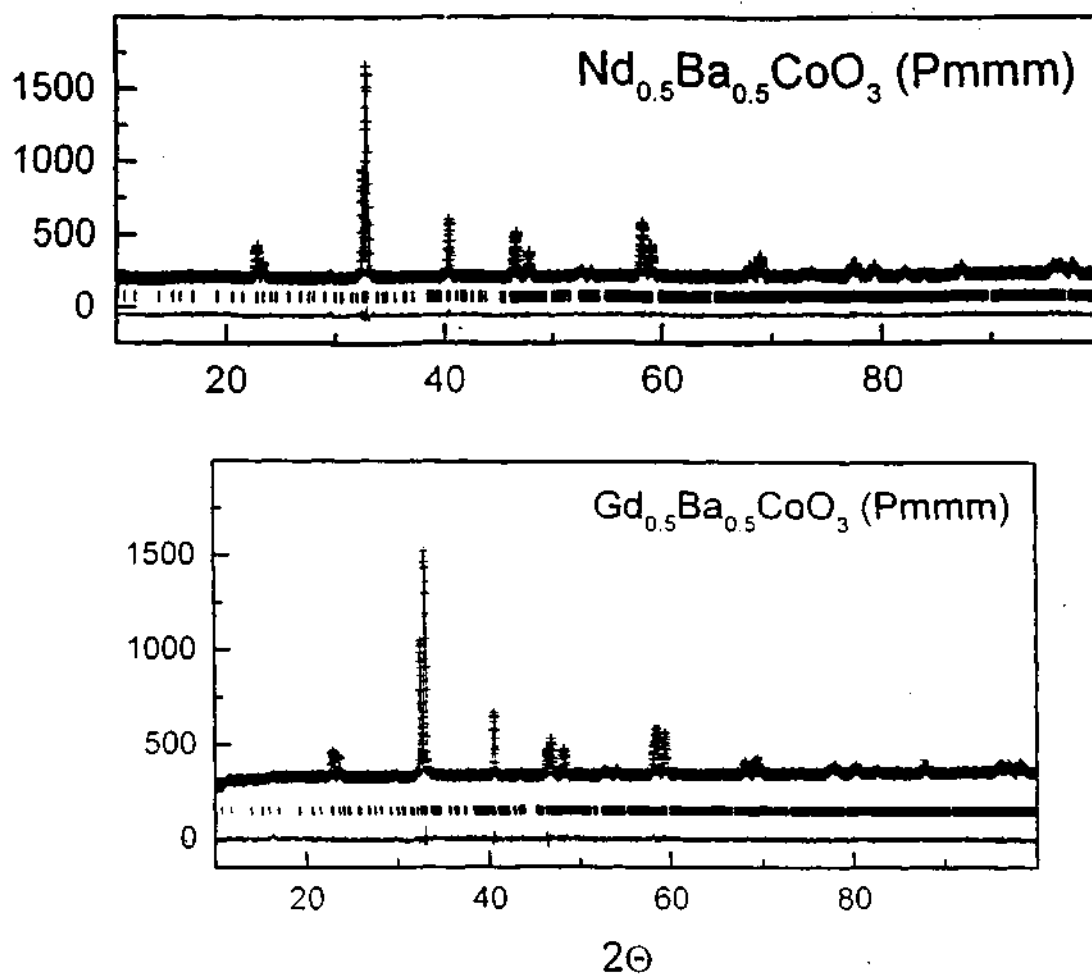
Fig. 4.6.2 Powder X-ray diffraction patterns for the representative members of $Ln_{0.5}Ba_{0.5}CoO_3$. The calculated profile and the difference curve obtained from Rietveld analysis are also shown.

Table 4.6.2
Atomic coordinates of a few members of $Ln_{0.5}A_{0.5}CoO_3$

Ln	A	atom	site	x	y	z	Uiso
La	Sr	La/Sr	2a	0.25000	0.25000	0.25000	0.00350
		Co	2b	0.00000	0.00000	0.00000	0.00376
		O	6e	0.28006	0.21994	0.75000	0.01221
Nd	Sr	Nd/Sr	2a	0.25000	0.25000	0.25000	0.00611
		Co	2b	0.00000	0.00000	0.00000	0.00606
		O	6e	0.29662	0.20338	0.75000	0.00118
Gd	Sr	Gd/Sr	4c	0.00407	0.25000	0.00490	0.02818
		Co	4b	0.00000	0.00000	0.50000	0.02018
		O	8d	0.30840	-0.00712	0.25408	0.05097
		O	4c	0.08477	0.2500	0.50490	-0.03259
Nd	Ba	Nd/Ba	1c	0.00000	0.00000	0.50000	0.00959
		Nd/Ba	2n	0.00000	0.67102	0.50000	0.01407
		Nd/Ba	2j	0.31649	0.00000	0.50000	0.04112
		Nd/Ba	4z	0.33870	0.67146	0.50000	0.00225
		Nd/Ba	1a	0.00000	0.00000	0.00000	-0.00658
		Nd/Ba	2m	0.00000	0.66496	0.00000	-0.01020
		Nd/Ba	2I	0.33424	0.00000	0.00000	-0.01217
		Nd/Ba	4y	0.32853	0.66496	0.00000	0.00080
		Co	2t	0.50000	0.50000	0.74589	-0.04881
		Co	4v	0.50000	0.82006	0.73592	0.04939
		Co	4x	0.84936	0.50000	0.74713	-0.00517
		Co	8μ	0.82403	0.16557	0.25343	-0.00720
		O	1h	0.50000	0.50000	0.50000	0.13774
		O	2p	0.50000	0.84084	0.50000	-0.03272
		O	2l	0.15382	0.50000	0.50000	0.06328
		O	4z	0.18089	0.84139	0.50000	0.09803
		O	2s	0.50000	0.00000	0.70000	-0.00021
		O	4v	0.50000	0.66554	0.69596	-0.07491
		O	4w	0.86807	0.00000	0.76102	-0.02076
		O	8μ	0.83519	0.33170	0.27143	-0.01216
		O	2r	0.00000	0.50000	0.71388	-0.00142
		O	4u	0.00000	0.83147	0.69421	0.02978
		O	4x	0.66299	0.50000	0.73289	0.04036
		O	8μ	0.67560	0.16653	0.28503	0.03245
		O	1f	0.50000	0.50000	0.00000	-0.04651
		O	2o	0.50000	0.81642	0.00000	-0.07971
		O	2k	0.18571	0.50000	0.00000	-0.04482
		O	4y	0.16576	0.85300	0.00000	0.07722

223

Table 4.6.3

Important structural parameters of a few members of $Ln_{0.5}A_{0.5}CoO_3$

$Ln_{0.5}A_{0.5}CoO_3$		bond distances (Å)	bond angles (deg.)
Ln	A	Co-O	Co-O-Co
La	Sr	6 × 1.9336	6 × 164.96
Nd	Sr	6 × 1.9217	6 × 164.94
Gd	Sr	2 × 1.7107	4 × 165.23
		2 × 1.9444	2 × 152.85
		2 × 2.1203	
Nd	Ba[a]	1× 2.0989	2 × 180.00
		1 × 2.0039	2 × 174.19
		1× 1.9488	2 × 159.31
		1 × 1.9448	
		1 × 1.8794	
		1 × 1.7546	
Gd	Ba[a]	1 × 1.9013	1 × 174.72
		1 × 1.8984	1 × 172.08
		2 × 1.8932	1 × 169.15
		1 × 1.8749	2 × 165.93
		1 × 1.8724	1 × 151.58

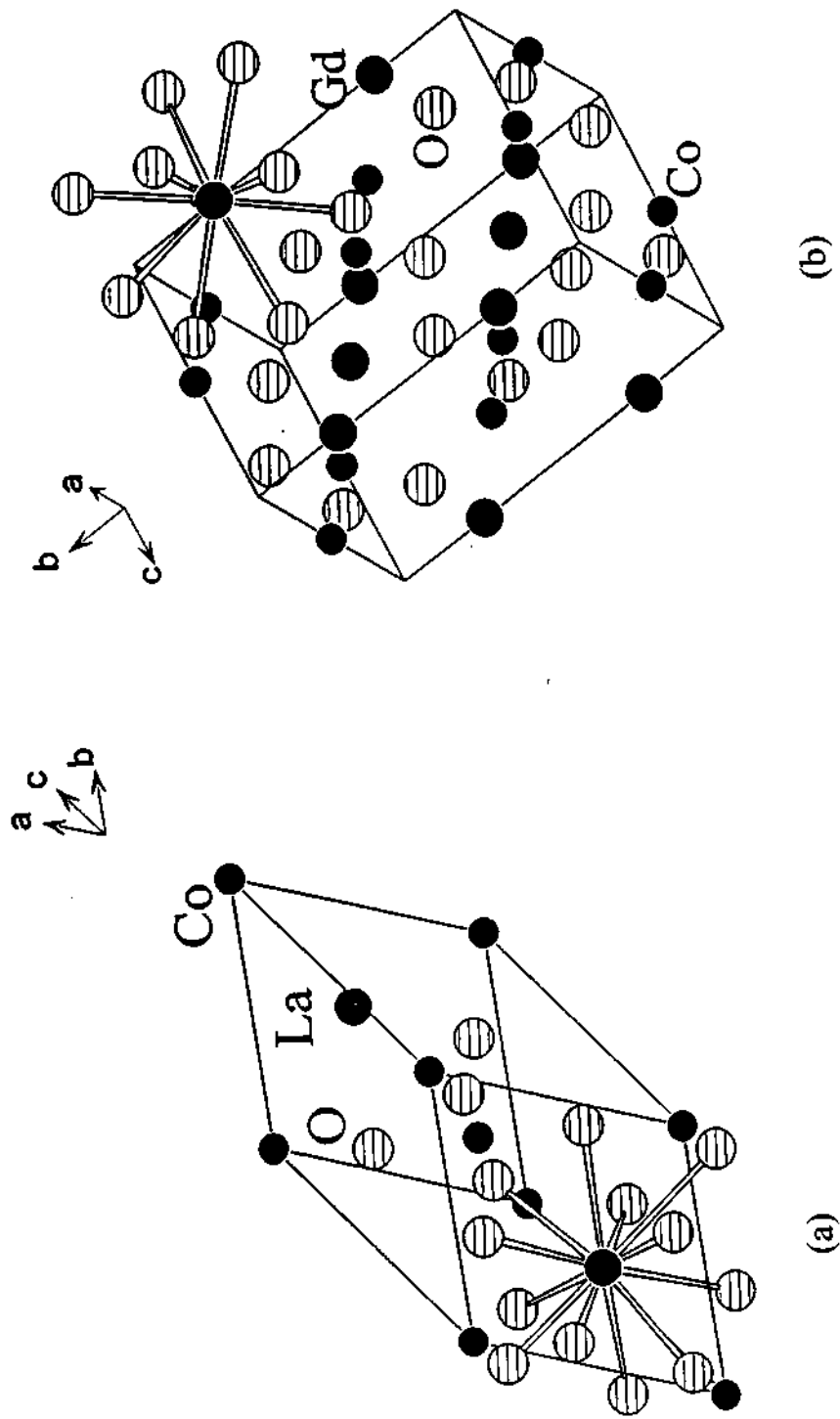[a] There are other unique sets of six Co-O distances in this compound and only one representative set is listed here.

Fig. 4.6.3 Rhombohedral and orthorhombic structures of representative members of $Ln_{0.5}A_{0.5}CoO_3$, showing different coordination of

the A-site cations: (a) La, Sr and (b) Gd, Sr.

with some of the data from the literature. The T_C increases up to a $\langle r_A \rangle$ value of 1.40Å and decreases thereafter. The shape of the curve in Fig. 4.6.5 is similar to the T_C - $\langle r_A \rangle$ plot for $Ln_{0.7}A_{0.3}MnO_3$ [1]. The decrease in T_C for $\langle r_A \rangle$ > 1.40Å is likely to arise from A-site cation-disorder, just as in the case of the manganates [2,3].

Electrical resistivity data of the cobaltates also reflect the effect of cation size and disorder. In Fig. 4.6.4(b), we show the temperature-variation of the electrical resistivity of the $Ln_{0.5}A_{0.5}CoO_3$ compounds. Both $La_{0.5}Sr_{0.5}CoO_3$ and $Nd_{0.5}Sr_{0.5}CoO_3$ show the expected metallic behaviour, but orthorhombic $Gd_{0.5}Sr_{0.5}CoO_3$ shows a slight departure from metallic behaviour. While $La_{0.5}Ba_{0.5}CoO_3$ is metallic, $Nd_{0.5}Ba_{0.5}CoO_3$ is an insulator. $Pr_{0.5}Ba_{0.5}CoO_3$ is reported to be an insulator [4]. It is interesting that $Pr_{0.5}Ba_{0.5}CoO_3$ and $Nd_{0.5}Ba_{0.5}CoO_3$ are insulating, in spite of the large $\langle r_A \rangle$, unlike $La_{0.5}Ba_{0.5}CoO_3$ and the strontium analogues. This is likely to be due to the large cation-size disorder, with σ^2 > $0.01Å^2$. $Gd_{0.5}Sr_{0.5}CoO_3$ with $\sigma^2 \approx 0.012Å^2$ tends to be insulating because it also has a relatively small $\langle r_A \rangle$. These results suggest that cation-size disorder can render a material insulating even though the $\langle r_A \rangle$ is considerably large, as in the case of $Ln_{0.5}Ba_{0.5}CoO_3$ (Ln = Pr, Nd). These results show the important role of cation size and disorder on both the magnetic and the electrical properties.

[1] (a) R. Mahesh, R. Mahendiran, A. K. Raychaudhuri and C. N. R. Rao, J. Solid State Chem. 120, 204 (1995). (b)H. Y. Hwang, S.-W. Cheong, P. G. Radaelli, M. Marezio and B. Batlogg, Phys. Rev. Lett. 75, 914 (1995).

[2] (a) L. M. Rodriguez-Martinez and J. P. Attfield, Phys. Rev. B54, R15622 (1996). (b) L. M. Rodriguez-Martinez and J. P. Attfield, Phys. Rev. B58, 2426 (1998).

[3] F. Damay, C. Martin, A. Maignan and B. Raveau, J. Appl. Phys. 82, 6181 (1997).

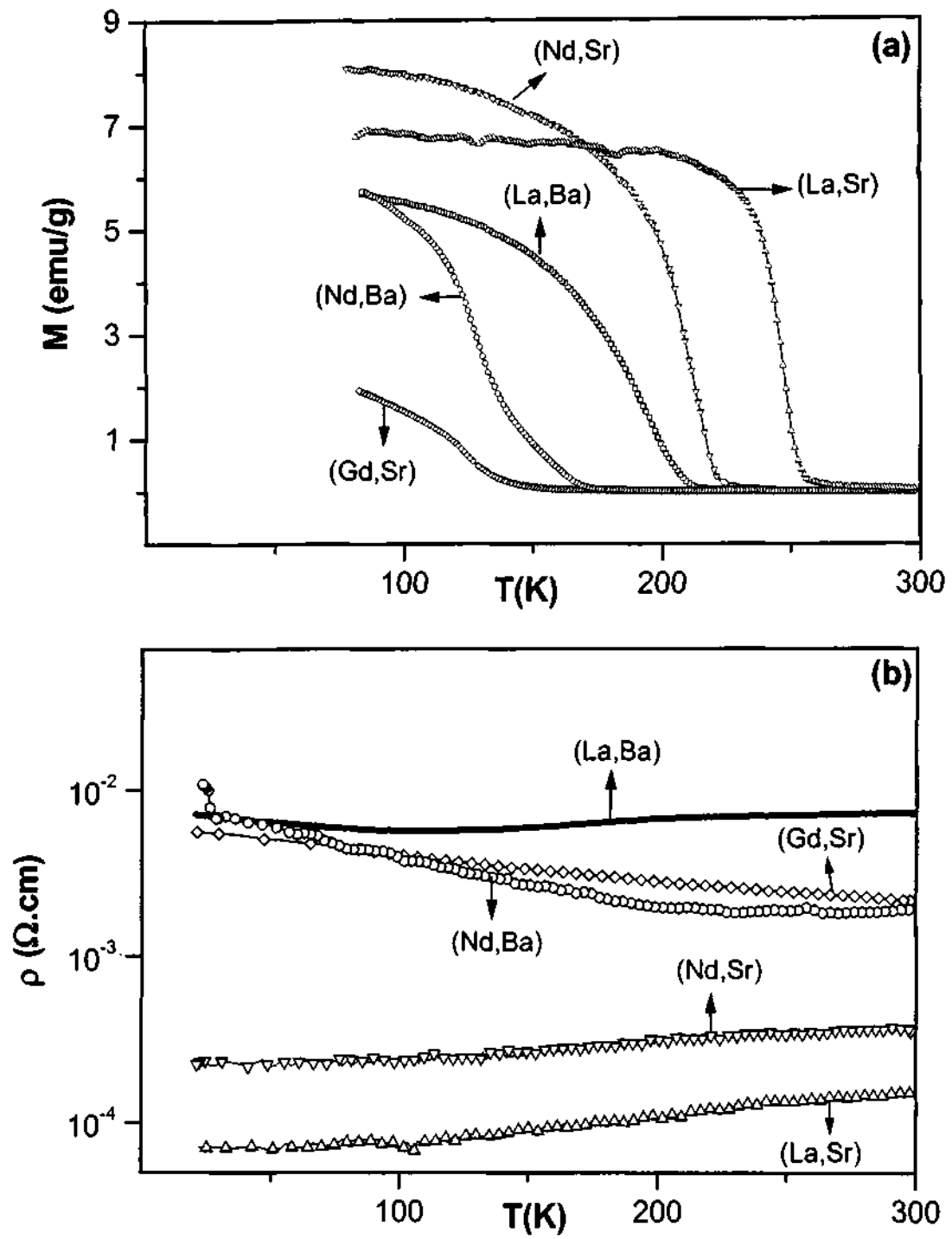Fig. 4.6.4 Temperature variation of (a) the magnetization and (b) the electrical resisitivity

of the cobaltates $Ln_{0.5}A_{0.5}CoO_3$. Ln and A are indicated in the figure.

227

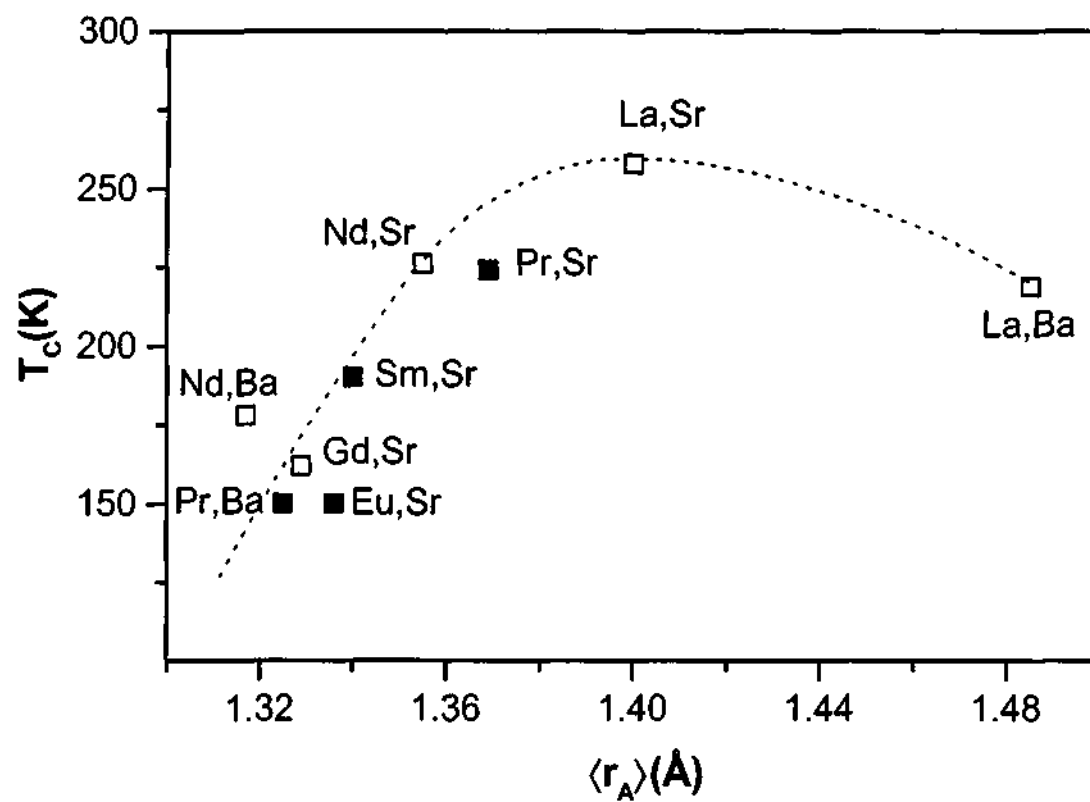Fig. 4.6.5 Variation of the ferromagnetic Curie temperature, T_C, with $\langle r_A \rangle$ in $Ln_{0.5}A_{0.5}CoO_3$. Ln and A are indicated in the figure. The filled symbols are the data from the literature. The broken curve is drawn as a guide to the eye.

$Gd_{0.5}Ba_{0.5}CoO_3$ ($\langle r_A \rangle$ = 1.288Å) with a large value of σ^2 ($0.033Å^2$) as well as orthorhombic distortion, exhibits unique magnetic and transport properties. It is not ferromagnetic as the La, Pr and Nd derivatives of the same series. Instead, it shows a metamagnetic type of transition around 240 K as illustrated in Fig. 4.6.6(a). A similar transition has been reported *by Troyanchuk et al.* [4]. Across the magnetic transition, the material remains an insulator. $Gd_{0.5}Ba_{0.5}CoO_3$ also exhibits a small resistivity transition at 340 K as revealed in Fig. 4.6.6(b), in agreement with the reports in the literature [4,5]. This transition has been attributed to charge ordering of the Co^{3+} and Co^{4+} ions [5].The electron diffraction pattern of $Gd_{0.5}Ba_{0.5}CoO_3$ along (001) in Fig. 4.6.7 shows the superlattice reflections. We do not however see the resistivity anomaly around 250 K reported by *Troyanchuk et al.* [4(b)]. Magnetoresistance measurements show about 17% negative magnetoresistance (MR) at 75 K in a field of 5T, but no MR maximum at 250 K as reported by *Troyanchuk et al.* [4(b)]. There is a small increase in MR at 340 K where the resistivity transition occurs (Fig. 4.6.6(b)).

In order to investigate the effect of the A-site cation size-mismatch on the magnetic and electrical properties of the cobaltates, we have systematically varied σ^2 in two series of compounds with fixed $\langle r_A \rangle$ values of 1.357 and 1.369Å. We list the lattice parameters and σ^2 values in Tables 4.6.4 and 4.6.5. We show typical magnetization data of the series with $\langle r_A \rangle$ = 1.357Å in Fig. 4.6.8(a) in order to illustrate how the ferromagnetic T_C

[4] (a) I. O. Troyanchuk, N. V. Kasper, D. D. Khalyavin, H. Szymczak, R. Szymczak and M. Baran Phys. Rev. B58, 2418 (1998). (b) I. O. Troyanchuk, N. V. Kasper, D. D. Khalyavin, H. Szymczak, R. Szymczak and M. Baran Phys. Rev. Lett. 80, 3380 (1998).

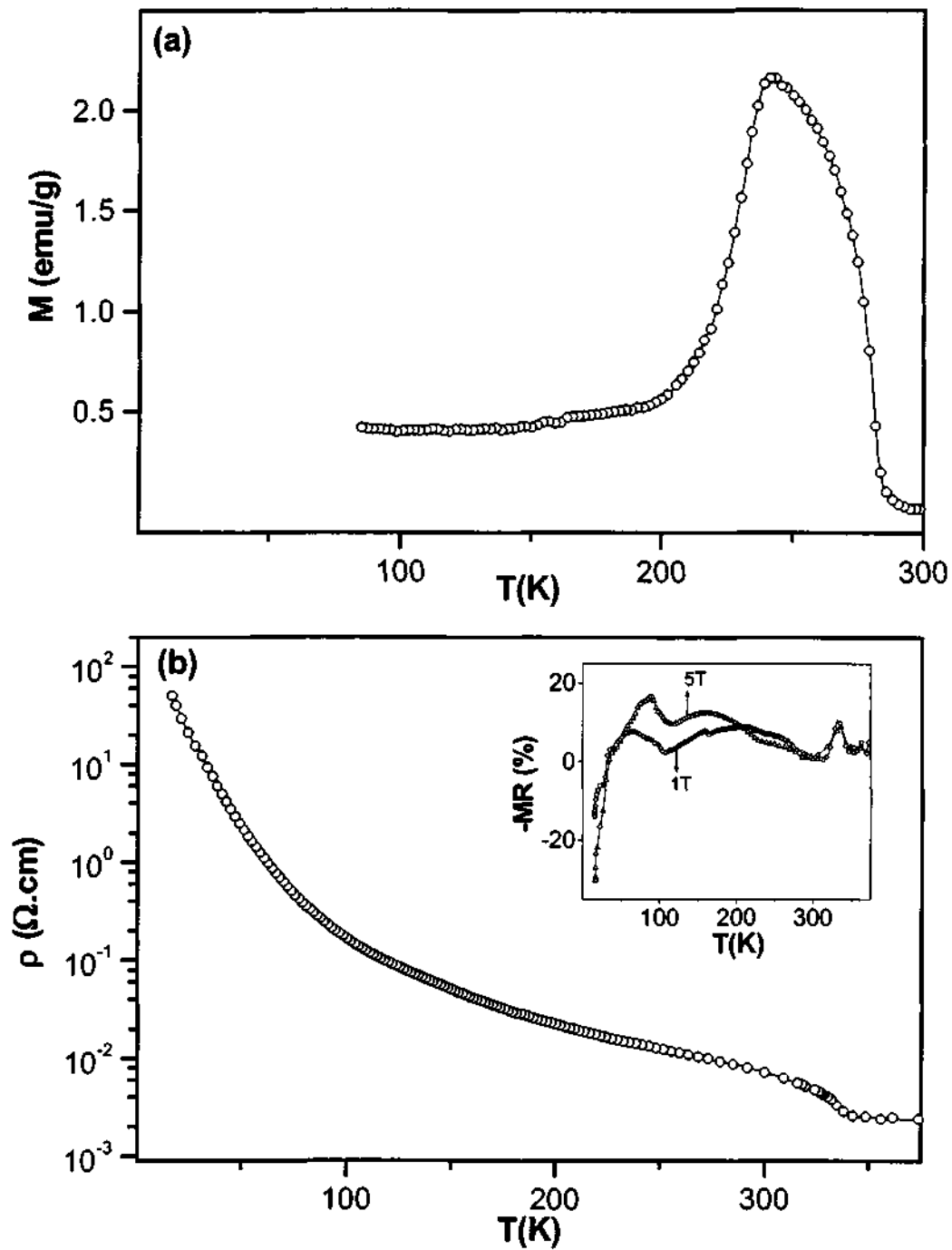[5] Y. Moritomo, M. Takeo, X. J. Liu, T. Akimoto and A. Nakamura Phys. Rev. B58, R13334 (1998).

Fig. 4.6.6 Temperature variation of (a) magnetization and (b) resistivity of the cobaltate

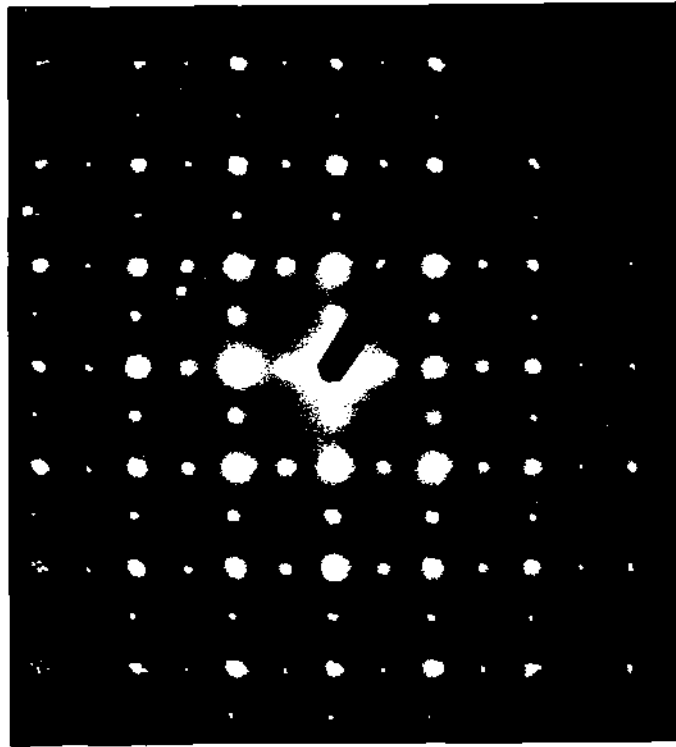$Gd_{0.5}Ba_{0.5}CoO_3$. The inset in (b) shows the −MR(%) versus temperature plot in a field of 1

and 5T.

230

Fig. 4.6.7 SAED pattern of $Gd_{0.5}Ba_{0.5}CoO_3$.

Table 4.6.4

Structure and properties of $Ln_{0.5-x}Ln'_xA_{0.5-y}A'_yCoO_3$ with a fixed $\langle r_A \rangle$ of 1.357 Å

Composition	σ^2 $(Å^2)$	Lattice parameter		T_C (K)
		$\underline{a}$ (Å)	α (deg)	
$Pr_{0.15}La_{0.35}Ca_{0.16}Sr_{0.34}CoO_3$	0.0026	5.3939	60.15	236
$Nd_{0.15}La_{0.35}Sr_{0.355}Ca_{0.145}CoO_3$	0.0034	5.3913	60.23	233
$Nd_{0.1}Pr_{0.4}Sr_{0.45}Ca_{0.05}CoO_3$	0.0053	5.3858	60.37	227
$Gd_{0.11}Pr_{0.39}Sr_{0.5}CoO_3$	0.0070	5.3887	60.32	222
$Nd_{0.5}Sr_{0.5}CoO_3$	0.0072	5.3770	60.28	226
$Sm_{0.315}La_{0.185}Sr_{0.5}CoO_3$	0.0077	5.3883	60.24	223
$Gd_{0.245}La_{0.255}Sr_{0.5}CoO_3$	0.0081	5.3948	60.16	217
$Nd_{0.35}Gd_{0.15}Sr_{0.45}Ba_{0.05}CoO_3$	0.0118	5.3882	60.24	207
$Sm_{0.5}Sr_{0.405}Ba_{0.095}CoO_3$	0.0157	5.3896	60.10	191
$Nd_{0.2}Gd_{0.3}Sr_{0.395}Ba_{0.105}CoO_3$	0.0168	5.3943	60.01	181

Table 4.6.5

Structure and properties of $Ln_{0.5-x}Ln'_{x}A_{0.5-y}A'_{y}CoO_3$ with a fixed $\langle r_A \rangle$ of 1.369 Å

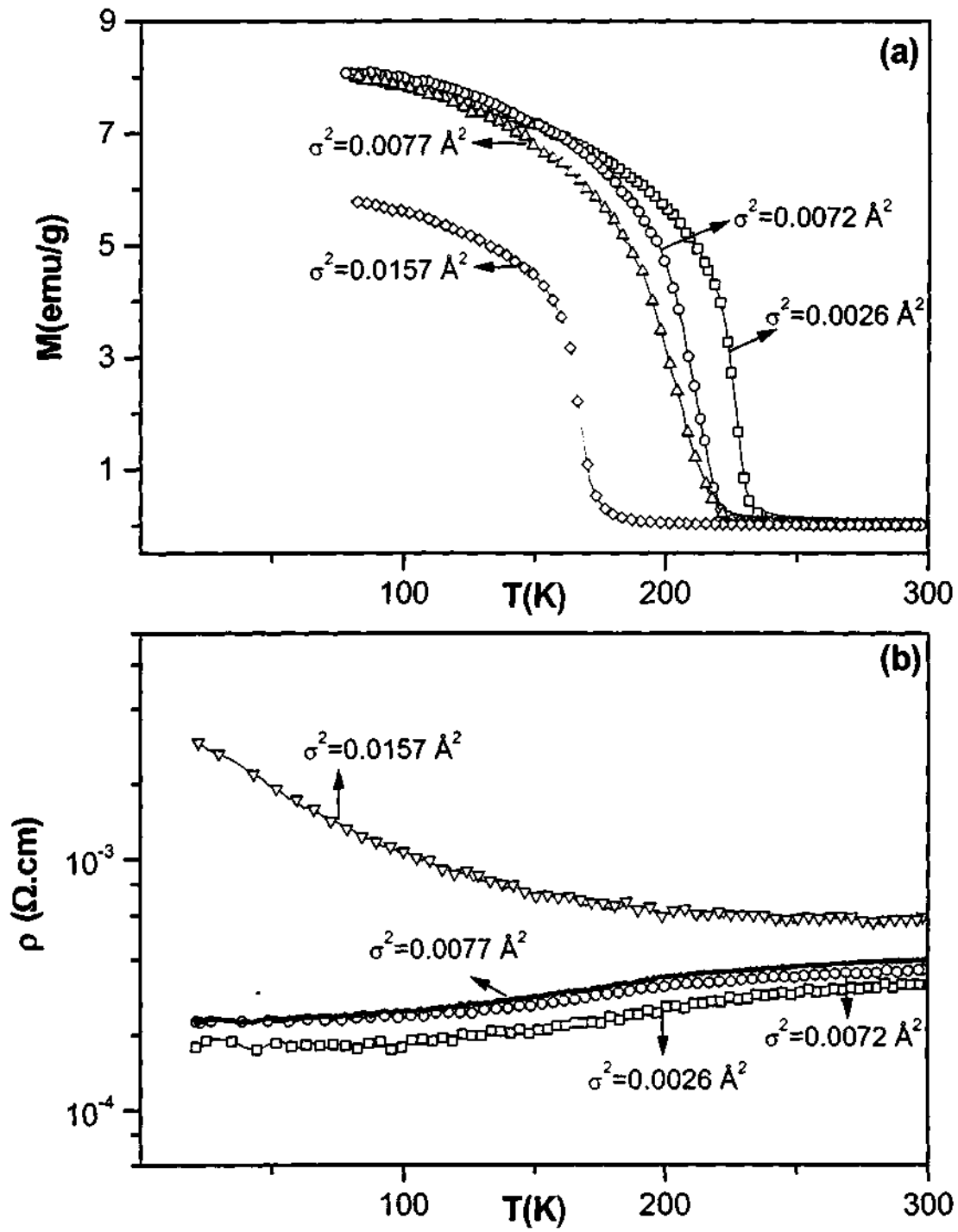| Composition	σ^2 (Å^2)	Lattice parameter		T_C (K)
		$\underline{a}$ (Å)	α (deg)	
$Pr_{0.5}Sr_{0.5}CoO_3$	0.0051	5.3839	60.41	230
$La_{0.235}Sm_{0.265}Sr_{0.5}CoO_3$	0.0070	5.3942	60.13	214
$La_{0.315}Dy_{0.185}Sr_{0.5}CoO_3$	0.0085	5.3957	60.10	200
$Pr_{0.3}Gd_{0.2}Sr_{0.41}Ba_{0.09}CoO_3$	0.0134	5.3982	60.08	176
$Pr_{0.2}Gd_{0.3}Sr_{0.36}Ba_{0.14}CoO_3$	0.0178	5.4021	60.08	143

Fig. 4.6.8 Temperature variation of (a) magnetization and (b) resistivity of rhombohedral $Ln_{0.5}A_{0.5}CoO_3$ with fixed $\langle r_A \rangle$ of 1.357 Å and variable σ^2. σ^2 values are shown in the figure.

234

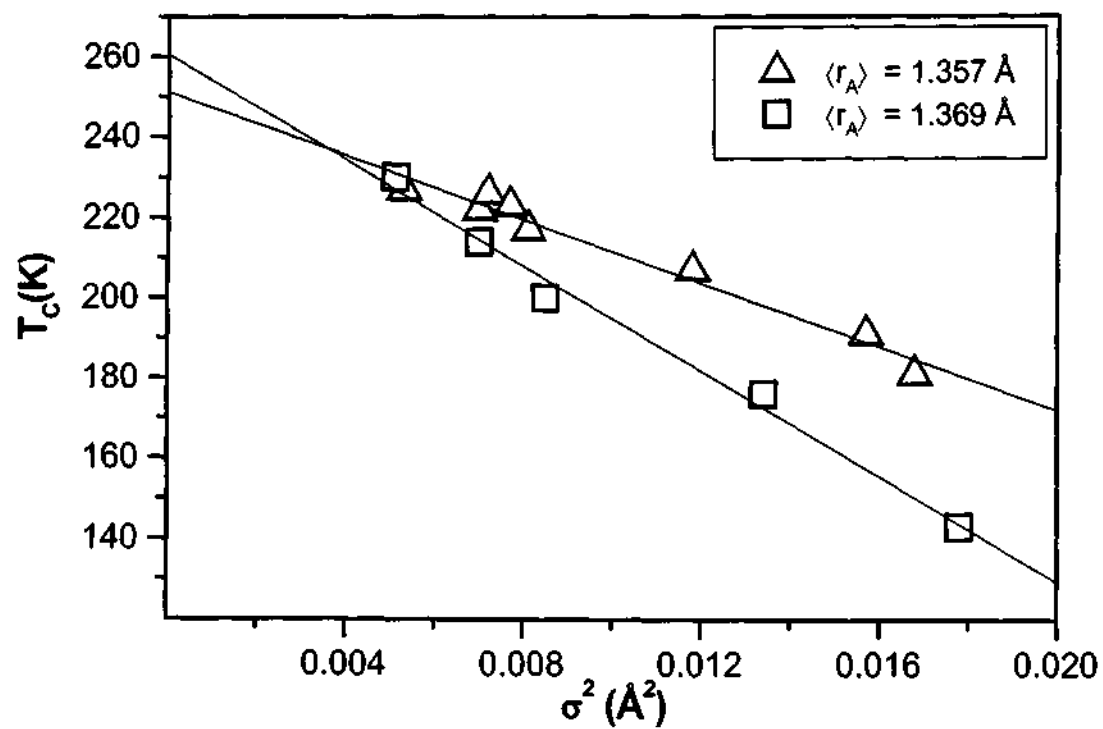Fig. 4.6.9 Variation of the ferromagnetic Curie temperature, T_C with σ^2 in rhombohedral

$Ln_{0.5}A_{0.5}CoO_3$ with fixed $\langle r_A \rangle$ values of 1.357 Å and 1.369 Å.

decreases with the increase in σ^2. We have listed the T_C values of the two series of cobaltates in Tables 4.6.4 and 4.6.5 and plotted the T_C values against σ^2 in Fig. 4.6.9. The plots are fairly linear. We can write the relation as,

$$T_C = T^0_C - p\sigma^2 \qquad\qquad (4.6.1)$$

where the value of the intercept, T^0_C is an estimate of the ideal ferromagnetic Curie temperature that would have been observed in the absence of A-site cation size-disorder ($\sigma^2 = 0$). We find T^0_C to be $251 \pm 3K$ and $261 \pm 4K$ respectively for $\langle r_A \rangle$ values of 1.357 and 1.369Å respectively, the corresponding slopes being $3961 \pm 270K\text{Å}^{-2}$ and $6558 \pm 369K\text{Å}^{-2}$. There is some variation in T^0_C in the cobaltates even for a change of 0.012 Å in $\langle r_A \rangle$, compared to the manganates where marked changes in T^0_C occur for larger changes in $\langle r_A \rangle$ [2,3]. Furthermore, the slope of the T_C - σ^2 plot increases with $\langle r_A \rangle$ in the cobaltates while it decreases in the manganates.

In Fig. 4.6.8(b), we have plotted the electrical resistivity of the cobaltates in Table 4.6.4 with a fixed $\langle r_A \rangle$ of 1.357Å. The materials are metallic for $\sigma^2 < 0.012\text{Å}^2$ and become insulating at higher σ^2, as also corroborated by the data in Fig. 4.6.4(b). This metal-insulator transition is brought about entirely by size disorder. The rare earth cobaltates are distinct from the rare earth manganates in that the latter show an insulator-metal transition around the ferromagnetic T_C and the transition temperature decreases with increase in σ^2. We have plotted the resistivity of $Ln_{0.5}A_{0.5}CoO_3$ at 25 K against σ^2 in Fig. 4.6.10. We see a general increase in resistivity with increase in σ^2 in the cobaltates studied.
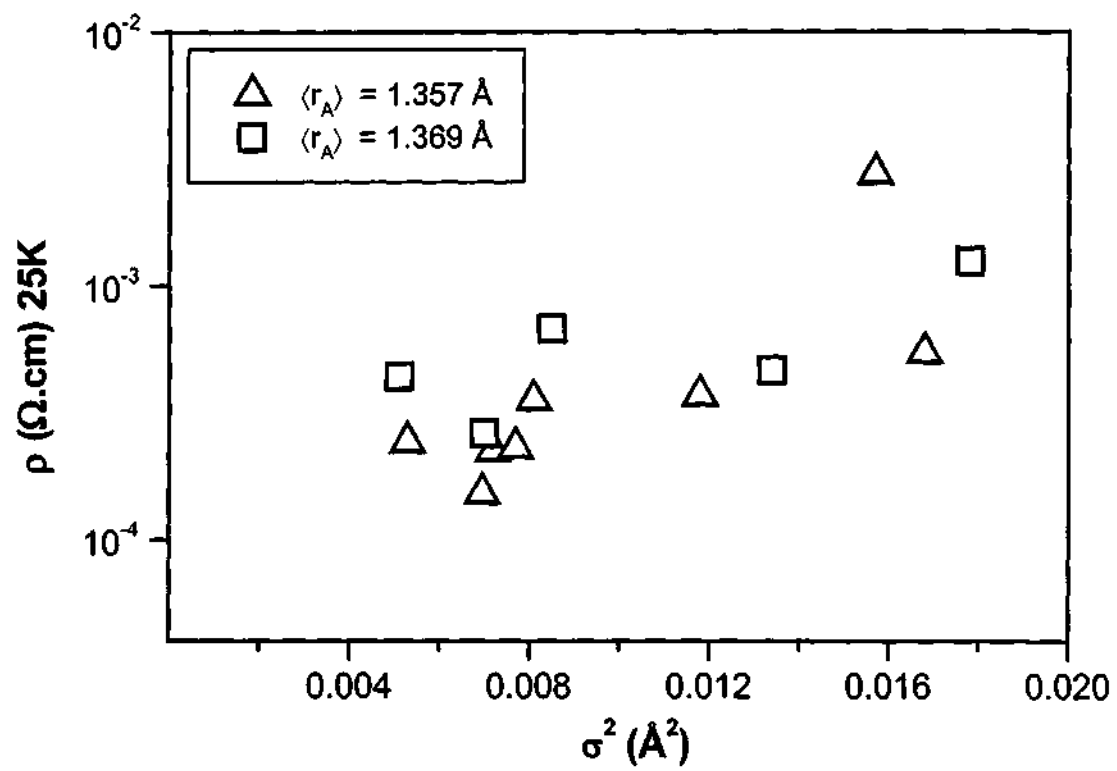
Fig. 4.6.10 Variation of the resistivity of rhombohedral $Ln_{0.5}A_{0.5}CoO_3$ at 25K with σ^2.

Conclusions

The study of rare earth cobaltates shows that the structure of $Ln_{0.5}Sr_{0.5}CoO_3$ is rhombohedral ($R\bar{3}c$) when Ln = La, Pr or Nd, but orthorhombic (Pnma) when Ln = Gd. The $Ln_{0.5}Ba_{0.5}CoO_3$ compounds are all orthorhombic (Pmmm). The ferromagnetic Curie temperature, T_C, of $Ln_{0.5}A_{0.5}CoO_3$ increases with the average size of the A-site cation upto an $\langle r_A \rangle$ of 1.40Å, and decreases thereafter due to size mismatch. Disorder due to cation size mismatch has been investigated by studying the properties of two series of cobaltates with fixed $\langle r_A \rangle$ and differing size variance, σ^2. It is found that T_C decreases linearly with σ^2, according to the relation, $T_C = T^0_C - p\sigma^2$. When σ^2 is large (> 0.012Å^2), the material becomes insulating, providing evidence for a metal-insulator transition caused by cation size-disorder. Thus, $Gd_{0.5}Ba_{0.5}CoO_3$ with a large σ^2 is a charge-ordered insulator below 340 K. The study demonstrates that the average A-cation radius, as well as the cation size-disorder affect the magnetic and transport properties of the rare earth cobaltates significantly.

538.44
.198